Advances in Quantum Nonlinear Optics

A nonclassical journey from the optimization of Silicon Photomultipliers for Quantum Optics to quantum Second-Harmonic Generation

PHD THESIS

UNIVERSITÀ DEGLI STUDI DELL'INSUBRIA

DIPARTIMENTO DI SCIENZA E ALTA TECNOLOGIA

Author:
Giovanni CHESI

Supervisor:
Prof. Alessia ALLEVI

Acronyms

SHG second-harmonic generation

SH second-harmonic

TWB twin-beam state

PDC parametric down conversion

NRF noise reduction factor

SiPM silicon photomultiplier

POVM positive operator-valued measure

PNR photon-number-resolving

MPPC Multi-Pixel Photon Counter

APD avalanche photodiode

GM Geiger-mode

SPAD single-photon avalanche photodiode

PDE photon-detection efficiency

DCR dark-count rate

OCT Optical Cross-Talk

OCT-P prompt cross-talk

OCT-D delayed cross-talk

PSAU Power Supply and Amplification Unit

PBS polarizing cube beam splitter

S/N signal-to-noise ratio

HWP half-wave plate

Contents

List of Figures

List of Tables

List of publications

- Chesi, G., Olivares, S. and Paris, M. G. A. Squeezing-enhanced phase-shift-keyed binary communication in noisy channels. Accepted for publication in *Proceedings*.
- Bondani, M., Chesi, G., Malinverno, L., Allevi, A., Santoro, R. and Caccia, M. Measuring nonclassicality of mesoscopic twin-beam states with Silicon Photomultipliers. Accepted for publication in *Proceedings*.
- Chesi, G., Allevi, A. and Bondani, M. Autocorrelation functions: a useful tool for both state and detector characterisation. *Quantum Meas. Quantum Metrol.* **2019**, *6*, 1-6.
- Chesi, G., Malinverno, L., Allevi, A., Santoro, R., Martemiyanov, A., Caccia, M., and Bondani, M. Optimizing Silicon Photomultipliers for Quantum Optics. *Sci. Rep.* **2019**, *9*, 1-12.
- Chesi, G., Malinverno, L., Allevi, A., Santoro, R., Caccia, M. and Bondani, M. Measuring nonclassicality with silicon photomultipliers. *Opt. Lett.* **2019**, *44*, 1371-1374.
- Chesi, G., Wauters, M. M., Fasola, N., Allevi, A. and Bondani, M. Second Harmonic Revisited: An Analytic Quantum Approach. *Appl. Sci.* **2019**, *9*, 1-14.
- Chesi, G., Olivares, S. and Paris, M. G. A. Squeezing-enhanced phase-shift-keyed binary communication in noisy channels. *Phys. Rev. A* **2018**, *97*, 1-6.
- Allevi, A., Chesi, G. and Bondani, M. Generation of quasi-single-mode twin-beam states in the high-intensity domain. *Int. J. Quantum Inf.* **2017**, **15**, 1-11.

Introduction

The idea of a light amplification system by stimulated emission of radiation, commonly known as *laser*, is one of the most crucial of the last century.
The whole field of Quantum Optics would hardly have been explored and the same idea of *photon*, introduced by Einstein in 1905 to describe the photoelectric effect [1], would not have the slightest experimental confirmation. The photoelectric effect, indeed, does not really require the quantization of the electromagnetic field to correctly explain the data: it has been shown [2] that a semiclassical model, where just the energy exchange with matter is discrete, fulfills the task. However, it was the same Einstein that in 1916 understood and provided a first model for the *stimulated emission* process [3], whose intuition is at the roots of lasers.
Moreover, almost all the Nonlinear Optics phenomena would still be unknown or, at least, mysterious without the localized high-intensity fields achievable with a laser source, even if Maxwell's equations already contain all the information required to classically model these processes and some of them had been already predicted long before the invention of the laser. In this sense, Nonlinear and Quantum Optics share a common story. The basis of these fields are briefly provided in the first chapter of this thesis.
Being a consequence of the invention of the laser, the empirical observations of Nonlinear and Quantum Optics phenomena are very young. As for the former, the first known experiments date back to 1961 and consist in the *second-harmonic generation* [6] (a nonlinear crystal is pumped with a laser whose frequency is doubled in the nonlinear process) and in the *two-photon absorption* [7] (a molecule is excited by the simultaneous absorption of two photons). The first Quantum Optics experiment, namely the observation of photoelectric counts in resonance fluorescence, is even posterior, since it dates back to 1977 [8]. Nevertheless, in few decades a huge number of results has been yielded, even touching the foundations of most current physical theories. Among the best known, we may quote cavity Quantum Electrodynamics and analogue gravity with nonlinear crystals. From the practical point of view, the achieved results pave the way to the improvement of current technologies and new inventions. Nowadays, light-based systems are crucial in Quantum Communication, Quantum-Key-Distribution, Quantum Estimation and Quantum Computation because the so called *quantum resources*, such as *entanglement*, can be efficiently exploited with the current optical technology.
Thus, the characterization of nonclassical states of light and their properties, in particular their correlations, is an essential tool for Quantum Information protocols. These have been originally developed for *qubits*, i.e. two-level quantum systems which can be optically implemented through the polarization of single-photon states. Later, much attention has been drawn by multi-photon states since they are easier to manipulate and may allow encoding of information on the energy eigenstates, i.e. the number states, and exploiting photon-number quantum correlations. To this aim, one needs to generate entangled states of light in the *mesoscopic-intensity regime* and to implement a suitable detection scheme. In particular, it is essential to employ detectors which are sensitive to the photon-number observable. These are the so-called

photon-number-resolving detectors, which give access to the shot-by-shot determination of the number of photons in single detected pulses.
Nowadays, several classes of photon-number-resolving detectors have been developed. In the low-intensity regime, shot-by-shot correlations have been determined through cooled CCDs [9, 10], time-multiplexed devices [82, 83, 11, 12], visible-light photon counters [13] and arrays of nanowire detectors [14]. However, if we look at the mesoscopic intensity domain, we can essentially use hybrid photoemissive detectors [15, 51], multipixel silicon photon counters [79, 81, 96] and other superconductor-based detectors, such as the transition edge sensors [16].
In particular, for the last ten years much interest has been focusing on multipixel silicon photon counters, also known as *silicon photomultipliers (SiPMs)*. They are arrays of single-photon avalanche diodes, called *pixels*, each of them working as an on-off photodetector. If one should link them to a mythological creature, it would be the one-hundred-eyed giant Argo Panoptes, father to the peacock feathers. Silicon photomultipliers benefit from a number of practical advantages which should be relevant in engineering a Quantum Information protocol. Indeed, as to the photon-number resolution, up to now, they beat the hybrid photodetectors and, contrarily to the superconductor-based devices, they work at room temperature. Moreover, their compactness, ruggedness and commercial availability is unique, for what concerns these applications. Nonetheless, they have been employed in many other research fields long before their introduction in Quantum Optics, such as biophotonics [17], gamma-ray spectroscopy [18], nuclear physics [19] and medicine [20]. The reason for that lies in the drawbacks of silicon photomultipliers, which, for Quantum Information applications, are particularly detrimental. Their quantum efficiency is very low (up to $50-60\%$) and serious spurious stochastic effects affect the reliability of the shot-by-shot determination of the photon number, especially because some of them are correlated with the detected light. The most important of these noise sources are *cross-talk* events, spurious counts triggered by avalanches related to proper counts. Afek et al., in their pioneering work [79], state that "*The full potential of these detectors will be realizable when cross talk between pixels is eliminated.*" As a matter of fact, in 2010 these devices could not even hold a candle to the hybrid photodetectors (HPDs) in revealing correlations, as Allevi et al. declare in [42]: "*As SiPMs are affected by dark counts and cross talk that lower the measured correlation coefficients, they are less suitable than HPDs for correctly revealing shot-by-shot photon number correlations.*" However, a new generation of silicon photomultipliers has been recently developed by Hamamatsu [63]. The most striking feature of these novel objects is the small impact of the cross-talk effects, which have been reduced of almost the 90% in ten years. Together with other improvements, this makes silicon photomultipliers definitely promising for quantum applications.
During the last three years at the University of Insubria, we have performed a series of measurements aiming at testing if these devices are really amenable for the detection of nonclassical states and correlations and to which extent. Having repeated the standard characterization which is commonly known in the literature and hence assessed the basic features of the detectors, we implemented a characterization procedure specific for Quantum Optics applications, which basically consists in the analysis of the detected-photon number statistics for different radiation fields, in particular coherent and chaotic light. This procedure allowed us to determine the impact of the most relevant sources of noise on the reconstruction of the statistics and correlations.
Since our results were encouraging, we decided to go quantum. We generated entangled states of light in a mesoscopic regime and used two silicon photomultipliers to reveal quantum correlations and perform conditional measurements. Eventually, we succeeded in detecting the nonclassical properties of these states. The performance of these devices can be further improved, but our research shows that their technological growth goes in this direction and, in particular, suggests how most of the noise sources can be definitely annihilated, pushing forward these novel sensors for future research in Quantum Information. This work is fully described in the second and third chapters of this thesis.
The challenges thrown by Quantum Nonlinear Optics also involve the very description of basic optical phenomena. Second-harmonic generation, as mentioned few lines above, is one of the first nonlinear

observed processes. Some years later, a complete classical model was suggested for that, by Armstrong et al. [21]. Yet, no analytical solutions can be provided for the quantum dynamics of the process. Approximations, perturbative and numeric approaches have been tried up to now, each of them enlightening different nuances of the phenomenon, which can be relevant also from the experimental point of view. Indeed, it has been proved that generating nonclassical states of light via second-harmonic generation is convenient in many respects. This topic is profusely addressed in the fourth chapter of this work, where we also show our results about the quantum dynamics of the process. In particular, we adopted a perturbative approach and used it to retrieve the statistics of the second-harmonic fields given different input pump states.

In summary, here we present our experimental and theoretical work on modern and old topics of Nonlinear Quantum Optics. The thesis is structured as follows.

In the first chapter, we provide a general introduction on the basis of this field, in particular on the main concepts and results that will be needed in the following.

In the second and third chapters, we explain our research [77, 95, 49] on the role of silicon photomultipliers in Quantum Optics experiments. After a specific characterization of the sensors, we used them to detect nonclassical states of light. Different strategies for the estimation of experimental quantities are suggested.

In the fourth chapter, we propose our quantum description for the second-harmonic-generation process [112], based on well-known perturbative methods. After a general introduction on the state of the art, we immediately dive into the problem by explaining the employed methods and showing our analytical results.

Finally, we resume the essence of our achievements and draw our conclusions.

Enjoy!

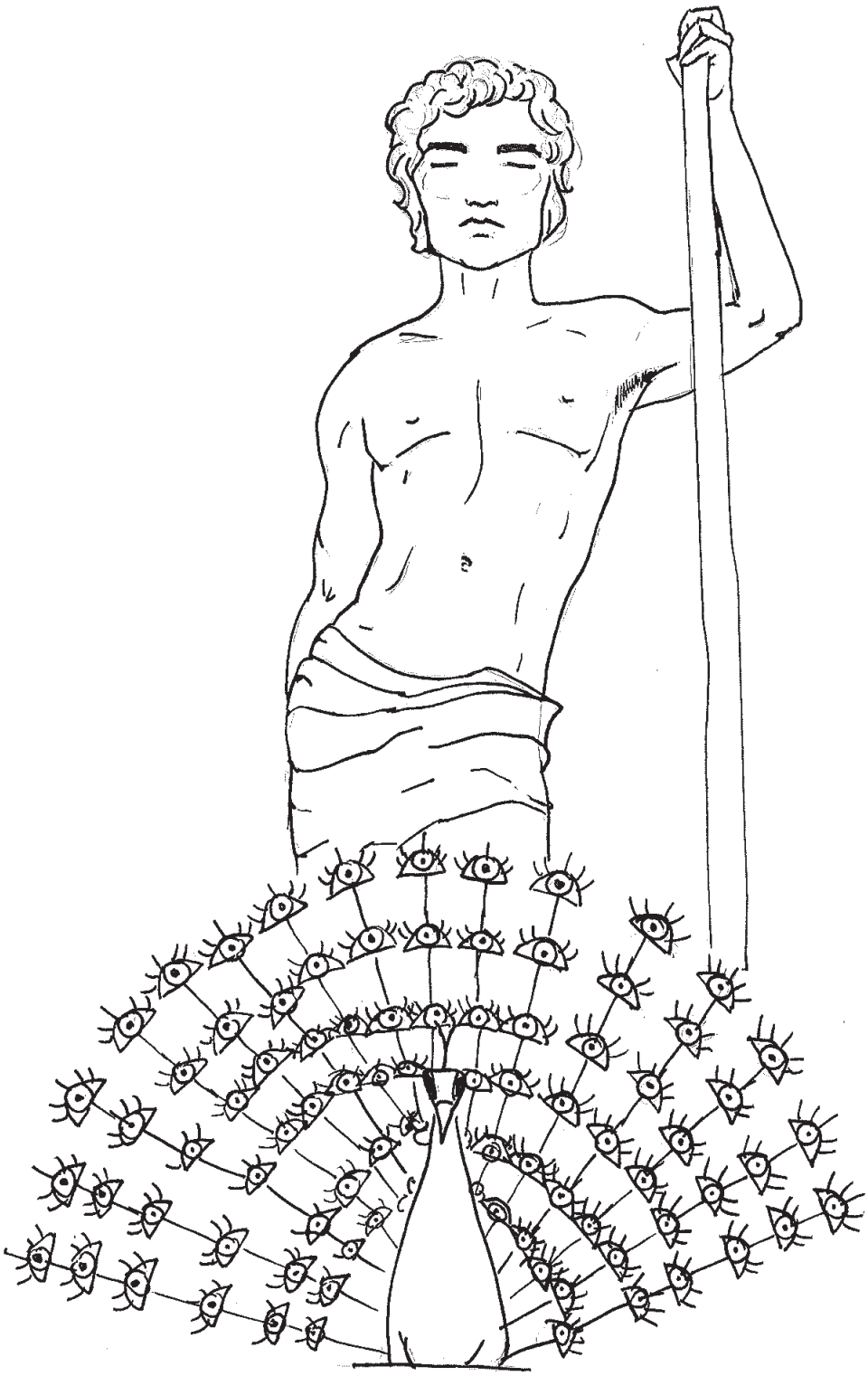

1

Theoretical framework

This chapter is aimed at defining the fundamental tools that have been investigated during this PhD work and that will be extensively used in the rest of the thesis. Where possible, the concepts and equations that are here presented are derived from first principles in order to provide a strong basis for what follows and a safe haven where we can compare the results of our research with what is well-known in the literature. Hardly anything is given for granted since nothing is really trivial.
The evolution of the light statistics in a second-order nonlinear crystal, which is the basis for the research presented in chapter four, is anticipated by a short introduction to Nonlinear Optics and by a deeper analysis on the most relevant results on second-harmonic generation.
Similarly, the concept of nonclassical state of light is retrieved from a brief but functional review of the quantum theory of the electromagnetic field. Most of the definitions and of the results we recall here will be employed in all the following chapters, especially for what concerns the detection of quantum states of light.

1.1 Nonlinear Optics: a brief introduction

> Physics would be dull and life most unfulfilling if all physical phenomena around us were linear.
>
> *Y. R. Shen*

Nonlinear responses of physical systems to light have already been predicted since the publication of Maxwell's *A dynamical theory of the electromagnetic field* in 1865. Indeed, by requiring that the dielectric constant depends on the incoming electric field, i.e. $\varepsilon = \varepsilon(E)$, Maxwell's equations can correctly account for the nonlinear properties of a material. However, due to the typically small size of the nonlinear coupling ($\chi < 10^{-12}$), nonlinear effects have been observed just in a few special cases. For instance, the cross-modulation between radio waves through the ionosphere, i.e. the so-called *Luxembourg-Gorky effect* [4, 5], was succsessfully explained as the nonlinear response of plasma to an external electromagnetic field in 1936. We are not considering here all the nonlinear phenomenology of ferromagnetic materials, which concerns solid-state physics rather than Nonlinear Optics.
Things changed when in 1959 the laser was invented. By then, collimated light beams in the high intensity domain could be achieved and focused on materials and their nonlinear response could be finally detected. The benchmark experiment, which is sometimes regarded as the beginning of Nonlinear Optics, is the

generation of second-harmonic light, performed by Franken et al. in 1961 [6, 21].

The polarization of dielectric crystals is due to the motion of valence electrons about their equilibrium position [22, 23, 24]. It is defined as the dipole moment per unit volume, i.e.

$$\mathbf{P}(t) \equiv -ne\mathbf{r}(t) \tag{1.1}$$

where n is the electronic density and e is the electronic charge. The application of an electromagnetic field $\mathbf{E}(\mathbf{r},t)$ to a material implies a spatial deviation of every loosely bounded charge from their starting position. Thus, the resulting polarization of the material is a response to the applied field and we say that it is linear if $\mathbf{P}$ depends on $\mathbf{E}$ according to

$$\mathbf{P}(\omega) = \varepsilon_0 \chi^{(1)}(\omega;\omega)\mathbf{E}(\omega) \tag{1.2}$$

where $\chi^{(1)}(\omega;\omega)$ is the coupling, which is called *susceptibility*. This is a 3×3 matrix where the number of independent elements depends on the spatial symmetries of the crystal. In particular, for cubic crystals the linear susceptibility is diagonal and the linear polarization is simply proportional to the electric field. In such a case, the material is called *isotropic*. But in general the polarization does not need to share the same direction of the input field. This is the case of *birefringent* materials.
The Lorentz model for light-matter interaction shows that such a linear response is obtained if the electron is assumed to be connected to an atom by a spring, i.e. the restoring force is such that the electrons swing around their equilibrium positions as harmonic oscillators. Thus, the interaction potential energy $V(x)$ is elastic. This description can be complicated a little bit more if we expand it as a perturbative power series. It is then straightforward to see that each new term in $V(x)$ involves the coupling of the charge with more than one electric field. For example, if ω_0 is a crystal resonance frequency and m is the electron mass, up to the first order the potential reads

$$V(x) \sim \frac{1}{2}m\omega_0^2 x^2 + \frac{1}{3}kx^3 + o(x^4). \tag{1.3}$$

Given an input electric field of the form

$$\begin{aligned}\mathbf{E}(x,t) &= \mathbf{E}_1(x)e^{-i\omega_1 t} + \mathbf{E}_2(x)e^{-i\omega_2 t} + c.c. \\ &= \mathbf{E}(\omega_1) + \mathbf{E}(\omega_2) + c.c.\end{aligned} \tag{1.4}$$

one finds out that a solution to the equations of motion with a restoring force corresponding to the potential in Eq. (1.3) cannot be found. Here, typically a Rayleigh-Schrŏdinger-like perturbative approach is applied [22], based on the assumption that the perturbative terms in Eq. (1.3) are negligible compared to the elastic potential. This trick allows to find that the cubic term in the potential energy couples the frequency components of the input electric field so that the frequency of some contributions to the spatial oscillations of the electron is a linear combination of ω_1 and ω_2. These contributions give rise to nonlinear polarization terms, defined by Eq. (1.3) with x depending on a combination of the input frequencies, e.g. $P(\omega_1+\omega_2) = -ne\cdot x(\omega_1+\omega_2)$. Note that also self-interactions are allowed, e.g. $P(2\omega_1) = -ne\cdot x(2\omega_1)$. This procedure allows to find an expression analogue to Eq. (1.2) for the second-order nonlinear polarizations, which, at a general level, can be stated as follows

$$P^{\sigma}(|\omega_1 \pm \omega_2|) = \varepsilon_0 \sum_{j\neq k=1}^{2} \chi^{\sigma}_{\nu\mu}(|\omega_1 \pm \omega_2|;\omega_j,\omega_k)E^{\nu}(\omega_j)E^{\mu}(\omega_k) \tag{1.5}$$

where the Greek indexes run over the cartesian coordinates (x,y,z) and χ is a rank-2 tensor such that

$$\chi : \mathbb{C}^3 \otimes \mathbb{C}^3 \to \mathbb{C}.$$

The simple perturbative model described above allows to find a scalar quantitative approximation for this coupling. The processes at $\omega_1+\omega_2$ and $|\omega_1-\omega_2|$ are respectively known as *sum-frequency* and *difference-frequency generation*.
Thus, nonlinear polarization arises from perturbative corrections to the interaction potential (1.3). In analogy with (1.5), nonlinear effects at the n-th order and at a given positive linear combination of the input frequencies Ω are described by

$$P^{\sigma}(\Omega)=\varepsilon_0\sum_{j_1=1}^{n}...\sum_{j_n=1}^{n}\chi^{\sigma}_{\nu_1\nu_2...\nu_n}(\Omega;\omega_{j_1},...,\omega_{j_n})E^{\nu_{j_1}}(\omega_{j_1})...E^{\nu_{j_n}}(\omega_{j_n}). \tag{1.6}$$

The number of components of the susceptibility tensor can be very large. However, the number of independent elements is in fact much smaller because of the presence of symmetries and can be further reduced by imposing some general constraints and specific conditions [22].
Most of all, symmetries play an important role in the understanding of a nonlinear process. In particular, the inversion symmetry provides a first main classification for crystals. If $V(\mathbf{r})$ is the potential acting on an electron due to its position $\mathbf{r}$ in the lattice, when $V(\mathbf{r})=V(-\mathbf{r})$ a crystal is called *centrosymmetric*. For example, this symmetry is apparent in NaCl, whereas the zinc blende (ZnS) structure is manifestly noncentrosymmetric. A simple argument can be used to show that these two classes allow different nonlinear processes. In the presence of inversion symmetry, $V(x)\sim 2^{-1}m\omega_0^2x^2+\alpha x^4+o(x^6)$, so that the polarization field changes sign accordingly with the sign of the alternating input field in Eq. (1.94). Then, since a reversal of $\mathbf{E}$ implies a reversal of $\mathbf{P}$, one is left with

$$-P=\chi^{(2)}(-E_1)(-E_2)=P$$

which is possible if and only if $\chi^{(2)}=0$. Thus, second-order nonlinear effects do not occur in centrosymmetric materials.
Note that, in principle, every material at some order could provide a nonlinear response to an electromagnetic field. When in the following we will say that a medium is nonlinear, we just mean that we are focusing on its nonlinear optical properties.
Even if symmetries can help, the computation of all the components of the whole set of tensors describing a nonlinear process is still a hard task. It is typically approached with a semiclassical method which exploits the density matrix formalism to treat the atomic energy states, while the radiation field is described as a plane wave. Here, we focus on the output of some nonlinear processes rather than on their cross-sections. Without loss of generality, we can assume to set the geometry of the process (i.e. the direction of propagation and the polarization of the fields) and the input and output frequency modes we want to observe, so that the coupling between a component of the input and output vectors in Eq. (1.6) is just a number, that we name $\chi^{(n)}_{eff}$.
The propagation of light through the nonlinear medium is described by Maxwell's equations in the absence of free charges

$$\nabla\times\mathbf{H}=\mathbf{J}+\frac{\partial\mathbf{D}}{\partial t}\qquad\nabla\times\mathbf{E}=-\frac{\partial\mathbf{B}}{\partial t}\qquad\nabla\mathbf{B}=0\qquad\nabla\mathbf{D}=0 \tag{1.7}$$

with

$$\mathbf{J}=\sigma\mathbf{E},\quad\mathbf{D}=\varepsilon_0\mathbf{E}+\mathbf{P},\quad\mathbf{P}=\mathbf{P}_L+\mathbf{P}_{NL}=\varepsilon_0\chi^{(1)}\mathbf{E}+\mathbf{P}_{NL}$$

where σ is the conductivity, while $\mathbf{P}_L$ and $\mathbf{P}_{NL}$ are the linear and nonlinear part of the polarization vector, respectively. Hence the equation of motion of the electric field is given by

$$\Box\mathbf{E}-\mu_0\sigma\frac{\partial\mathbf{E}}{\partial t}=\mu_0\frac{\partial^2\mathbf{P}_{NL}}{\partial t^2} \tag{1.8}$$

where $\Box\equiv\Delta-\mathrm{v}^{-2}\partial^2/\partial t^2$ is the dalambertian operator and $\mathrm{v}\equiv c/n$ is the so-called phase velocity, with $n=\sqrt{1+\chi^{(1)}_{eff}}$ refractive index of the material. Note that, in the absence of free currents, Eq. (1.8) is an

inhomogeneous wave equation where the nonlinear polarization is the source term. This is equivalent to ask that the medium is transparent to the frequencies ω_k of the propagating fields, i.e. $\sigma(\omega_k) = 0$.
Equation (1.8) can be easily generalized to a dispersive and dissipative material. If dispersion is not negligible, one has to consider the evolution of every frequency component of $\mathbf{E}$ and $\mathbf{P}_{NL}$ through Eq. (1.8) separately. Also, one can account for losses if the susceptibility of the material is allowed to be complex and if $\sigma(\omega) \neq 0$.

In the case of second-order processes, we have that the nonlinear polarization, given by Eq. (1.5), is a source for a third field $\mathbf{E}_3(\omega_3)$, different from the two input fields $\mathbf{E}_1(\omega_1)$ and $\mathbf{E}_2(\omega_2)$. Before and after the interaction with the nonlinear medium, it is natural to assume free propagation for all the fields, so that they can be described as plane waves travelling along, say, z, i.e.

$$E_j(z,t) = A_j e^{i(k_j z - \omega_j t)} + c.c.$$

with $k = 1,2,3$ and A_k amplitude of the k-th field. But what about the propagation in the medium? For a lossless material, the energy of the field is conserved and the field amplitudes can be taken as constant in time, thus $A_j = A_j(z)$. If, in addition, the variation of the field amplitude along the crystal length is assumed to be small, the plane wave solution as a first approximation still holds. This is known as *slowly-varying-amplitude approximation* and formally reads

$$\left| \frac{\partial^2 A_j}{\partial z^2} \right| \ll \left| k \frac{\partial A_j}{\partial z} \right|. \tag{1.9}$$

Then the nonlinear polarization generating the field $E_3(\omega_3)$ can be similarly described as a plane wave

$$P_3(z,t) = p_3(z) e^{-i\omega_3 t}. \tag{1.10}$$

In the case of sum-frequency generation, P_3 is given by Eq. (1.5) as well, which can now be conveniently rewritten in a scalar form as

$$P_3(\omega_1 + \omega_2) = 2\varepsilon_0 \chi^{(2)}_{eff} A_1 A_2 e^{i(k_1+k_2)z} e^{-i(\omega_1+\omega_2)t} \tag{1.11}$$

where the factor 2 is just a symmetry factor descending from the sum over the frequencies. By comparing Eq. (1.10) and (1.11), we immediately find

$$\begin{aligned} \omega_3 &= \omega_1 + \omega_2 \\ p_3(z) &= 2\varepsilon_0 \chi^{(2)}_{eff} A_1 A_2 e^{i(k_1+k_2)z}. \end{aligned}$$

Under these assumptions, we get from Eq. (1.8) a much simpler equation for the amplitude, namely

$$\frac{\partial^2 A_3}{\partial z^2} + 2ik_3 \frac{\partial A_3}{\partial z} = -\frac{2\omega_3^2 \chi^{(2)}_{eff}}{c^2} A_1 A_2 e^{i(k_1+k_2-k_3)z}$$

which furtherly simplifies by requiring the slowly-varying-amplitude approximation in Eq. (1.9). The resulting equation is the so-called *coupled-amplitude equation*

$$\frac{\partial A_3}{\partial z} = \frac{i\omega_3^2 \chi^{(2)}_{eff}}{k_3 c^2} A_1 A_2 e^{i(k_1+k_2-k_3)z}. \tag{1.12}$$

Similarly, one can find out that the evolution of the input field amplitudes throughout the medium is provided by

$$\frac{\partial A_1}{\partial z} = \frac{i\omega_1^2 \chi^{(2)}_{eff}}{k_1 c^2} A_3 A_2^* e^{-i(k_1+k_2-k_3)z} \tag{1.13}$$

$$\frac{\partial A_2}{\partial z} = \frac{i\omega_2^2 \chi^{(2)}_{eff}}{k_2 c^2} A_3 A_1^* e^{-i(k_1+k_2-k_3)z}. \tag{1.14}$$

The coupling coefficients here share the same symbol $\chi^{(2)}_{eff}$ because, due to the so-called *full permutation symmetry*, for lossless material they are equal to each other.
Moreover, note that we did not fix $k_3 = k_1 + k_2$. The difference $\Delta k \equiv k_3 - k_2 - k_1$ is the *momentum mismatch* and the condition

$$\Delta k = 0 \tag{1.15}$$

is called *phase matching*. Equation (1.15) is the conservation of momentum, which is guaranteed if the medium is dispersionless, i.e. if the refractive index of the material is not a function of the driving field frequency. In such a case, the phase matching condition is just a consequence of the conservation of energy since frequency and momentum are linked by the dispersion relation

$$k = \frac{n}{c}\omega.$$

If the phase matching condition holds, there is a fixed phase relation among the fields generated by the oscillations of the atomic dipoles in the material. The coherent sum of the generated fields results in a total output intensity proportional to the square of the number of atomic dipoles. On the other hand, if $\Delta k \neq 0$, the output intensity $I(\omega_3) = 2\varepsilon_0 nc|A_3|^2$ drops drastically. Indeed, if A_1 and A_2 are assumed to be constant along a path l inside the crystal, the integration of Eq. (1.12) shows that

$$I(\omega_3) \propto \mathrm{sinc}^2\left(\frac{\Delta k l}{2}\right), \tag{1.16}$$

i.e. the efficiency of the nonlinear process decreases as Δkl increases, due to the back-conversion from ω_3 to ω_1 and ω_2 for $\Delta k > l$. This is the reason why achieving the perfect phase matching condition is so important. As already mentioned, the condition is automatically fulfilled if the refractive index of the material does not depend on the field frequency. But dispersionless materials hardly exist. The problem can be overcome either by exploiting anomalous dispersion or, more typically, by using birefringent materials.

1.2 Second-harmonic generation

In the case of *second-harmonic generation SHG*, we have that the frequency ω_{SH} of the field generated by the second-order nonlinear polarization of the material is twice the frequency of the input beam, from now on named fundamental frequency ω_{F}. In particular, the components of the nonlinear polarization contributing to the process are [22, 23, 24]

$$P(\omega_{\mathrm{F}}) = 2\varepsilon_0 \chi^{(2)}_{eff} A_{\mathrm{SH}} A^*_{\mathrm{F}} e^{i(k_{\mathrm{SH}} - k_{\mathrm{F}})z} e^{-i\omega_{\mathrm{F}} t} \tag{1.17}$$

and

$$P(\omega_{\mathrm{SH}}) = \varepsilon_0 \chi^{(2)}_{eff} A^2_{\mathrm{F}} e^{2ik_{\mathrm{F}} z} e^{-i\omega_{\mathrm{SH}} t}. \tag{1.18}$$

Thus, the system of Eqs. (1.12-1.13-1.14) reduces to

$$\begin{cases} \dfrac{\partial A_{\mathrm{F}}}{\partial z} = \dfrac{i\omega^2_{\mathrm{F}} \chi^{(2)}_{eff}}{k_{\mathrm{F}} c^2} A_{\mathrm{SH}} A^*_{\mathrm{F}} e^{-i\Delta k z} \\ \dfrac{\partial A_{\mathrm{SH}}}{\partial z} = \dfrac{i\omega^2_{\mathrm{SH}} \chi^{(2)}_{eff}}{2k_{\mathrm{SH}} c^2} A^2_{\mathrm{SH}} e^{i\Delta k z} \end{cases} \tag{1.19}$$

with $\Delta k = 2k_{\mathrm{F}} - k_{\mathrm{SH}}$. Note that the field amplitudes are complex variables: $A_j(z) = \rho_j(z) e^{i\phi_j(z)}$ so that $\mathbf{E}_j = \hat{u}_j A_j(z) e^{i(k_j z - \omega_j t)} + c.c. = \hat{u}_j \rho_j(z) \cos[k_j z - \omega_j t + \phi_j(z)]$ where $\rho_j(z)$ and $\phi_j(z)$ are real functions.

Then Eqs. (1.19) reduce to the following four-differential-equation system [21]

$$\begin{aligned}
\frac{d\rho_{\mathrm{F}}}{dz} &= -\frac{\omega^2\chi^{(2)}_{eff}}{k_{\mathrm{F}}c^2}\rho_{\mathrm{F}}(z)\rho_{\mathrm{SH}}(z)\sin[2\phi_{\mathrm{F}}(z)-\phi_{\mathrm{SH}}+\Delta kz] \\
\frac{d\rho_{\mathrm{SH}}}{dz} &= \frac{2\omega^2\chi^{(2)}_{eff}}{k_{\mathrm{SH}}c^2}\rho^2_{\mathrm{F}}(z)\sin[2\phi_{\mathrm{F}}(z)-\phi_{\mathrm{SH}}+\Delta kz] \\
\frac{d\phi_{\mathrm{F}}}{dz}\rho_{\mathrm{F}}(z) &= -\frac{\omega^2\chi^{(2)}_{eff}}{k_{\mathrm{F}}c^2}\rho_{\mathrm{F}}(z)\rho_{\mathrm{SH}}(z)\cos[2\phi_{\mathrm{F}}(z)-\phi_{\mathrm{SH}}+\Delta kz] \\
\frac{d\phi_{\mathrm{SH}}}{dz}\rho_{\mathrm{SH}}(z) &= -\frac{2\omega^2\chi^{(2)}_{eff}}{k_{\mathrm{SH}}c^2}\rho^2_{\mathrm{F}}(z)\cos[2\phi_{\mathrm{F}}(z)-\phi_{\mathrm{SH}}+\Delta kz]
\end{aligned}$$

where we set $\omega_{\mathrm{F}} = \omega$. The system can be simplified by defining the total phase $\theta \equiv 2\phi_{\mathrm{F}}(z) - \phi_{\mathrm{SH}} + \Delta kz$ so that we are left with the three equations

$$\begin{cases}
\dfrac{d\rho_{\mathrm{F}}}{dz} = -\dfrac{\omega^2\chi^{(2)}_{eff}}{k_{\mathrm{F}}c^2}\rho_{\mathrm{F}}(z)\rho_{\mathrm{SH}}(z)\sin[\theta(z)] \\
\dfrac{d\rho_{\mathrm{SH}}}{dz} = \dfrac{2\omega^2\chi^{(2)}_{eff}}{k_{\mathrm{SH}}c^2}\rho^2_{\mathrm{F}}(z)\sin[\theta(z)] \\
\dfrac{d\theta}{dz} = \Delta k - \dfrac{2\omega^2\chi^{(2)}_{eff}}{c^2}\left(\dfrac{\rho_{\mathrm{SH}}(z)}{k_{\mathrm{F}})} - \dfrac{\rho^2_{\mathrm{F}}/\rho_{\mathrm{SH}}}{k_{\mathrm{F}})}\right)\cos[\theta(z)].
\end{cases} \tag{1.20}$$

The first and the second equation of (1.20) yield the conservation of energy in the form of the so-called *Manley-Rowe relations*. Since $I_j = 2\varepsilon_0 nc\rho_j^2$, it is straightforward to see that $d(I_{\mathrm{F}} + I_{\mathrm{SH}})/dz = 0$. Hence, we are tempted to rename the modulus of the amplitudes ρ_j in terms of the total intensity $\mathrm{I} = I_{\mathrm{F}} + I_{\mathrm{SH}}$, which is conserved. In particular, a smart choice is

$$\rho_{\mathrm{F}} \to u \equiv \frac{I_{\mathrm{F}}}{\mathrm{I}} \qquad\qquad \rho_{\mathrm{SH}} \to v \equiv \frac{I_{\mathrm{SH}}}{\mathrm{I}}$$

so that

$$u^2 + v^2 = 1. \tag{1.21}$$

The third equation in (1.20) can be much simplified with the help of the first and the second ones, namely

$$\frac{d\theta}{dz} = \Delta k + \cot[\theta(z)]\frac{d}{dz}\ln[\rho^2_{\mathrm{F}}(z)\rho_{\mathrm{SH}}(z)].$$

Now, it is convenient to replace the amplitude modulus ρ_j with u and v, as long as we suitably redefine the variable z. With the substitution

$$z \to \zeta \equiv \frac{2\omega^2\chi^{(2)}_{eff}}{k_{\mathrm{F}}c^2}\sqrt{\frac{8\mathrm{I}\chi^{(2)}_{eff}\omega}{k_{\mathrm{SH}}c^2}}z$$

the system (1.20) is expressed in the more compact form

$$\begin{cases}
\dfrac{du}{d\zeta} = -u(\zeta)v(\zeta)\sin[\theta(\zeta)] \\
\dfrac{dv}{d\zeta} = u^2(\zeta)\sin[\theta(\zeta)] \\
\dfrac{d\theta}{d\zeta} = \Delta s + \cot[\theta(\zeta)]d_\zeta\ln[u^2(\zeta)v(\zeta)]
\end{cases} \tag{1.22}$$

where Δs is the rescaled mismatch $\Delta s \equiv \Delta k\frac{z}{\zeta}$.

1.2.1 Perfect phase matching

If the phase-matching condition is fulfilled (i.e. $\Delta s = 0$), we expect to find another conservation law from the system (1.22). This is the case since the third equation in (1.22) now reads

$$\frac{d\theta}{d\zeta} = \cot[\theta(\zeta)]\frac{d}{d\zeta}\ln[u^2(\zeta)v(\zeta)]$$

and hence

$$\frac{d}{d\zeta}(u^2 v\cos\theta) = 0. \tag{1.23}$$

The conserved quantity $\Gamma \equiv |u^2 v\cos\theta|$ is proportional to the energy density of the nonlinear process, i.e.

$$U_{\mathrm{NL}} = \frac{1}{2}\int \mathbf{E}\cdot d\mathbf{P}_{\mathrm{NL}}.$$

Thus, in a dispersionless medium the nonlinear field energy is separately conserved. Note that, at variance with the second-harmonic (SH) field intensity, Γ has a maximum for $v^2 = 1/3$. In particular, $0 \le \Gamma^2 \le 4/27$. Through the third equation in (1.22) and Eq. (1.21), one finally gets the evolution equation for the second-harmonic beam intensity, which is

$$\frac{d}{d\zeta}v^2 = \pm 2\sqrt{v^2(1-v^2)^2 - \Gamma^2}$$

leading to

$$\zeta = \pm\frac{1}{2}\int_{v^2(0)}^{v^2(\zeta)} d(v^2)\frac{1}{\sqrt{v^2(1-v^2)^2-\Gamma^2}}. \tag{1.24}$$

The integrand has three poles, which are the solutions of the equation $v^2(1-v^2)^2 - \Gamma^2 = 0$. For $0 \le \Gamma^2 \le 4/27$, all of them are real and positive. Let us name them v_1^2, v_2^2 and v_3^2 with $v_1^2 \le v_2^2 \le v_3^2$. Note that $v_3^2 > 1 \quad \forall\Gamma > 0$, so that (see Eq. (1.21)) $v^2 \neq v_3^2$ except for $\Gamma = 0$. The integral in Eq. (1.24) can be easily recognized and solved [21] if we write the radicand in terms of v_1^2, v_2^2 and v_3^2 and change the integration variable with

$$w^2 = \frac{v^2 - v_1^2}{v_2^2 - v_1^2}.$$

Simple calculations yield

$$\zeta = \pm\frac{1}{\sqrt{v_3^2 - v_1^2}}\int_{w(0)}^{w(\zeta)}\frac{dw}{\sqrt{(1-w^2)(1-\gamma^2 w^2)}}. \tag{1.25}$$

which is an elliptic integral of the first kind with elliptic modulus $\gamma = \sqrt{(v_2^2 - v_1^2)/(v_3^2 - v_1^2)}$. The amplitude is given by the Jacobi elliptic sine, i.e. $w(\zeta) = \mathrm{sn}\left[\sqrt{v_3^2 - v_1^2}(\zeta + \zeta_0), \gamma\right]$. Thus,

$$v^2 = v_1^2 + (v_2^2 - v_1^2)\,\mathrm{sn}^2\left[\sqrt{v_3^2 - v_1^2}(\zeta + \zeta_0), \gamma\right] \tag{1.26}$$

and, from Eq. (1.21),

$$u^2 = 1 - v_1^2 - (v_2^2 - v_1^2)\,\mathrm{sn}^2\left[\sqrt{v_3^2 - v_1^2}(\zeta + \zeta_0), \gamma\right]. \tag{1.27}$$

If $\Gamma^2 = 0$, $v_1^2 = 0$ and $v_2^2 = v_3^2 = 1$. Then, $\gamma = 1$ and Eqs. (1.26) and (1.27) reduce to

$$\begin{cases} v(\zeta) = \tanh(\zeta_0 + \zeta) \\ u(\zeta) = \operatorname{sech}(\zeta_0 + \zeta). \end{cases} \tag{1.28}$$

Typically, no second-harmonic beam is pumped into the crystal and the nonlinear field is generated from scratch. This is the case if $v^2(0) = v_1^2 = 0$, which implies $\zeta_0 = 0$. On the other hand, if $v^2(0) \neq 0$, the conservation law in Eq. (1.23) requires that $\phi_{\mathrm{SH}}(0) - 2\phi_{\mathrm{F}}(0) = \pm\frac{\pi}{2}$, which is preserved by the conservation of momentum. An arbitrary interaction length L can be defined to study the evolution of the normalized amplitude. For example, in the case of $v^2(0) = 0$, one can set L so that $\zeta(L) = 1$. Hence,

$$L \equiv \frac{k_{\mathrm{F}} c^2}{2\omega^2 \chi^{(2)}_{eff} \rho_{\mathrm{F}}(0)}. \tag{1.29}$$

For $z = L$, the 76% of the input beam has been converted into the second-harmonic field (see Fig. 1.1). Note that in this case we have no back-conversion. Indeed, there is no interaction between the generated second-harmonic field and the nonlinear polarization induced by the input beam ($\Gamma = 0$).

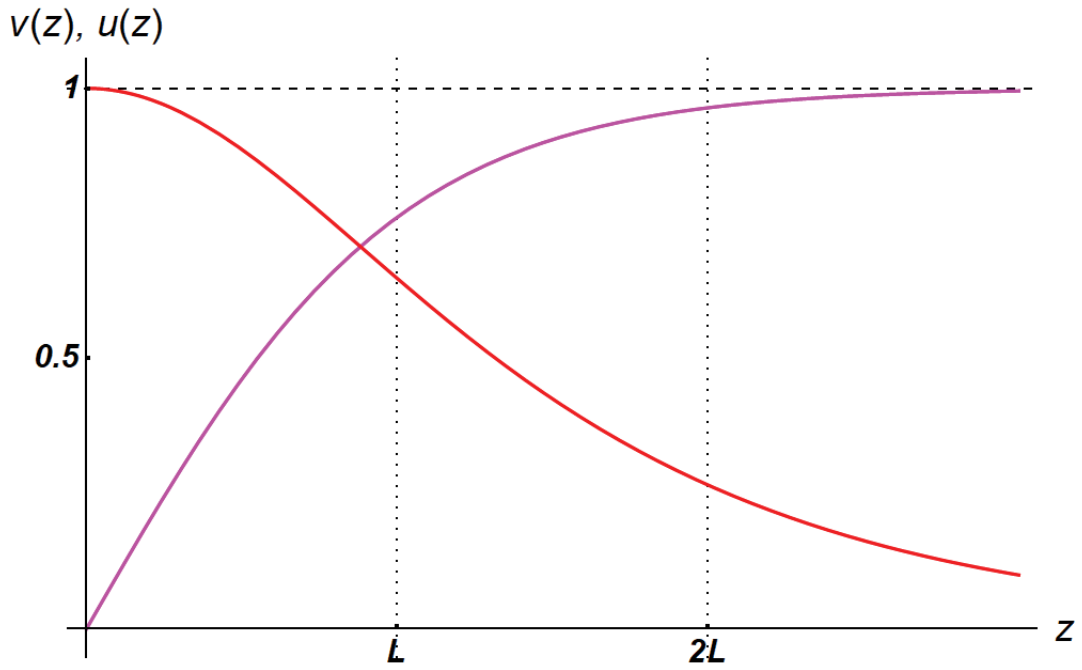

Fig. 1.1: Eqs. (1.28) with $v(0) = 0$. Magenta line: $v(z)$. Red line: $u(z)$. L is the interaction length (see the text for details).

The other extreme case is given by $\Gamma^2 = 4/27$. But this is not very significant since $v^2(\zeta) = v_1^2 = v_2^2 = 1/3 \quad \forall\zeta$, which is to say that if the second-harmonic and the fundamental beam are mixed in the nonlinear crystal so that $I_{\mathrm{SH}}(0) = \mathrm{I}/3$ and $\phi_{\mathrm{SH}}(0) = 2\phi_{\mathrm{F}}(0)$ in phase-matching condition, then the system does not really evolve along the propagation because there is a perfect balance between up- and down-conversion. For $0 < \Gamma^2 < 4/27$ we find field oscillations described by the elliptic sine in Eq. (1.26), due to a non-null

interaction energy between the second-harmonic field and the nonlinear polarization, providing a back-conversion from the highest to the lowest frequency (see Fig. 1.1). At the beginning of the evolution, the dominant process is determined by the initial conditions, i.e. if $0 < I_{\rm SH} < \mathrm{I}/3$ or $\mathrm{I}/3 < I_{\rm SH} < \mathrm{I}$. The normalized intensity of the SH swings between v_1^2 and v_2^2 with period

$$S_\gamma \equiv \int_0^\pi \frac{d\phi}{\sqrt{1-\gamma^2\sin^2\phi}}. \tag{1.30}$$

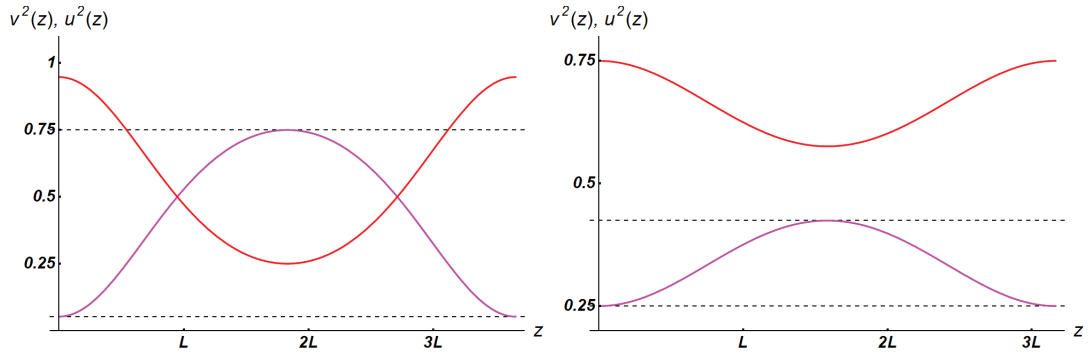

Fig. 1.2: Eqs. (1.26-1.27) with $\Gamma \neq 0$ and $\phi_{\rm SH}(0) - 2\phi \mathrm{F}(0) = 0, \pi$. Magenta line: $v(z)$. Red line: $u(z)$. L is the interaction length (see the text for details). One full period is plotted. Left: $\Gamma^2 = 3/64$, $S_\gamma \sim 3.7L$. Right: $\Gamma^2 = 9/64$, $S_\gamma \sim 3.2L$. Note that, for a fixed phase relation, the stronger the second-harmonic input intensity $v^2(0)$, the larger the nonlinear interaction mean energy, the smaller the variation of the intensity.

1.2.2 Effects of phase mismatch

The effects of dispersion does not affect the kind of solutions given by Eqs. (1.26) and (1.27), but simply transform them into other solutions of the same equations. Since now $\Delta k \neq 0$, we cannot neglect the term $\Delta s = L\Delta k$ in the third equation of the system (1.22). However, this just leads to a new conservation equation, i.e.

$$\frac{d}{d\zeta}(u^2 v\cos\theta + \frac{1}{2}v\Delta s) = 0, \tag{1.31}$$

which replaces Eq. (1.23). Note that this is true if and only if Δk is not a function of the propagation distance z, which we implicitly assumed. The new constant of the motion is $\Gamma_s \equiv \Gamma + \frac{1}{2}v^2\Delta s$, which is proportional to the total energy density of the nonlinear process. The evolution of the fields is still described by the elliptic integral in Eq. (1.25) with the only difference that Γ must be replaced with $\Gamma_s - \frac{1}{2}v^2\Delta s$, so that v_1^2, v_2^2 and v_3^2 are now the roots of the equation

$$v^2(1-v^2)^2 - \left[\Gamma_s - \frac{1}{2}v^2\Delta s\right]^2 = 0.$$

Thus, in the presence of dispersion we have that the interaction between the second-harmonic field and the nonlinear polarization induced by the fundamental beam is modified.
In particular, in the case $\Gamma_s = 0$ shown in Fig. 1.3, the mismatch breaks the degeneracy of the roots v_2^2 and v_3^2 that we found for $\Gamma = 0$. Here, the contribution to the nonlinear interaction energy given by $\frac{1}{2}v^2\Delta s$ makes the down-conversion process possible. But then, due to the two conservation laws (1.21) and (1.31),

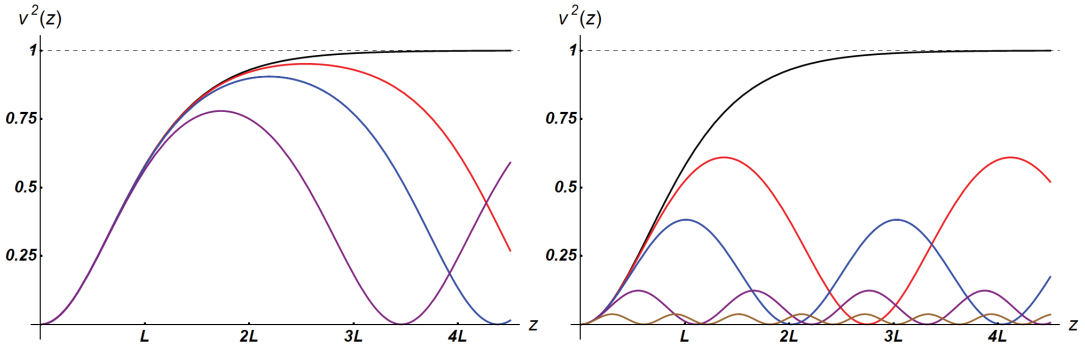

Fig. 1.3: Eq. (1.26) in the presence of dispersion, with $\Gamma_s = 0$ for different choices of Δs. In particular, in the left panel $\Delta s < 1$, in the right panel $\Delta s > 1$. The case $\Delta s = 0$ (black line) is shown for both as a comparison with the $\Gamma = 0$ case studied in Fig. (1.1). Left panel. Red line: $\Delta s = 0.1$. Blue line:$\Delta s = 0.2$. Purple line: $\Delta s = 0.5$. Right panel. Red line: $\Delta s = 1$. Blue line:$\Delta s = 2$. Purple line: $\Delta s = 5$. Brown line:$\Delta s = 10$.

the effect of dispersion consists in a reduction of the second-harmonic generation, as expected. The evolution is the same explored in the previous section with $\Gamma = \frac{1}{2}v^2\Delta s$. The main parameters of the process are

$$v_1^2 = 0, \qquad v_{2,3}^2 = \left[\frac{\Delta s}{4} \pm \sqrt{1+\left(\frac{\Delta s}{4}\right)^2}\right]^2$$

and the period is the same as in Eq. (1.30) with $\gamma = |v_2/v_3|$.
We expect that, if the generated SH field is so small that the pump beam can be considered undepleted (i.e. $du/d\zeta \sim 0$), then we recover the dependence on the phase mismatch outlined in Eq. (1.16). This is the case because

$$\gamma \xrightarrow[\Delta s \gg 1]{} 0 \Rightarrow \mathrm{sn}(x) \sim \sin(x)$$

so that, from Eq. (1.26),

$$v^2(z) = v_2^2\,\mathrm{sn}^2(v_3\zeta,\gamma) \sim \left(\frac{2}{\Delta kL}\right)^2 \sin^2\left(\frac{\Delta kz}{2}\right)$$

where we used $\Delta s = \Delta kL$ and $\zeta = z/L$. Then, for a crystal length $z_{out} \equiv l$,

$$I_{\mathrm{SH}}(l) = \mathrm{I}\cdot v^2(l) = \mathrm{I}\cdot\left(\frac{l}{L}\right)^2 \mathrm{sinc}^2\left(\frac{\Delta kl}{2}\right) \tag{1.32}$$

quod erat demostrandum.

1.3 Statistical properties of light

> The true mystery of the world is the visible, not the invisible.
>
> *O. Wilde*

In general, different sources of light produce different intensity patterns. For instance, we expect that the intensity distribution of sunlight is not the same as that emitted by a laser. On the other hand, we may think that the light from a bulb should have something in common with the gleam of a star since both of them are black bodies. Definitely, light can be classified according to the statistical behavior of the intensity, i.e. according to the physical nature of its source. A given intensity distribution is characterized by specific *coherence* and *correlation* properties.
There is a whole family of functions commonly used to study these properties, i.e. the so-called *Glauber's normalized correlation functions* [36, 37]. Upon defining the n-th order correlation function as

$$G^{(n)}(r_1,...,r_n,r_{n+1},...,r_{2n};t_1,...,t_n,t_{n+1},...,t_{2n}) \equiv \langle \prod_{j=1}^{n} E_j^* \prod_{k=n+1}^{2n} E_k \rangle \tag{1.33}$$

$E_j = E(r_j,t_j)$ being the amplitude of a given electric field, a suitable normalization with respect to $\langle E_j^* E_j \rangle \quad \forall j$ yields the Glauber's functions

$$g^{(n)}(r_1,...,r_{2n};t_1,...,t_{2n}) \equiv \frac{G^{(n)}(r_1,...,r_{2n};t_1,...,t_{2n})}{\prod_{j=1}^{2n} \sqrt{\langle E_j^* E_j \rangle}} \tag{1.34}$$

which are, by definition, real and positive definite.
We will focus on the second-order correlation function because it is of particular interest for the discrimination between the classical and the quantum case. Indeed, a number of intrinsically quantum states of light has unique statistical properties that can be identified through their Glauber's intensity correlation functions. In the classical case, this tool helps determine the correlation degree of the light distribution under investigation. As follows from Eq. (1.34), the second-order correlation function reads

$$g^{(2)}(\tau) = \frac{\langle I(t) I(t+\tau) \rangle}{\langle I(t) \rangle^2} \tag{1.35}$$

where, for the sake of simplicity, we focus only on temporal correlations and name $t_1 \equiv t$, $\tau \equiv t_2 - t_1$. The reference experiment for the determination of the correlation $\langle I(t) I(t+\tau) \rangle$ is the historic *Hanbury-Brown and Twiss experiment* [28], originally conceived to provide an estimation for the diameter of stars through intensity interferometry of spatially separated detectors.
Two fundamental inequalities can be inferred from first principles for the $g^{(2)}$ functions [29]. First, from the positivity of the variance $\sigma^2(I) \geq 0$ directly follows that

$$\langle I \rangle^2 \leq \langle I^2 \rangle. \tag{1.36}$$

Second, from the Cauchy-Schwarz inequality it is straightforward to see that

$$\langle I(t+\tau) I(t) \rangle \leq \langle I(t) \rangle^2. \tag{1.37}$$

From Eqs. (1.36) and (1.37), we respectively find

$$g^{(2)}(0) \geq 1 \tag{1.38}$$

$$g^{(2)}(\tau) \leq g^{(2)}(0) \quad \forall \tau. \tag{1.39}$$

These properties will be useful in the following.
Typically, we are not only interested in the distribution of the intensity, but also in the statistics that results after a detection process, which is described by the photoelectric effect. The consequence of the detection

is the transformation of the intensity probability into the discrete photoelectron distribution, which, under the assumption that $I(t)$ is a stochastic ergodic process, can be retrieved through the Mandel's formula [29]

$$P(m,T) = \int_0^\infty d\tilde{I} p(\tilde{I}) \frac{\tilde{I}^m}{m!} e^{-\tilde{I}} \tag{1.40}$$

where

$$\tilde{I}(t) = \frac{\eta}{T} \int_t^{t+T} dt' I(t')$$

and η is the photodetection efficiency of the detector.
The simplest light distribution is the case of a constant intensity emission I_0, i.e.

$$p(I) = \delta(I - I_0). \tag{1.41}$$

Hence $\langle I^2(t)\rangle = \langle I(t)\rangle^2$ and $g^{(2)}(0) = 1$, which is the inferior limit in Eq. (1.38). This is the case of monochromatic plane waves. We define a radiation field described like this as *second-order coherent*. In general, if $g^{(n)}(0) = 1 \quad \forall n$ we say that the field is coherent. The typical example for this kind of statistics is the light emitted by a laser. The statistics of photoelectrons for detected coherent light is straightforward from Eq. (1.40) and reads

$$P(m) = \frac{\langle m\rangle^m}{m!} e^{-\langle m\rangle} \tag{1.42}$$

which is a Poissonian distribution with $\langle m\rangle = \eta\langle I\rangle$.
On the contrary, if $g^{(2)}(0) > 1$, we are dealing with *incoherent* light. The most common case of incoherent light is the so called *thermal*, or *chaotic*, radiation, which is emitted by a source at a given temperature. The intensity distribution reads

$$p(I) = \frac{1}{I_0} e^{-\frac{I}{I_0}} \tag{1.43}$$

which is just the Boltzmann energy distribution as a function of the intensity. Here $\langle I\rangle = I_0$ and $\langle I^2\rangle = 2I_0^2$ so that $g^{(2)}(0) = 2$. Actually, this is a particular case of a more general distribution. Indeed, a thermal source typically emits more than one mode, each mode described by a thermal distribution. The statistics of the superposition of μ modes is then given by the convolution of μ thermal distributions, which, if the modes are *equally populated*, yields

$$p(I) = \frac{1}{(\mu-1)!} \left(\frac{\mu}{I_0}\right)^\mu I^{\mu-1} \exp\left(-\frac{\mu}{I_0} I\right) \tag{1.44}$$

so that $\langle I^2\rangle = (\mu+1)/\mu I_0^2$ and $g^{(2)}(0) = (\mu+1)/\mu$. Note that the convolution of infinite modes reduces to the coherent case (Eq. (1.41)). The photoelectron distribution in this case is given by

$$P(m) = \binom{m}{\mu-1} \mu^\mu \frac{\langle m\rangle^m}{(\langle m\rangle + \mu)^{m+\mu}}. \tag{1.45}$$

Note that the single-thermal distribution ($\mu = 1$) is the well-known Bose-Einstein statistics, which is consistent with the idea of a thermal source. Indeed, the Bose-Einstein statistics describes an harmonic oscillator at given temperature and energy, emitting a mean number of excitations $\langle m\rangle$. Also in this discrete case, as expected, the coherent case is recovered for $\mu \to \infty$ since, via Stirling's approximation, the limit in Eq. (1.45) yields the Poissonian distribution in Eq. (1.42).

1.3.1 Transformation of light statistics in a SHG process

So far, we have introduced some ideas about the statistics of a radiation field. Now we want to investigate how the propagation through a nonlinear medium affects the intensity distribution of light. In particular, we will focus on the transformation due to a SHG process. Let us assume a lossless medium and set as initial conditions $I_{\rm SH}(0)=0$ and $\Gamma_s \sim 0$. Therefore, the evolution of the SH and fundamental beams is described by Eqs. (1.26) and (1.27) with $\zeta_0 = 0$. However, in a typical experimental situation, the SH intensity is small and dispersion effects cannot be neglected. Then we can use Eq. (1.32) to describe the output. It is important to outline the dependence of the output intensity on the total intensity I, which is not explicit in Eq. (1.32) since the interaction length L is a function of I (see the dependence on $\rho_{\rm F}(0)$ in Eq. (1.29)):

$$I_{\rm SH}(l) = \frac{16\omega^2 l^2 (\chi^{(2)}_{eff})^3}{c^2 n_1^2 n_2}\,\mathrm{sinc}^2\left(\frac{\Delta k l}{2}\right)\mathrm{I}^2. \tag{1.46}$$

Given the link between the incoming light intensity and the SH one in Eq. (1.46), it is possible to find a relation between the two corresponding light distributions [25, 27, 26], which means that we can find out how a given light statistics is transformed in the propagation through a SHG crystal. Upon writing Eq. (1.46) as $I_{\rm SH}(l,\omega_{\rm SH}) = a f(\mathrm{I}(\omega_{\rm F})) = a\mathrm{I}^2(\omega_{\rm F})$, where a is the coupling constant and $f(\mathrm{I})$ is a positive invertible function, the second-harmonic light distribution, say $q(I_{\rm SH})$, can be expressed as a function of the incoming one, $p(\mathrm{I})$,

$$q(I_{\rm SH}) = p(f^{-1}(I_{\rm SH}))\left[\frac{df(\mathrm{I})}{d\mathrm{I}}\right]^{-1}_{f^{-1}(I_{\rm SH})}, \tag{1.47}$$

which implies

$$q(I_{\rm SH}) = \frac{p(\sqrt{I_{\rm SH}/a})}{2\sqrt{aI_{\rm SH}}}. \tag{1.48}$$

In the case of a coherent input field, the output SH distribution reads

$$q(I_{\rm SH}) = \frac{1}{2\sqrt{aI_{\rm SH}}}\delta\left(\sqrt{\frac{I_{\rm SH}}{a}} - \mathrm{I}\right) \tag{1.49}$$

which, by applying the properties of the delta distribution, takes the more familiar form

$$q(I_{\rm SH}) = \delta(I_{\rm SH} - a\mathrm{I}^2). \tag{1.50}$$

Therefore, the SH distribution in this case is the same as the input light distribution, which means that the detected-photon statistics of the SH light is Poissonian as well.
In the case of a multithermal input field, we find from Eq. (1.46) that the output SH light reads

$$q(I_{\rm SH}) = \frac{1}{(\mu-1)!}\left(\frac{\mu}{\langle \mathrm{I}\rangle}\right)^{\mu}\frac{I_{\rm SH}^{\mu/2-1}}{2a^{\mu/2}}\exp\left(-\frac{\mu}{\langle \mathrm{I}\rangle\sqrt{a}}\sqrt{I_{\rm SH}}\right). \tag{1.51}$$

whose first and second moments are

$$\langle I_{\rm SH}\rangle = \frac{\mu+1}{\mu}a\langle \mathrm{I}\rangle^2 \tag{1.52}$$

$$\langle I_{\rm SH}^2\rangle = \frac{(\mu+3)(\mu+2)(\mu+1)}{\mu^3}a^2\langle \mathrm{I}\rangle^4 \tag{1.53}$$

and the variance reads

$$\langle \Delta I_{\rm SH}^2\rangle = 2\frac{(2\mu+3)(\mu+1)}{\mu^3}a^2\langle \mathrm{I}\rangle^4. \tag{1.54}$$

Mandel's formula [29] provides the detected-photon distribution for the SH field [27], that is

$$Q(m) = \frac{\Gamma[1/2+m+\mu/2]\Gamma[m+\mu/2]}{4\sqrt{\pi}m!(\mu-1)!\{\langle m\rangle/[\mu(1+\mu)]\}^{(\mu+1)/2}} \cdot U\left[\frac{1}{2}+m+\frac{\mu}{2},\frac{3}{2},\frac{\mu(\mu+1)}{4\langle m\rangle}\right], \tag{1.55}$$

where $\langle m\rangle$ and μ are the mean number of detected photons and the number of modes in the fundamental beam respectively, $\Gamma[j]$ is the Gamma function, and $U[i,j,k]$ is the Tricomi confluent hypergeometric function. The mean value and the variance of this distribution can be computed analytically and read

$$\langle m_{\rm SH}\rangle = \frac{\mu+1}{\mu} a\eta\langle \mathrm{I}\rangle^2 = \eta\langle I_{\rm SH}\rangle \tag{1.56}$$

$$\langle \Delta m^2_{\rm SH}\rangle = 2\frac{(2\mu+3)}{\mu(\mu+1)}\langle m_{\rm SH}\rangle^2 + \langle m_{\rm SH}\rangle = \eta^2\langle \Delta I^2_{\rm SH}\rangle + \zeta\langle I_{\rm SH}\rangle. \tag{1.57}$$

Note that, while the SHG process leaves unchanged the statistical properties of a coherent beam, the correlations of a chaotic field are enhanced. This can be shown in many ways. First of all, upon defining a detected-photon correlation coefficient $C_{\rm SH}$ between two intensity distributions $f(I_1)$ and $f(I_2)$ as in [27]

$$C_{\rm SH} \equiv \frac{\langle m_1 m_2\rangle - \langle m_1\rangle\langle m_2\rangle}{\sqrt{\langle \Delta m_1^2\rangle\langle \Delta m_2^2\rangle}}, \tag{1.58}$$

one finds that, if $f(I)$ is given by Eq. (1.45), then

$$C_{\rm SH} = \frac{\sqrt{\langle m_1\rangle\langle m_2\rangle}}{\sqrt{(\langle m_1\rangle+\mu)(\langle m_2\rangle+\mu)}} \tag{1.59}$$

whereas, if $f(I)$ is given by Eq. (1.55), we have

$$C_{\rm SH} = \frac{\sqrt{\langle m_1\rangle\langle m_2\rangle}}{\sqrt{(\langle m_1\rangle+k)(\langle m_2\rangle+k)}} \tag{1.60}$$

with

$$k = \frac{\mu(\mu+1)}{2(2\mu+3)} < \mu \qquad \forall\mu\in\mathbb{N}.$$

Hence, the correlation coefficient for the output SH distribution is larger than the input multithermal one. In general, this is true for every higher-harmonic field and this is the reason why the statistics of harmonics is usually called *superthermal*. Alternatively, the enhancement of correlation can be seen directly from the Glauber's correlation functions. In particular, it can be shown [25] that

$$g^{(2)}_{n\omega} = \frac{g^{(2n)}_{\omega}}{(g^{(n)}_{\omega})^2}. \tag{1.61}$$

This fact will be proved for $n=2$ in the fourth chapter. Thus, in the simple case of thermal light we have that $g^{(2)}_{\omega}=2$ and $g^{(2)}_{2\omega}=12$, where we used $g^{(2)}_{\omega}=n!$.
Equivalently, one can say that chaotic light enhances the rate of multiphoton effects with respect to a coherent pump beam. In particular, [30] managed to use the ultrafast intensity fluctuations of twin-beam states produced via parametric down-conversion, which are endowed with a multithermal statistics (see the next sections for details), in order to measure an increased *statistical efficiency* of second-, third- and

fourth- harmonic generation. They defined the statistical efficiency $\zeta^{(n)}$ for an n-photon process, with rate $R^{(n)}$ and photon flux F, as

$$\zeta^{(n)} \equiv \frac{R^{(n)}}{F^n}$$

and showed that it is proportional to the nth-order normalized correlation function $g^{(n)}$.
Finally, we recall that, for what concerns the detected-photon statistics, the convolution of a large number of thermal distributions converges to a Poissonian distribution and, on the contrary, to a delta distribution in the continuous case. It is worth noting that this is true also for a superthermal distribution as we can see from Eqs. (1.54) and (1.57) since $\langle \Delta I_{\mathrm{SH}}^2 \rangle \overset{\mu\to\infty}{\longrightarrow} 0 \Rightarrow \langle \Delta m_{\mathrm{SH}}^2 \rangle \overset{\mu\to\infty}{\longrightarrow} \langle m_{\mathrm{SH}} \rangle$. In particular, the convergence of the superthermal distribution to a Poissonian is four times faster than that of the multithermal distribution. Indeed, for $\mu \gg 1$

$$\frac{\langle \Delta I_{\mathrm{SH}}^2 \rangle}{\langle I_{\mathrm{SH}} \rangle^2} \sim \frac{4}{\mu} \qquad \frac{\langle \Delta I_{\mathrm{F}}^2 \rangle}{\langle I_{\mathrm{F}} \rangle^2} \sim \frac{1}{\mu}. \tag{1.62}$$

1.4 Elements of Quantum Optics

> These are my principles. If you don't like them, I have others.
>
> *G. Marx*

1.4.1 Quantization of the Electromagnetic Field

The quantum theory of the electromagnetic field basically consists in the classical theory for a gauge field with the fundamental prescription that takes the canonical variables into noncommuting operators ([31, 32]). Here we briefly go through this procedure.
We have already written Maxwell's equations in Eqs. (1.7) in the absence of free charges. If now we remove this hypothesis, we have

$$\nabla \times \mathbf{H} - \frac{\partial}{\partial t}\mathbf{D} = \mathbf{J} \tag{1.63}$$

$$\nabla \times \mathbf{E} + \frac{\partial}{\partial t}\mathbf{B} = 0 \tag{1.64}$$

$$\nabla \cdot \mathbf{B} = 0 \tag{1.65}$$

$$\nabla \cdot \mathbf{D} = \rho. \tag{1.66}$$

Eqs. (1.64) and (1.65) are homogeneous and can be solved by introducing a scalar and a vector potential, respectively ϕ and $\mathbf{A}$, such that

$$\begin{cases} \mathbf{E} = -\nabla\phi - \dfrac{\partial}{\partial t}\mathbf{A} \\ \mathbf{B} = \nabla \times \mathbf{A}. \end{cases} \tag{1.67}$$

The fields are uniquely determined by the potentials, but the converse is not true. There is something arbitrary in the choice of the potentials such that the fields remain unchanged under different choices. Given an arbitrary function of spacetime Ω, the transformations

$$\phi \to \phi + \partial_t \Omega \tag{1.68}$$

$$\mathbf{A} \to \mathbf{A} - \nabla\Omega \tag{1.69}$$

leave the fields invariant and are called *gauge transformation*. This structure can be expressed in a more compact way by defining the *gauge field* as the four-vector potential $A^\mu \equiv (\phi, \mathbf{A})$. Upon requiring the invariance under the abelian symmetry group $U(1)$, the *field strength* $F = dA$ is found to be the antisymmetric tensor

$$F^{\mu\nu} \equiv \partial^\mu A^\nu - \partial^\nu A^\mu.$$

A simple comparison with Eqs. (1.68) and (1.69) shows that $F^{0i} = E^i$ and $F^{ij} = \varepsilon^{ijk} B_k$. Thus, the four Maxwell's equations can be summarized as

$$\partial_\nu F^{\mu\nu} = J^\mu \tag{1.70}$$

$$\varepsilon_{\mu\nu\rho\sigma} \partial^\rho F^{\mu\nu} = 0 \tag{1.71}$$

where $J \equiv (\rho, \mathbf{J})$ is the four-current vector. In particular, Eq. (1.70) replaces Eqs. (1.63) and (1.66), Eq. (1.71) replaces Eqs. (1.64) and (1.65). Note that, if we take the derivative of Eq. (1.70) and exploit the symmetry of $F^{\mu\nu}$, we find the conservation of the four current, which is the continuity equation

$$\partial_\mu J^\mu = 0. \tag{1.72}$$

Finally, the gauge transformations given by Eqs. (1.68) and (1.69) in this formalism are

$$A^\mu \to A^\mu - \partial^\mu \Omega \tag{1.73}$$

and the invariance of $F^{\mu\nu}$ is still guaranteed by the fact that it is antisymmetric.
Maxwell's equations (1.70) and (1.71) are the equations of motions for an electromagnetic field with external sources J^μ. Hence, by requiring some symmetry properties such as the invariance under Lorentz and gauge transformations, one finds that the Lagrangian can be given only by

$$\mathscr{L} = -\frac{1}{4} F^{\mu\nu} F_{\mu\nu} + J^\mu A_\mu \tag{1.74}$$

and the corresponding action is $S = \int d^4x \mathscr{L}$.
Now the procedure is hampered by a a difficulty due to the gauge invariance, which is the fact that we are left with too many degrees of freedom. This is evident, for example, by the absence of the time-derivative of A^0 in the Lagrangian in Eq. (1.74). Explicitly,

$$\mathscr{L} = -\frac{1}{2} \partial^\mu A^\nu \partial_\mu A_\nu + \frac{1}{2} \partial^\mu A^\nu \partial_\nu A_\mu + J^\mu A_\mu.$$

This is a serious problem since the canonically conjugate momentum Π^μ is defined as

$$\Pi^\mu = \frac{\partial \mathscr{L}}{\partial(\partial_0 A^\mu)} \tag{1.75}$$

and we need it for the Hamiltonian density

$$\mathscr{H} = \Pi^\mu A_\mu - \mathscr{L}. \tag{1.76}$$

This field seems to have no dynamics. The problem arises because the electromagnetic field has no component along the direction of propagation, which is the reason why we have an extra degree of freedom due to the gauge invariance. We have to fix it by imposing a *gauge condition* on A^μ.
A class of gauge conditions fixes $\partial^\mu A_\mu$ to a generic function of spacetime. In particular, the condition $\partial^\mu A_\mu = 0$ is called *Lorenz gauge*. Another strategy is $n^\mu A_\mu = 0$, with n^μ being a given constant four-vector. The typical choice in Quantum Optics is the *Coulomb gauge*, i.e.

$$\nabla \cdot \mathbf{A} = 0. \tag{1.77}$$

Note that the Fourier transform of Eq. (1.77) is $\mathbf{k}\cdot\tilde{\mathbf{A}}=0$, where $\tilde{\mathbf{A}}=(2\pi)^{-3}\int d^3x\mathbf{A}(\mathbf{x})e^{i\mathbf{kx}}$, which implies that the component of $\mathbf{A}$ that is parallel to the direction of propagation $\hat{\mathbf{k}}$ is set to zero. Thus, this choice has a physical significance since only the component of $\mathbf{A}$ parallel to $\hat{\mathbf{k}}$ depends on the gauge, as follows from the Fourier transform of Eq. (1.73).
The condition in Eq. (1.77) is naturally imposed if we replace A_i with $(\delta_{ij}-\nabla_i\nabla_j/\nabla^2)A_j$. Now we can try to determine the components of A^μ in the Lagrangian with the variational method. The variation of ϕ with $\delta S=0$ yields a Poisson equation for the scalar potential

$$-\nabla^2\phi=\rho \tag{1.78}$$

whose solution is the well-known Coulomb potential

$$\phi(\mathbf{x},t)=\int d^3y\frac{\rho(\mathbf{y},t)}{4\pi|\mathbf{x}-\mathbf{y}|}. \tag{1.79}$$

Upon requiring that both ϕ and ρ vanish at infinity, this solution is unique. However, it has no particular physical meaning by itself since it is non-local (the charge density instantaneously generates the potential), but we can plug it into the Lagrangian and find

$$\mathscr{L}=\frac{1}{2}\partial_0A_i\partial_0A_i-\frac{1}{2}\partial_jA_i\partial_jA_i+J_iA_i-\frac{1}{2}\int d^3y\frac{\rho(\mathbf{x},t)\rho(\mathbf{y},t)}{4\pi|\mathbf{x}-\mathbf{y}|}. \tag{1.80}$$

The variation of A_i yields the massless Klein-Gordon equation with source, i.e.

$$-\partial^2A_i(x)=\left(\delta_{ij}-\frac{\nabla_i\nabla_j}{\nabla^2}\right)J_i(x). \tag{1.81}$$

Hence, for a free field, the solution is

$$\mathbf{A}(x)=\sum_{\alpha=1}^{2}\int\frac{d^3k}{(2\pi)^32E_{\mathbf{k},\alpha}}\left[\varepsilon_\alpha^*(\mathbf{k})a_\alpha(\mathbf{k})e^{ikx}+\varepsilon_\alpha(\mathbf{k})a_\alpha^*(\mathbf{k})e^{-ikx}\right] \tag{1.82}$$

where a_α are the so-called *normal modes*, pure harmonic oscillation of the free field, whereas ε_1 and ε_2 are the polarization vectors. The relativistic invariant $d^3k/[(2\pi)^32E_{\mathbf{k},\alpha}]$ is normalized with the energy of the modes $E_{\mathbf{k},\alpha}\equiv\hbar\omega_{\mathbf{k},\alpha}$. The polarization vectors have to be orthogonal to $\hat{\mathbf{k}}$ to satisfy the Coulomb gauge. Thus, $(\varepsilon_1,\varepsilon_2,\mathbf{k})$ is an orthonormal complete set. In particular,

$$\mathbf{k}\cdot\varepsilon_\alpha(\mathbf{k})=0 \tag{1.83}$$

$$\varepsilon_{\alpha'}(\mathbf{k})\varepsilon_\alpha^*(\mathbf{k})=\delta_{\alpha'\alpha} \tag{1.84}$$

$$\sum_{\alpha=1}^{2}\varepsilon_{i\alpha}^*(\mathbf{k})\varepsilon_{j\alpha}(\mathbf{k})=\delta_{ij}-\frac{k_ik_j}{k^2}. \tag{1.85}$$

Note that Eq. (1.82) can be inverted to find out the normal modes as follows

$$a_\alpha(\mathbf{k})=i\varepsilon_\alpha(\mathbf{k})\cdot\int d^3x[e^{-ikx}\partial_0\mathbf{A}(x)-\mathbf{A}(x)\partial_0(e^{-ikx})]. \tag{1.86}$$

Now we are ready to move to a Hamiltonian formalism since the absence of the component Π^0 of the momentum is balanced by the choice of the gate. We have

$$\Pi^i=\partial_0A_i. \tag{1.87}$$

Hence, from Eq. (1.76), we get the Hamiltonian density for the electromagnetic field

$$\mathscr{H} = \frac{1}{2}(\Pi_i)^2 - \frac{1}{2}(\partial_j A_i)^2 - J_i A_i + \frac{1}{2}\int d^3y \frac{\rho(\mathbf{x},t)\rho(\mathbf{y},t)}{4\pi|\mathbf{x}-\mathbf{y}|}. \tag{1.88}$$

The quantization of the field is now straightforward from the canonical commutation relations for the field operators, in analogy with the classical Poisson brackets, i.e.

$$\begin{cases} [\hat{A}_i(\mathbf{x},t), \hat{\Pi}_j(\mathbf{x},t)] = i\hbar \left(\delta_{ij} - \frac{\nabla_i \nabla_j}{\nabla^2}\right) \delta^{(3)}(\mathbf{x}-\mathbf{y}) \\ [\hat{A}_i(\mathbf{x},t), \hat{A}_j(\mathbf{x},t)] = 0 \\ [\hat{\Pi}_i(\mathbf{x},t), \hat{\Pi}_j(\mathbf{x},t)] = 0. \end{cases} \tag{1.89}$$

The normal modes are also promoted to operators, as a consequence of the quantization of the field $A(x)$ and from Eq. (1.82). Moreover, from Eq. (1.89), one finds that they satisfy themselves a set of commutation relations, which is the following

$$\begin{cases} [\hat{a}_\alpha(\mathbf{k}), \hat{a}^\dagger_{\alpha'}(\mathbf{k}')] = (2\pi)^3 2\hbar\omega \delta^{(3)}(\mathbf{k}'-\mathbf{k})\delta_{\alpha\alpha'} \\ [\hat{a}_\alpha(\mathbf{k}), \hat{a}_{\alpha'}(\mathbf{k}')] = 0 \\ [\hat{a}^\dagger_\alpha(\mathbf{k}), \hat{a}^\dagger_{\alpha'}(\mathbf{k}')] = 0. \end{cases} \tag{1.90}$$

$\hat{a}_\alpha(\mathbf{k})$ and $\hat{a}^\dagger_\alpha(\mathbf{k})$ are the so called *annihilation* and *creation operators* because, given an empty state $|0\rangle$ defined as the lowest energy state of the field, the application of the latter generate an excitation of the field $|\mathbf{k},\alpha\rangle$, which is a quantum of energy $\hbar\omega$ and momentum $\mathbf{k}$ called *photon*, namely

$$\hat{a}^\dagger_\alpha(\mathbf{k})|0\rangle = |\mathbf{k},\alpha\rangle. \tag{1.91}$$

The action of the former on the empty state is

$$\hat{a}_\alpha(\mathbf{k})|0\rangle = 0. \tag{1.92}$$

Thus, the n-photon state can be seen as the result of the application of the creation operator to the empty state n times, i.e.

$$|\mathbf{k}_1,\alpha_1;...;\mathbf{k}_n,\alpha_n\rangle = \frac{1}{\sqrt{n!}}\prod_{j=1}^{n} \hat{a}^\dagger_{\alpha_j}(\mathbf{k_j})|0\rangle. \tag{1.93}$$

These free-field states are vectors in a Hilbert space, made of compositions, via direct sum and cartesian products, of the single-photon Hilbert spaces. In the free theory, the space is called *Fock space*.
Note that, through Eqs. (1.67), we can also define an operator for the electric and magnetic fields, i.e.

$$\hat{E} = i\sum_{\alpha=1}^{2}\int \frac{d^3k\hbar\omega_{\mathbf{k},\alpha}}{(2\pi)^3 2E_{\mathbf{k},\alpha}} \left[\varepsilon^*_\alpha(\mathbf{k})\hat{a}_\alpha(\mathbf{k})e^{ikx} - \varepsilon_\alpha(\mathbf{k})\hat{a}^\dagger_\alpha(\mathbf{k})e^{-ikx}\right] \tag{1.94}$$

$$\hat{B} = i\sum_{\alpha=1}^{2}\int \frac{d^3k}{(2\pi)^3 2E_{\mathbf{k},\alpha}} \left[(\mathbf{k}\times\varepsilon)^*_\alpha(\mathbf{k})\hat{a}_\alpha(\mathbf{k})e^{ikx} + \mathbf{k}\times\varepsilon_\alpha(\mathbf{k})\hat{a}^\dagger_\alpha(\mathbf{k})e^{-ikx}\right]. \tag{1.95}$$

The Hamiltonian operator is straightforward from the integration of Eq. (1.88) through Eqs. (1.90), namely

$$\hat{H} = \sum_{\alpha=1}^{2}\int \frac{d^3k}{(2\pi)^3 2E_{\mathbf{k},\alpha}}\hbar\omega_{\mathbf{k},\alpha}\hat{a}^\dagger_\alpha(\mathbf{k})\hat{a}_\alpha(\mathbf{k}) + E_0 - \int d^3x \hat{\mathbf{j}}(x)\cdot\hat{\mathbf{A}}(x) + \frac{1}{2}\int d^3x d^3y \frac{\hat{\rho}(\mathbf{x},t)\hat{\rho}(\mathbf{y},t)}{4\pi|\mathbf{x}-\mathbf{y}|} \tag{1.96}$$

where $E_0 \equiv (2\pi)^{-3}\int d^3k\hbar\omega V$ is the zero-point energy of all the oscillators.

1.4.2 Quantum states of light

Fock states

The *Fock states* in Eq. (1.93) are by definition eigenstates of the free field Hamiltonian

$$\hat{H} = \sum_{\alpha=1}^{2} \int \frac{d^3k}{(2\pi)^3 2E_{\mathbf{k},\alpha}} \hbar\omega_{\mathbf{k},\alpha} \hat{a}^\dagger_\alpha(\mathbf{k}) \hat{a}_\alpha(\mathbf{k}) + E_0. \tag{1.97}$$

The well-known problem of the infinite zero-point energy is typically solved imposing a cutoff at the upper integration limit, justified by the fact that at some large scale one expects that the formalism of quantum field theory breaks down. In this sense, the zero-point energy term is just a shift and, for the sake of simplicity, can be set to zero. Again for the sake of simplicity, we will neglect the sum over the two polarization in the following, giving it for granted. We will focus on one of the two polarizations. Moreover, from now on, we will operate the following substitution

$$\hat{a} \to \frac{\hat{a}}{\sqrt{(2\pi)^3 2E_{\mathbf{k},\alpha}}}$$

so that the first commutation rule in Eqs. (1.90) is simply

$$[\hat{a}(\mathbf{k}), \hat{a}^\dagger(\mathbf{k}')] = \delta^{(3)}(\mathbf{k} - \mathbf{k}') \tag{1.98}$$

and the free Hamiltonian in Eq. (1.97) reads

$$\hat{H} = \sum_{\alpha=1}^{2} \int d^3k \hbar\omega_{\mathbf{k}} \hat{a}^\dagger(\mathbf{k}) \hat{a}(\mathbf{k}). \tag{1.99}$$

The operator $\hat{a}^\dagger(\mathbf{k})\hat{a}(\mathbf{k})$ is called *number operator* because, as follows from the eigenvalue equation for $\hat{H}$, it counts the number of photons with a given energy $\hbar\omega_{\mathbf{k}}$, namely

$$\hat{n}(\mathbf{k}) \equiv \hat{a}^\dagger(\mathbf{k}) \hat{a}(\mathbf{k}). \tag{1.100}$$

The number operator is a proper observable, not only in the sense that it is linear and self-adjoint by definition, but also because it is a measurable quantity (for details, see chapter 4). In Quantum Optics [29], the capability of detecting the number of discrete excitations of the light field leads to focus on the photon number n rather than on other variables, so that the Fock states are often labeled with n as follows

$$|n\rangle \equiv |\mathbf{k}_1; \ldots; \mathbf{k}_n\rangle_{\alpha=\bar{\alpha}} \qquad \bar{\alpha} = 1, 2$$

and the eigenvalue equation for $\hat{n}$ reads

$$\hat{n}|n\rangle = n|n\rangle. \tag{1.101}$$

The set of Fock states is an orthonormal complete basis in the Fock space. From now on, this will be the most used basis over which other light states will be expanded, i.e. $|\psi\rangle = \sum_n c_n |n\rangle$. As outlined in the previous section, it is the intensity distribution which mostly characterizes different radiation fields. In the quantum regime, this is still true with the intensity distribution replaced by the probability $p(n) = |c_n|^2$ of finding n photons in the state $|\psi\rangle$.
The action of the creation and the annihilation operators on the number states is straightforward from

Eqs. (1.91 - 1.93). Explicitly

$$\begin{aligned}
&\hat{a}|0\rangle = 0 \\
&|n\rangle = \frac{1}{\sqrt{n!}}(\hat{a}^\dagger)^n|0\rangle \\
&\hat{a}|n\rangle = \sqrt{n}|n-1\rangle \\
&\hat{a}^\dagger|n\rangle = \sqrt{n+1}|n+1\rangle.
\end{aligned} \tag{1.102}$$

The last two equations can be verified through the commutation relations between $\hat{a}$ and $\hat{a}^\dagger$. In particular, note that the operators $\hat{a}$, $\hat{a}^\dagger$, $\hat{n}$ and $\hat{\mathbb{1}}$ are the elements of a closed Lie algebra, called *Heisenberg algebra* [33].

Coherent states

The coherent states were introduced by Glauber [36] as the eigenstates of the strength field in Eq. (1.94). Thus, for a single mode, they are the oscillator states $|\alpha\rangle$ such that

$$\hat{a}|\alpha\rangle = \alpha|\alpha\rangle. \tag{1.103}$$

From the last of Eqs. (1.102) follows that the application of $\hat{a}^\dagger$ to Eq. (1.103) leads to a recursion formula for the projection $\langle n|\alpha\rangle$, which is

$$\sqrt{n+1}\langle n+1|\alpha\rangle = \alpha\langle n|\alpha\rangle.$$

Then, for induction, the following relation must hold

$$\langle n|\alpha\rangle = \frac{\alpha^n}{\sqrt{n!}}\langle 0|\alpha\rangle. \tag{1.104}$$

These projections are the coefficients of the expansion of the coherent state over the number states $|\alpha\rangle = \sum_n \langle n|\alpha\rangle|n\rangle$, so that

$$|\alpha\rangle = \langle 0|\alpha\rangle \sum_n \frac{\alpha^n}{\sqrt{n!}}|n\rangle. \tag{1.105}$$

From the normalization of the state $\langle\alpha|\alpha\rangle = 1$, one immediately finds

$$\langle 0|\alpha\rangle = \exp\left(-\frac{1}{2}|\alpha|^2\right) \tag{1.106}$$

so that

$$|\alpha\rangle = \exp\left(-\frac{1}{2}|\alpha|^2\right)\sum_n \frac{\alpha^n}{\sqrt{n!}}|n\rangle. \tag{1.107}$$

Hence, the probability distribution $|\langle n|\alpha\rangle|^2$ is Poissonian, i.e.

$$p(n) = \frac{|\alpha|^{2n}}{n!}e^{-|\alpha|^2} \tag{1.108}$$

which means that Glauber's coherent states are the quantum description of the second-order coherent fields in Eq. (1.41).
Finally, we remark that coherent states belong to the class of *minimum uncertainty states*, which means that they saturate the uncertainty relation for the quadratures [33]. The quadrature operators are defined

as a linear combination of the creation and annihilation operators and are the analog of the position and momentum operator for a radiation field, namely

$$\begin{aligned} \hat{x} &= \hat{a}+\hat{a}^{\dagger} \\ \hat{p} &= -i(\hat{a}-\hat{a}^{\dagger}). \end{aligned}$$

From Eqs. (1.90) it is straightforward to find that

$$[\hat{x},\hat{p}] = 2i \tag{1.109}$$

and hence the correspondent uncertainty relation reads

$$\langle \Delta\hat{x}^2\rangle\langle \Delta\hat{p}^2\rangle \geq 1. \tag{1.110}$$

It is easy to verify that for coherent states $\langle \Delta\hat{x}^2\rangle = \langle \Delta\hat{p}^2\rangle = 1$. As a last remark, we note that the quadrature operators are usually generalized to include the phase of the field as follows

$$\hat{x}_{\theta} = \hat{a}^{\dagger}e^{-i\theta} + \hat{a}^{\dagger}e^{i\theta}. \tag{1.111}$$

Chaotic states

A chaotic state [29] is the quantum description of the thermal field introduced for μ modes in Eq. (1.44). By definition, the light state emitted by a single thermal source cannot be a pure state, since we do not have control on the preparation of the states, being them determined by the temperature T of the source. Thus, the thermal state is a statistical mixture drawn from the Maxwell-Boltzmann energy distribution, i.e.

$$\hat{\rho} = \frac{e^{-\beta\hbar\omega\hat{n}}}{\mathrm{Tr}[e^{-\beta\hbar\omega\hat{n}}]} \tag{1.112}$$

where $\beta \equiv (k_B T)^{-1}$ and k_B is the Boltzmann constant. The computation of the trace yields

$$\hat{\rho} = (1-e^{-\beta\hbar\omega})e^{-\beta\hbar\omega\hat{n}}.$$

Hence, we see that it can be represented over the number states [32] as

$$\hat{\rho} = \sum_n p(n)|n\rangle\langle n|$$

with $p(n)$ given by the Bose-Einstein statistics

$$p(n) = \frac{N^n}{(N+1)^{n+1}} \tag{1.113}$$

where $N = \mathrm{Tr}[\hat{\rho}\hat{n}] = (\exp[\beta\hbar\omega]-1)^{-1}$. Equation (1.113) easily generalizes to a multi-mode case, for which, provided that the modes are assumed to be equally populated, $p(n)$ should be the same distribution as Eq. (1.44) for the discrete variable n. Such a distribution has been already computed for the photoelectrons (Eq. (1.45)) and can be rewritten as

$$p(n) = \binom{n+\mu-1}{n}\frac{N^n}{(N+1)^{n+\mu}}. \tag{1.114}$$

The computation of the mean value and variance for the number of photons from (1.114) yields

$$\begin{cases} \langle\hat{n}\rangle = \mu N \\ \langle\Delta\hat{n}^2\rangle = \mu N(N+1). \end{cases} \tag{1.115}$$

In particular, the variance can be rewritten in terms of the mean value as

$$\langle\Delta\hat{n}^2\rangle = \langle\hat{n}\rangle\left(\frac{\langle\hat{n}\rangle}{\mu}+1\right).$$

Squeezed states

A *squeezed state* [29] is an element belonging to the class of minimum-uncertainty states such that $\langle\Delta\hat{x}^2\rangle \neq \langle\Delta\hat{p}^2\rangle$. In other words, we talk about *squeezing* if the second moment of an observable, or of a set of observables, is smaller than the corresponding vacuum level.
A single-mode squeezed state is generated through a transformation of the kind $\hat{H} \propto (\hat{a}^\dagger)^2 + h.c.$. Thus, the squeezing evolution operator can be written as

$$\hat{S}(r) = \exp\left(\frac{r}{2}(\hat{a}^\dagger)^2 - h.c.\right) \tag{1.116}$$

where the complex number $r = \rho e^{i\phi}$ is the so called *squeezing parameter*. Note that the evolution of the creation and annihilation operators through Eq. (1.116) yields a famous isomorphism of the canonical commutation relations (Eq. (1.98)), which is the *Bogoliubov transformation*:

$$\hat{S}^\dagger(r)\hat{a}\hat{S}(r) = \mu\hat{a} + \nu\hat{a}^\dagger \tag{1.117}$$
$$\hat{S}^\dagger(r)\hat{a}^\dagger\hat{S}(r) = \mu\hat{a}^\dagger + \nu^*\hat{a} \tag{1.118}$$

where $\mu = \cosh(\rho)$ and $\nu = e^{i\phi}\sinh(\rho)$.
We note that the Hamiltonian of this process is a combination of elements of the Schwinger two-boson representation of the $SU(1,1)$ algebra. Hence, we know how to disentangle the operator in Eq. (1.116), so that we can apply it to the vacuum state and expand the squeezed states over the number-state basis [33, 38]. This procedure yields

$$|r\rangle = \hat{S}(r)|0\rangle = \frac{1}{\mu}\sum_k \left(\frac{\nu}{2\mu}\right)^k \frac{\sqrt{2k!}}{k!}|2k\rangle \tag{1.119}$$

which is called *squeezed vacuum state*. The computation of the variances of the quadratures shows that these states are really minimum uncertainty states in the sense outlined at the beginning: $\langle\Delta\hat{x}^2\rangle\langle\Delta\hat{p}^2\rangle = 1$, but $\langle\Delta\hat{x}^2\rangle \neq \langle\Delta\hat{p}^2\rangle$. It may seem counter-intuitive but, even if this state is called squeezed vacuum, it is not empty since the mean value of the photon-number observable is worth $\langle r|\hat{n}|r\rangle = |\nu|^2$. On the contrary, the mean value of the quadrature is empty, $\langle r|\hat{x}_\theta|r\rangle = |0 \quad \forall\theta$, whereas the variance reads

$$\langle\Delta\hat{x}_\theta\rangle = e^{2r}\cos(\theta) + e^{-2r}\sin(\theta). \tag{1.120}$$

In the case of two-mode squeezing, the Hamiltonian of the process should be something like $\hat{H} \propto \hat{a}^\dagger\hat{b}^\dagger + h.c.$, for which the unitary evolution reads

$$\hat{S}_2(r) = \exp\left(r\hat{a}^\dagger\hat{b}^\dagger - h.c.\right) \tag{1.121}$$

where r has the same meaning as before. The Bogoliubov transformations are given by

$$\hat{S}_2^\dagger(r)\hat{a}\hat{S}_2(r) = \mu\hat{a} + \nu\hat{b}^\dagger \tag{1.122}$$
$$\hat{S}_2^\dagger(r)\hat{b}^\dagger\hat{S}_2(r) = \mu\hat{b}^\dagger + \nu^*\hat{a}. \tag{1.123}$$

Again, the Hamiltonian is an element of the $SU(1,1)$ algebra, even if the representation is different, and we can find the expansion of the *two-mode squeezed vacuum* over the number states, i.e.

$$|r\rangle\rangle = \hat{S}_2(r)|0\rangle\otimes|0\rangle = \frac{1}{\mu}\sum_k \left(\frac{\nu}{\mu}\right)^k |k\rangle\otimes|k\rangle \tag{1.124}$$

which is often written also as

$$|r\rangle\rangle = \sqrt{1-|\lambda|^2}\sum_k \lambda^k |k\rangle \otimes |k\rangle \tag{1.125}$$

with $\lambda \equiv \nu/\mu$. Note that this state is *entangled* [48]. Due to the quantum correlations between the two modes related to one of the most significant implementations in Nonlinear Quantum Optics, the two-mode squeezed vacuum is also known as *twin-beam state TWB*. This specific implementation of the squeezed-vacuum deserves an independent Section, which is the following, since in that case the state in Eq. (1.125) arises as a consequence of an approximation to a more complicated nonlinear process.

Twin-beam states

The typical optical implementation of the two-mode squeezed vacuum states are the TWBs. These states are generated through a quantum nonlinear process known as *parametric down conversion PDC*, which could be generally described as a difference-frequency generation where the pump interacts with the fluctuations of the vacuum state [29]. However, while the difference-frequency generation is a nonlinear effect which is well described in the classical context outlined in the first section [22], the PDC is a genuine quantum process. As summarized in Fig. 1.4, it basically consists in the interaction, mediated by the nonlinear crystal, between two vacuum states and the pump mode resulting in the population of the input vacuum states, which are usually called *signal* and *idler*. The interaction Hamiltonian reads

$$\hat{H}_{\mathrm{TWB}} \propto \hat{a}_p \hat{a}_s^\dagger \hat{a}_i^\dagger + h.c. \tag{1.126}$$

where the indices p, s and i refer respectively to pump, signal and idler.
The conservation of energy and the phase-matching condition set a condition on the frequencies and the wave vectors of the fields, i.e.

$$\begin{cases} \omega_p = \omega_s + \omega_i \\ \mathbf{k}_p(\omega_p) = \mathbf{k}_s(\omega_s) + \mathbf{k}_i(\omega_i). \end{cases} \tag{1.127}$$

We recall that, as already noted above, the fulfillment of both the conditions requires the crystal to be birefringent. Moreover, note that these conditions fix the geometry and the frequency of the generated states. In particular, as to the geometry, we have that the output wave-vectors originate from the output surface of the crystal and are symmetric with respect to rotations around the pump direction. Therefore, the geometry of the PDC is a cone, whose aperture angle is determined by the frequency of the generated beams. A section of the cone is shown in Fig. 1.5.
The reason for the name *parametric* is that the effect itself is parametric, since at the end of the process the energy states of the molecules interacting with the fields are unchanged. The nonlinear crystal just acts as a medium between the fields.
Note that the Hamiltonian in Eq. (1.126) is not the same as the one originating the two-mode squeezed vacuum state previously described, but then what do we mean by saying that a TWB is a two-mode squeezed vacuum? The point here is that the temporal evolution given by the Hamiltonian in Eq. (1.126) cannot be disentangled because such Hamiltonian does not belong to a subalgebra of the affine metasimplectic group [38, 33]. One can try to solve the quantum dynamics with numeric [34] or perturbative [35] methods. However, we can also use a very practical assumption. It is surely true that the pump field is very intense compared to the vacuum fluctuations, so much stronger that it could be approximated to a c-number, a parameter. The so called *parametric approximation* allows us to rewrite Eq. (1.126) as

$$\hat{H}_{\mathrm{TWB}} \propto \alpha_p \hat{a}_s^\dagger \hat{a}_i^\dagger + h.c. \tag{1.128}$$

which is exactly the two-mode squeezing Hamiltonian described in the previous Section. Thus, the evolution is given by the squeezing operator in Eq. (1.121), i.e.

$$\hat{S}_{\mathrm{TWB}}(r) = \exp\left(r(\mathbf{k}_p, \mathbf{k}_s, \alpha_p)\hat{a}_s^\dagger \hat{a}_i^\dagger - h.c.\right) \tag{1.129}$$

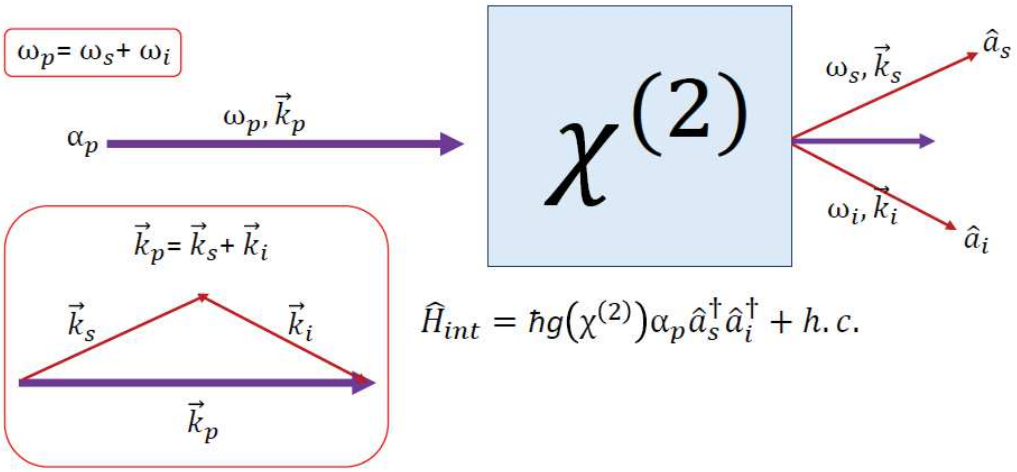

Fig. 1.4: A scheme of the PDC process. In the boxes, the conditions on frequencies and wave vectors of Eqs. (1.127) are shown.

where the squeezing parameter here depends on the phase-matching geometry, on the specific nonlinear material and on the pump intensity. Hence, a TWB can be expressed as the entangled state in Eq. (1.125) with $\lambda = \lambda(\mathbf{k}_p, \mathbf{k}_s, \alpha_p)$ and photon-number mean value

$$N \equiv \langle r|\hat{n}|r\rangle = \sinh^2(r).$$

In this respect, a TWB $|r\rangle\rangle_{\rm TWB}$ can be described as a two-mode squeezed vacuum $|r\rangle\rangle$. Note that, by fixing

$$\lambda^2 = \frac{N}{N+1}. \tag{1.130}$$

such state can be rewritten as

$$|r\rangle\rangle_{\rm TWB} = \sum_n \sqrt{p(n)} e^{i\phi_0} |n,n\rangle \tag{1.131}$$

where

$$p(n) = \frac{N^n}{(N+1)^{n+1}},$$

ϕ_0 is the phase of the pump and $|n,n\rangle \equiv |n\rangle \otimes |n\rangle$. Therefore, we have retrieved that a two-mode squeezed vacuum state is endowed with a thermal distribution. In other words, signal and idler are speckle fields. However, in a mesoscopic regime, each of the two generated beams may include more than one spatial and temporal mode. In such a case, we have a *multimode TWB* and the Hamiltonian describing the process is better defined as the sum over all the spatial and temporal modes of the single spatio-temporal-mode Hamiltonians in Eq. (1.126), i.e.

$$\begin{aligned} \hat{H}_{\rm TWB} &= \sum_{j=1}^{\mu} \hat{a}_{p,j} \hat{a}_{s,j}^\dagger \hat{a}_{i,j}^\dagger + h.c. \\ &\sim \sum_{j=1}^{\mu} \alpha_{p,j} \hat{a}_{s,j}^\dagger \hat{a}_{i,j}^\dagger + h.c. \end{aligned} \tag{1.132}$$

where in the second line we applied the parametric approximation. Note that this definition of the Hamiltonian holds only if the modes are independent from each other, which is reasonable since there is no reason for them to interact out of the nonlinear crystal. Another assumption is required to provide a solution for the temporal evolution given by the Hamiltonian in Eq. (1.132), but still a reasonable one: we ask that the modes are equally populated. Under this hypothesis, the energy contribution of every mode is the same and the output state $|r_\mu\rangle\rangle_{\rm TWB}$ is a tensor product of all the single-spatio-temporal-mode TWBs. Namely,

$$|r_\mu\rangle\rangle_{\rm TWB} = \bigotimes_{j=1}^{\mu} |r\rangle\rangle_{\rm TWB_j} = \sum_n \sqrt{p_\mu(n)}\,\delta\left(n - \sum_{l=1}^{\mu} n_l\right) \bigotimes_{k=1}^{\mu} |n\rangle_k \bigotimes_{j=1}^{\mu} |n\rangle_j \tag{1.133}$$

where $p_\mu(n)$ is a multithermal distribution, defined in Eq. (1.114). Therefore, mean value and variance read

$$\begin{aligned} \langle \hat{n} \rangle &= \mu N \\ \langle \Delta \hat{n}^2 \rangle &= \langle \hat{n} \rangle \left(\frac{\langle \hat{n} \rangle}{\mu} + 1 \right) \end{aligned}$$

and hence one has an indirect measure of the number of modes, i.e.

$$\mu = \frac{\langle \hat{n} \rangle^2}{\langle \Delta \hat{n}^2 \rangle - \langle \hat{n} \rangle}. \tag{1.134}$$

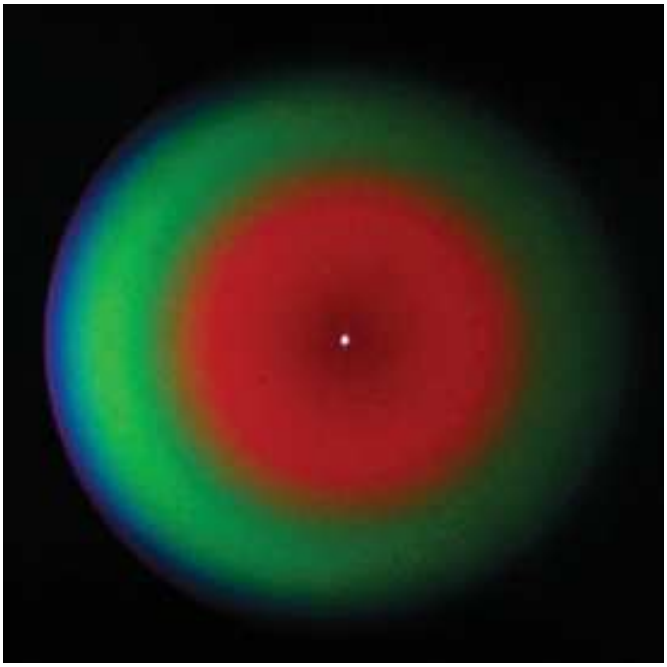

Fig. 1.5: The output of PDC in the mesoscopic domain is a light cone whose distribution of the photon numbers is multithermal and the geometry is determined by Eqs. (1.127). This is a section of the light cone.

1.4.3 Nonclassicality

The basic concept of the previous section is that there is a number of light states whose measurable properties do not fit a classical description. In such a case, we say that these are *nonclassical properties*. To be measurable, they have to be somehow statistical properties. By saying that they do not fit a classical description, we mean that there are some statistical laws which are verified by any classical light distribution, but which fail to be true for a nonclassical state. These statistical laws are the relations in Eqs. (1.38) and (1.39). To better understand why, we have to redefine the Glauber's second-order autocorrelation function in Eq. (1.35) for quantum operators. Following [37], we consider the kind of measurements performed in the Hanbury-Brown and Twiss experiment, consisting in detecting photon coincidences through two detectors placed in different positions, $\mathbf{r}$ and $\mathbf{r}'$. If $|i\rangle$ and $|f\rangle$ are respectively the state of the field before and after detection and $\hat{E}^{(\pm)}$ the positive and negative frequency components of the electric field operator in Eq. (1.94), the amplitude of the transition from $|i\rangle$ to $|f\rangle$ is

$$\langle f|\hat{E}^{(+)}(\mathbf{r},t)\hat{E}^{(+)}(\mathbf{r}',t')|i\rangle. \tag{1.135}$$

Hence, the probability that a photon is detected at the spacetime coordinates $(t,\mathbf{r})$ and the other at $(t',\mathbf{r}')$ is proportional to

$$\sum_f |\langle f|\hat{E}^{(+)}(\mathbf{r},t)\hat{E}^{(+)}(\mathbf{r}',t')|i\rangle|^2 = \langle i|\hat{E}^{(-)}(\mathbf{r}',t')\hat{E}^{(-)}(\mathbf{r},t)\hat{E}^{(+)}(\mathbf{r},t)\hat{E}^{(+)}(\mathbf{r}',t')|i\rangle \tag{1.136}$$

since $(\hat{E}^{(+)})^\dagger = \hat{E}^{(-)}$. This is the fundamental quantity that is measured in a photon correlation experiment, i.e. the second-order correlation function, which is a particular case of Eq. (1.33).
In general, we do not know the initial state of the radiation field. Thus, we should better express it as a mixed state ρ rather than the pure state $|i\rangle$, so that Eq. (1.136) reads

$$G^{(2)}(r_1,r_2,r_3,r_4;t_1,t_2,t_3,t_4) = \mathrm{Tr}[\rho\hat{E}^{(-)}(\mathbf{r}_1,t_1)\hat{E}^{(-)}(\mathbf{r}_2,t_2)\hat{E}^{(+)}(\mathbf{r}_3,t_3)\hat{E}^{(+)}(\mathbf{r}_4,t_4)] \tag{1.137}$$

For a generic number n of photon coincidences in an experiment, we should consider the nth-order correlation functions, which easily generalize from Eq. (1.137) as

$$G^{(n)}(r_1,...,r_{2n};t_1,...,t_{2n}) = \mathrm{Tr}[\rho\hat{E}^{(-)}(\mathbf{r}_1,t_1)...\hat{E}^{(-)}(\mathbf{r}_n,t_n)\hat{E}^{(+)}(\mathbf{r}_{n+1},t_{n+1})...\hat{E}^{(+)}(\mathbf{r}_{2n},t_{2n})]. \tag{1.138}$$

The usual normalization of Eq. (1.137) provides the Glauber's second-order correlation function in the quantum case

$$g^{(2)}(r_1,r_2,r_3,r_4;t_1,t_2,t_3,t_4) = \frac{G^{(2)}(r_1,r_2,r_3,r_4;t_1,t_2,t_3,t_4)}{\prod_{j=1}^4\sqrt{G^{(1)}(r_j,r_j;t_j,t_j)}}. \tag{1.139}$$

The generalization to $g^{(n)}$ is straightforward.
The factors $G^{(1)}(r_j,r_j;t_j,t_j)$ are proportional to the mean value of the Hamiltonian operator, which, in absence of external potentials, is conserved. In such a case, $G^{(1)}(r_j,r_j;t_j,t_j) = G^{(1)}(r_i,r_i;t_i,t_i) \quad \forall j \neq i$. Then Eq. (1.139) can be rewritten as

$$g^{(2)}(r_1,r_2,r_3,r_4;t_1,t_2,t_3,t_4) = \frac{\mathrm{Tr}[\rho\hat{E}^{(-)}(\mathbf{r}_1,t_1)\hat{E}^{(-)}(\mathbf{r}_2,t_2)\hat{E}^{(+)}(\mathbf{r}_3,t_3)\hat{E}^{(+)}(\mathbf{r}_4,t_4)]}{\mathrm{Tr}^2[\rho\hat{E}^{(-)}\hat{E}^{(+)}]}. \tag{1.140}$$

Being $\hat{E}^{(-)}$ and $\hat{E}^{(+)}$ respectively proportional to the creation and annihilation operator, the normalized seond-order correlation function is more commonly defined in the following form

$$g^{(2)} = \frac{\langle\hat{a}^\dagger\hat{a}^\dagger\hat{a}\hat{a}\rangle}{\langle\hat{a}^\dagger\hat{a}\rangle^2}. \tag{1.141}$$

Now we clearly see that in the quantum formalism it is not possible to find the classical inequalities (1.38) and (1.39). In general, they do not hold any more. We can just say that the $g^{(2)}$ is a positive semidefinite function. This implies that we can also have $g^{(2)} < 1$, which is not possible in the classical case. We have found a *nonclassicality criterion*, i.e. a strategy to decide if a light state is nonclassical, in the sense outlined at the beginning of the section. Explicitly, we say that a given radiation field is nonclassical if

$$0 \leq g^{(2)} < 1. \tag{1.142}$$

Note that this is a sufficient, but not necessary condition. Indeed if Eq. (1.142) is satisfied, then the state cannot be classical, but the vice versa does not hold since this condition is not some fundamental property of quantum states.
Moreover, we see that the coherent states ($g^{(2)} = 1$) are the boundary case between quantum and classical states. In particular, we can use the relation between the mean and the variance of light distributions to retrieve another way to state the nonclassicality criterion in Eq. (1.142). The trick consists in writing Glauber's function in terms of the number operator, as follows

$$g^{(2)} = \frac{\langle : \hat{n}^2 : \rangle}{\langle \hat{n} \rangle^2} \tag{1.143}$$

where the notation :: stands for the normal ordering of the operators. Expanding Eq. (1.143), one finds

$$g^{(2)} = \frac{\langle \hat{n}^2 \rangle}{\langle \hat{n} \rangle^2} - \frac{1}{\langle \hat{n} \rangle} = 1 + \frac{\frac{\langle \Delta \hat{n}^2 \rangle}{\langle \hat{n} \rangle} - 1}{\langle \hat{n} \rangle} \tag{1.144}$$

and, hence, we see that $g^{(2)} < 1 \iff \langle \Delta \hat{n}^2 \rangle < \langle \hat{n} \rangle$ and $g^{(2)} \geq 1 \iff \langle \Delta \hat{n}^2 \rangle \geq \langle \hat{n} \rangle$. But the mean value $\langle \hat{n} \rangle$ is equal to the variance in the Poissonian case. Thus, we deduce that the condition in Eq. (1.142) has the following meaning: if the variance of a given distribution is smaller than the Poissonian variance, then the radiation field described by such a distribution cannot be classical. As mentioned before, the coherent-state case is rigorously a boundary between the classical and the quantum worlds, even if in a weak sense. Then, we can capture this notion by introducing the ratio [29]

$$F \equiv \frac{\langle \Delta \hat{n}^2 \rangle}{\langle \Delta \hat{n}^2 \rangle_{\text{POISS}}} \tag{1.145}$$

and re-stating equivalently the condition in Eq. (1.142) as

$$0 \leq F < 1. \tag{1.146}$$

From this formulation, we see that the quantum states described by the criterion in Eq. (1.142) are *sub-Poissonian*. The quantity F is called *Fano factor*. The advantage of re-writing the criterion in Eq. (1.142) as Eq. (1.146) is the fact that only the mean value and the variance of the distribution under investigation are needed to establish the nonclassicality of the field. The relation between $g^{(2)}$ and F is straightforward from Eq. (1.144), i.e.

$$g^{(2)} = 1 + \frac{F-1}{\langle \hat{n} \rangle}. \tag{1.147}$$

As a final remark about Glauber's correlation functions, note that, from Eq. (1.141) on, we implicitly omitted the dependence on the spacetime coordinates. For the sake of simplicity, we can write the nth-correlation function as $g^{(n)}_{x_1,\ldots,x_{2n}}$, so that the subscripts make the arguments $x_j \equiv (t_j, \mathbf{r}_j)$ explicit [40, 39]. If $x_1 = x_2 = \ldots x_{2n}$, the Glauber's function is the normalized nth-intensity moment, i.e.

$$g^{(n)}_{x_1,\ldots,x_1} \equiv g^{(n)}_{x_1 \times 2n} = \frac{\langle \hat{I}^n \rangle}{\langle \hat{I} \rangle^n}$$

where $\hat{I} \propto \hat{E}^{(-)}\hat{E}^{(+)}$. In the particular case with $n = 1$, Glauber's functions correspond to well-known quantities since $g^{(1)}_{x_1,x_2}$ is the *mutual coherence function* and $g^{(1)}_{x\times 2}$ is the *autocorrelation function*. Their Fourier transforms are the field *spectral densities*. In the case we are interested about, we have two detectors for two beams and a given number n of fields. Consider, for instance, the case of the TWB outlined in the previous section and say that these two beams are the signal and the idler. Then, Glauber's correlation functions read [39]

$$g^{(n)}_{x_1\times j,x_2\times k} = \frac{\langle : \hat{n}_s^j \hat{n}_i^k : \rangle}{\langle \hat{n}_s \rangle^j \langle \hat{n}_i \rangle^k} \tag{1.148}$$

where $j + k = n$.

However, there are more practical functions that can be used to detect nonclassical correlations between signal and idler [39]. An inspection of the two-boson realization of the SU$(1,1)$ algebra, which describes the evolution in Eq. (1.121) for the two-mode squeezed states, shows that the difference in the mean photon-number $\langle \hat{a}^\dagger \hat{a} - \hat{b}^\dagger \hat{b} \rangle$ is a constant of motion [33, 38]. Thus, if $\hat{\rho}_{\rm out} = \hat{S}_2^\dagger(r)\hat{\rho}_{\rm in}\hat{S}_2(r)$, then

$$\langle \hat{a}^\dagger \hat{a} - \hat{b}^\dagger \hat{b} \rangle_{\hat{\rho}_{\rm out}} = \langle \hat{a}^\dagger \hat{a} - \hat{b}^\dagger \hat{b} \rangle_{\hat{\rho}_{\rm in}}. \tag{1.149}$$

For a TWB, $\langle \hat{N}_- \rangle \equiv \langle \hat{n}_s - \hat{n}_i \rangle$ is a conserved quantity. Since this is generally not true for classical states of light, we can think to estabilish a nonclassicality criterion to detect the quantum correlation in the photon-number observable by following the strategy of the Fano factor: we compare the variance of the photon-number difference between signal and idler in a given state $\hat{N}_-$ to the same quantity related to a coherent state. Then we can consider the function [41, 42, 39]

$$R \equiv \frac{\langle \Delta(\hat{N}_-)^2 \rangle}{\langle \Delta(\hat{N}_-)^2 \rangle_{\rm POISS}} \tag{1.150}$$

and say that signal and idler are surely nonclassically correlated in number if

$$0 \leq R < 1. \tag{1.151}$$

Note that in the case of a two-mode squeezed state, $R = 0$. The quantity in Eq. (1.150) is known as *noise reduction factor (NRF)*. It can be made more explicit by computing the variance of $\hat{N}_-$, as follows

$$R = \frac{\langle \Delta(\hat{N}_-)^2 \rangle}{\langle \hat{N}_+ \rangle} \tag{1.152}$$

where $\hat{N}_+ \equiv \hat{n}_s + \hat{n}_i$. We outline that here the fundamental physical observable we are employing to discriminate between classical and nonclassical correlations is the photon-number difference $\hat{N}_-$. The NRF is just a function useful to state in a simple way the nonclassicality criterion based on this quantity, the same as in Eq. (1.142). In the following, we will show that one could equivalently use the second-order correlation function as long as the variable is the photon-number difference [49].

We also observe that a measurement of the photon-number difference consists in the *difference photocurrent* $\hat{D} \equiv \hat{m}_1 - \hat{m}_2$, where $\hat{m}_j$ with $j = 1, 2$ are the observable for the detected-photon number. It is not trivial that a nonclassicality criterion based on this observable, instead of the pure photon-number difference, still holds, but, under some constraints, it has been shown that this is the case [41]: it can be used to reveal entanglement, even if it cannot provide a full characterization of the quantum correlations between signal and idler. For instance, it can be surely used to discriminate between the entanglement of TWB states and the classical correlations of a mesoscopic thermal source. We will briefly resume this topic in the next Section.

Finally, note that so far we have considered ideal photodetectors, i.e. we have actually neglected the whole process of detection. In the following, we will introduce a more realistic description by considering as observable the photoelectron number $\hat{m}$, which basically implies that we will keep into account the nonidealities of the detector.

1.5 Detection of quantum states of light

Do you see the light? Do you see the light? Have you seen the light?

Reverend Cleophus James
The blues brothers

Measuring an observable is the way by which we extract some information from a quantum state. Typically, one does not implement a proper projective measure because the detector is affected by nonidealities. We know from Naimark's theorem [43, 38] that this is equivalent to perform a projective measure on a subsystem of a larger system, i.e. the so called *positive operator-valued measure (POVM)* $\hat{\Pi}$ or *generalized measure*. Explicitly, given a state of the radiation field $\hat{\rho}_A$ over which we would like to measure the observable $\hat{X}$, the measurement process can be described as a unitary transformation $\hat{U}$ over a larger Hilbert space $H_A \otimes H_B$, so that the probability of getting the outcome x must be given by

$$p_x = \mathrm{Tr}[\hat{U}\hat{\rho}_A \otimes \hat{\rho}_B \hat{U}^\dagger \hat{\mathbb{1}} \otimes \hat{P}_x] = \mathrm{Tr}_A[\hat{\rho}_A \mathrm{Tr}_B[\hat{\mathbb{1}}_A \otimes \hat{\rho}_B \hat{U}^\dagger \hat{\mathbb{1}} \otimes \hat{P}_x \hat{U}]] = \mathrm{Tr}_A[\hat{\rho}_A \hat{\Pi}_x]$$

where $\hat{P}_x \equiv |x\rangle\langle x|$ and the POVM is thus defined as $\hat{\Pi}_x \equiv \mathrm{Tr}_B[\hat{\mathbb{1}}_A \otimes \hat{\rho}_B \hat{U}^\dagger \hat{\mathbb{1}} \otimes \hat{P}_x \hat{U}]$. By definition, a POVM is a set $\{\hat{\Pi}_x\}_{x\in X}$ of positive and normalized operators which are not, in general, idempotent like the projectors. In summary,

$$\begin{aligned} &\hat{\Pi}_x \geq 0 \quad (\Rightarrow \hat{\Pi}_x = \hat{\Pi}_x^\dagger) \\ &\int_X \hat{\Pi}_x dx = \hat{\mathbb{1}}. \end{aligned} \tag{1.153}$$

For what concerns the quantum states of light, we can distinguish two main detection strategies, differing for the observable which is to be measured [44, 39, 38]. An *optical homodyne detection* scheme [46] allows to record the electric field $\hat{E}$, giving access to the distribution of quadratures. On the other hand, if one wishes to measure the discrete excitations of the field, the desired observable is the photon-number operator $\hat{n}$ and the experimental scheme is called *direct detection*. Then, the two techniques are somehow complementary. The former is based on an interferometer where the input state is mixed with a local oscillator, i.e. a high-intensity coherent beam. The latter consists essentially in addressing the field on a device which clicks whenever triggered by the light. If the detector response is proportional to the light intensity and is single-photon sensitive, we are dealing with *photon-number-resolving (PNR) detectors*. In the following, will focus on this kind of detection strategy, since it is consistent with the aim of our work.

1.5.1 Direct detection

The direct detection of light is basically described by the photoelectric effect. The incoming photons ionize atoms or promote electrons to a conduction band, then the resulting current is amplified to get a pulse that can be measured. However, the available photodetectors cannot count all the photons: there is a non null probability that the device does not click after a light event because some photons can be reflected from the surface of the detector or, also, absorbed without being converted into electric pulses. We can describe this effect by saying that only a fraction η of the impinging photons effectively leads to a count. This parameter is usually called *quantum efficiency*. We would like to find the POVM that catches this notion [38].
Provided that the detector is small with respect to the coherence length of the field and has a window T,

the probability of observing m counts in T is given by [45]

$$p(m;T) = \mathrm{Tr}\left[\hat{\rho} : \frac{(\eta \hat{I}(T)T)^m}{m!} \exp(-\eta \hat{I}(T)T) :\right] \tag{1.154}$$

where $\hat{I}(T)$ is the integrated intensity operator

$$\hat{I}(T) \propto \frac{1}{T}\int_0^T dt \hat{E}^{(-)}(t)\hat{E}^{(+)}(t). \tag{1.155}$$

Note that Eq. (1.154) is nothing but the quantum expression for Mandel's formula in Eq. (1.40). By suitably rescaling the quantum efficiency, one can rewrite the probability in Eq. (1.154) with the creation and annihilation operators, as follows

$$p_\eta(m) = \mathrm{Tr}\left[\hat{\rho} : \frac{(\eta \hat{a}^\dagger \hat{a})^m}{m!} \exp(-\eta \hat{a}^\dagger \hat{a}) :\right]. \tag{1.156}$$

Now we can use the identities

$$\begin{aligned} &: (\hat{a}^\dagger \hat{a})^m := \hat{a}^\dagger \hat{a}(\hat{a}^\dagger \hat{a} - 1)...(\hat{a}^\dagger \hat{a} - m + 1) \\ &: e^{-\eta \hat{a}^\dagger \hat{a}} :\sim (1-\eta)^{\hat{a}^\dagger \hat{a}} \end{aligned}$$

and finally find

$$p_\eta(m) = \sum_{k=m}^{\infty} \binom{k}{m} \langle k|\hat{\rho}|k\rangle \eta^m (1-\eta)^{k-m}. \tag{1.157}$$

Note that in the ideal case $\eta = 1$ the detector measures the photon-number distribution of the state $p(k) = \langle k|\hat{\rho}|k\rangle$, but in general the probability of measuring m photoelectrons is a Bernoullian convolution of the ideal distribution, which makes sense since the detection events can be equivalently thought in terms of success and failure. The POVM of the photodetector, obtained from $p_\eta(m) = \mathrm{Tr}[\hat{\rho}\hat{\Pi}_\eta(m)]$ and Eq. (1.157), reads

$$\hat{\Pi}_\eta(m) = \eta^m \sum_{k=m}^{\infty} \binom{k}{m} (1-\eta)^{k-m} |k\rangle\langle k|. \tag{1.158}$$

A brief inspection of Eq. (1.158) shows that it satisfies the properties of POVMs in Eq. (1.153) without being a projector since $[\hat{\Pi}_\eta(k), \hat{\Pi}_\eta(s)] \neq 0$ for $k \neq s$.
This is a general model describing a photodetector with a given quantum efficiency. Anyway, every particular devices is also affected by specific drawbacks hampering their performance. We will focus on the nonidealities of the detectors we employed in our work in the following chapter.
The light statistics we commonly deal with in this research is multimode since several temporal and spatial modes μ are simultaneously detected in TWB and thermal states. Thus, we should generalize Eq.(1.158) to a multimode POVM, given by the tensor product of the sum over all the single-mode POVM related to each mode and consistent with the total observed detected-photon number, i.e.

$$\hat{\Omega}(m) = \bigotimes_{j=1}^{\mu} \left[\sum_{m_j=0}^{\infty} \hat{\Pi}_\eta(m_j)\right] \delta\left(\sum_j m_j - m\right), \tag{1.159}$$

where we have assumed that each mode is equally populated.
For what concerns the measurement of correlations, we can try to compare the entanglement between the two parties of a TWB with the correlations between the outputs of a beam splitter whose entries are a

classical state and the vacuum. If the incoming state is $\hat{\rho} = \sum_{n,m} \rho_{n,m} |n\rangle\langle m|$, with $\rho_{n,m} = \langle n|\hat{\rho}|m\rangle$, and the transmittivity of the beam splitter is T, then the output is given by

$$\hat{\omega} = \sum_{s,t,p,q} \sqrt{\binom{s+p}{s}\binom{t+q}{q}} \rho_{s+p,t+q} (\sqrt{T})^{s+t} (\sqrt{1-T})^{p+q} |s,p\rangle\rangle\langle\langle t,q|. \tag{1.160}$$

Hence, the joint photodetection distribution of the counts and its moments in the single-mode case are straightforward from

$$\begin{aligned} p(m_1,m_2) &= \mathrm{Tr}[\hat{\omega}\hat{\Pi}_{\eta_1}(m_1) \otimes \hat{\Pi}_{\eta_2}(m_2)] \\ \widehat{m^p} &= \sum_{m=0}^{\infty} m^p \hat{\Pi}_{\eta}(m). \end{aligned} \tag{1.161}$$

Note that we are dealing with operatorial moments, so that in general $\widehat{m^p} \neq \hat{m}^p$. In particular, the first two moments are given by

$$\begin{aligned} \hat{m} &= \eta \hat{n} \\ \widehat{m^2} &= \eta^2 \hat{n}^2 + \eta(1-\eta)\hat{n} \end{aligned} \tag{1.162}$$

and the variance reads

$$\langle \Delta \hat{m}^2 \rangle \equiv \langle \widehat{m^2} \rangle - \langle \hat{m} \rangle^2 = \eta^2 \langle \Delta n^2 \rangle + \eta(1-\eta)\langle \hat{n} \rangle. \tag{1.163}$$

Thus, the variance of the photoelectron number is not determined uniquely by the photon number variance, but also by the mean photon number and just in the case $\eta = 1$ this dependence disappears [47].
Anyway, as mentioned above, we do not reveal entanglement through a measure of counts, but from the statistics of the difference photocurrent instead. Why? We could as well evaluate a correlation coefficient defined from the moments in Eq. (4.11), i.e.

$$\Gamma \equiv \frac{\langle (\hat{m}_1 - \langle \hat{m}_1 \rangle)(\langle \hat{m}_2 - \langle \hat{m}_2 \rangle) \rangle}{\sqrt{\langle \Delta m_1^2 \rangle \langle \Delta m_2^2 \rangle}} \tag{1.164}$$

which is analog to the coefficient C_{SH} that we used to highlight the difference between thermal and super-thermal correlations in Eq. (1.58) [27]. The problem with this parameter is that it cannot reliably discriminate entanglement from classical correlations even for small mean photon-number, as it has been shown in [41].
On the contrary, the difference photocurrent $\hat{D}$ can be used to reveal entanglement. The POVM for such a measure in the single-mode case can be simply built from Eq. (1.158) as follows

$$\hat{\Theta}(d) = \sum_{m=0}^{\infty} \begin{cases} \hat{\Pi}_{\eta_1}(m) \otimes \hat{\Pi}_{\eta_2}(m+d) & d > 0 \\ \hat{\Pi}_{\eta_1}(m) \otimes \hat{\Pi}_{\eta_2}(m) & d = 0 \\ \hat{\Pi}_{\eta_1}(m+d) \otimes \hat{\Pi}_{\eta_2}(m) & d < 0 \end{cases} \tag{1.165}$$

where the numbers d are the eigenvalues of $\hat{D}$. Hence, the distribution and moments of the photocurrent difference read

$$\begin{aligned} p(d) &= \mathrm{Tr}[\hat{\omega}\hat{\Theta}(d)] \\ \widehat{D^p} &= \sum_{d=0}^{\infty} d^p \hat{\Theta}(d). \end{aligned} \tag{1.166}$$

The simplest statistical quantity discriminating quantum and classical correlations is the variance of the distribution, which is shown [41] to be smaller for TWB states than for thermal and coherent states. In particular, if $\eta_1 = \eta_2$ this is always true and, of course, the larger the quantum efficiency, the larger the difference between quantum and classical cases. If $\eta_1 \neq \eta_2$, the difference between the quantum efficiencies imposes a superior limit on the number of photons that can be detected preserving the entanglement, i.e.

$$n < \tilde{n} \equiv \frac{2\eta_1\eta_2}{(\eta_1 - \eta_2)^2}. \tag{1.167}$$

We see that one just needs $\Delta\eta \sim 10^{-2}$ to achieve a threshold $\tilde{n} \sim 100$ larger than the typical number of photons measured in Quantum Optics experiments.
The generalization to the multimode case can be easily retrieved by replacing $\hat{\Pi}_\eta(m)$ with $\hat{\Theta}(d)$ in Eq. (1.159).
Now we would like to restate the previously introduced nonclassicality criteria for the detected photons and for the measured difference photocurrent.

1.5.2 Nonclassicality with detected photons and difference photocurrent

We start by defining Glauber's correlation functions for detected photons. They are sometimes written in analogy with the normalized correlation functions for photons, but irrespective of the normal ordering [50, 49, 39, 51]. In the case of a bipartite system the analogy is with Eq. (1.148), which yields

$$g^{(n)}_{x_1\times j, x_2\times k}(m_1, m_2) = \frac{\langle \widehat{m_1^j m_2^k} \rangle}{\langle \hat{m}_1 \rangle^j \langle \hat{m}_2 \rangle^k} \tag{1.168}$$

where again $j+k=n$ and the operators $\widehat{m^p}$ are given in Eq. (4.11). Note that the absence of the normal ordering has relevant effects on the final form of these functions. Consider the second-order autocorrelation function for detected photons, i.e.

$$g^{(2)}(m) = \frac{\langle \widehat{m^2} \rangle}{\langle \hat{m} \rangle^2}. \tag{1.169}$$

The form of Eq. (1.169) is explicitly different from $g^{(2)}(n)$ in Eq. (1.144). If we had built the correlation functions for detected photons by replacing the moments $\hat{n}^p$ with $\widehat{m^p}$, i.e. by preserving the normal ordering (see for example [56]), we would have ended with the same functions. On the contrary, Eqs. (1.169) and (1.144) are related by

$$g^{(2)}(m) = g^{(2)}(n) + \frac{1}{\langle \hat{m} \rangle}. \tag{1.170}$$

Strictly speaking, one could even say that the functions in Eq. (1.168) are not Glauber's correlation functions, but it is a fact [50] that they are connected by Eq. (1.170) and, more generally, by

$$g^{(n)}_{x_1\times j, x_2\times k}(m_1, m_2) = \sum_{s,t=0}^{j,k} c_{s,t}\, g^{(n)}_{x_1\times s, x_2\times t}(n_1, n_2) \tag{1.171}$$

so that nonclassical boundaries similar to the ones defined for Glauber's functions are inherited by these detected-photon correlation functions [39]. The coefficients $c_{s,t}$ depend on the parameters of the system.
We recall that, since we are using the criterion imposed by the second-order correlation function, the investigated states of light exhibit their nonclassicality through sub-Poissonianity. Then, we are led to define a Fano factor for detected photons in full analogy with Eq. (1.145), i.e. [56, 51]

$$F(m) \equiv \frac{\langle \widehat{\Delta m^2} \rangle}{\langle \Delta \hat{m}^2 \rangle_{\mathrm{POISS}}} = \frac{\langle \widehat{\Delta m^2} \rangle}{\langle \hat{m} \rangle} \tag{1.172}$$

which, by making explicit the expressions of the first and second moments, is easily shown to depend on the photon-number Fano factor as follows [47]

$$F(m) = \eta F(n) + 1 - \eta. \tag{1.173}$$

Hence, the nonclassicality criterion which holds in Eq. (1.146) for photons can be restated for detected photons as

$$1 - \eta \leq F(m) < 1 \tag{1.174}$$

if $F(n)$ is a monotone function. We see that, as expected, our capability of revealing nonclassicality is determined by the quantum efficiency. Note that by exploiting Eqs. (1.147) and (1.173) one can easily retrieved the Glauber's second-order correlation of the light distribution from the Fano factor of the measured photoelectrons, i.e. [51]

$$g^{(2)}(n) = 1 + \frac{F(m) - 1}{\langle \hat{m} \rangle}. \tag{1.175}$$

Moreover, one could also define a notion of distance in the space of Glauber's functions as the difference between the correlation of a given light statistics with mean value $\langle \hat{n} \rangle = n$ and the correlation of an n-photon Fock state and evaluate it through an analog distance defined for the detected-photon Fano factor as follows

$$\Delta g^{(2)}(n) \equiv g^{(2)}(n) - g^{(2)}_{\text{Fock}}(n) = \frac{\Delta F(m)}{\langle \hat{m} \rangle}. \tag{1.176}$$

Here $\Delta F(m) \equiv F(m) - F_{\min}$ is the mentioned distance for the detected-photon Fano factor with respect to $F_{\min} = 1 - \eta$, which is the lower bound of $F(m)$ (see Eq. (1.174)), and $g^{(2)}_{\text{Fock}}(n) = 1 - \langle \hat{n} \rangle^{-1}$ is the second-order autocorrelation function for the n-photon Fock state.
Finally, we need to express the cross-correlations in terms of the measured difference photocurrent $\hat{D}$. As explained above, the nonclassicality criterion for entanglement based on the difference photocurrent is defined through the noise reduction factor, which is expressed as a function of the first two moments of $\hat{D}$ in analogy with Eq. (1.150), i.e.

$$R \equiv \frac{\langle \Delta \widehat{D^2} \rangle}{\langle \Delta \widehat{D^2} \rangle_{\text{POISS}}} = \frac{\langle \Delta \widehat{D^2} \rangle}{\langle \hat{m}_1 + \hat{m}_2 \rangle}. \tag{1.177}$$

From the second of Eqs. (1.166), one finds that the variance of the difference photocurrent yields

$$\begin{aligned}
\langle \Delta \widehat{D^2} \rangle &\equiv \langle \widehat{D^2} \rangle - \langle \hat{D} \rangle^2 = \\
&= \langle \hat{D}^2 \rangle + (1 - \eta_1)\langle \hat{m}_1 \rangle + (1 - \eta_2)\langle \hat{m}_2 \rangle - \langle \hat{D} \rangle^2 \\
&= \langle \Delta \hat{D}^2 \rangle + (1 - \eta_1)\langle \hat{m}_1 \rangle + (1 - \eta_2)\langle \hat{m}_2 \rangle \\
&= \langle \Delta \hat{m}_1^2 \rangle + \langle \Delta \hat{m}_2^2 \rangle - 2(\langle \hat{m}_1 \hat{m}_2 \rangle - \langle \hat{m}_1 \rangle \langle \hat{m}_2 \rangle) + (1 - \eta_1)\langle \hat{m}_1 \rangle + (1 - \eta_2)\langle \hat{m}_2 \rangle.
\end{aligned}$$

Note that the term $\gamma \equiv \langle \hat{m}_1 \hat{m}_2 \rangle - \langle \hat{m}_1 \rangle \langle \hat{m}_2 \rangle$ is proportional to the correlation coefficient Γ mentioned in Eq. (1.164). Therefore, the definition of the noise reduction factor for the difference photocurrent in Eq. (1.177) provides

$$R = 1 + \frac{\langle \Delta \hat{m}_1^2 \rangle + \langle \Delta \hat{m}_2^2 \rangle - 2\gamma - \eta_1 \langle \hat{m}_1 \rangle - \eta_2 \langle \hat{m}_2 \rangle}{\langle \hat{m}_1 \rangle + \langle \hat{m}_2 \rangle}. \tag{1.178}$$

The variance of the detected photons can be expressed as

$$\langle \Delta \hat{m}^2 \rangle = \langle \hat{m} \rangle (\langle \hat{m} \rangle + \eta)$$

which allows to simplify Eq. (1.178) as follows

$$R = 1 + \frac{\langle \hat{m}_1 \rangle^2 + \langle \hat{m}_2 \rangle^2 - 2\gamma}{\langle \hat{m}_1 \rangle + \langle \hat{m}_2 \rangle}. \tag{1.179}$$

We note that the revealed nonclassicality of the detected state depends on the balance between the sum of the second moments and the cross-correlations. In particular, we will now retrieve the noise reduction factor in the case of non-ideal detection of single-mode TWB states. The correlation term $\langle \hat{m}_1 \hat{m}_2 \rangle$ is given by

$$\begin{aligned} \langle \hat{m}_1 \hat{m}_2 \rangle &= \langle\langle r | \hat{m}_1 \otimes \hat{m}_2 | r \rangle\rangle = \\ &= \eta_1 \eta_2 \langle\langle r | \hat{n}_1 \otimes \hat{n}_2 | r \rangle\rangle = \\ &= \eta_1 \eta_2 N(2N+1) = \\ &= 2\langle \hat{m}_1 \rangle \langle \hat{m}_2 \rangle + \sqrt{\eta_1 \eta_2} \sqrt{\langle \hat{m}_1 \rangle \langle \hat{m}_2 \rangle} \end{aligned}$$

where $|r\rangle\rangle$ is the single-mode TWB state with photon number-mean value $\langle\langle r | \hat{n}_1 + \hat{n}_2 | r \rangle\rangle = 2N$ defined in Eq. (1.131). Thus, the noise reduction factor reads

$$R = 1 + \frac{(\langle \hat{m}_1 \rangle - \langle \hat{m}_2 \rangle)^2}{\langle \hat{m}_1 \rangle + \langle \hat{m}_2 \rangle} - 2\sqrt{\eta_1 \eta_2} \frac{\sqrt{\langle \hat{m}_1 \rangle \langle \hat{m}_2 \rangle}}{\langle \hat{m}_1 \rangle + \langle \hat{m}_2 \rangle}. \tag{1.180}$$

We recall that, from the very definition of noise reduction factor, we can say that nonclassical correlations are detected if $R < 1$, which is a sufficient but not necessary condition. From Eq. (1.180) we see that, as expected, a strong limitation is given by the imbalance between the quantum efficiencies of the detectors. We have already outlined the effect of different quantum efficiencies on the variance of the photocurrent difference by finding a threshold photon-number value $\tilde{n}(\eta_1, \eta_2)$ in Eq. (1.167) over which quantum correlations cannot be correctly discriminated with this procedure. Note that the noise reduction factor in Eq. (1.180) can be written in terms of this threshold, as follows

$$R = 1 + 2\frac{\eta_1 \eta_2}{\eta_1 + \eta_2} \left(\frac{N}{\tilde{n}} - 1 \right). \tag{1.181}$$

Again, we find that entanglement can be revealed only if $N < \tilde{n}$. For $N \ll \tilde{n}$ we are in the limit $\frac{N}{\tilde{n}} \to 0$, which yields the lower bound given by the quantum efficiencies of the detectors to the noise reduction factor, i.e.

$$R \geq 1 - 2\frac{\eta_1 \eta_2}{\eta_1 + \eta_2}. \tag{1.182}$$

If $\eta_1 = \eta_2 = \eta$, it reduces to $R \geq 1 - \eta$.
The generalization to the multi-mode case is easily done by replacing the single-mode TWB state with the multi-mode case $|r_\mu\rangle\rangle$ in Eq. (1.133). The effect of this operation on the noise reduction factor is a factor $1/\mu$ multiplying the second term in Eq. (1.180). Therefore, in a perfectly balanced condition the noise reduction factor is insensitive to the number of modes.

1.5.3 Conditional measurements

Detecting quantum correlations is not the only way to reveal nonclassicality. An alternative well-known mechanism exploits the *reduction postulate* [52], which basically can be stated as follows [53]. Given a generic POVM $\hat{\Pi}$ for our generalized measure and a composite system $\hat{\rho}_{s,i}$, when we perform a measure on the idler state i and get an outcome x with probability $\mathrm{p}_x = \mathrm{Tr}[\hat{\rho}_{s,i} \hat{\mathbb{1}} \otimes \hat{\Pi}]$, then, accordingly with Naimark's theorem, the subsystem s, the signal, is left in the state

$$\hat{\rho}_s^{(x)} = \frac{1}{\mathrm{p}_x} \mathrm{Tr}_i[\hat{\rho}_{s,i} \hat{\mathbb{1}} \otimes \hat{\Pi}] \tag{1.183}$$

where Tr_i is the partial trace over the idler. For a TWB state, $\hat{\rho}_{s,i} = |r_\mu\rangle\rangle\langle\langle r_\mu|$, where $|r_\mu\rangle\rangle$ is defined in Eq. (1.133). Therefore, if the system is entangled, when the idler is measured and x photons are detected, then the signal is conditionally reduced as in Eq. (1.183) according to the outcome of the measurement. The process is interesting not only from a fundamental point of view, but also because it may give access to states which cannot be achieved with existing Hamiltonian processes [52].
Conditional states of light have been successfully detected in the case of TWB states via photon-counting techniques in the mesoscopic intensity regime [54, 55]. Given the POVM describing the losses of the detectors $\hat{\Pi}_\eta$ in Eq. (1.158), the detected-photon joint probability distribution is given by

$$\begin{aligned} \mathrm{p}_{s,i} &= \mathrm{Tr}_{s,i}[|r_\mu\rangle\rangle\langle\langle r_\mu|\hat{\Pi}_{m_s}\otimes\hat{\Pi}_{m_i}] = \\ &= \left(\frac{\mu\eta}{\langle\hat{m}\rangle+\mu\eta}\right)^{\mu}\left(\frac{\eta}{1-\eta}\right)^{m_s+m_i}\sum_l \binom{l+\mu-1}{l}\binom{l}{s}\binom{l}{t}\left[\frac{\langle\hat{m}\rangle(1-\eta)^2}{\langle\hat{m}\rangle+\mu\eta}\right]^l \end{aligned}$$

where $\langle\hat{m}\rangle = \eta\langle\hat{n}\rangle$ is the total detected-photon mean number. After measuring w photons on the idler, the signal is left in a conditional state $\hat{\rho}_s^{(w)}$, that can be derived from Eq. (1.183), so that the detected-photon mean value for the signal state can be retrieved as

$$\langle m\rangle_w = \mathrm{Tr}_s\left[\rho_s^{(w)}\sum_{m_s} m_s\hat{\Pi}_{m_s}\right] = \frac{\eta(\langle\hat{n}\rangle+\mu)}{\eta\langle\hat{n}\rangle+\mu}w + \frac{\eta(1-\eta)\mu\langle\hat{n}\rangle}{\eta\langle\hat{n}\rangle+\mu}. \tag{1.184}$$

Note that the mean value on the signal is a linear function of the conditioning value w because of the effect of the quantum efficiency of the detector. Of course, for $\eta = 1$ we get $\langle m\rangle_w = w$. Similarly, we can compute the second moment for $\hat{\rho}_s^{(w)}$ and determine the Fano factor, thus finding [55]

$$F_w = (1-\eta)\left[1+\frac{\eta\langle\hat{n}\rangle(w+\mu)(\langle\hat{n}\rangle+\mu)}{(\eta\langle\hat{n}\rangle+\mu)[(w+\mu)(\langle\hat{n}\rangle+\mu)-\mu(\eta\langle\hat{n}\rangle+\mu)]}\right]. \tag{1.185}$$

2

Characterization of Silicon Photomultipliers for Quantum Optics Experiments

The search for optimal receivers endowed with photon-number-resolving capability has led us to consider silicon photomultipliers (SiPMs) for Quantum Optics experiments. In particular, Afek et al. [79] provided a former model for the photodetection via SiPMs, including the effect of the main nonidealities of these devices. Ramilli et al. [81] applied the model for the reconstruction of pseudo-thermal and coherent light, while Kalashnikov et al. [96] used their SiPMs to detect TWB states and estimated the nonclassicality of the detected-photon statistics. Despite the promising results, the old generations of these detectors were proved to be worst than other existing detectors, such as hybrid photodetectors [42], mainly due to the sources of correlated noise affecting them.
However, the new generation of SiPMs opens new perspectives [63]. Indeed, technological improvements has made the impact of some of these spurious effects almost negligible, paving the way for Quantum Optics experiments. Therefore, we gave them a chance by testing their performances with classical and nonclassical light and optimizing them for a reliable reconstruction of light statistics.
Here, after a technical introduction, we will show and examine the results of our detector characterizations. Firstly, we will assess the main parameters of the sensors through a standard procedure which is well-known in the literature. Then, we will implement a specific characterization for the reconstruction of the statistics and the estimation of correlations.
In the following chapter, we will use our devices to explore the quantum world and explain what we retrieved. Finally, we will see a comprehensive method to estimate with a single tool, i.e. Glauber's correlation functions, both the parameters of the detectors and the detected-light nonclassicality.

2.1 Introduction to Silicon Photomultipliers

The story of SiPMs dates back to the early Nineties in Russia [57, 58, 59, 60, 71]. A SiPM is a *Multi-Pixel Photon Counter (MPPC)* and, more precisely, a matrix of Geiger-Müller-avalanche-photodiodes connected in parallel to a common output. This paragraph is devoted to clarify and detail this definition.

2.1.1 Architecture of the device

Near the breakdown voltage, a diode is operated differently according to the bias voltage. If the applied voltage is below the breakdown level, we have an avalanche photodiode (APD), which means that an impact ionization process is triggered by the absorption of a photon. As a result, a number of electron-hole pairs proportional to the number of absorbed photons is created. On the contrary, if the bias is above the breakdown voltage, a single carrier crossing the depletion region can start a self-sustaining avalanche. In this case, we say that the device works in a Geiger-mode (GM) regime. Note that in this case the detector acts like an on/off photodetector, i.e. it cannot count the number of impinging photons since the output is the same regardless of the intensity of the impinging light. In a word, the detector is described by the two-value POVM [38]

$$\hat{\Pi}_\eta(0) = \sum_{k=0}^{\infty} (1-\eta)^k |k\rangle\langle k| \qquad \hat{\Pi}_\eta(1) = \hat{\mathbb{1}} - \hat{\Pi}_\eta(0) \tag{2.1}$$

where η is the quantum efficiency of the GM-APD. Note that we are implicitly requiring that this APD is single-photon sensitive, which is the reason why it is known as Single-Photon Avalanche Diode (SPAD) [61, 62]. In Fig. 2.1 on the left we show the typical electrical model of a SPAD with a quenching circuit [78]. There are a voltage source, which is set at the breakdown voltage V_{BD}, a resistor R_S modeling the space-charge resistance of the avalanche region, the junction capacitance C_D and a switch. Externally, we can find the bias supply and the quenching resistor. Provided that $V_{BIAS} > V_{BD}$, the switch is closed by a carrier triggering an avalanche and is opened when the avalanche is quenched. If the switch is open, no current flows in the circuit and the voltage over the capacitance equals the bias voltage. When, at a given time t_0, an avalanche starts, the switch closes and the capacitance discharges, its voltage evolving from V_{BIAS} to V_{BD}. As shown in Fig. 2.1 on the right, a current I_{INT} starts flowing inside the SPAD at the time t_0, but it drops down exponentially as the capacitance discharges. In the same time, an external current I_{EXT} is generated in the quenching circuit and increases as the exact inverse of the I_{INT} decay. While they are reaching the plateau, the avalanche may be quenched. When this happens, at time t_1, the switch is opened, no more current flows inside the SPAD, the capacitance recharges to the original bias voltage and *the external current decays exponentially*. The external current is the output current signal of this device. The exponential decay characterizing the output waveform will be crucial in the following.

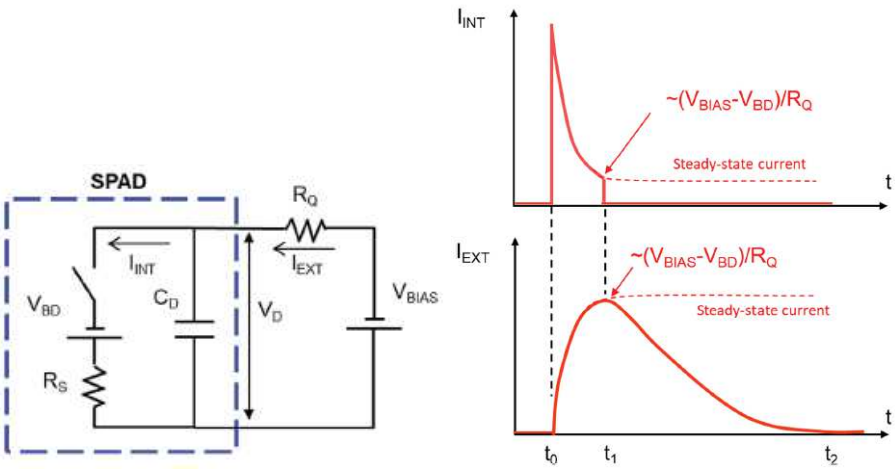

Fig. 2.1: Left: equivalent circuit of a SPAD with external quenching resistor and bias supply. Right: plot of the internal and external currents I_{INT} and I_{EXT} as a function of time. Source: [78].

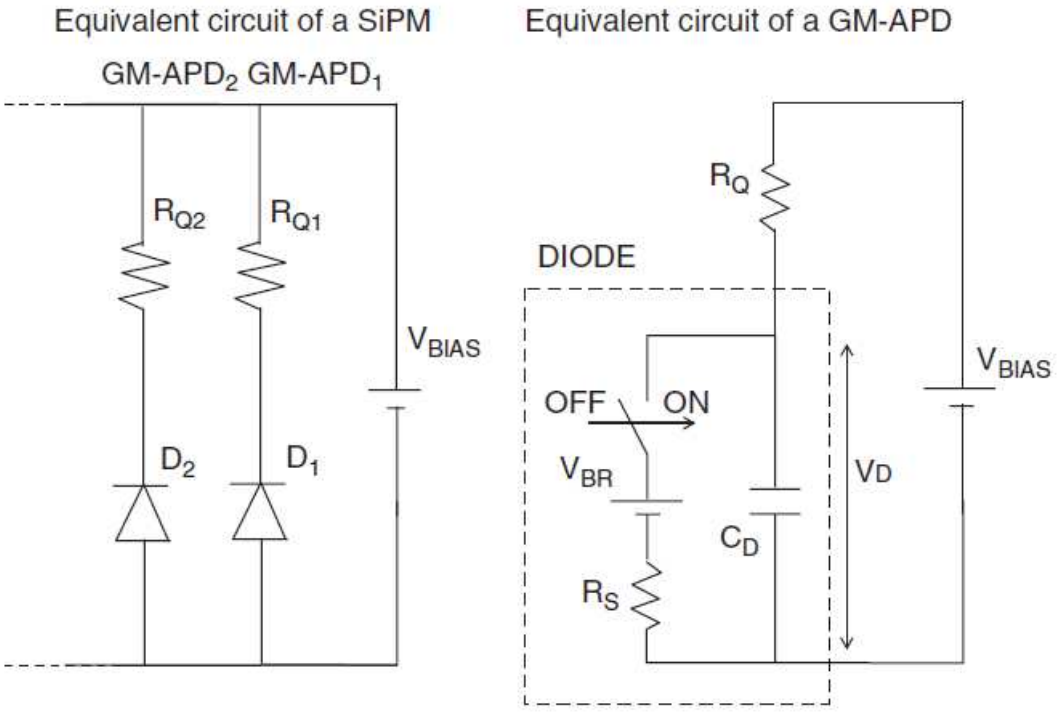

Fig. 2.2: Equivalent circuits of a SiPM (left) and of a GM-APD (right). Source:[60]

If we want a PNR detector, we can consider an array of micro-GM-APDs, that from now on will be called *cells* or *pixels*, connected in parallel to a single common output. In this configuration, in the absence of all nonidealities, except a limited quantum efficiency, the output signal must be proportional to the number of fired cells and then, under the non-trivial assumption that every cell is fired by at most one photon, the output signal must be proportional to the number of incident photons. In particular, the current output signal is the sum of the external currents I_{EXT} related to each fired cell [78]. The name of the whole structure is *silicon photomultiplier* SiPM [59, 60]. The equivalent circuits of a SiPM and, again, of one of its GM-APDs are outlined in Fig. 2.2. Schematic pictures of the SiPM structure and of the photodetection process are shown in Fig. 2.3.
The new generations of SiPMs are endowed with a number of features [63] which makes them convenient and feasible for Quantum Optics experiments and Quantum Information protocols. They are ideal for a portable system since they are compact, rugged and insensitive to magnetic fields. Moreover, they operate at room temperature and at low operation voltages ($V_{BR} \sim 50$ V). The gain is high compared to the previous generations [58]: it ranges from 10^5 to 10^6. The dynamic range depends on the number of cells, which is high despite the small size of SiPMs because the density of cells is high ($\sim 10^4/\text{mm}^2$). These detectors could be particularly interesting in the Quantum Optics community because of their photon-number resolution capability, i.e. because the peaks of the detected-light histogram are highly resolved. Each peak corresponds to a measured number of photons. Last but not the least, they are sensitive in the visible spectral range, which is the domain of many laser sources. We will better explore the SiPM features in the following with the characterization of the specific detectors we employed in our research. In Fig. 2.4 we show the typical waveform of a digitized output signal. The information on the number of photoelectrons is commonly extracted by integrating the signal over a suitable temporal interval, as shown in Fig. 2.5. By collecting the data from all the signals, one can obtain the histogram of the counted photons,

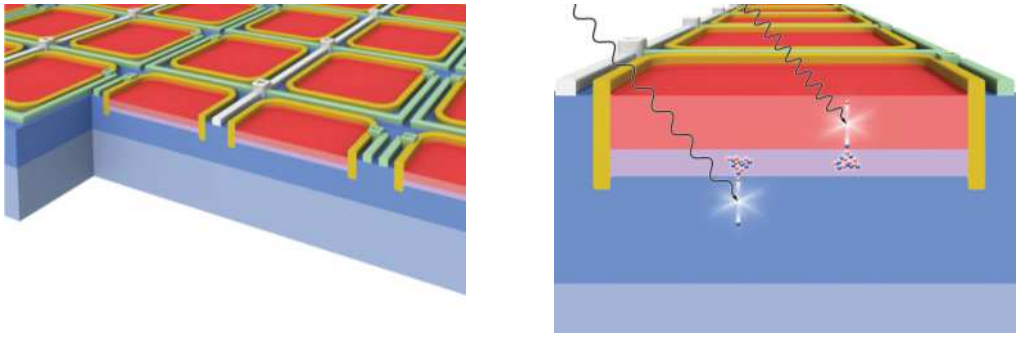

Fig. 2.3: SiPMs are high-density ($\sim 10^4/\text{mm}^2$) matrixes of SPADs with a common output.

known as *pulse-height-spectrum*. An example for that is shown in Fig. 2.6. The probability related to a given number of avalanches per pulse is proportional to the area underneath the corresponding peak in the histogram [79].

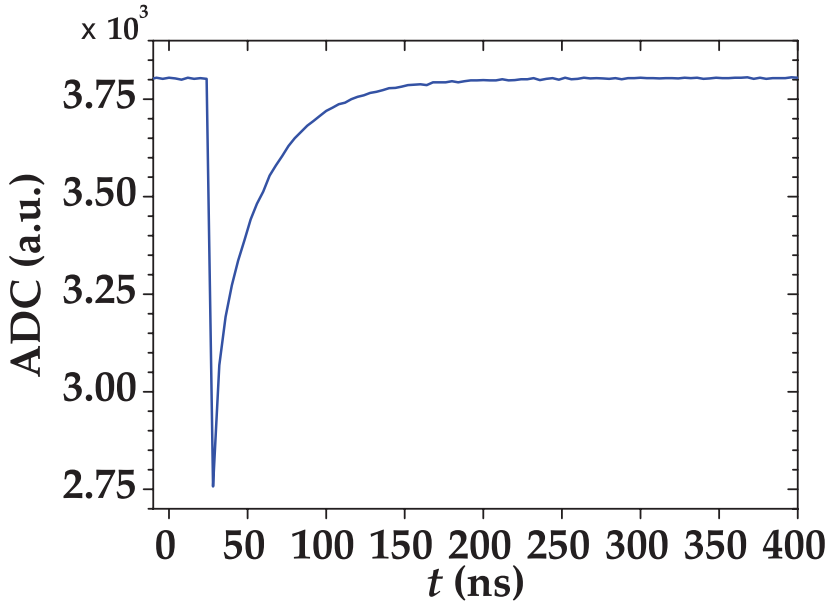

Fig. 2.4: Digitized output signal from a SiPM Hamamatsu S13360-1350CS [63].

On the other hand, SiPMs are affected by a limited quantum efficiency, three spurious stochastic effects and saturation. These drawbacks are addressed one by one in the next sections.

2.1.2 Quantum efficiency

The low quantum efficiency is one of the most detrimental aspects of SiPMs for Quantum Optics applications. Luckily, a model for photodetection can link the distribution of the detected photons to the distribution of the incident photons (see next section). Moreover, quantum efficiency has been enhancing

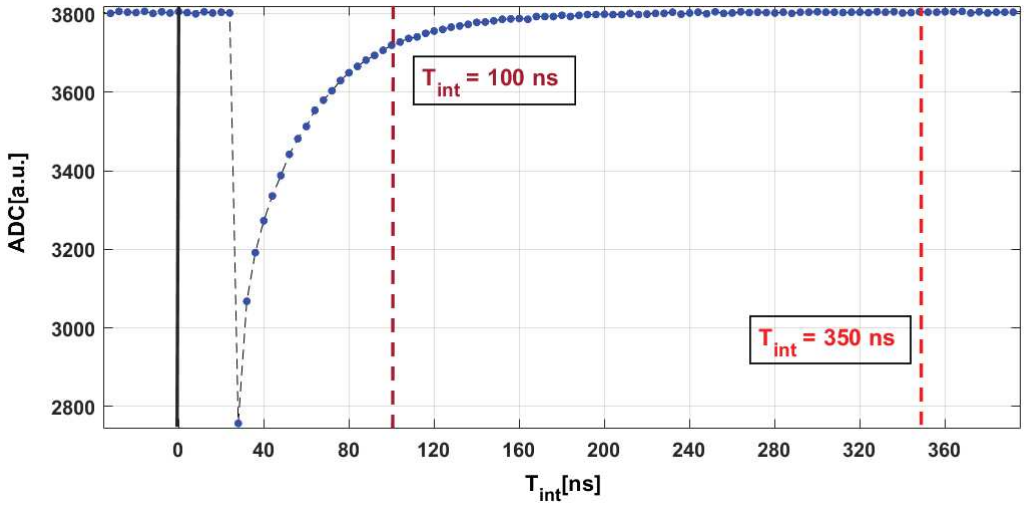

Fig. 2.5: Digitized output signal from a SiPM Hamamatsu S13360-1350CS [63]. The temporal integral of the whole waveform is proportional to the number of detected photons. By collecting the information from all the measured signals, one can build a photon-number histogram, like the one in Fig. (2.6). Here, two different choices for the integration interval T_{int} are outlined. Details on the strategy behind this choice in the following sections.

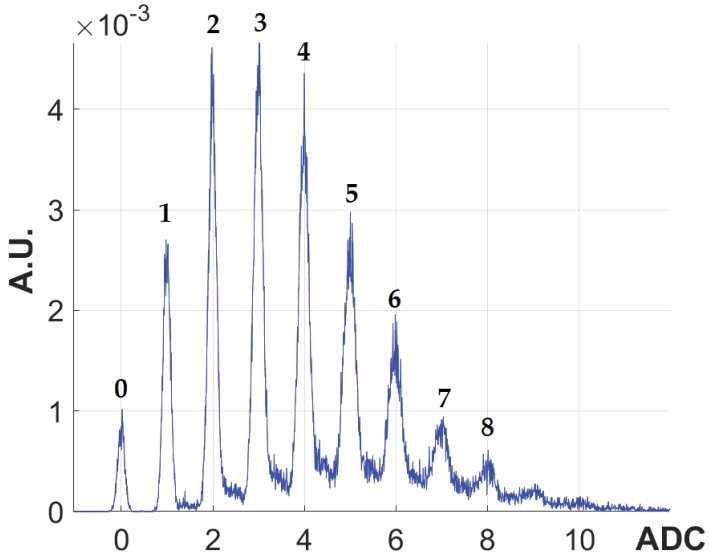

Fig. 2.6: A photon-number histogram, namely *pulse-height-spectrum*, obtained with a SiPM Hamamatsu S13360-1350CS [63] from Poissonian input light. The first peak is the zero-photon peak, the second is the one-photon peak and so on. The counts on the vertical axis are in arbitrary units.

with technological improvements. The new generations attained $\eta \sim 60\%$ in the blue spectral range.
More precisely, the definition of quantum efficiency we gave in the first chapter is usually referred to as *photon-detection efficiency PDE* [60], which is the product of three distinct contributions.
The first is a more specific contextualization of the quantum efficiency, i.e. the probability for a photon to generate an e-h pair. It depends on the transmittance of the dielectric layer over the silicon surface and on the probability that the e-h pair is generated in the active layer of the detector once the photon has passed the dielectric layer. Both of these quantities are wavelength dependent, as the absorption spectrum of silicon is.
The second contribution is the *triggering probability* p_{trig}, which is the probability that the e-h pair triggers an avalanche. It is proportional to the overvoltage and is related to the recovery time τ of the cells as follows [65]

$$p_{\text{trig}} = p_{\text{trig},0}[1 - \exp(-t/\tau)] \tag{2.2}$$

where $p_{\text{trig},0}$ is the triggering probability in a fully recharged cell.
Finally, the contribution of the geometrical efficiency is of major importance. It is the so called *fill factor*, which is the percentage of the detector surface area that is sensitive to light. Indeed, each cell is often separated from its neighbors to limit crosstalk effects (see next Sections). In addition, there is an edge structure, called *guard ring*, needed to lower the electric fields at the borders and some surface area is required for the quench resistor and signal tracks. All of this space results in a dead region around the cell contributing to a reduction of the fill factor. Since the separation between cells is more or less constant, regardless of the cell size, larger cells result in a larger percentage of active area. A higher fill factor (larger cells) results in higher PDE and gain as well as in higher capacitances, longer recovery times and a smaller dynamic range. On the contrary, a lower fill factor (smaller cells) results in lower PDE and gain as well as in lower capacitances, shorter recovery times and higher dynamic range.
The PDE can be experimentally evaluated [66]. In Fig. 2.7 we show the dependence of the PDE on the overvoltage (plots on the left) and on the wavelength (plots on the right) for three SiPMs with different cell sizes and cell numbers, but with the same overall detector size. These detectors have the maximum of the PDE at $\lambda \sim 465$ nm. From the plots on the left, it is clear that the PDE is a growing function of the overvoltage, but, moreover, note that the also derivative of the PDE with respect to U_{over} depends on the wavelength. In particular, as the wavelength approaches the value such that the PDE is maximal, the growth of the PDE as a function of U_{over} is faster. As a last remark, we highlight that, as expected, at fixed overvoltage and wavelength, the PDE is larger for larger pixel sizes.

2.1.3 Dark Counts

The carrier initiating the discharge can be the consequence of a pure detection event, but it can also be thermally generated. As a result, one gets spurious avalanches which are random and independent of the input field. These spurious avalanches are known as *dark counts* and, at the single photon level, they represent an important source of noise. We can think the detector to be embedded in an external thermal bath and, being the times of arrival of each thermal excitation independent of each other, we can fairly say that the temporal distribution of the induced dark counts is Poissonian.
Dark counts are usually quantified as a pulse rate (kHz) or pulse rate per unit area (kHz/mm^2). The dark-count rate (DCR) is a function of the thickness of the active area, of the overvoltage and of temperature. In particular, the junction thickness and the triggering probability grow with the overvoltage, and so does the DCR [60, 68]. A simple counting system can be used to measure DCR. It consists in setting the threshold of a discriminator at the half-photon level when no signal impinges on the detector. The DCR can thus be identified with the threshold-exceeded rate. This method is commonly called *Stair Case*. A typical Stair Case plot is shown in Fig. 2.8. Since the Stair Case plot is typically recorded in the absence of light, the corresponding peak-height spectrum consists of three visible peaks. The 0-photon peak, which in this case is the highest, the 1-photon peak, due to dark count, and the 2-photon peak, revealing the presence of

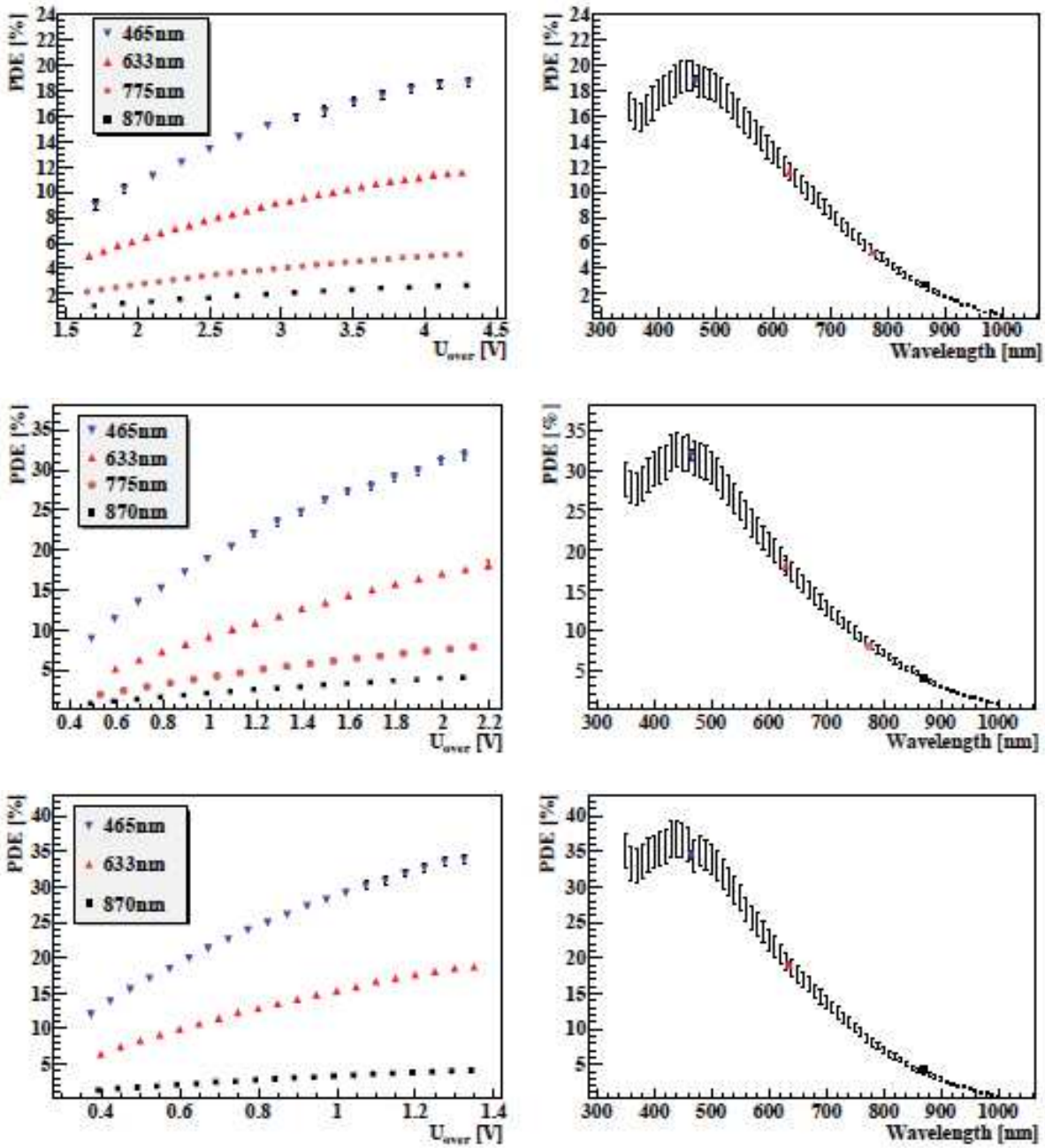

Fig. 2.7: Left: PDE as a function of the overvoltage U_{over} for different wavelengths. Right: PDE as a function of the incident light wavelength at room temperature. The three rows refer to Hamamatsu S10362 detectors [67] with effective active area $\sim 1 \times 1$ mm and differing for the cell sizes. First row: $625\mu m^2$ pixel size, at an over voltage of $U_{over} = (4.3 \pm 0.05)$V. Second row: $2500\mu m^2$ pixel size, at an over voltage of $U_{over} = (2.15 \pm 0.05)$V. Third row: $10^4\mu m^2$ pixel size, at an over voltage of $U_{over} = (1.3 \pm 0.05)$V. Source: [66]

optical cross-talk events (see the next section for details).
Note that, since the DCR increases with the overvoltage (see Fig. (2.9)), we have a natural trade-off between increasing PDE and DCR.

2.1.4 Optical Cross-Talk

One of the most detrimental spurious effects of SiPMs for quantum applications is the *optical cross-talk (OCT)*. It is defined as the probability that an avalanching cell will cause an avalanche in a second cell. What happens is that a primary avalanche emits bremsstrahlung secondary photons that can reach another cell and make it fire. Note that the emission of visible light from a reverse-biased p-n junction has been known since 1955 [70].
From the point of view of the timing, this process can happen in at least three different ways. The photon generated by the primary avalanche can either directly fire a neighboring cell or be reflected at one of the detector surfaces or finally be absorbed in the substrate from where the excited carrier can diffuse up to the active region and fire a cell. For what concerns the secondary avalanche triggering time, the first two phenomena can be stark distinguished from the last one [65]. In particular, if the neighboring cell is directly fired by the secondary photon, then the OCT event is almost simultaneous with the effective light signal ($T_{\text{signal}} - T_{\text{OCT}} < 1\text{ps}$). The same can be said for the second case, where the photon can be reflected either from the window material on the top of the sensor (usually epoxy or glass) or from the bottom of the silicon substrate, since the photon time of flight is approximately a few picoseconds. At the nanosecond scale (see the typical signal in Fig. (2.5)), these OCT events are almost indistinguishable from the light events and the process is called *prompt cross-talk OCT-P*. On the contrary, in the third case the OCT signal is measurably delayed with respect to the light signal due to the diffusive process from the substrate to the active region, which can be up to tens of nanoseconds long. Hence, we can typically distinguish the light signal peak and the OCT peak and we talk about *delayed cross-talk OCT-D*. A schematic representation of the OCT-P and OCT-D processes is shown in Fig. 2.10.
Since about 2006 [60, 71], direct migration of a secondary photon to a neighboring cell has been somehow prevented by applying suitable trenches between the cells [65], so that OCT-P has been noticeably reduced in the new generations of SiPMs [72]. However, reflections on the device surfaces and OCT-D cannot be prevented through this expedient.

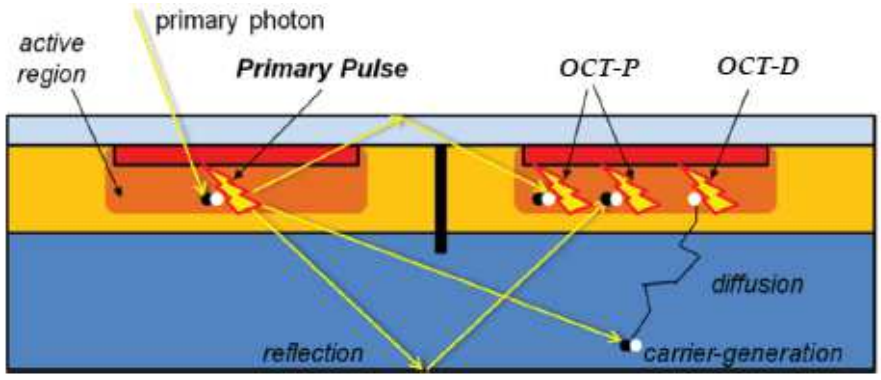

Fig. 2.10: Scheme of the OCT-P and OCT-D processes. Source: [65].

OCT is that bad for Quantum Optics applications and, in general, for measurements with SiPMs because it spoils two of the fundamental features of these devices. On the one hand, OCT-D compromises the peak-to-peak resolution. Indeed, given an integration interval for the output waveform, OCT-D signals

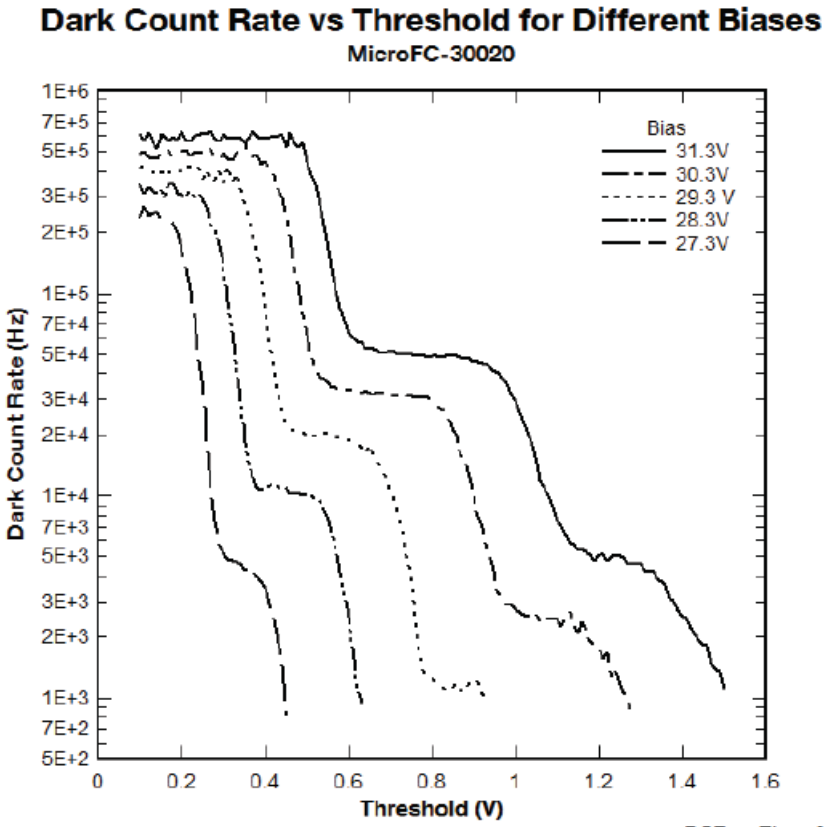

Fig. 2.8: A Stair Case plot measuring the DCR of a $3 \times 3\text{mm}^2$ SiPM with pixel size $35 \times 35\mu\text{m}^2$ at room temperature. Source: [69].

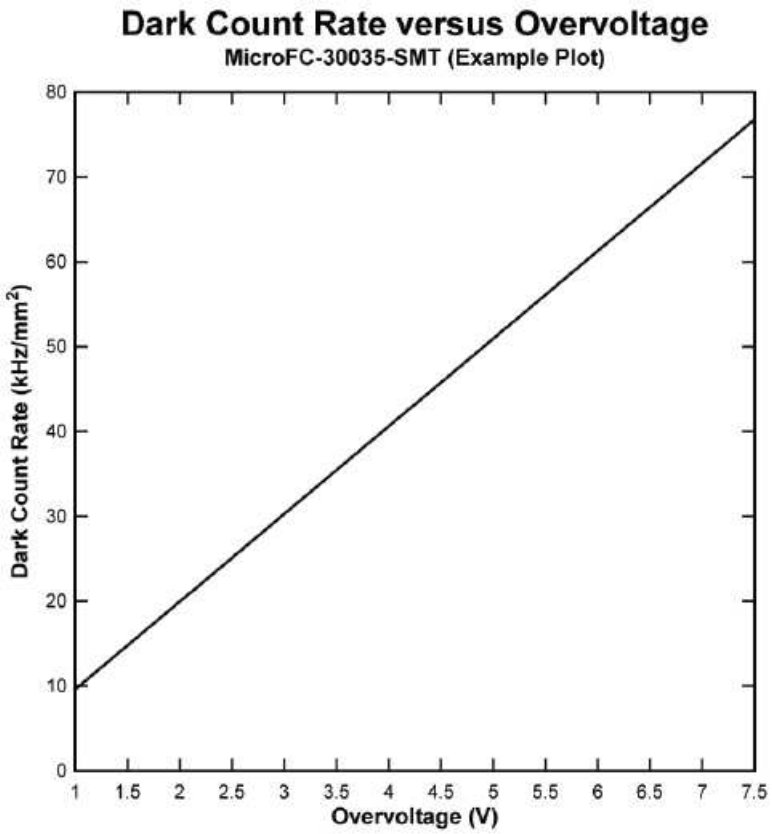

Fig. 2.9: DCR as a function of the overvoltage for a $3 \times 3\text{mm}^2$ SiPM with pixel size $35 \times 35\mu\text{m}^2$ at room temperature. Source: [69].

are not completely integrated and do not contribute to the photon-number statistics as integers. They can either broaden the peaks or fill the range between two peaks. On the other hand, OCT-P is even worse because, as dark counts do, it modifies the statistics, being the secondary-photon induced breakdown indistinguishable from the primary avalanches. Unlike dark counts, the number of false avalanches can be larger than one, and so the extent up to which the statistics is influenced.

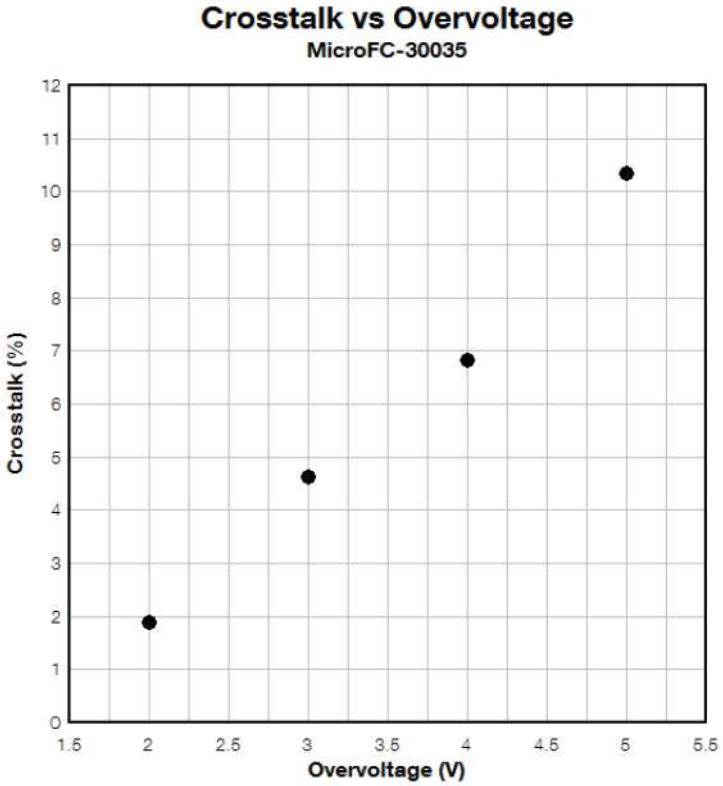

Fig. 2.11: A plot of the OCT probability as a function of the overvoltage. Source: [69].

Note that there is a faint analogy between dark counts and OCT since the secondary photons emitted by the decelerating carriers are typically in the near infrared region. This is why they can travel long distances inside the device. From this point of view, also OCT is something like a thermal effect, the difference with the dark counts being in the source: the acceleration of the avalanche charges for the former, the environment for the latter.
OCT is a function of the overvoltage (see Fig. 2.11), of the gain and of the detector fill factor. The larger the number of carriers crossing the junction, the larger the probability that secondary avalanches will be triggered. Once again, we end with a trade-off with the PDE, as both of them grow with the overvoltage. An experimental estimation for the OCT probability can be easily achieved [66, 68]. The most common OCT measure exploits the fact that at the nanosecond scale, which is the reference scale for signal evolution (see Fig. 2.5), the DCR is small, so that it is unlikely for two dark-count signals to be simultaneous. More explicitly, the new generations of SiPMs feature a DCR $\sim 10^2$kHz $= 1/(10^4$ns$)$ and the duration of the signal is of the order of 10^2ns. Based on this evidence, one can fairly say that, in the absence of OCT, the two-photon peak height should be negligible. Hence, an empirical estimation of the OCT consists in the ratio of the dark-count frequencies for pulses exceeding the 0.5 and 1.5 levels of the single cell amplitude,

namely

$$\varepsilon \sim \frac{\nu_{1.5}}{\nu_{0.5}}. \tag{2.3}$$

In other words, this estimation is a comparison between the event rate above a one-photoelectron threshold and the total measured DCR. The frequency values can be inferred from a Stair Case plot, as in Fig. (2.12).

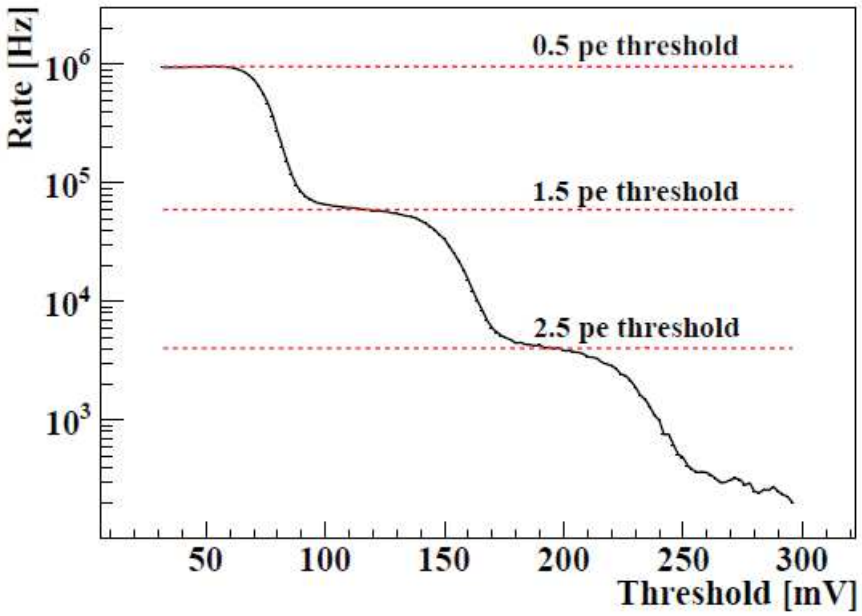

Fig. 2.12: A Stair Case plot for the evaluation of the OCT. The amplitudes for the rate thresholds are given in terms of number of photoelectrons (pe). Source: [66].

The old SiPM series S10362 typically had $\varepsilon \sim 25\%$ [68], against the $\sim 3\%$ of the new generation.

2.1.5 Afterpulsing

OCT avalanches are not the only spurious pulses that are correlated to the genuine light signal. During the breakdown, defects in the silicon structure of the device can become a trap for the carriers. Therefore, shortly following the primary avalanche (< 1 ns) [65] or after several ns or even μs [66], secondary avalanches can be triggered by the released charges. The phenomenon is known as *afterpulsing*. The amplitude of the resulting pulses depends on the recovery time of the cells and can be calculated [66, 65]. In particular, if the delay is shorter than the recovery time, the afterpulse must be smaller than one photoelectron since no other avalanches could be triggered. On the contrary, if the delay is longer than the pixel recovery time, a standard signal similar to the the photon-induced ones is generated. Thus, afterpulses with short delay have negligible impact, while the long-delayed afterpulses are dangerous for the photon-number resolution as much as OCT. As for the previously described spurious effects, the afterpulse probability increases with the overvoltage.

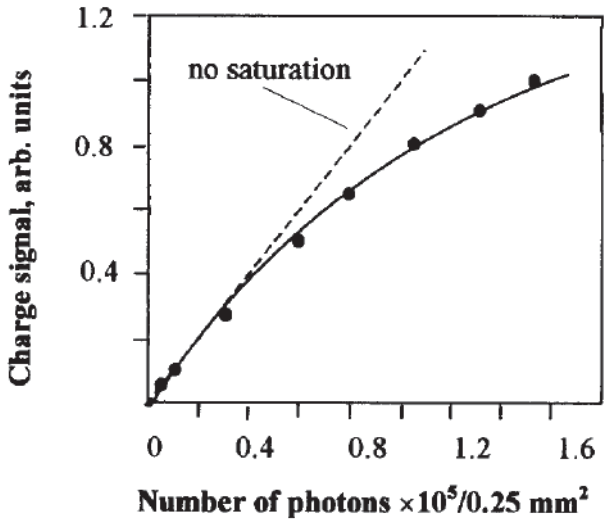

Fig. 2.13: Saturation curve for signals acquired with a limited GM silicon photodiode (an old SiPM model). The solid line, well superimposed to the experimental data, is the plot of Eq. (2.6), which is to be compared with the linear trend (dotted line). Source: [58].

2.1.6 Pile up

The spurious stochastic effects described above are essentially detrimental because they spoil the proportionality between the number of photons impinging on the sensor and the number of fired cells, which is the reason why these devices are interesting. Unfortunately, even in an ideal future, when all these stochastic effects will be overcome, the detector response will be anyway affected by a deviation from linearity [59] due to the very idea of counting devices with a finite number of GM-APDs. In particular, the possible nonlinearity can be ascribed to the limited number N of the cells and the fact that more than one photon can hit a single cell without changing its response [73]. This saturation problem, called *pile up*, is usually modeled with the well-known statistical distribution of ηn balls, representing the detected photons with PDE η, into N urns, which are the cells. Starting from the distribution of the empty cells x [74]

$$P(x) = \sum_{j=x}^{N} (-1)^{j-x} \binom{j}{x} \binom{N}{j} \frac{x}{j} \left(1 - \frac{j}{N}\right)^{\eta n} \tag{2.4}$$

one can retrieve the moments of the distribution for the cells $N - x \equiv m$ that are hit by at least one photon, and hence

$$\begin{aligned} \langle m \rangle &= N \left[1 - \left(1 - \frac{1}{N}\right)^{\eta n}\right] \\ \langle \Delta m^2 \rangle &= N(n-1)\left(1 - \frac{2}{N}\right)^{\eta n} + N\left(1 - \frac{1}{N}\right)^{\eta n} - N^2 \left(1 - \frac{1}{N}\right)^{2\eta n}. \end{aligned} \tag{2.5}$$

If the cell number is large, note that the mean number is approximated by an exponential function, i.e.

$$\langle m \rangle \sim N \left[1 - \exp\left(-\frac{\eta n}{N}\right)\right] \tag{2.6}$$

and, in particular, for $N \to \infty$ we find the linear scaling $\langle m \rangle \sim \eta n$. This simple model has always been consistent with experimental data, as shown in Fig. 2.13.

However, it has at least two important flaws. First of all, it does not take into account other spurious stochastic effects. Secondly, while in a semiclassical approach the analogy between photons impinging on the cells of the sensor and balls invading urns could be fine as long as the photon can be reduced to a particle, this may be critical for a quantum-optical description because the incoming field is not necessarily in an eigenstate of the number operator and one should also consider the distribution of the state.
Anyway, the dependence of the pile up effect on the number of cells for fixed dimensions of the device is a fact, which implies that smaller cells result in a larger dynamic range. Moreover, it is intuitive that the pile-up effect must depend on the number of incoming photons, so that the chosen intensity regime largely determines the incidence of pile-up effects. Hence we see that, at the single-photon regime, the deviation from nonlinearity is negligible, as it will be shown in the following section.

2.2 Standard characterization

2.2.1 MPPC S13360: preliminary comments from datasheet

Consistently with the project outlined in the introduction and the specific features of SiPM, our search focused on devices with minimum OCT and with a PDE value as high as possible. The new generation of SiPMs produced by Hamamatsu, series S13360, offered the variety of possibilities shown in Fig. (2.14).

Type no.	Pixel pitch (μm)	Effective photosensitive area (mm)	Number of pixels	Package	Fill factor (%)
S13360-1325CS	25	1.3 × 1.3	2668	Ceramic	47
S13360-1325PE				Surface mount type	
S13360-3025CS		3.0 × 3.0	14400	Ceramic	
S13360-3025PE				Surface mount type	
S13360-6025CS		6.0 × 6.0	57600	Ceramic	
S13360-6025PE				Surface mount type	
S13360-1350CS	50	1.3 × 1.3	667	Ceramic	74
S13360-1350PE				Surface mount type	
S13360-3050CS		3.0 × 3.0	3600	Ceramic	
S13360-3050PE				Surface mount type	
S13360-6050CS		6.0 × 6.0	14400	Ceramic	
S13360-6050PE				Surface mount type	
S13360-1375CS	75	1.3 × 1.3	285	Ceramic	82
S13360-1375PE				Surface mount type	
S13360-3075CS		3.0 × 3.0	1600	Ceramic	
S13360-3075PE				Surface mount type	
S13360-6075CS		6.0 × 6.0	6400	Ceramic	
S13360-6075PE				Surface mount type	

Fig. 2.14: Table of the SiPM series S13360 by Hamamatsu. Source: [63].

The 25-μm-pixel-pitch sensor features the largest number of cells at fixed size but also with the smallest fill factor, which limits the sensor PDE to a maximum of $\sim 25\%$. It is suitable to count a large number of photons (~ 100) since the cells are enough to overcome pile-up effects at high-intensity regimes, but it is not ideal for single-photon quantum measurements. Thus, we ruled it out and chose between the 50-μm-pixel-pitch and the 75-μm-pixel-pitch detectors. For what concerns the size, the best choice is the smallest surface able to collect all the incident light, which is the case of the 1.3×1.3 mm photosensitive area. A picture of the geometric structure of these objects is shown in Fig. 2.15.
In Fig. 2.16 we show the dependence of the PDE on the wavelength and in Fig. 2.17 the dependence of gain, OCT and PDE on the overvoltage. Note that the peak of the PDE is reported at ~ 450 nm. As expected, at fixed overvoltage the OCT probability is larger for larger cells. But the 75-μm-pixel-pitch device is endowed with a higher PDE. Our characterization of the sensors has been essential to take a decision.

2.2.2 Light Source

For this preliminary standard characterization, following the scheme in [68], as a light source we employed a Picosecond Pulsed Diode Laser produced by PicoQuant (PDL 800-D) [64] and emitting 6-ns long pulses at ~ 400 nm.

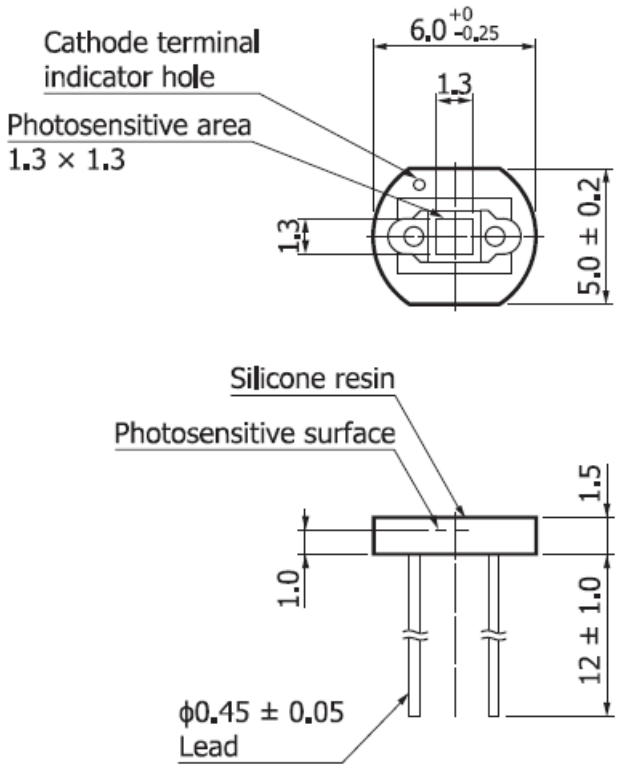

Fig. 2.15: External geometry of the sensors. Dimensional units: mm. Source: [63].

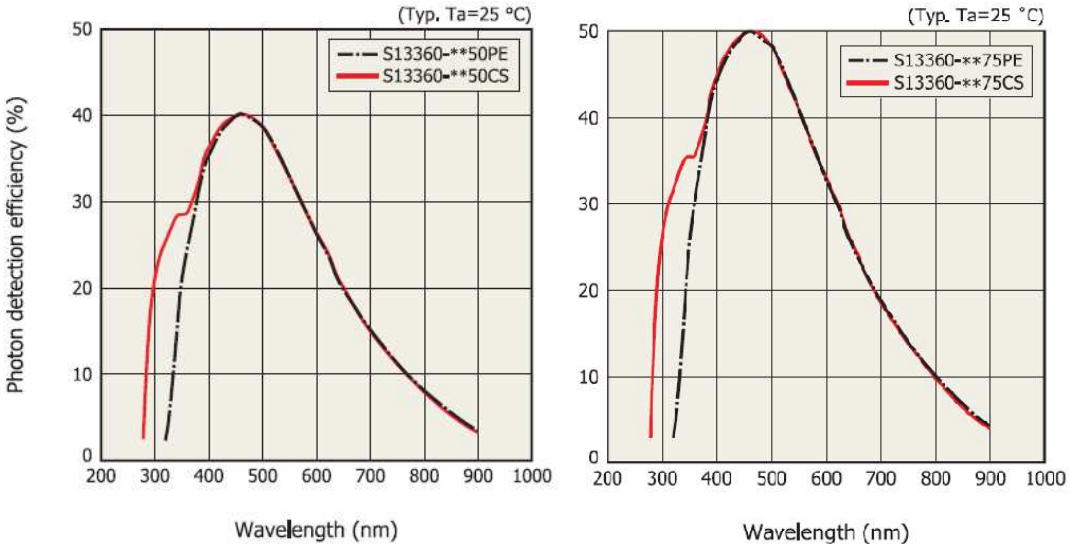

Fig. 2.16: PDE as a function of wavelength for the detectors S13360-1350CS (on the left) and S13360-1375CS (on the right). Source: [63].

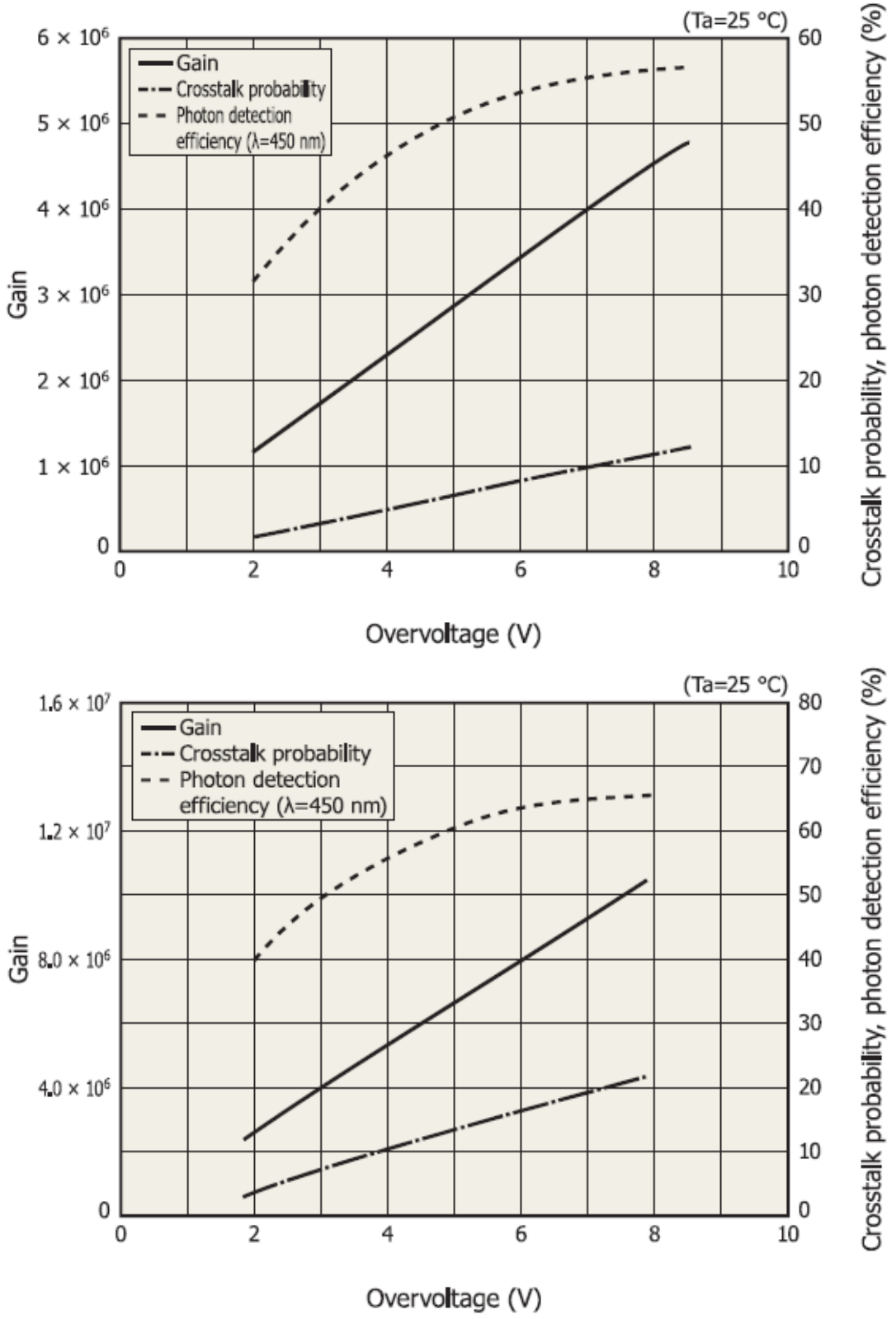

Fig. 2.17: Plot of gain, OCT probability and PDE as a function of the overvoltage for the detectors S13360-1350CS (top) and S13360-1375CS (bottom). Source: [63].

2.2.3 Data Acquisition

Both the detectors we tested were powered and amplified by the computer-based Caen SP5600 Power Supply and Amplification Unit (PSAU) [75]. In particular, the two SiPMs were mounted in single interchangeable heads. This device is monitored via USB port, allowing for the setting of the bias voltage and the gain. The amplification factor is variable in a range up to 50 dB with 1-dB gain step. Moreover, the temperature of the detectors is monitored and stabilized via an integrated feedback circuit.
For what concerns the acquisition of the amplified signal, we sampled the output with the computer-based Caen DT5720 desktop waveform digitizer, a device endowed with 12-bit resolution and a sampling rate ranging from 31.25 to 250 MS/s, simultaneously on each channel. The sampled waveforms were then integrated offline over suitable integration intervals. The histogram of the integrated values is the so-called *pulse-height-spectrum* containing the statistical information on the detected light. The pulse-height-spectrum displays peaks corresponding to different numbers of detected photons. See the next Sections for details.

2.2.4 Peak-to-peak distance

One of the most important parameters to monitor in the analysis of a pulse-height-spectrum is the distance between two consecutive peaks, called *peak-to-peak distance* Δ_{pp}. It is the very essence of the detector resolution power, the variable determining the number of resolved peaks. The peak-to-peak distance is a function of the gain of the single cell and is proportional to the overvoltage according to [68]

$$\Delta_{pp} \propto \frac{C}{e} V_{ov} \tag{2.7}$$

where C is the diode single-cell capacitance and e is the electron charge. Thus, we firstly evaluated the dependence of the peak-to-peak distance on the overvoltage for two 1350CS and two 1375CS SiPMs. Results are shown in Figs. 2.18 and 2.19. A simple way to estimate the optimal bias voltage is given by the maximization of the ratio [68]

$$R \equiv \frac{\Delta_{pp}}{\sqrt{\sigma_1^2 - \sigma_0^2}} \tag{2.8}$$

where $\sigma_{0,1}^2$ are the variances of the 0- and 1- photon-number peaks. For the detectors under investigation, this figure of merit is nearly constant over the whole interesting bias-voltage range, as shown in Fig. 2.20 for one of the 13360-50CS series. Thus, we set the optimal bias voltage value reported on the datasheets, i.e. 54,79 V and 55,07 V for the 50-μm-pixel-pitch sensors and 54,57 V for both the 75-μm-pixel-pitch. This constant trend of the ratio R is quite unusual since it is commonly displayed as a parabola, where a maximum can be easily found, corresponding to the optimal bias voltage [68]. If this is not the case, we guess that the effect of a limited quantum efficiency is balanced by the spurious effects of the correlated noise. Hence, apparently we have no trade-off between losses and correlated noise here. However, we can certainly say that, for Quantum Optics application, the latter is the most detrimental since it makes the output statistics unreliable and spoils the detected correlations. Therefore, in the following, our criterion for choosing between our two sensor classes will focus on *the minimization of the correlated-noise sources, i.e. OCT and afterpulsing*.
The peak-to-peak distance is also a function of the temporal gate over which the signal is integrated. It is maximum when the integration gate covers the whole duration of the output waveform. As shown in Fig. 2.21, we see that, for what concerns this SiPM generation, the largest gate over which we need to integrate the signal is ~ 350 ns. From hereon in, for what concerns this standard characterization, we will always consider the integration of the whole waveform, i.e. we set $T = 350$ ns.

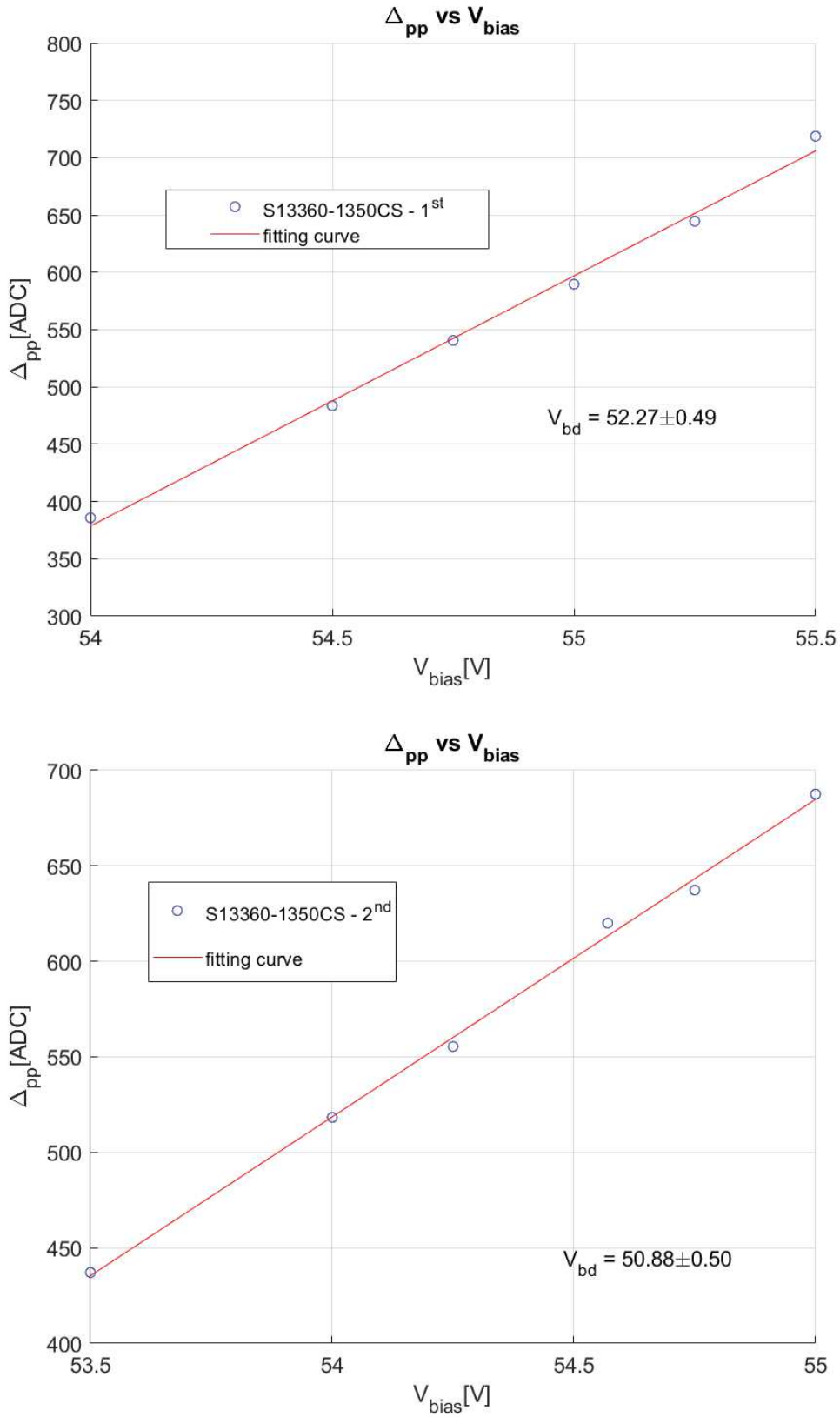

Fig. 2.18: Peak-to-peak distance as a function of the bias voltage $V_{bias} = V_{bd} + V_{ov}$, where V_{bd} is the measured breakdown voltage, for the first and the second of the 50-μm-pixel-pitch SiPMs 1350CS.

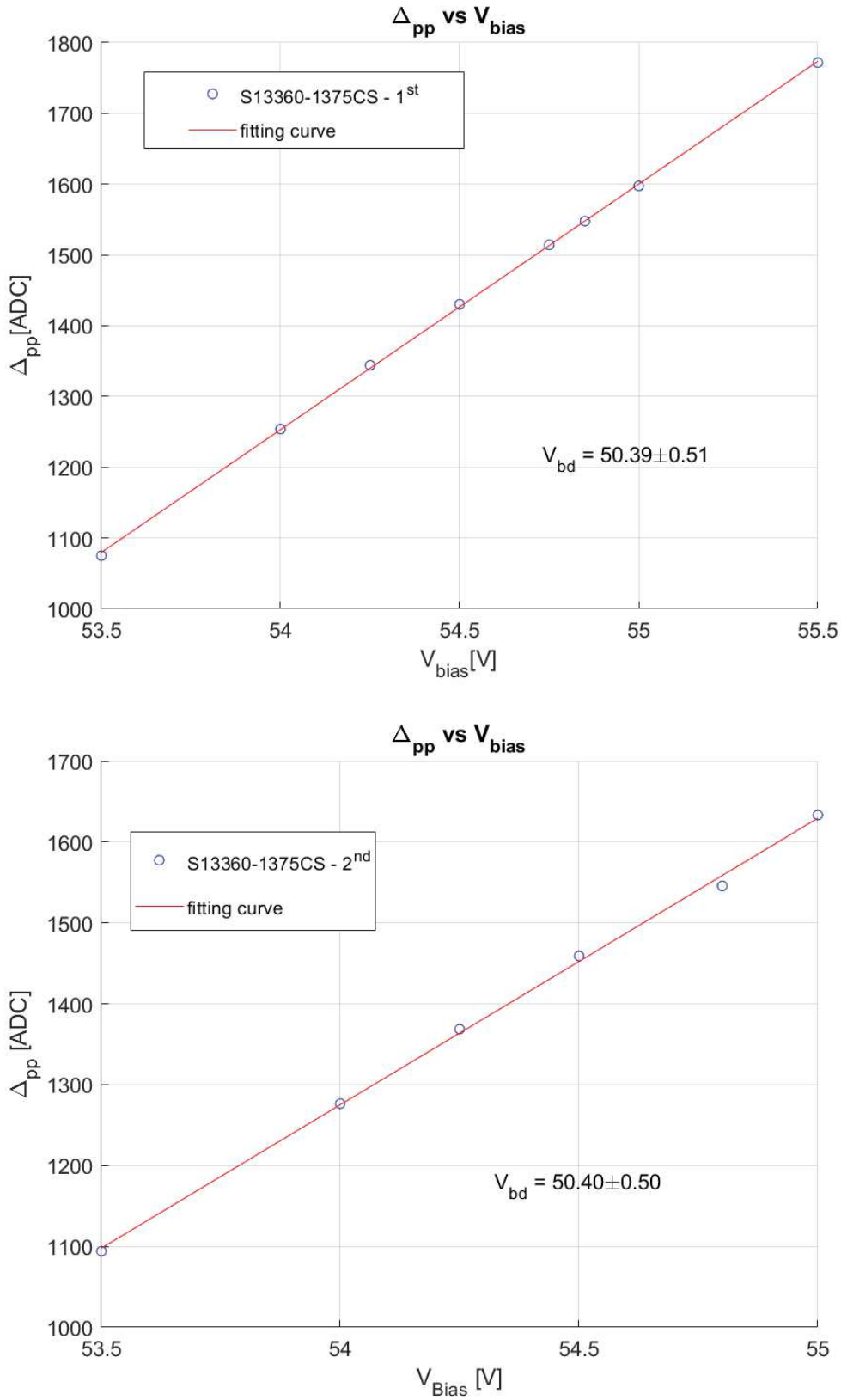

Fig. 2.19: Peak-to-peak distance as a function of the bias voltage $V_{bias} = V_{bd} + V_{ov}$, where V_{bd} is the measured breakdown voltage, for the first and the second of the 75-μm-pixel-pitch SiPMs 1375CS.

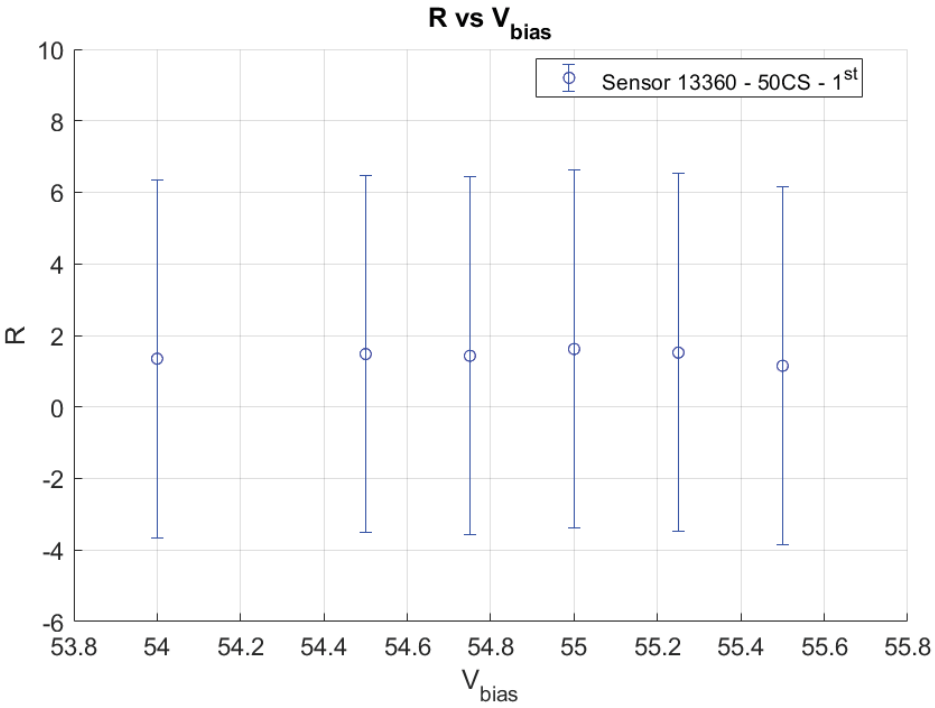

Fig. 2.20: Estimator of the optimal bias voltage R in Eq. 2.8 for the detector 13360-50CS. An analog behavior is displayed for the other sensors. Note that no maximum can be fairly identified for the function R in this case.

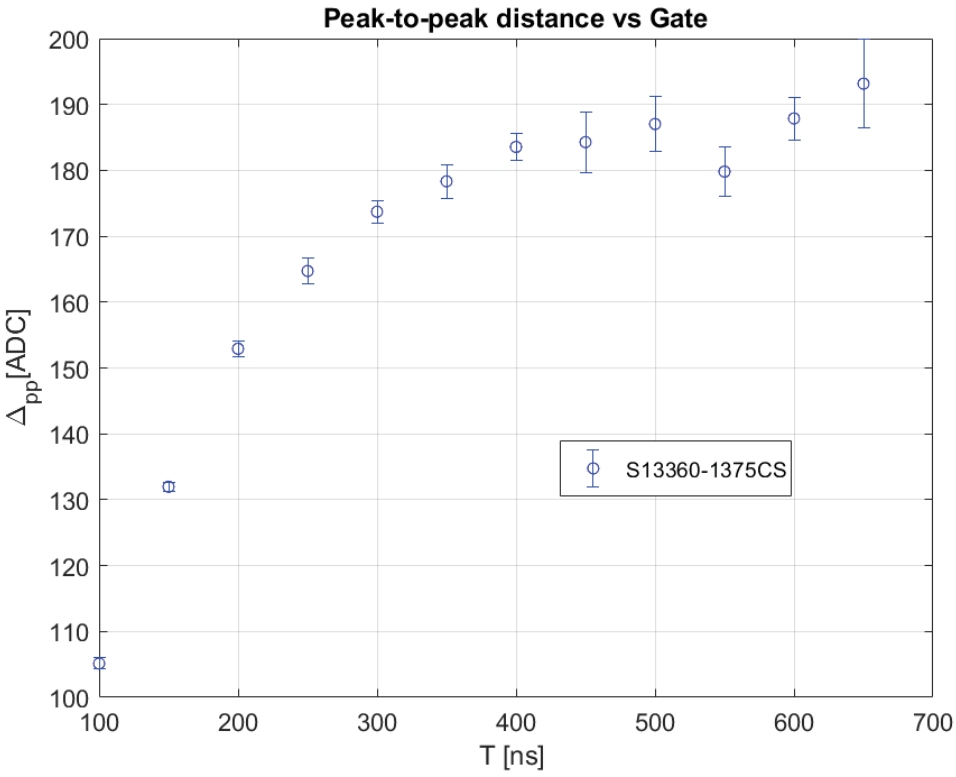

Fig. 2.21: Peak-to-peak-distance values Δ_{pp} recorded for different choices of the gate length T. Note that the dependence of the peak-to-peak distance on the gate is proportional to the temporal evolution of the integrated signal $\sim 1-\exp(1-t/\tau)$, where τ is the time constant of the exponential decay.

2.2.5 Evaluation of DCR

By exploiting the methods outlined in the introduction to this chapter, we estimated the DCR ν_{dc} for our detectors. We measured the frequencies of one- and two-photon signals for different bias voltages, thus retrieving Stair Case plots like that shown in Fig. (2.12). An example for the 1350CS model at the optimal bias voltage is shown in Fig. (2.22) [77]. The Stair Case plot is recorded by sampling and integrating online the signal from the PSAU through the digitizer. The measurements of the DCRs for our sensors set at their optimal bias voltages are shown in Tab. (2.1).

Sensor	DCR [kHz]	$V_{bias}^{(opt)}$ [V]	Gain [dB]	Gate [ns]	Temperature [°C]
1350CS - 1^{st}	540	54,79	40	304	25,0
1350CS - 2^{nd}	298	55,07	40	304	26,6
1375CS - 1^{st}	185	54,57	40	352	25,8
1375CS - 2^{nd}	130	54,57	40	352	27,6

Tab. 2.1: DCR inferred from the StairCase plot. As expected, for detectors with a high number of cells the DCR is larger. Note that the Gain here is referred to the amplifier in the PSAU unit.

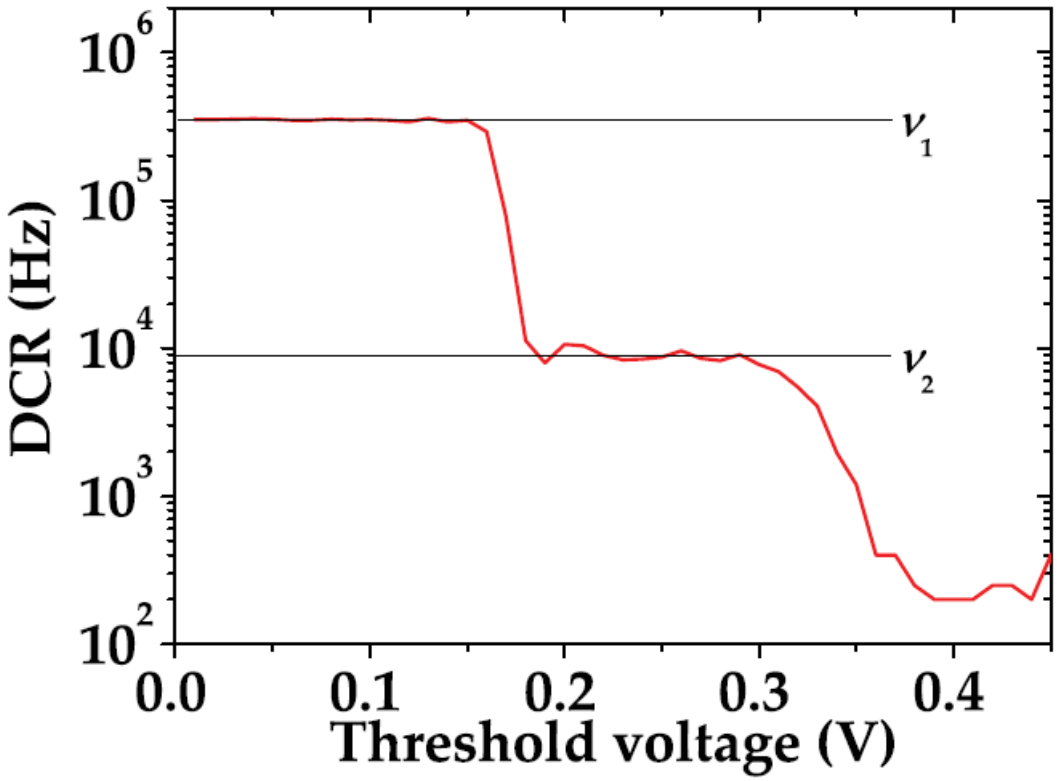

Fig. 2.22: A Stair Case plot for a 1350CS model, performed at room temperature with no impinging light. ν_1 and ν_2 are the DCRs related to a one- and two-photon signal amplitude. The ratio ν_2/ν_1 yields an empiric estimation of the cross-talk probability ε.

2.2.6 Evaluation of Afterpulsing

The probability of an afterpulse event is easy to compute from experimental data because, due to the very nature of this effect, it is possible to select an interval over the integration gate where only dark-counts and afterpulses can occur, i.e. after that the light signal is completely extinguished. If τ_{rec} is the recovery time of an avalanche triggered by a light event in a single pixel, the fraction of charge carried by the pulse at a given time is proportional to the triggering probability in Eq. (2.2) according to [66, 60, 78]

$$\frac{q(t)}{q_0} = 1 - \exp\left(-\frac{t}{\tau_{rec}}\right).$$

These carriers are likely to be trapped in the high-field region and then re-emitted, starting a secondary avalanche in the same pixel. In particular, each secondary avalanche is independent of the others, so that the captured charges are released according to an exponential decay [65]

$$\frac{1}{\tau_{AP}} \exp\left(-\frac{t}{\tau_{AP}}\right)$$

where τ_{AP} is the time constant of the process, which strongly depends on temperature [78] and, also, on the energy level of the traps. Then, if we correctly choose the integration gate T as explained before, we can define the afterpulse probability as

$$P_{AP} = \frac{\int_0^T dt \left[1 - \exp\left(-\frac{t}{\tau_{rec}}\right)\right] \frac{\bar{N}_{AP}}{\tau_{AP}} \exp\left(-\frac{t}{\tau_{AP}}\right)}{\int_0^T dt \left[1 - \exp\left(-\frac{t}{\tau_{rec}}\right)\right] \left[\frac{\bar{N}_{AP}}{\tau_{AP}} \exp\left(-\frac{t}{\tau_{AP}}\right) + \frac{\bar{N}_{DC}}{\tau_{DC}} \exp\left(-\frac{t}{\tau_{DC}}\right)\right]} \tag{2.9}$$

where $\bar{N}_{AP}$ and $\bar{N}_{DC}$ are the mean number of cells fired respectively because of an afterpulse or a dark-count event over T. For large T, Eq. (2.9) reduces to

$$P_{AP} \sim \frac{\bar{N}_{AP}\tau_{AP}(\tau_{DC} + \tau_{rec})}{\bar{N}_{AP}\tau_{AP}(\tau_{DC} + \tau_{rec}) + \bar{N}_{DC}\tau_{DC}(\tau_{AP} + \tau_{rec})}. \tag{2.10}$$

For what concerns the dark counts, $\bar{N}_{DC} \sim \nu_{dc} T$.
The mean number of afterpulse events can be retrieved from experimental data. Our strategy is based on the method outlined in [80]. It basically consists in dividing the integration intervals $\Delta t_1 \equiv T_1 - T_0$, $\Delta t_2 \equiv T_2 - T_1$ and $\Delta t_3 \equiv T_3 - T_2$ with $T_0 < T_1 < T_2 < T_3$, as shown in Fig. (2.23).

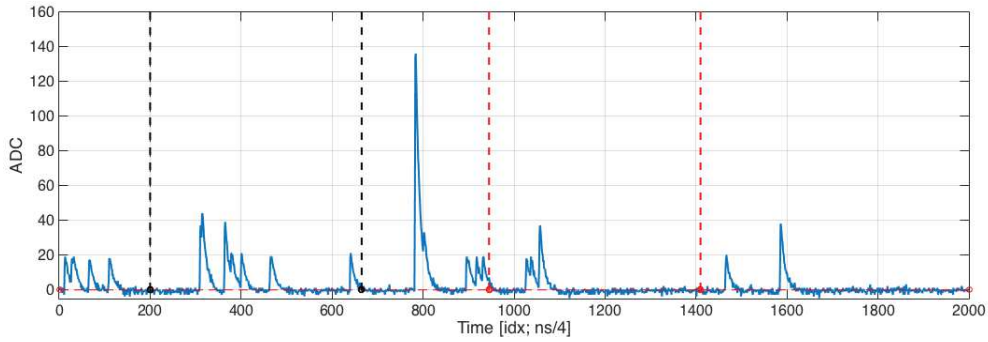

Fig. 2.23: Scan of a large integration gate for a SiPM output signal. The whole gate is partitioned in three smaller intervals. On the left (dark gridlines), Δt_1 is set before the beginning of the light signal, which is fully integrated in Δt_2, between the dark and the red gridline. On the right (red gridlines), in the interval Δt_3 one can find either dark counts or afterpulses.

Note that Δt_2 is the interval over which the full light-event signal is integrated, so that the events occurring in Δt_1 can just be dark counts while the events occurring in Δt_3 are either dark counts or afterpulses. OCT events are all supposed to be integrated together with the signal over the interval Δt_2. We expect that, on the average, the charge integrated over Δt_3 is larger than that over Δt_1 due to the occurrence of afterpulses triggered by the light-event signal. Thus, the quantity

$$\bar{N}_{AP} \equiv \frac{\bar{Q}(\Delta t_3) - \bar{Q}(\Delta t_1)}{\Delta_{pp}}, \tag{2.11}$$

where $\bar{Q}(\Delta t)$ is the mean value of the total sum of the charges integrated over a gate Δt, provides an estimation of the mean number of afterpulses over the interval Δt_3. The averages of the integrated charges $\bar{Q}(\Delta t)$ were retrieved by assuming a Gaussian distribution for them, which is guaranteed by the central limit theorem. The measurement of $Q(\Delta t_3)$ was made by collecting the signals from our pulsed laser and integrating them over the gate Δt_3, whereas the measurement of $Q(\Delta t_1)$ was performed as a pure dark-count measurement, i.e. in the absence of impinging light (see the previous section for details). The experimental distributions of $Q(\Delta t_1)$ and $Q(\Delta t_3)$ are shown in Fig. (2.24).

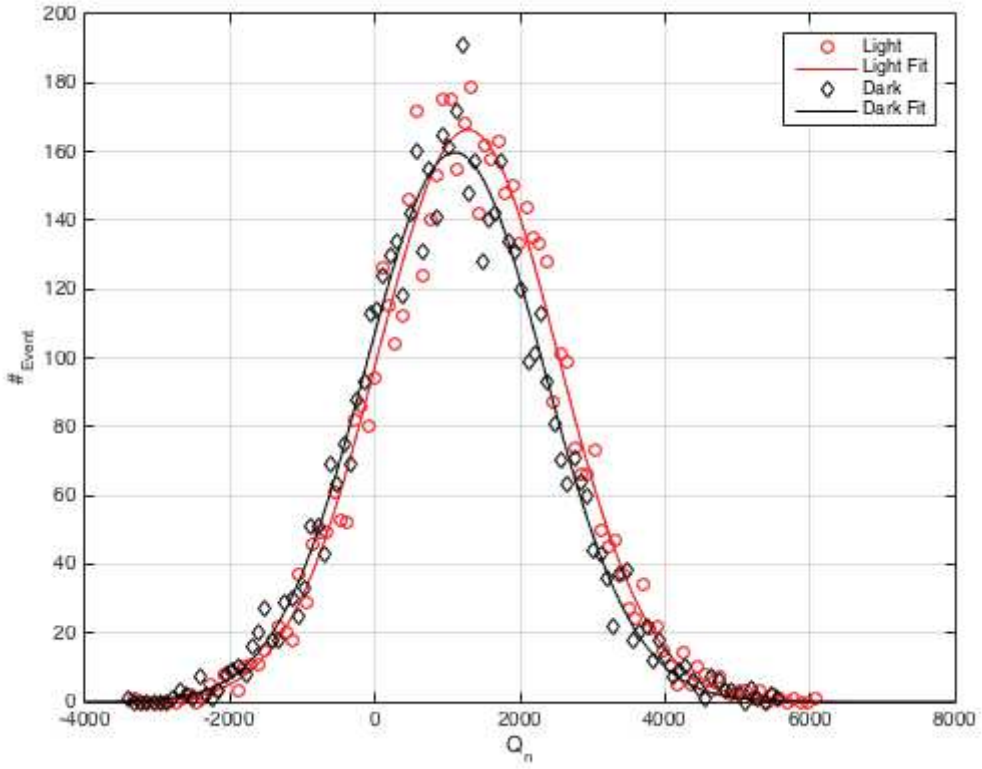

Fig. 2.24: Distributions of the sum Q of 300 charges integrated over Δt_1 (dark rhombuses + line) and over Δt_3 (red circles + line). Rhombuses and circles: experimental data. Lines: Gaussian fit. The distributions are well approximated with Gaussians because here the central limit theorem holds. The difference of the mean values of the Gaussian fits normalized to the peak-to-peak distance yields the estimation for the mean value of the number of afterpulses in Eq. (2.11).

Being the statistics of both, the laser impinging light and the dark counts, Poissonian, the time-of-arrival distribution of light and of dark-count signals is exponential. But then the mean number of afterpulses in Eq. (2.11) may also be retrieved from

$$\begin{aligned}\bar{N}_{AP} &= \bar{N}_{tot} P_L(\Delta t_2)[1 - P_{DC}(\Delta t_3)] P_{AP}(\Delta t_3) \\ &= \bar{N}_{tot} e^{-\frac{\Delta t_2}{\tau_{rec}}} [1 - e^{-\frac{\Delta t_3}{\tau_{DC}}}] P_{AP}(\Delta t_3)\end{aligned} \tag{2.12}$$

where $\bar{N}_{tot}$ is the total mean value of detected photons, P_L, P_{DC} and P_{AP} are the time-of-arrival distribution for respectively light, dark-count and afterpulse events and τ_{rec} and τ_{DC} are the corresponding time constants. Eq. (2.12) just states that the probability for an afterpulse event to occur in Δt_3 is given by the combination of three independent contribution, i.e. the probability that a light signal is detected in Δt_2 ($P_L(\Delta t_1)$), the probability that a dark count does not fire the same cell as the afterpulse in Δt_3 ($P_{DC}(\Delta t_3)$) and the probability that a carrier of the primary avalanche is trapped during Δt_3 ($P_{AP}(\Delta t_3)$). The time constants can be retrieved from the saturation of the peak-to-peak distance as a function of the integration gate T for light-event signals (τ_{rec}) and dark counts (τ_{DC}). Therefore, the afterpulse probability can be estimated from Eqs. (2.11) and (2.12) as

$$P_{AP} = \frac{\bar{N}_{AP} e^{\frac{\Delta t_2}{\tau_{rec}}}}{\bar{N}_{tot}[1 - e^{-\frac{\Delta t_3}{\tau_{DC}}}]}. \tag{2.13}$$

For our SiPMs, we found that $P_{AP} = 0.07\% \pm 0.01\% \ll 1\%$. Therefore, hereon we will neglect the contribution of afterpulse events.

2.2.7 Evaluation of OCT

The cross-talk probability ε is the parameter we are most interested in, since, as mentioned in the introduction to this chapter, OCT is the most detrimental drawback for Quantum Optics applications. Therefore, this is the parameter tipping the balance in favor of one of the two types of SiPMs, the 50-μm or the 75-μm-pixel-pitch. In particular, we expect the latter, endowed with a larger fill factor, to be more deeply affected by OCT. If on the contrary they were found to share the same cross-talk probability up to few percentage points, the 75-μm-pixel-pitch sensors should be preferable due to their larger PDE. A simple analysis from the Stair Case plot and from Eq. (2.3) allows to retrieve an estimation of OCT at different bias voltages. We report in Fig. 2.25 the dependence of the cross-talk probability on the bias voltage for both our types of sensors. As expected, the 1375CS model is affected by OCT more than the 1350CS model. In particular, at the optimal bias voltage the cross-talk probability for the 1375CS model is three times larger. *Such experimental evidence led us to choose the 1350CS model to measure nonclassical states of light.* Hereon we will characterize and employ the two 50-μm-pixel-pitch detectors only.

2.2.8 Evaluation of pile up

Another advantage of the model 1350CS with respect to the 1375CS is the fact that the large number of cells (667 against 285) makes pile up effects completely negligible for our photon-number working regime, i.e. few photons per pulse, up to $\langle n \rangle \sim 10$ (*mesoscopic regime*). If we consider the effects of losses and pile up only, Eq. (2.6) holds and, being $N \ll \eta n$, we find that $\langle m \rangle \sim \eta \langle n \rangle$.

2.3 A model for photodetection via Multi-Pixel Photon Counters

We are now ready to model the detection process of our SiPM, taking into account every relevant drawback. In a few words, the model consists in a generalization of the POVM introduced in Eq. (1.158). Following

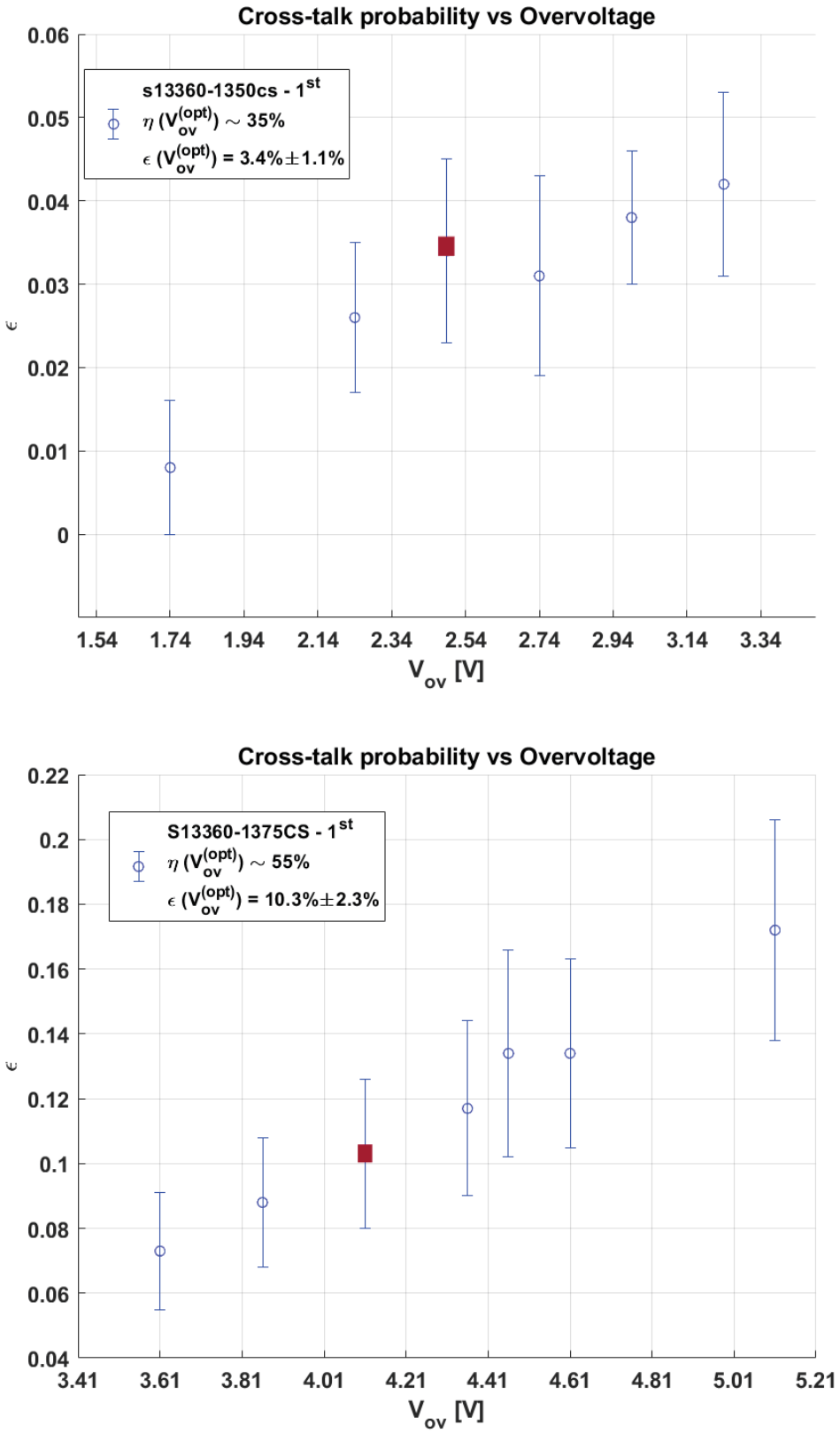

Fig. 2.25: Dependence of the cross-talk probability ε on the overvoltage $V_{ov} = V_{bias} - V_{bd}$, measured at room temperature with no impinging light for the 1350CS (top) and the 1375CS (bottom) model. The red box highlights the optimal-bias-voltage point $V_{ov}^{(opt)}$, which are 2.49 and 4.18 V respectively. We recall that here we set the optimal bias voltage to the value reported by the manufacturer. The PDE as expected from datasheet at the optimal overvoltage together with the corresponding OCT probability are shown in the box.

[79] and [81], we describe the detector response as

$$\hat{\Pi}(k) = \sum_{n=0}^{\infty} M_n^{(k)} |n\rangle\langle n| \tag{2.14}$$

where $M_n^{(k)}$ is the probability to detect k photons when a n-photon Fock state impinges on the device. Equation (1.158) holds for any phase-independent MPPC. We have to specialize $M_n^{(k)}$ to our particular situation by considering the effects that the standard characterization presented above highlighted, i.e. a non-unit PDE, dark counts and OCT. In such a case, it has been shown [79, 82, 83] that the transformations $M_n^{(k)}$ are linear. More explicitly, if P_n is the probability to find the state $\hat{\rho}$ in the n-th eigenstate of the Fock basis

$$\mathrm{P}_n \equiv \langle n|\hat{\rho}|n\rangle$$

and p_k is the probability given by the area of the k-th peak in the pulse-height spectrum

$$\mathrm{p}_k \equiv \mathrm{Tr}[\hat{\rho}\hat{\Pi}(k)],$$

the relation between the two is just given by

$$\mathrm{p}_k = M_n^{(k)} \mathrm{P}_n. \tag{2.15}$$

The probabilities $M_n^{(k)}$ are elements of a matrix $\mathbf{M}$ given by the convolution of the three mentioned stochastic process. For what concerns the losses, we have already seen in the Introduction that the process is Bernoullian, so that

$$\mathrm{p}_m = \eta^m \sum_{n=m}^{\infty} \binom{n}{m} (1-\eta)^{n-m} \mathrm{P}_n \tag{2.16}$$

with mean value and variance of the photoelectron number given by

$$\begin{aligned} \langle m\rangle &= \eta\langle n\rangle \\ \langle \Delta m^2\rangle &= \eta^2\langle \Delta n^2\rangle + \eta(1-\eta)\langle n\rangle \end{aligned} \tag{2.17}$$

where η is the PDE of the detector.
The dark-count statistics, as mentioned above, is Poissonian. Therefore, it results in a shift of the mean value and variance in Eq. (2.17) of a quantity $\langle m_{dc}\rangle = \nu_{dc} T$, i.e.

$$\begin{aligned} \mathrm{p}_{\tilde{m}} &= \sum_{m=0}^{\tilde{m}} \eta^m \sum_{n=m}^{\infty} \binom{n}{m} (1-\eta)^{n-m} \frac{\langle m_{dc}\rangle^{\tilde{m}-m}}{(\tilde{m}-m)!} \exp(-\langle m_{dc}\rangle) \mathrm{P}_n \\ \langle \tilde{m}\rangle &= \langle m\rangle + \langle m_{dc}\rangle \\ \langle \Delta\tilde{m}^2\rangle &= \langle \Delta m^2\rangle + \langle m_{dc}\rangle. \end{aligned} \tag{2.18}$$

The OCT effect acts exactly in the opposite sense with respect to the PDE, the latter reducing with a given success probability η the number of counting photons, the former enhancing it with probability ε [79]. Thus, we are left with a Binomial-like contribution

$$\binom{m}{n-m} \varepsilon^{n-m} (1-\varepsilon)^{2m-n} \tag{2.19}$$

leading to

$$\mathrm{p}_k = \sum_{\tilde{m}=0}^{k} \binom{\tilde{m}}{k-\tilde{m}} \varepsilon^{k-\tilde{m}} (1-\varepsilon)^{2\tilde{m}-k} \sum_{m=0}^{\tilde{m}} \eta^m \sum_{n=m}^{\infty} \binom{n}{m} (1-\eta)^{n-m} \frac{\langle m_{dc}\rangle^{\tilde{m}-m}}{(\tilde{m}-m)!} \exp(-\langle m_{dc}\rangle) \mathrm{P}_n \tag{2.20}$$

whose mean value and variance read

$$\begin{aligned}\langle k\rangle &= (1+\varepsilon)\langle\tilde{m}\rangle \\ \langle\Delta k^2\rangle &= (1+\varepsilon)^2\langle\Delta\tilde{m}^2\rangle + \varepsilon(1-\varepsilon)\langle\tilde{m}\rangle.\end{aligned} \tag{2.21}$$

Finally, we have to consider the gain introduced in the amplification stage. This parameter is here assumed to be a multiplicative factor $\gamma > 1$ [81] scaling the photoelectron detection probability in Eq. (2.20) so that

$$\mathrm{p}_x = \gamma\,\mathrm{p}_\mathrm{k} \tag{2.22}$$

and $\mathrm{p}_x < 1$. Consequently, the first moment and the variance are rescaled according to γ and γ^2 respectively.

2.4 Characterization via detection of classical states of light

Having defined through the standard characterization which are the most important parameters to optimize SiPMs and having introduced a model accounting for them, we then assessed the performance of these devices by reconstructing the statistics of classical radiation fields, namely *coherent* and *chaotic* light [77]. First of all, we showed that the comprehensive theoretical model leading to Eq. (2.20) fits the experimental data, so that we can fairly say that the occurrence of the most relevant spurious effects of SiPMs can be predicted. Secondly, we succeeded in further optimizing these devices for Quantum Optics applications by consistently reducing the impact of their drawbacks.

2.4.1 Experimental setup and the integration gate issue

As shown in Fig. 2.26, we generated coherent light by exploiting the 523-nm second harmonic of a mode-locked Nd:YLF laser amplified at 500 Hz (High Q Laser) and the multi-mode thermal light by passing the same laser beam through a rotating ground-glass disk. In this second scheme, we collected nearly one single coherence area with an iris located at the distance of 1 m from the disk [84]. Each light source was equally divided through a half-wave plate followed by a polarizing cube beam splitter (PBS). At the outputs of the PBS, the two SiPMs were positioned. Light was delivered to the detectors by multi-mode optical fibers with 600-μm-core-diameter. As previously explained, our detectors measure the intensity of the incoming field at the single-photon level. From one measurement to another we changed the mean number of photons with a variable neutral density filter wheel attenuating the light intensity from 0 to 2 optical densities. For each intensity, we recorded the response to $\sim 120,000$ consecutive laser pulses. In general, the data acquisition system was the same as that described for the standard characterization. In particular, we recall that the integration of the waveform with this apparatus still has to be done in post-processing.

First of all, our work focused on the effects of the integration-gate length on the reconstruction of light statistics. We investigated the effect of integrating the signal waveform over a gate smaller than the duration of the signal on the reconstructed light distribution. If the information on the incoming light intensity is only contained in the integral of the whole signal, then we have no hope that, integrating over a smaller gate, the detected light statistics may be correctly retrieved. In particular, we expect that in such a case the processed data are not superimposed on our theoretical predictions, as if the integration over a smaller gate were equivalent to a source of noise that our model does not take into account. If, on the contrary, the information on the detected photon-number is proportional to the signal-peak height, then we expect that a reduction of the integration gate does not compromise the reconstruction of the statistics. Not only, we dare think that the final results are improved by this operation since dark-count and OCT-D-pulses, typically occurring during the evolution of the signal, can be rejected. This hypothesis is deeply connected to the SiPM electronic circuit. Indeed, as mentioned in Sect. 2.1.1, a SiPM output waveform is composed of a

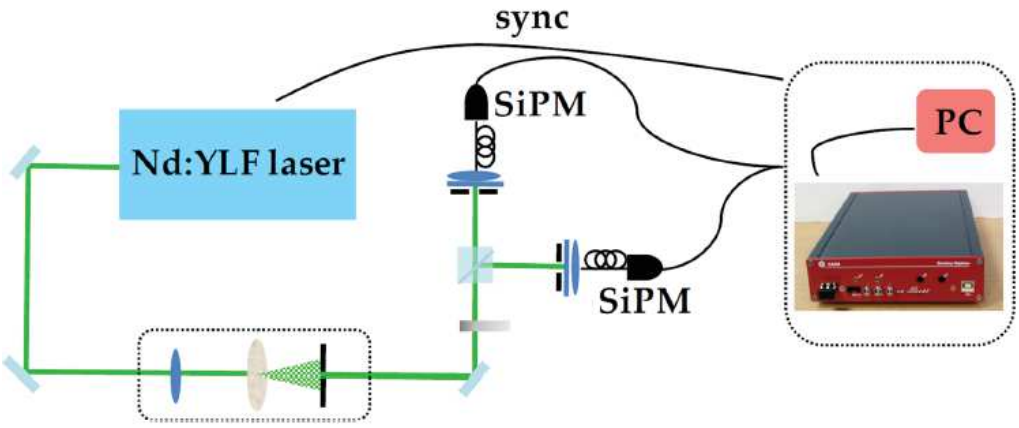

Fig. 2.26: Experimental setup for the measurement of Poissonian and multi-mode thermal states.

rising edge followed by an exponential decay [78]. In particular, Figs. 2.4 and 2.5 show that the rising edge lasts few nanoseconds, which is a negligible time compared to the duration of the whole signal (> 100 ns). Thus, the integral of the waveform $w(t)$ is approximately the same as the integral of the exponential decay, i.e.

$$\int_0^T w(t)dt \sim A\int_0^T \exp(-t/\tau)dt = A\tau[1-\exp(-T/\tau)] \tag{2.23}$$

where T is the integration gate, A is a factor mostly depending on the probability that the avalanches quench and on the number of fired cells, τ is the time constant of the decay, depending on the junction capacitances and on the resistances of the fired cells. The integration of the whole waveform ideally requires to take the limit $T \to \infty$ for Eq. (2.23), so that

$$\int_0^\infty w(t)dt \sim A\tau. \tag{2.24}$$

However, the signal-peak height is none other than $w(0) = A$. Thus, the only assumption that the output waveform can be modeled with an exponential decay leads directly to $\int_0^\infty w(t)dt \propto w(0)$, i.e. the information collected by integrating the whole waveform in the absence of noise is proportional to the information carried by the peak and the proportionality constant, which is τ, does not depend on the incident light, but just on specific electronic parameters of the SiPM.

Motivated by these considerations, we plotted the signal-to-noise ratio S/N given by a multi-mode thermal state with mean detected-photon-number $\langle k \rangle \sim 2$. The S/N is here defined as the ratio between the mean value of the integrated 1-photon peak and its variance. As shown in Fig. 2.27, the signal can be considered already extincted at ~ 150 ns. Nevertheless, we kept considering the gate $T_{max} = 350$ ns found through the standard characterization as a reference to be sure to compare other gate choices with the integration of the full waveform. We also note that similar values of the S/N are achieved for small gates as $T \sim 50$ ns and long gates as $T \sim 350$ ns. The pulse-height spectra we retrieved with this two different choices of the gates are compared in Fig. 2.28, where $x_{out} \equiv \gamma k$. Two important considerations can be made from the inspection of this histogram. First, the peak resolution is better for the longer gate. This is a consequence of the larger impact that the integration of a noisy signal over shorter gates has on the derived number of photons. Second, we have to note that the statistics inferred from the histograms are consistently different from each other, which means either that the 50-ns-gate histogram is completely wrong, implying that we should have integrated the whole waveform, or that the 350-ns-gate histogram is deeply affected by correlated noise. We will prove in the following that the latter is the case. The possibility that the

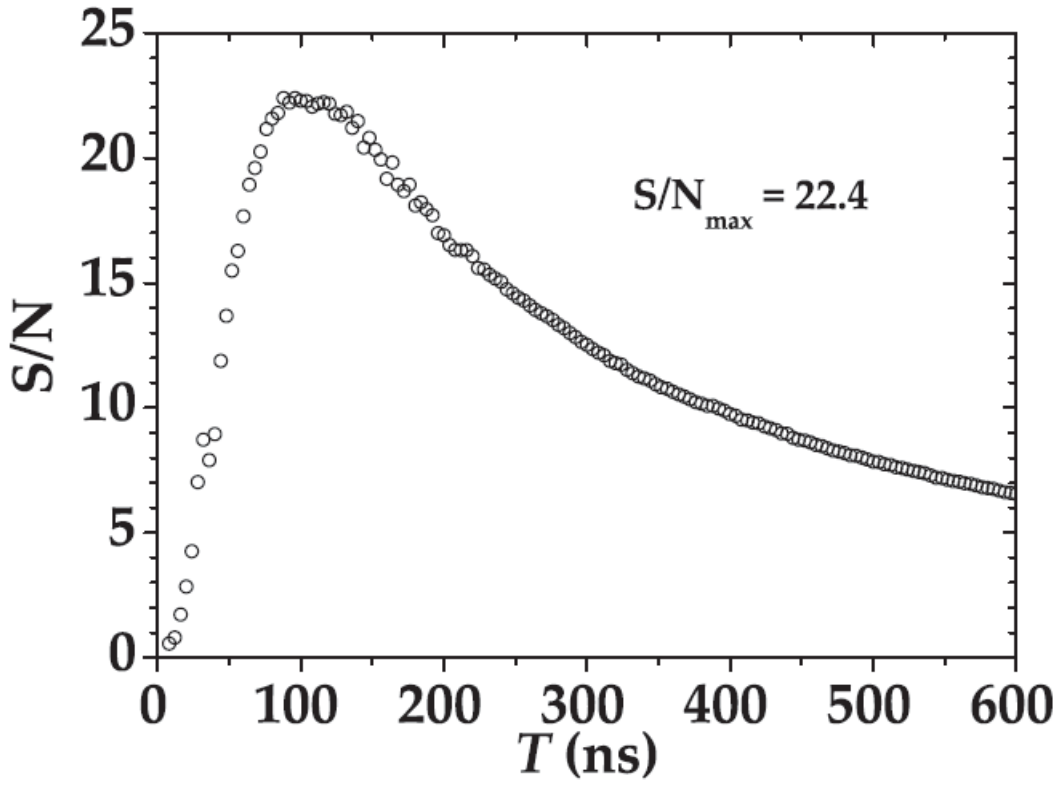

Fig. 2.27: S/N for a multi-mode thermal state as a function of the integration gate T.

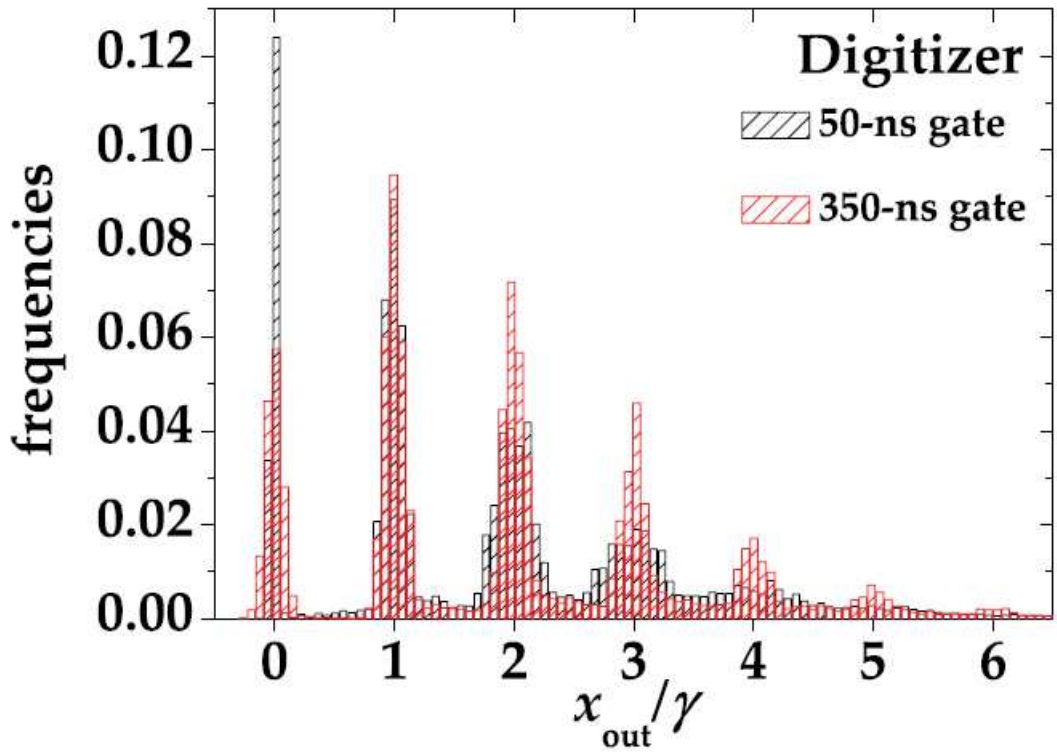

Fig. 2.28: Normalized pulse-height-spectra for a multi-mode thermal state acquired with the digitizer and then integrated over different gate widths. Black: 50-ns gate; red: 350-ns gate.

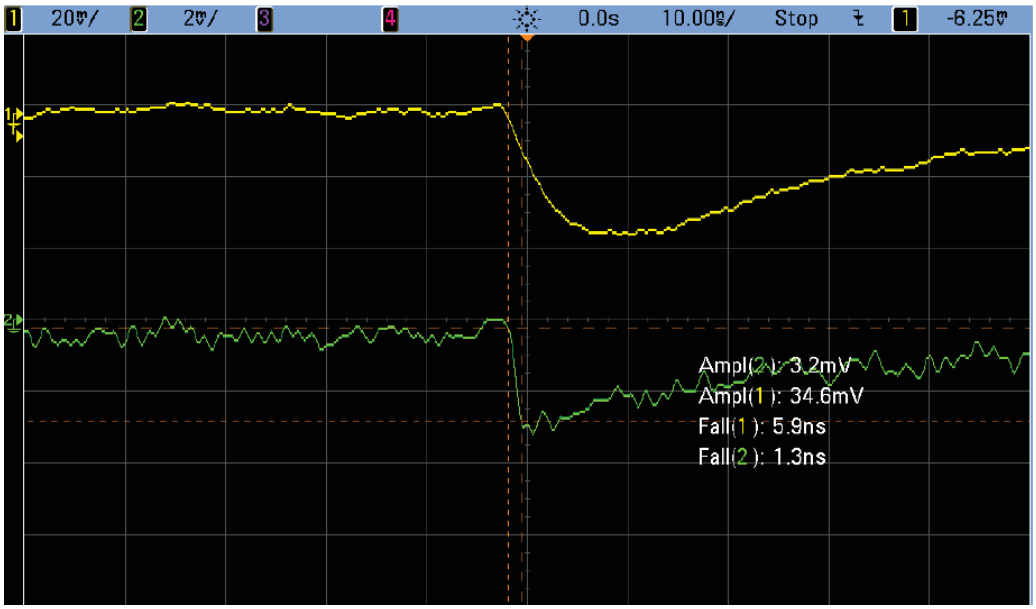

Fig. 2.29: We show the rise time of both outputs for a 1-photoelectron signal from a 50-μm^2-pixel-size SiPM. The high gain output has 6 ns rise time, whereas the low gain output has 1.3 ns.

integration of the whole waveform is not needed to retrieve the number of detected photons, as long as the same information is provided by recording the peak heights, stimulated us to implement a low-noise shaping amplifier instead of the one embedded in the PSAU. The card of such amplifier has one input and two outputs. The gain of one of the outputs is 34 dB, while the gain of the other is equal to 12 dB. We employed just the high gain output. In Fig. 2.29 we show the two outputs of the amplifier, corresponding to a 1-detected-photon input signal from our SiPMs. The yellow line is the high gain output. This device, endowed with a 6-ns-long rise time, can shape the pulse by widening it so that the peak can be fairly sampled by the digitizer and discriminated shot-by-shot. Here we employed a faster digitizer, so that the peak-height could be determined with higher accuracy. In particular, we used a CAEN DT5730 digitizer sampling at 500 MS/s, twice as the previous one. As shown in Fig. 2.30, our amplifier was used in a sort of *peak-and-hold mode*. It may be counterintuitive if Figs. 2.5 and 2.30 are compared since the peak in the latter is wider. However, exactly for this reason, the wider output of the amplifier can be sampled with a larger number of points, also thanks to the faster digitizer.

2.4.2 A model for the time evolution of the OCT probability

Inspired by the model for afterpulses in [65] and by the experimental results on the OCT-D, we elaborated a model for the time evolution of OCT probability given an integration gate T. Our aim here is to find a theoretical and experimental proof for the search of an optimal integration gate by analyzing how it influences the OCT probability.
The probability density function related to OCT-D is an exponential distribution, i.e.

$$p_{dct}(t) = \frac{1}{\tau_{dct}} \exp\left(-\frac{t}{\tau_{dct}}\right) \tag{2.25}$$

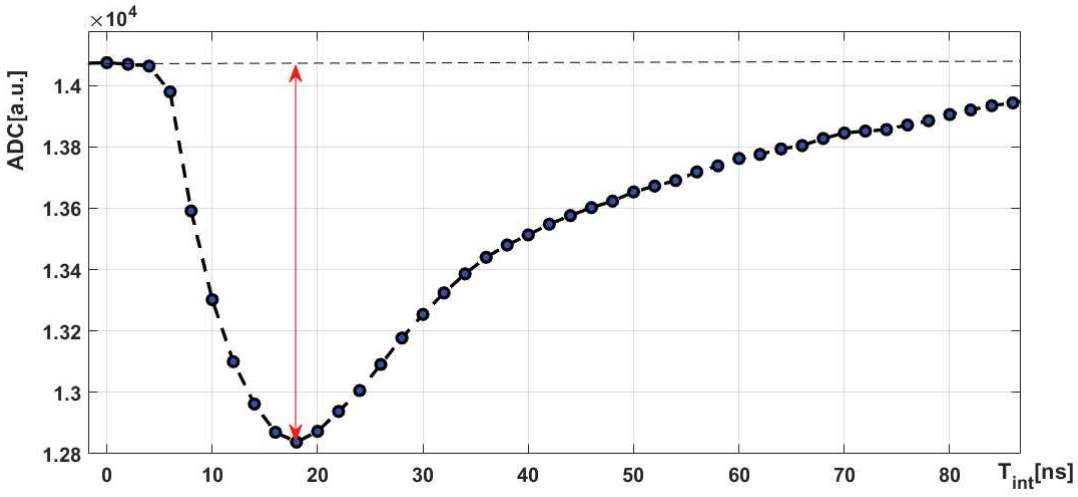

Fig. 2.30: A single-shot detector signal, acquired with the peak-and-hold circuit, is indicated as a black dashed curve, joining the sampled points (blue dots). The red arrow indicates that in this case the height of the peak was extracted shot-by-shot.

where τ_{dct} is the specific time constant for a OCT-D event. Then, the infinitesimal OCT-D probability reads

$$\mathrm{dP} = \mathrm{p}(t)\mathrm{dt} \tag{2.26}$$

which, integrated over a given gate T, yields

$$\mathrm{P}(T) = 1 - \exp\left(-\frac{T}{\tau_{\mathrm{dct}}}\right). \tag{2.27}$$

Equation (2.27) gives the probability of integrating an OCT-D signal when a light event is integrated over a gate T. If we want to describe the probability that a generic OCT pulse affects the integration of a single detected-light waveform, we have also to consider the probability ε_0 that secondary photons trigger an avalanche in a neighbour cell, i.e. an OCT-P event, and the probability that secondary photons effectively reach farther cells $\varepsilon_{\mathrm{dct}}$. Then, we are left with the following OCT probability

$$\varepsilon(T) = \varepsilon_0 + \varepsilon_{\mathrm{dct}}\left[1 - \exp\left(-\frac{T}{\tau_{\mathrm{dct}}}\right)\right] \tag{2.28}$$

since the OCT-P events are generally not correlated with the OCT-D events. This last assumption is not true only if the latter are generated by the former, but the probability of an OCT-D signal generated by an OCT-P signal is negligible compared to ε_0 and $\varepsilon_{\mathrm{dct}}(T)$. The same can be extended to OCT-D signals generated by OCT-D signals. However, we are not allowed to keep such assumptions for OCT-D events triggered by dark counts, especially if the gate is longer than the detected-light signal ($T > 150$ ns). Therefore, they should be kept into account. By estimating the mean value of dark counts as $\langle m_{dc}\rangle \sim \nu_{dc} T$, where ν_{dc} is the dark-count rate, and indicating as ε_{dc} the generic probability that a dark-count photon triggers an OCT event, we find that the OCT probability over an integration gate T reads

$$\varepsilon(T) = \varepsilon_0 + \varepsilon_{\mathrm{dct}}\left[1 - \exp\left(-\frac{T}{\tau_{\mathrm{dct}}}\right)\right] + \varepsilon_{dc}\nu_{dc}T. \tag{2.29}$$

We experimentally tested this simple model by counting the OCT events in a set of data acquired in the case of coherent light with mean photon number ~ 1.2. In Fig. 2.31 we plotted our experimental data. We see that they are superimposed to Eq. (2.29) with the following fitting parameters: $\varepsilon_0 = 0.016 \pm 0.005$, $\varepsilon_{dct} = 0.022 \pm 005$, $\tau_{dct} = (31 \pm 5)$ ns, $\varepsilon_{dc} = 0.038 \pm 0.007$ and $\nu_{dc} = (562 \pm 49)$ kHz. Note that by integrating over a 350-ns gate we retrieve the expected cross-talk probability for these detectors $\varepsilon(350\text{ns}) \sim 0.045$. Both the overall OCT probability and the dark-count rate are compatible with the typical values given by the manufacturer and with our measurements, reported in Tab. (2.1).

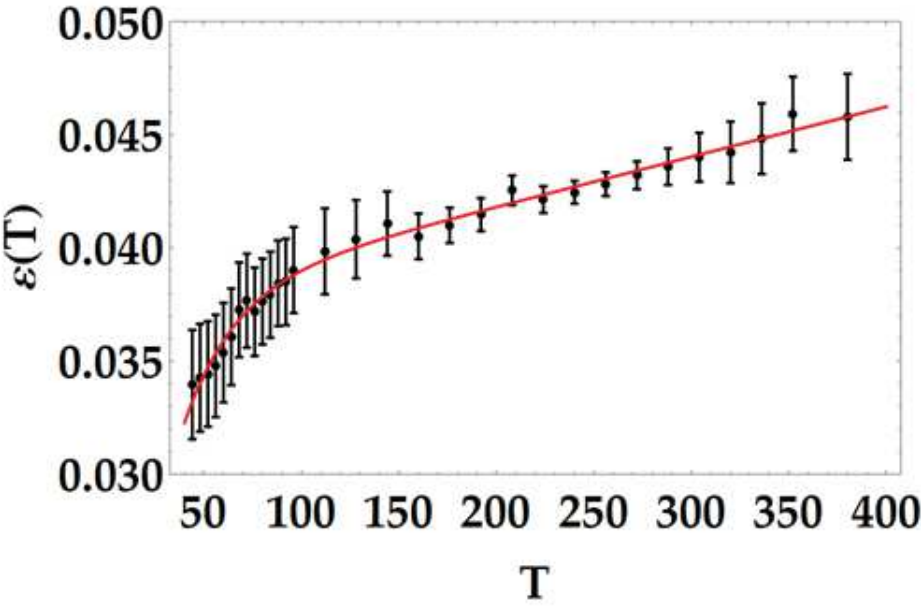

Fig. 2.31: Cross-talk probability as a function of the length of the gate for detected-photon mean value ~ 1.2. Dots: experimental data; red curve: theoretical fit from Eq. (2.29).

2.4.3 Results

Fano factor

As we recalled in the first chapter, the Fano factor can be used to assess a sufficient but not necessary condition for nonclassicality. For the same reason, it is also a necessary and sufficient criterion to discriminate between Poissonian and super-Poissonian statistics. In this sense, the first and second moments of a given light distribution are the simplest parameter that we need to check the reliability of SiPMs in characterizing states of light. From the model of light detection described above, we find that the Fano factor is a linear function of the detected-photon mean value $\langle x_{out} \rangle$, i.e. [81]

$$F(x_{out}) \equiv \frac{\langle \Delta x_{out}^2 \rangle}{\langle x_{out} \rangle} = \frac{Q(\tilde{m})}{\langle \tilde{m} \rangle} \langle x_{out} \rangle + \gamma \frac{1+3\varepsilon}{1+\varepsilon} \tag{2.30}$$

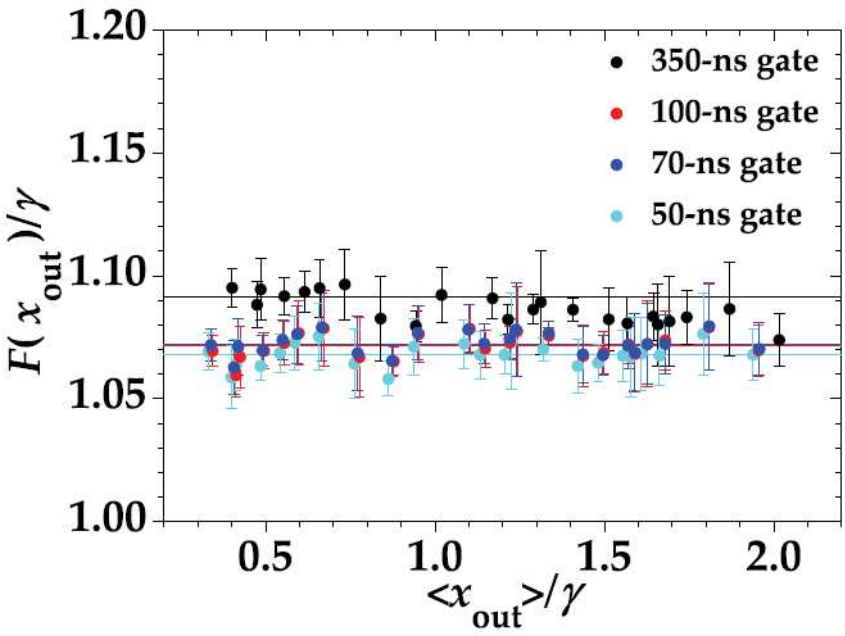

Fig. 2.32: Fano factor for Poissonian statistics as a function of the mean output. Different colors are related to different integration-gate widths: black to 350-ns gate, red to 100-ns gate, blue to 70-ns gate, and cyan to 50-ns gate. Dots: experimental data; lines: fitting linear curves, where ε is the only fitting parameter.

where $Q(\tilde{m}) \equiv F(\tilde{m}) - 1$ is the Mandel factor [85] for the detected photons.
In the case of a Poissonian photon-number distribution, we have $\langle \Delta n^2 \rangle = \langle n \rangle$, implying that

$$\begin{aligned} F(\tilde{m}) &\equiv \frac{\langle \Delta \tilde{m}^2 \rangle}{\langle \tilde{m} \rangle} = \\ &= \frac{\langle \Delta m^2 \rangle + \langle m_{dc} \rangle}{\langle m \rangle + \langle m_{dc} \rangle} = \\ &= \frac{\eta^2 \langle \Delta n^2 \rangle + \eta(1-\eta)\langle n \rangle + \langle \tilde{m}_{dc} \rangle}{\eta \langle n \rangle + \langle \tilde{m}_{dc} \rangle} = \\ &= \frac{\eta^2 \langle n \rangle + \eta(1-\eta)\langle n \rangle + \langle \tilde{m}_{dc} \rangle}{\eta \langle n \rangle + \langle \tilde{m}_{dc} \rangle} = \\ &= 1 \end{aligned}$$

so that $Q(\tilde{m}) = 0$ and the Fano factor in Eq. (2.30) reads

$$F(x_{out}) = \gamma \frac{1+3\varepsilon}{1+\varepsilon} \tag{2.31}$$

i.e. constant with respect to the output signal. We show in Fig. (2.32) the Fano factors retrieved from the first moments of the detected distributions. They are plotted as functions of the mean value of the output and fitted with Eq. (2.31), where ε is the only fitting parameter while γ is fixed. In particular, the value of γ is estimated independently, since it is proportional to the peak-to-peak distance in the pulse-height-spectrum and thus, by modeling each peak of the histogram with a Gaussian distribution (see [81]), it is easily determined. All the data presented in the figure are derived by the same dataset, acquired

and post-processed as previously explained. The different colors correspond to different integration gates, as outlined in the caption. The retrieved fitting parameters are shown in Table (2.2). Note that the constant behavior predicted by Eq. (2.31) is well supported by the experimental data. Moreover, we see that the Fano factor value seems to increase with the gate width. Flagrant is the case of the 350-nm gate. However, having fixed γ, the Fano factor, according to this model, depends on the OCT probability only and, in particular, is a monotonous growing function of ε. We conclude that, as expected from the simple model outlined above, the OCT increases with the gate width. However, note that other factors could influence the output statistics, e.g. the stability of the source or the thermal gradient affecting the sensors. Moreover, the offline integration process itself may be affected by errors. This could be the reason why we see an anomalous trend for the estimated ε in Table (2.2) at $T = 70$ ns and 100 ns.

Gate Width [ns]	ε	CI(ε)	χ^2_ν
350	0.0480	(0.0467, 0.0494)	2.34
100	0.0370	(0.0356,0.0383)	0.68
70	0.0374	(0.0359, 0.0390)	0.60
50	0.0351	(0.0336, 0.0366)	0.75

Tab. 2.2: The values of the fitting parameter ε in Eq. (2.31) for different choices of the gate width are listed in the case of coherent light. The symbol CI indicates the 95% confidence interval, whereas in the last column χ^2_ν stands for the χ^2 per degree of freedom.

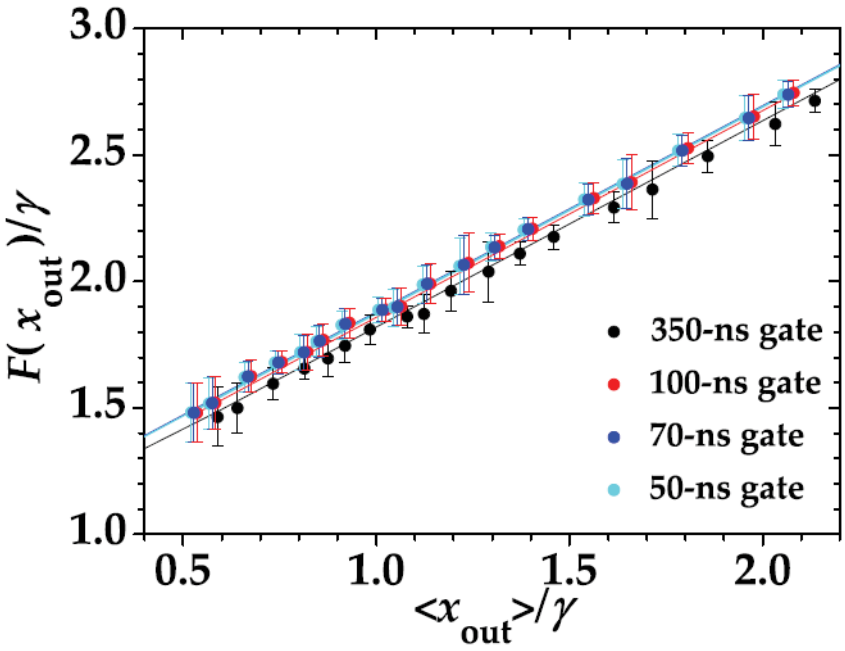

Fig. 2.33: Fano factor for multi-mode thermal statistics as a function of the mean output. Different colors are related to different integration-gate widths: black to 350-ns gate, red to 100-ns gate, blue to 70-ns gate and cyan to 50-ns gate. Dots: experimental data; lines: fitting curves where the fitting parameters are $\langle x_{dc} \rangle$ and μ. The OCT probability ε is fixed from the plots in Fig. (2.32).

In the case of pseudo-thermal light, the distribution is multi-mode, with μ equally populated modes.

For this radiation field, the Fano factor reduces to [81]

$$F(x_{out}) = \frac{1}{\mu}\left(1 - \frac{\langle x_{dc}\rangle}{\langle x_{out}\rangle}\right)^2 \langle x_{out}\rangle + \gamma\frac{1+3\varepsilon}{1+\varepsilon} \tag{2.32}$$

where $\langle x_{dc}\rangle \equiv \gamma\langle m_{dc}\rangle$ is the mean dark-count photon number. Note that in this case the Fano factor is a rational polynomial function of the output mean value whose minimum is given by the Fano factor for coherent input light in Eq. (2.31). We used Eq. (2.32) to fit the experimental data plotted in Fig. (2.33). Again, the amplification factor γ was retrieved independently with the same method as before. Here we

Gate Width [ns]	$\langle x_{dc}\rangle$	CI($\langle x_{dc}\rangle$)	DCR[kHz]	μ	CI(μ)
350	0.0563	(0.0544, 0.0582)	161±11	1.2234	(1.2225, 1.2243)
100	0.0187	(0.0168, 0.0206)	187±38	1.2234	(1.2225, 1.2243)
70	0.0086	(0.0065, 0.0107)	123±60	1.2234	(1.2225, 1.2243)
50	0.0080	(0.0078, 0.0082)	160±8	1.2234	(1.2225, 1.2243)

Tab. 2.3: The values of the fitting parameter $\langle x_{dc}\rangle$ in Eq. (2.32) for different choices of the gate width are listed in the case of multi-mode thermal light. The symbol CI indicates the 95% confidence interval.

also fixed the OCT probability ε by using for each choice of the gate width (50 ns, 70 ns, 100 ns, and 350 ns) the values obtained for coherent light. Moreover, given that the different sets of data share the same parameters μ and $\langle x_{out}\rangle$, for each gate width we performed a common fitting procedure, i.e. we fixed $\chi^2_\nu = 1$ and assumed a linear scaling of the mean value of dark counts with the gate width. Finally, being the detected light the same for every choice of the gates, we assumed that they shared the same number of modes. Our results are listed in Table (2.3). As we can infer from the plot in Fig. 2.33, smaller Fano factors correspond to larger integration gates at fixed $\langle x_{out}\rangle$. However, by inspecting Eq. (2.32) we see that we are not allowed to guess that a smaller OCT probability follows, as in the previous case, because only the minimum of $F(x_{out})$ depends on ε. For $\langle x_{out}\rangle > \langle x_{dc}\rangle$ the growth of the function is determined by the mean value of dark counts $\langle x_{dc}\rangle$ which, in particular, reduces the Fano factor. We could say that it suppresses the thermal autocorrelations. As confirmed by the values in Table (2.3) and as one could expect, the mean values of dark counts $\langle x_{dc}\rangle$ are higher for larger gate widths as the integration is likely to collect more dark-count pulses.

Statistics

Now we deal with the reconstruction of the whole photon-number distribution of the input radiation fields, which is of course more informative than its first two moments. Furthermore, the knowledge of the detected-light statistics is all one needs in many applications, such as some cases of state-preparation for Quantum Key Distribution [86] and Quantum Metrology [87]. Having noted that reducing the integration gate width seems promising for the rejection of spurious events, here we consider a 100-ns and a 50-ns gate. We have now reached the first crucial point of this analysis: if the detected-light statistics will be reconstructed in accordance with the theoretical prediction despite having integrated over small gates, we will have demonstrated a posteriori that the information collected by integrating the whole output waveform is preserved by signal peak-height, as explained above.
In the case of Poissonian light, the detected-photon-number statistics is shown in Fig. 2.34 on a logarithmic scale. The mean value of the measured light was roughly $\langle k\rangle = 1.3$ for both. The experimental data are shown as gray columns with black error bars, while the triangles and the dots are two different fitting theoretical curves. The blue triangles represent the photoelectron probability distribution in the absence of OCT $\mathrm{p}_{\tilde{\mathrm{m}}}$ in Eq. (2.18), where the photon-number distribution P_n is Poissonian (see Eq. (1.108) with $|\alpha|^2 = \langle n\rangle$), and $\mathrm{p}_{\tilde{\mathrm{m}}}$ is itself Poissonian since the convolution of Poissonian distributions is still Poissonian.

Thus

$$\mathrm{p}_{\tilde{m}}^{(\mathrm{coh})} = \frac{\langle \tilde{m} \rangle^{\tilde{m}}}{\tilde{m}!} e^{-\langle \tilde{m} \rangle} \tag{2.33}$$

where the superscript indicates the input photon-number statistics. The magenta dots provide the theoretical curve in the presence of OCT, which plots Eq. (2.20). If we replace there $\mathrm{P_n}$ with the Poissonian photon-number distribution, we are left with the following expression [81]

$$\mathrm{p}_{\mathrm{k}}^{(\mathrm{coh})} = e^{-\langle \tilde{m} \rangle}(1-\varepsilon^{-k})\varepsilon^{k}\,\mathrm{sinc}(k\pi)\,{}_2F_2\left(1,-k;\frac{1-k}{2},\frac{2-k}{2};-\frac{1-\varepsilon^2\langle \tilde{m} \rangle}{4\varepsilon}\right) \tag{2.34}$$

where ${}_pF_q(a_1,...,a_p;b_1,...,b_q;x) \equiv \sum_{k=0}^{\infty} c_k x^k$ is the generalized hypergeometric function, which means that the ratio between consecutive coefficients of the series are given by the ratio between polynomial functions of k. Again, the values of the OCT probability were fixed from the results in Table (2.2). By a quick comparison of the parameter χ_ν^2 estimating the fit in the caption of Fig. 2.34, it is immediate to see that the model including the OCT effect better reproduces the experimental data. Moreover, a comparison between the two panels reveals that the different choice for the integration gate does not appreciably affect the reconstructed statistics.

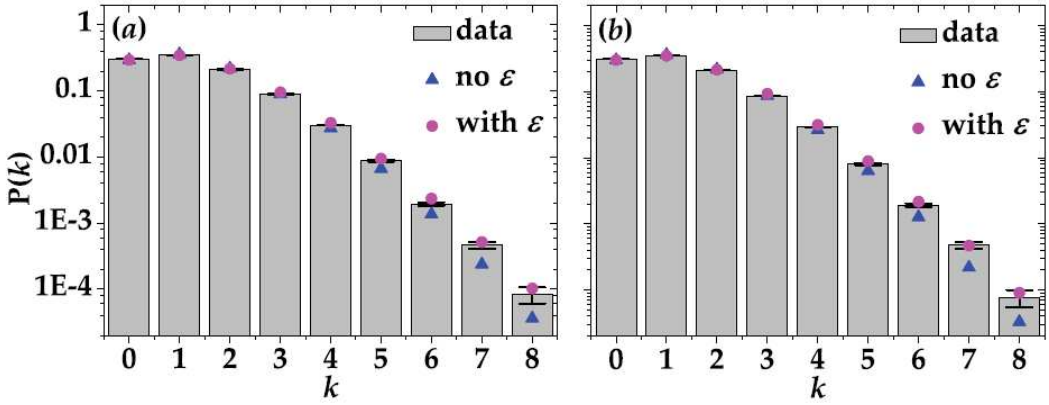

Fig. 2.34: Reconstructed photon-number distribution $P(k)$ in the case of coherent light for two choices of the gates: 100 ns in panel (a) and 50 ns in panel (b). Gray columns + black error bars: experimental data; magenta dots: theoretical fitting curves from the model comprehensive of OCT in Eq. (2.20); blue triangles: theoretical curves in the absence of cross talk (Eq. (2.18)). The values of the χ_ν^2 factor are respectively 34.47 and 28.02 in the absence of OCT and 25.19 and 23.07 in the presence of OCT.

Again, we repeated the same analysis for multi-mode thermal light. The detected-photon-number distribution $P(k)$ was plotted in Fig. 2.35 with $\langle k \rangle = 1.3$ for both the choices of gate width. The model in the absence of OCT (blue triangles) is given by Eq. (2.18) in which the photon-number distribution P_n is multi-mode thermal (see Eq. (1.114)) with $N = \langle n \rangle$. As in the previous case, the effect of losses is a rescaling of the mean value, while the convolution with the dark-count Poissonian statistics just shifts the mean value and the variance of a quantity $\langle m_{dc} \rangle$. The output statistics is the convolution of multi-mode thermal and a Poissonian distribution. In the presence of OCT (magenta dots), the detected-photon-number distribution is more complicated. By inspecting Eq. (2.20), one finds [81]

$$\mathrm{p}_{\mathrm{k}}^{(\mathrm{th})} = e^{k}(1-\varepsilon^{-k})\left(1+\frac{\langle \tilde{m} \rangle}{\mu(\varepsilon+1)}\right)^{-\mu}{}_3F_2\left(1,-k,\mu;\frac{1-k}{2},\frac{2-k}{2};\frac{(\varepsilon-1)^2\langle \tilde{m} \rangle}{4\varepsilon[\mu(\varepsilon+1)+\langle \tilde{m} \rangle]}\right). \tag{2.35}$$

Note that the magenta dots in Fig. 2.35 plot Eq. (2.35) in the absence of dark counts, i.e. we replaced $\tilde{m}$ with m. We decided to neglect this contribution as the values of $\langle x_{dc}\rangle$ retrieved in Table (2.3) are small compared to $\langle x_{out}\rangle$.

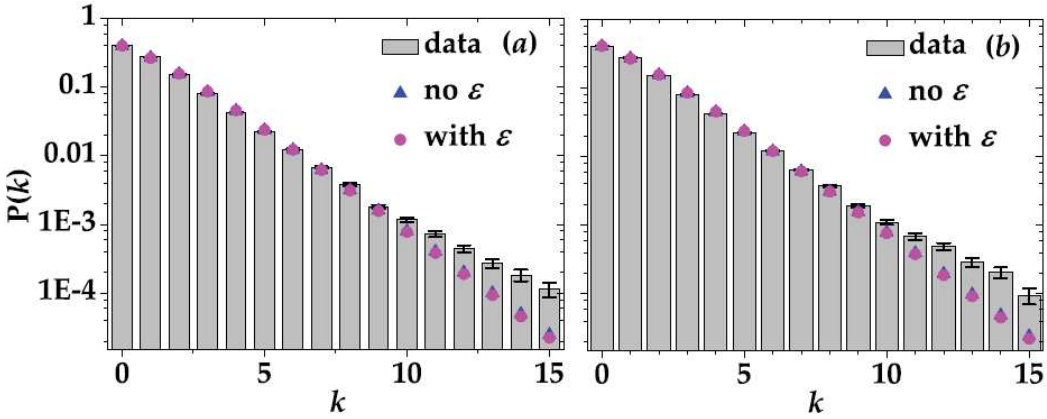

Fig. 2.35: Reconstructed photon-number distribution $P(k)$ in the case of multi-mode thermal light for two choices of the gates: 100 ns in panel (a) and 50 ns in panel (b). Gray columns + black error bars: experimental data; magenta dots: theoretical fitting curves from the model comprehensive of OCT in Eq. (2.20); blue triangles: theoretical curves in the absence of cross talk (Eq. (2.18)). In the presence of OCT effect, the values of the number of modes are respectively $\mu = 1.5148 \pm 0.5387$ and $\mu = 1.4790 \pm 0.5201$, while the corresponding χ^2_ν per degree of freedom is 14.24 in (a) and 14.79 in (b). In the absence of OCT, we found $\mu = 1.3972 \pm 0.0113$ in panel (a) and $\mu = 1.3733 \pm 0.0113$ in panel (b), while the corresponding χ^2_ν per degree of freedom is 10.85 in (a) and 11.91 in (b). The contribution of dark counts in the theoretical fitting curves was here neglected.

The results in Fig. 2.35 deserve at least two important comments. Firstly, we remark that the difference between the two models in this case seems negligible and the impression is confirmed by the inspection of the χ^2_ν factors (see the caption of the figure). This is due to the very nature of the thermal distribution and of the OCT as correlated noise. The probability that an m-detected-photons pulse produces s OCT events is binomial, i.e.

$$\mathrm{p_{oct}}(s|m) = \binom{m}{s}\varepsilon^s(1-\varepsilon)^{m-s} = \binom{m}{s}\left(\frac{\varepsilon}{1-\varepsilon}\right)^s(1-\varepsilon)^m. \tag{2.36}$$

For what concerns our detected-photon range ($m \leq 15$) and the typical values of ε ($< 1-\varepsilon$), the conditional probabilities $\mathrm{p_{oct}}(s > 1|m)$ are all negligible with respect to $\mathrm{p_{oct}}(s = 1|m) = m\varepsilon(1-\varepsilon)^{m-1}$. This function of m is monotonous and growing up to $m_{\max} = -\ln^{-1}(1-\varepsilon)$. Thus, if we assume $\varepsilon < 0.04$ (see Table (2.2) keeping in mind which gate widths we are considering here), then the stationary point is attained for $m_{\max} = 24$ detected photons, i.e. far from the explored range. For $s > 1$, it is easy to see that $m_{\max}$ is even higher. Therefore, up to $m = 15$, the probability of triggering a secondary avalanche is surely a monotonous growing function of m. However, a multi-mode thermal distribution with a small number of modes (here $\mu < 2$, see the caption of the figure) has the maximum around the 0-peak, while the height of the subsequent peaks drops quasi-exponentially. Thus, the OCT and the thermal distributions have an opposite growth with respect to m. In other words, an OCT event is most likely to be detected when the probability for the same event to be triggered is almost negligible. A thermal distribution kills the OCT at the utmost of its power. This is why the difference between the two models in this case is damped.
A second comment concerns the quality of the fit. Apparently the peaks corresponding to the largest detected-photon numbers are not matched by the theory. Notwithstanding, this is an illusion due to the logarithmic scale. Indeed, for the same reason, we see that the error bars seem to grow with k, too. On the

contrary, the absolute values are similar and almost negligible ($\sim 10^{-4}$).
Therefore, we can conclude again that the reduction of the integration-gate width has not affected the reconstruction of the statistics. On the other hand, due to the effect described above, here it is not possible to see a corresponding reduction of OCT.

Cross-correlations

The determination of the cross-correlations between the two parties of bipartite systems can highlight the fluctuations of photon numbers far beyond the direct reconstruction of the photon-number distribution. It should be enough to recall that in the Introduction we discriminated between thermal and super-thermal statistics by means of a cross correlation-coefficient C_{SH} (Eq. (1.58)) following [27]. Moreover, there are many and important applications based on correlations, such as imaging [88, 89] and generation of conditional states [90, 91].
Here we want to test the capability of SiPMs in properly revealing the presence of classical cross-correlations. The super-Poissonian light we employ is a pseudo-thermal field divided at a balanced beam splitter. Again, we compare the results from different choices of the integration gate. We use as a figure of merit the cross-correlation factor defined in Eq. (1.164). In the case of an input multi-mode thermal distribution, the expression of the cross-correlation coefficient for detected photons reduces to [41, 42]

$$\Gamma = \left[\left(1 + \frac{\mu_1}{\langle m_1 \rangle} \right) \left(1 + \frac{\mu_2}{\langle m_2 \rangle} \right) \right]^{-\frac{1}{2}} . \tag{2.37}$$

Equation (2.37) is retrieved in the absence of OCT. By exploiting the previously outlined model for photodetection, in particular Eq. (2.21), we can express the correlation parameter as a function of k_1 and k_2, the numbers of detected photons affected by dark counts and OCT, i.e. our experimental data. This operation yields

$$\Gamma = \left[\left(1 + \frac{(1+\varepsilon_1)\mu_1}{\langle k_1 \rangle - (1+\varepsilon_1)\langle m_{dc,1} \rangle} \right) \left(1 + \frac{(1+\varepsilon_2)\mu_2}{\langle k_2 \rangle - (1+\varepsilon_2)\langle m_{dc,2} \rangle} \right) \right]^{-\frac{1}{2}} . \tag{2.38}$$

We used this model to fit the reconstructed shot-by-shot correlation coefficient in Fig. 2.36. Again, the chosen integration-gate width were 350 ns (black dots), 100 ns (red dots), 70 ns (blue dots), and 50 ns (cyan dots). We proved above that the information on the detected-photon number is collected by the peak-height as well as by the integral of the whole signal waveform. Therefore, the only effect of a long integration gate is a noisier measurement. Provided this, it is immediately evident from the plot that OCT and dark counts decrease the amount of cross-correlation, which is reasonable because such effects independently occur in the two detectors. Note that the OCT probability and the mean value of dark counts were fixed from Tables (2.2) and (2.3). Thus, the only fitting parameter was the number of modes μ, which was assumed to be the same for the two outputs of the beam splitter. Our results are listed in Table (2.4). Actually, the number of modes does not depend on the integration gate, and this is why in the analysis of the Fano factor we determined it once for all by setting $\chi^2_\nu = 1$. Here we employed a different procedure which allows to have a glance on the quality of the fits. Note that the best fit is reached in the case $T = 50$ ns, where the estimated value of μ is comparable to the one found in Table (2.3). Moreover, we remark that the latter is contained in the confidence interval of the former.

Acquisition with the peak-and-hold circuit

Motivated by the results described in the previous sections, we employed the low-noise shaping amplifier mentioned above and sampled the output signal peaks with the faster digitizer. Such a system is effectively a primitive peak-and-hold circuit. Note that in principle this system not only allows to get rid of every

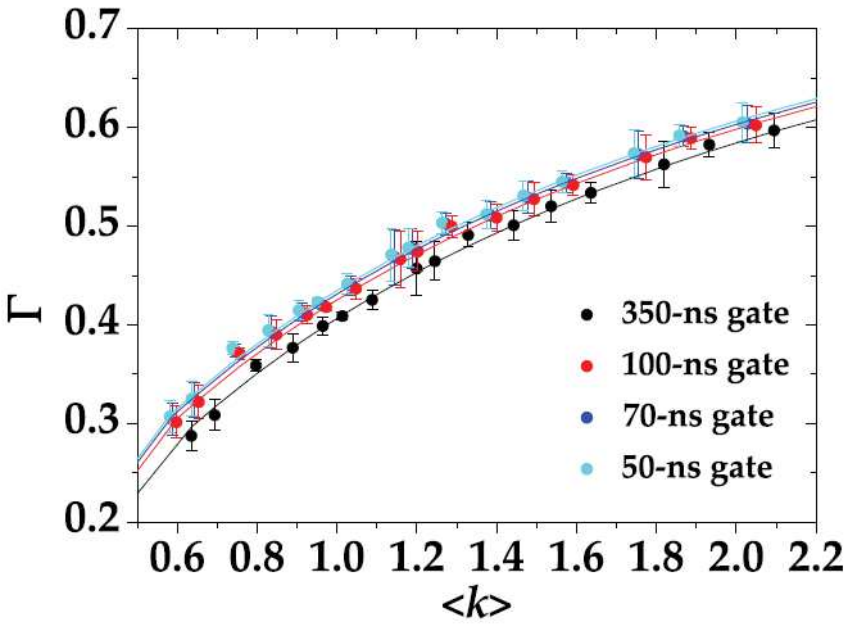

Fig. 2.36: Experimental correlation coefficient Γ (dots + error bars) as a function of the mean detected-photon number $\langle k \rangle$ for pseudo-thermal light fitted by Eq. (2.38) (lines). Different colors are related to different gate widths, namely 350 ns (black), 100 ns (red), 70 ns (blue), and 50 ns (cyan). The fitting parameter is the number of modes μ, while ε is fixed from the values in Table (2.2) and $\langle m_{dc} \rangle$ from the values in Table (2.3). The values of fitting parameter obtained in the four cases are shown in Table (2.4).

Gate Width [ns]	μ	CI(μ)	χ^2_v
350	1.3015	(1.2876, 1.3154)	0.28
100	1.2647	(1.2543, 1.2750)	0.34
70	1.2473	(1.2370, 1.2576)	0.30
50	1.2331	(1.2230, 1.2432)	0.38

Tab. 2.4: Values of the fitting parameter μ for the correlation coefficient as a function of the gate width in the case of multi-mode thermal light. The symbol CI indicates the 95% confidence interval.

source of delayed noise, but also overcomes an issue intrinsic to the choice of a short gate, which is the accurate control of temporal delays in the delicate setting of the gate.
A pulse-height-spectrum obtained by means of this system for coherent input light is shown in Fig. 2.37. Note that, thanks to our full digital peak capture procedure, the resulting resolving power is consistently enhanced. It is worth noting that, at variance with the pulse-height spectra obtained from the integration of the digitized signals in Fig. 2.28, the peak corresponding to 0 photons in Fig. 2.37 is asymmetric and its distance from the 1-photon peak is different from the peak-to-peak distance of the spectrum. The reason for this bias is due to our specific analysis procedure, consisting in evaluating shot-by-shot the peak-height. Since the maximum of the signal is calculated also in the absence of light, the 0-photon peak is not centered in 0, but rather translated.

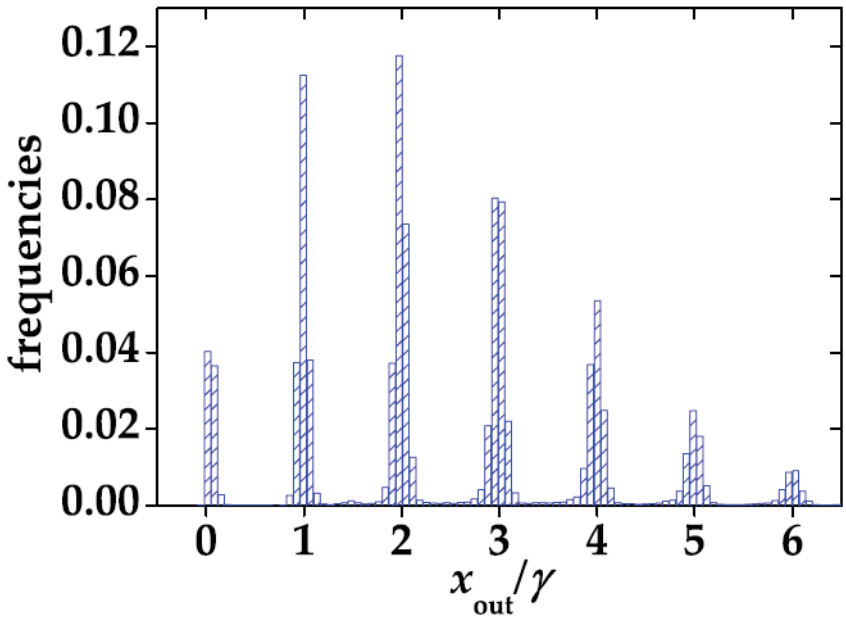

Fig. 2.37: Normalized pulse-height spectrum related to a Poissonian distribution with $\langle k \rangle = 2.56$, obtained by means of the peak-and-hold acquisition system.

The S/N related to Fig. 2.37 is calculated as the ratio between the mean value of the 1-photon peak and its width. In particular, its value is 13 ± 1.2. We see from Fig. 2.27 that there is a range of integration gates having larger S/N values. This is probably due to the fact that the acquisition of the peak-height is more sensitive to the sampling noise than the integral of the waveform. Indeed, in the latter case the errors caused by the digitization of the signal are averaged in the integration, which cannot happen in a procedure where the maximum among a small number of points has to be selected. However, the peak-and-hold circuit allows for a better reconstruction of the statistical properties since the stochastic effects are essentially negligible. On the contrary, in the case of an integration over a specific gate width we have shown that such effects play an important role, modifying the statistical properties of the detected light. In Fig. 2.38 we plotted the detected-photon-number distribution for Poissonian light with different mean values. The result is remarkable because the theoretical model (blue triangles) which reproduces, with high fidelity, the experimental data is the cross-talk- and dark-count-free detected-photon-number distribution. Therefore, this reconstructed distribution does not require the inclusion of the most detrimental non-idealities to match the theoretical expectations. Such a configuration and such results encouraged us to exploit this new

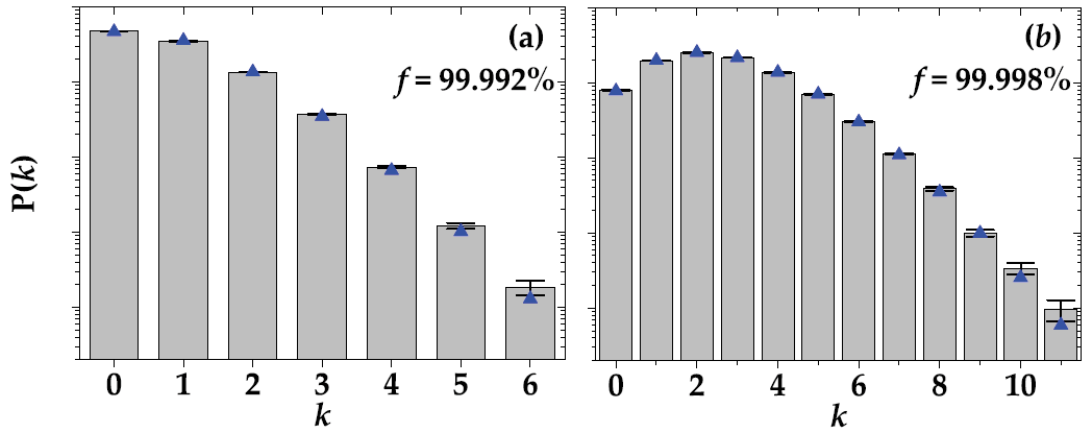

Fig. 2.38: Reconstructed distributions $P(k)$ in the case of coherent light acquired with the peak-and-hold circuit. (a) Coherent light with $\langle k \rangle = 0.76$. (b) Coherent light with $\langle k \rangle = 2.56$. Gray columns + black error bars: experimental data; blue triangles: theoretical curves in the absence of cross talk. The corresponding χ^2_ν per degree of freedom is 8.31 in (a) and 1.33 in (b).

generation of SiPMs in the Quantum Optics context.

3

Detection of nonclassical states of light with Silicon Photomultipliers

Having assessed the performance of the new generation of SiPMs for what concerns the reconstruction of the detected-photon-number distribution and of shot-by-shot correlations and having elaborated an optimization strategy to reduce their main drawbacks, we tested these devices on the detection of non-classical states of light [95]. In particular, we focused on multi-mode TWB states in the mesoscopic regime (see the first chapter for details). Firstly, we determine the analytic expression of the NRF in the presence of OCT spurious events. Then, we employ this model to fit the experimental data. Moreover, we performed conditional measurements and analyzed the nonclassicality of the conditional states in terms of the detected-photon number. We succeeded in revealing the entanglement and the wave-function collapse, proving that these devices, despite their severe non-idealities, can be employed for Quantum Optics applications.

3.1 Experimental setup

As mentioned above, here we investigate the reconstruction of the nonclassical properties of TWB states generated via type-I PDC in quasi-collinear interaction geometry. The experimental setup is shown in Fig. 3.1. The pumping field is the fourth harmonics of a Nd:YLF laser (4.5-ps pulse duration and 500-Hz repetition rate), while the nonlinear material was a β-barium-borate (BBO) crystal (BBO2, cut angle = 46.7 deg, 6 mm long). The generated TWB state was intrinsically multi-mode [39, 51]. Thus, the photon-number statistics of each of the two parties was described by a multi-mode thermal distribution. Two portions of the light-cone around frequency degeneracy (523 nm) were spatially and spectrally filtered by means of two variable irises and two bandpass filters and then delivered to the sensors via two multi-mode optical fibers (600-μm core diameter). The effective number of independent thermal modes was larger than 100 [39], so that the photon statistics closely resembled a Poissonian distribution. As for the characterization of classical states, we performed measurements of the input intensity, which was modified through a half-wave plate (HWP) followed by a PBS. For each energy value, 10^5 single shots were acquired by our SiPMs.
For what concerns the data acquisition system, we tested three different schemes. In particular, we compared the procedure explained in the previous Section, consisting in signal sampling and offline integration, with an analogical shot-by-shot integration (see Fig. 3.1). We decided to try also this latter strategy because the integration over short gates (< 50 ns) of digitized pulses is deeply affected by sampling

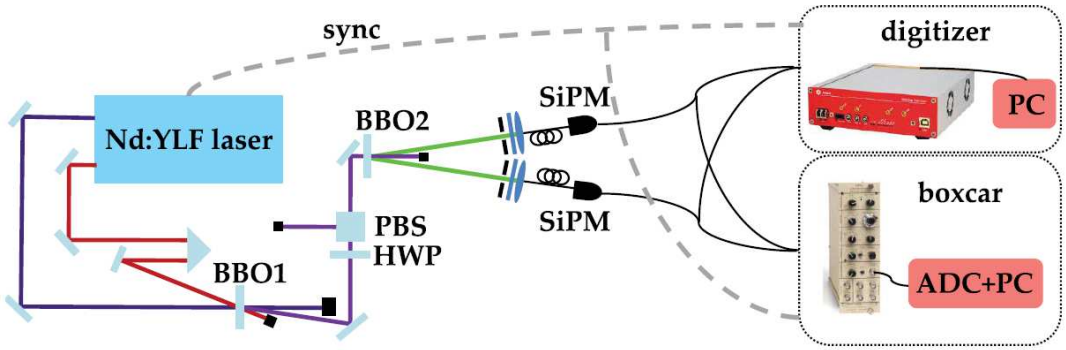

Fig. 3.1: Experimental setup for the measurement of multi-mode TWB states with SiPMs.

noise. Indeed, the digitizer DT5720 records one point every 4 ns and a section of the output waveform reconstructed from too few points is not reliable. Therefore, we used an analogical acquisition to fairly integrate over very short gates (down to 10 ns). This technique was finally compared with the results of the digital peak-and-hold system described above.
The analogic integration was performed with two synchronous boxcar-gated integrators (Stanford Research Systems SR250 [76]). They are high-speed NIM modules able to recover fast analog signals. An internal gate generator allows to set an integration interval, whose width can be chosen in the interval (2 ns - 15 μs). The delay with respect to the trigger is adjustable as well between few nanoseconds and 100 ms. Gates of variable widths were selected in advance and centered on the signal peak. The benchmark gate we used to compare the two different approaches was the shortest useful gate for the digitalization system, i.e. 50 ns.

3.2 Further noise contributions to the noise reduction factor

3.2.1 Quantum efficiency imbalance

We have outlined in the first chapter that one of the major issues in employing the variance of the difference photocurrent as an entanglement estimator is the imbalance of the quantum efficiency of the two detectors, which sets a threshold on the number of photons among which nonclassical correlations can be revealed (Eq 1.167). However, by analyzing the NRF to vary the input light intensity, it is easy to see if our measurements are affected by this problem and possibly estimate the difference between the quantum efficiencies. Starting from Eq. (1.180), we can express our estimator of nonclassicality as a function of the mean photon-number, i.e.

$$R = 1 - 2\frac{\eta_1\eta_2}{\eta_1+\eta_2} + \frac{(\eta_1-\eta_2)^2}{\eta_1+\eta_2}\langle n\rangle \tag{3.1}$$

which now can be rewritten as a function of a single experimental variable as $\Sigma \equiv \langle m_1 + m_2\rangle/2$, so that

$$R = 1 - 2\frac{\eta_1\eta_2}{\eta_1+\eta_2} + 2\left(\frac{\eta_1-\eta_2}{\eta_1+\eta_2}\right)^2\Sigma. \tag{3.2}$$

Thus, if the contribution of $\Delta\eta$ were relevant, we would expect to find a linear growth of $R(\Sigma)$. This is not the case. As shown in Fig. 3.2, for large mean detected-photon numbers the noise reduction factor tends to an horizontal asymptotic value. This evidence validates R as a reliable estimator for the nonclassical correlations and allows us to assume $\eta_1 \sim \eta_2 \equiv \eta$. Therefore, the inferior bound in the nonclassicality criterion based on the NRF is $1-\eta$.

3.2.2 Optical cross-talk

If we can neglect the imbalance between the quantum efficiencies, surely, accordingly with the results of our characterization, we cannot do the same for the OCT. As far as we know, a model for the difference photocurrent operator $\hat{D}$ in the presence of OCT is still missing, but it can be directly derived in analogy with the photodetection model presented in the Introduction. The POVM describing the losses in Eq. (1.158) can be generalized to account for dark counts and cross-talk as follows

$$\begin{aligned}\hat{\Pi}_{\eta,\langle m_{dc}\rangle,\varepsilon}(k) = &\sum_{\tilde{m}=0}^{k}\binom{\tilde{m}}{k-\tilde{m}}\varepsilon^{k-\tilde{m}}(1-\varepsilon)^{2\tilde{m}-k}\\ &\sum_{m=0}^{\tilde{m}}\eta^m\sum_{n=m}^{\infty}\binom{n}{m}(1-\eta)^{n-m}\frac{\langle m_{dc}\rangle^{\tilde{m}-m}}{(\tilde{m}-m)!}\exp(-\langle m_{dc}\rangle)|n\rangle\langle n|.\end{aligned} \tag{3.3}$$

Note that by computing $\mathrm{Tr}[\hat{\rho}\hat{\Pi}_{\eta,\langle m_{dc}\rangle,\varepsilon}(k)]$ for a given state $\hat{\rho}$ with photon-number distribution P_n, one gets the detected-photon-number distribution in Eq. (2.20). In the next intermediate results, we will neglect dark counts to highlight the effect of the OCT and the relation with the primitive form of the NRF in Eq. (1.180), but we will re-introduce it in the final equation. As expected from the moments of the detected-photon number retrieved above, we get

$$\begin{aligned}\hat{k} &= (1+\varepsilon)\eta\hat{n}\\ \widehat{k^2} &= (1+\varepsilon)^2[\eta^2\hat{n}^2+\eta(1-\eta)\hat{n}]+\varepsilon(1-\varepsilon)\eta\hat{n}.\end{aligned} \tag{3.4}$$

Here we are interested in the moments of the photocurrent difference. Given the POVM for a single detector, the generalization of Eq. (1.165) is straightforward, i.e.

$$\hat{\Theta}(d) = \sum_{m=0}^{\infty}\begin{cases}\hat{\Pi}_{\eta_1,\langle m_{dc,1}\rangle,\varepsilon_1}(k)\otimes\hat{\Pi}_{\eta_2,\langle m_{dc,2}\rangle,\varepsilon_2}(k+d) & d>0\\ \hat{\Pi}_{\eta_1,\langle m_{dc,1}\rangle,\varepsilon_1}(k)\otimes\hat{\Pi}_{\eta_2,\langle m_{dc,2}\rangle,\varepsilon_2}(k) & d=0\\ \hat{\Pi}_{\eta_1,\langle m_{dc,1}\rangle,\varepsilon_1}(k+d)\otimes\hat{\Pi}_{\eta_2,\langle m_{dc,2}\rangle,\varepsilon_2}(k) & d<0\end{cases} \tag{3.5}$$

and hence, for $\langle m_{dc}\rangle = 0$, we have

$$\begin{aligned}\hat{D} =&\hat{k}_1-\hat{k}_2\\ \widehat{D^2} =&\sum_{j=1}^{2}\{(1+\varepsilon_j)^2[\eta_j^2\hat{n}_j^2+\eta_j(1-\eta_j)\hat{n}_j]+\varepsilon_j(1-\varepsilon_j)\eta_j\hat{n}_j\}\\ &-2(1+\varepsilon_1)(1+\varepsilon_2)\eta_1\eta_2\langle\hat{n}_1\hat{n}_2\rangle.\end{aligned} \tag{3.6}$$

Now we are ready to compute the variance of the photocurrent difference $\langle\Delta\hat{D}^2\rangle \equiv \langle\widehat{D^2}\rangle - \langle\hat{D}\rangle^2$ normalized to the shot-noise $\langle\hat{k}_1+\hat{k}_2\rangle$ for a TWB state, thus generalizing Eq. (1.180)

$$R = 1+\frac{1}{\mu}\frac{(\langle k_1\rangle-\langle k_2\rangle)^2}{\langle k_1\rangle+\langle k_2\rangle}-2\sqrt{\eta_1\eta_2(1+\varepsilon_1)(1+\varepsilon_2)}\frac{\sqrt{\langle k_1\rangle\langle k_2\rangle}}{\langle k_1\rangle+\langle k_2\rangle}+\sum_{j=1}^{2}\frac{2\varepsilon_j}{1+\varepsilon_j}\frac{\langle k_j\rangle}{\langle k_1\rangle+\langle k_2\rangle}. \tag{3.7}$$

Note that the effect of the OCT consists in a reduction of the correlations, which is evident from the rescaling of the third term by a factor $\sqrt{(1+\varepsilon_1)(1+\varepsilon_2)}$, and in the widening of the photocurrent difference distribution by a term proportional to the mean detected-photon numbers. In the presence of dark counts,

Eq. (3.7) becomes

$$R = 1 + \frac{1}{\mu}\frac{(\langle k_1\rangle - \langle k_2\rangle)^2}{\langle k_1\rangle + \langle k_2\rangle} + \frac{2}{\langle k_1\rangle + \langle k_2\rangle}\left(\sum_{j=1}^{2}\frac{\varepsilon_j}{1+\varepsilon_j}\langle k_j\rangle - \sqrt{\prod_{j=1}^{2}(1+\varepsilon_j)\eta_j[\langle k_j\rangle - (1+\varepsilon_j)\langle m_{j,dc}\rangle]}\right) + \frac{1}{\mu}[(1+\varepsilon_1)\langle m_{1,dc}\rangle - (1+\varepsilon_2)\langle m_{2,dc}\rangle]\cdot\left[(1+\varepsilon_1)\langle m_{1,dc}\rangle - (1+\varepsilon_2)\langle m_{2,dc}\rangle - 2\frac{\langle k_1\rangle - \langle k_2\rangle}{\langle k_1\rangle + \langle k_2\rangle}\right]. \tag{3.8}$$

If $\langle m_{1,dc}\rangle = \langle m_{2,dc}\rangle = 0$ and $\varepsilon_1 = \varepsilon_2 = 0$, we find the expression retrieved in the first chapter and described in [39]. If instead $\langle m_{1,dc}\rangle = \langle m_{2,dc}\rangle = 0$, $\varepsilon_1 = \varepsilon_2 \equiv \varepsilon$ and $\eta_1 = \eta_2 \equiv \eta$, i.e. perfect balancing without dark counts, we find the model used in [96]. We will keep the perfect balancing assumption, having corroborated it above, but we will not neglect the dark-count contribution. Given that $\eta_1 = \eta_2 \equiv \eta$, $\varepsilon_1 = \varepsilon_2 \equiv \varepsilon$ and $\langle m_{1,dc}\rangle = \langle m_{2,dc}\rangle \equiv \langle m_{2,dc}\rangle$, Eq. 3.8 reduces to

$$R = 1 - \eta(1+\varepsilon)\left[1 - \frac{(1+\varepsilon)\langle m_{dc}\rangle}{\langle k\rangle}\right] + \frac{2\varepsilon}{1+\varepsilon} \tag{3.9}$$

where

$$\langle k\rangle \equiv \frac{\langle k_1\rangle + \langle k_2\rangle}{2}.$$

It is worth noting here that the photocurrent difference is broadened also by a term which does not depend on the mean detected-photon number, i.e. $\eta(1+\varepsilon)^2\langle m_{dc}\rangle$, related to the number of cross-talk events triggered by dark counts $(1+\varepsilon)\langle m_{dc}\rangle$. We have shown with the standard characterization that this quantity is negligible in the presence of light events, but as $\langle k\rangle \to 0$ it becomes relevant, to the extent that it can be used to estimate the OCT, as in Eq. (2.3). This contribution explains the divergent growth of the noise reduction factor for low-intensity measurements shown in Fig. (3.2), where we used Eq. (3.9) to interpolate the experimental data.

3.3 Results

3.3.1 Noise reduction factor

As anticipated above, we used the NRF as a test for the detection of the entanglement, being the sub-Poissonianity condition $R < 1$ sufficient for nonclassicality. The expression of this estimator in the presence of losses, dark counts and OCT is derived above (see Eq. (3.8)). Also, we have shown that our detectors can be assumed to be balanced, i.e. $\eta_1 = \eta_2$, $\langle m_{1,dc}\rangle = \langle m_{2,dc}\rangle$, $\varepsilon_1 = \varepsilon_2 \Rightarrow \langle k_1\rangle = \langle k_2\rangle$, so that the NRF can be safely rewritten as in Eq. (3.9). The measured values of R are plotted in Fig. (3.2) as a function of $\langle k\rangle \equiv (\langle k_1\rangle + \langle k_2\rangle)/2$. Different colors correspond to different gate widths. We remark that the procedure of shortening the gate is effective for the elimination of delayed noise, being the nonclassicality more pronounced for shorter gates. This result is consistent with the optimization strategy elaborated for the characterization of the detectors [77]. On the other hand, we note that, from the comparison between the digitizer and the boxcar at fixed gate (50 ns), the performance of the former is beaten by the latter, which is reasonable since we expect that some sampling noise affects the digitalization process. In particular, the problem is the finite sampling rate of the digitizer, which is not enough to reliably sample the fast output waveform in correspondence of the signal peak.

On the contrary, the peak-and-hold circuit performance was not as good as expected. We compared this

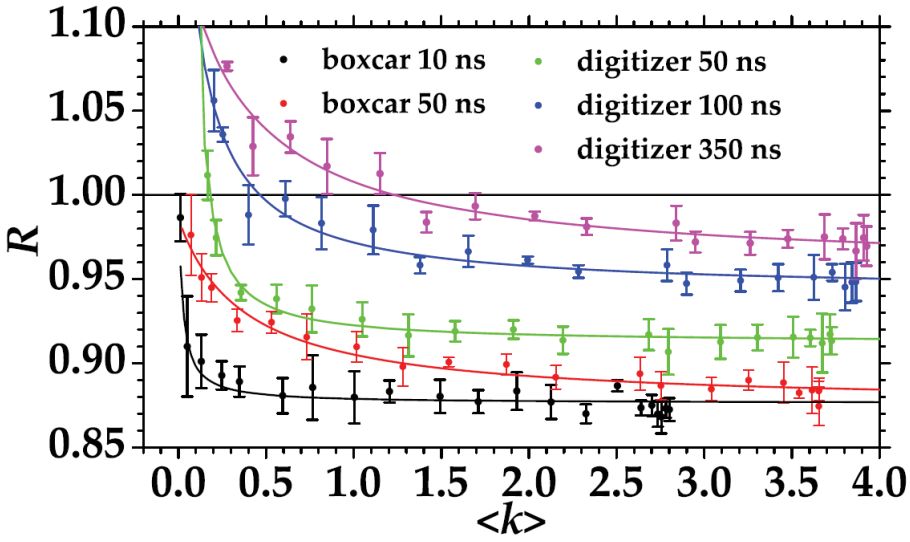

Fig. 3.2: Noise reduction factor R as a function of $\langle k\rangle \equiv (\langle k_1\rangle + \langle k_2\rangle)/2$ for different integration gates. Full symbols: experimental data; lines: theory, provided by Eq. (3.9). The perfect balancing assumption reduces Eq. (3.8) to the form $R = (A+B)/(C+x)$, where A and B are related to the non-idealities of the detectors, while C accounts for errors in the determination of the zero. The value of η determined for data with 10-ns gate width, which is $\eta = 0.1646 \pm 0.0004$, was used to fit all the other datasets. As for the OCT probabilities, we found: $\varepsilon = 0.07 \pm 0.040$ (magenta), 0.062 ± 0.002 (blue), 0.0437 ± 0.0008 (green), 0.022 ± 0.002 (red), 0.0228 ± 0.0007 (black). As for the mean dark-count number, we found: $\langle m_{dc}\rangle = 0.06 \pm 0.02$ (magenta), 0.028 ± 0.007 (blue), 0.009 ± 0.001 (green), 0.04 ± 0.009 (red), 0.0026 ± 0.0006 (black).

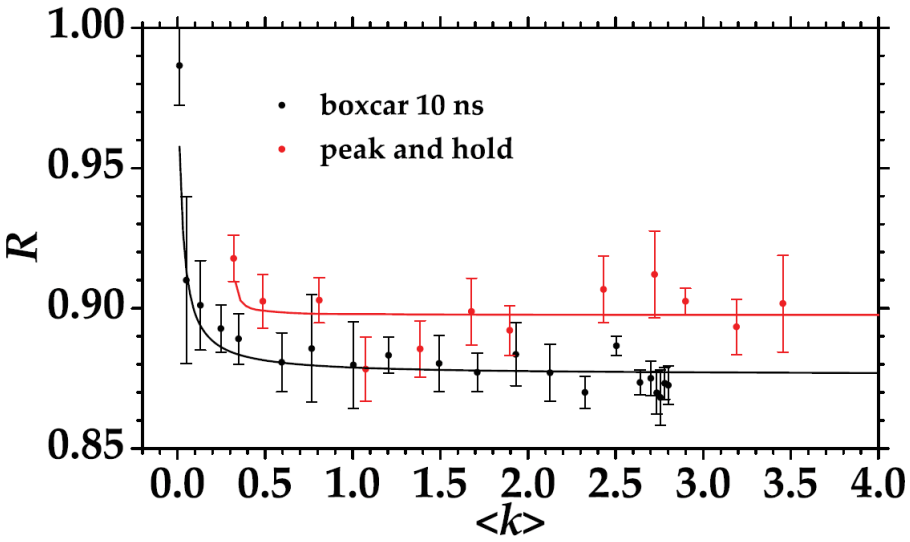

Fig. 3.3: Noise reduction factor R as a function of $\langle k\rangle$: peak-and-hold (red) and minimum boxcar gate (10 ns, black). Full symbols: experimental data; lines: theoretical fit according to Eq. (3.9). The values of the mean dark-count number retrieved from the fit are $\langle m_{dc}\rangle \sim 0$ (red) and 0.0026 ± 0.0006 (black). As to the OCT probability, we got $\varepsilon = 0.035 \pm 0.003 (red)$ and 0.0228 ± 0.0007 (black).

procedure with the best result from Fig. 3.2, i.e. 10-ns analogic integration. As shown in Fig. 3.3, the peak-and-hold improves the performance of the digitizer, but it still gives worse results in comparison with the boxcar-gated integrator. Further improvement of the peak-and-hold acquisition system is still necessary to assess the limit of this technology.
Finally, note that the interpolation of the NRF allows to provide an estimation of the quantum efficiency. We found from the fit of the 10-ns case $\eta \sim 16.5\%$, which is smaller than the half of the quantum efficiency declared by the manufacturer at 523 nm (see Fig. 2.16). This flaw is a consequence of the setup being much more complicated than the one employed for the standard characterization of the detectors. In particular, there is a number of losses, due either to the reflectivity or to the dissipation of some optical elements, which should be taken into account. The transmittivity of the interferential filter employed to select 523-nm wavelength is $\sim 93\%$. The achromatic doublets and the epoxy layer over the sensors also contributes with small losses, their transmittivity being $\sim 99\%$. The critical elements are the fibers, mainly because of the coupling rather than their losses. Overall, the quantum efficiency related to the fibers is $\sim 52\%$. The product of all these contributions provides the effective quantum efficiency estimated in Fig. 3.2.

3.3.2 Conditional measurements

Another measure of nonclassicality that can be used to test the performance of our detectors is a conditional one. We chose the Fano factor as an estimator for the sub-Poissonianity of the conditional state, as in [92], [93] and [94]. The Fano factor, in the presence of losses, has the form shown in Eq. (1.185). Here, for the sake of clarity, we rename the conditioning value w as k_{cond}. Note that the results we obtained for the NRF do not imply that the same devices can detect the nonclassicality of the conditional states, since the condition $R < 1$ is necessary but not sufficient for the generation of sub-Poissonian states.
Having applied the conditioning procedure, we retrieved the results shown in Fig. 3.4. In particular, Fig. 3.4(a) provides the measured mean values of the conditional states generated by selecting different values of k_{cond} on the idler for signal acquisition with the boxcar integrator on 10-ns gate width, which we have proved to be the best achievable experimental condition. The initial mean value of the signal is $\langle k_2 \rangle = 2.52$ (indicated as an horizontal line in the figure), a value for which the contribution of dark counts is negligible ($\langle m_{dc} \rangle \sim 0.026$). Since also the OCT probability is small ($\varepsilon \sim 0.0228$), we observe that the photon statistics of the detected light is unaffected by detector imperfections. This is why we have compared our experimental data with the basic theory outlined in the Theoretical Framework and, more specifically, Eqs. (1.184) and (1.185). OCT effects should be taken into account only to define an effective estimation of quantum efficiency. From the value of R we get $\eta' = 1 - R = \eta(1+\varepsilon) - 2\varepsilon/(1+\varepsilon) \sim 0.124$. All the theoretical predictions in Fig. 3.4 are evaluated by using the effective value η and the measured number of modes $\mu \sim 2000$. As expected, the mean value of the conditional state increases or decreases linearly with the conditioning value.
In Fig. 3.4(b), we plot the measured Fano factor for the same conditional states shown in panel (a). The horizontal line in the figure is at the value of the Fano factor of the original signal ($F \sim 1.00126$).
Finally, Fig. 5(c) shows the statistical distribution of the detected photons for the state obtained by conditioning at $k_{cond} = 5$ (black dots) along with the original distribution on signal. Even if the value of sub-Poissonianity is quite small, the effect is present and interesting: we have obtained a mesoscopic sub-Poissonian state with $\langle k \rangle \sim 2.79$. We note that similar conditioning operations performed on the data acquired by the digitizer do not perform equally well, and that the best results are obtained for the shortest gate explored.

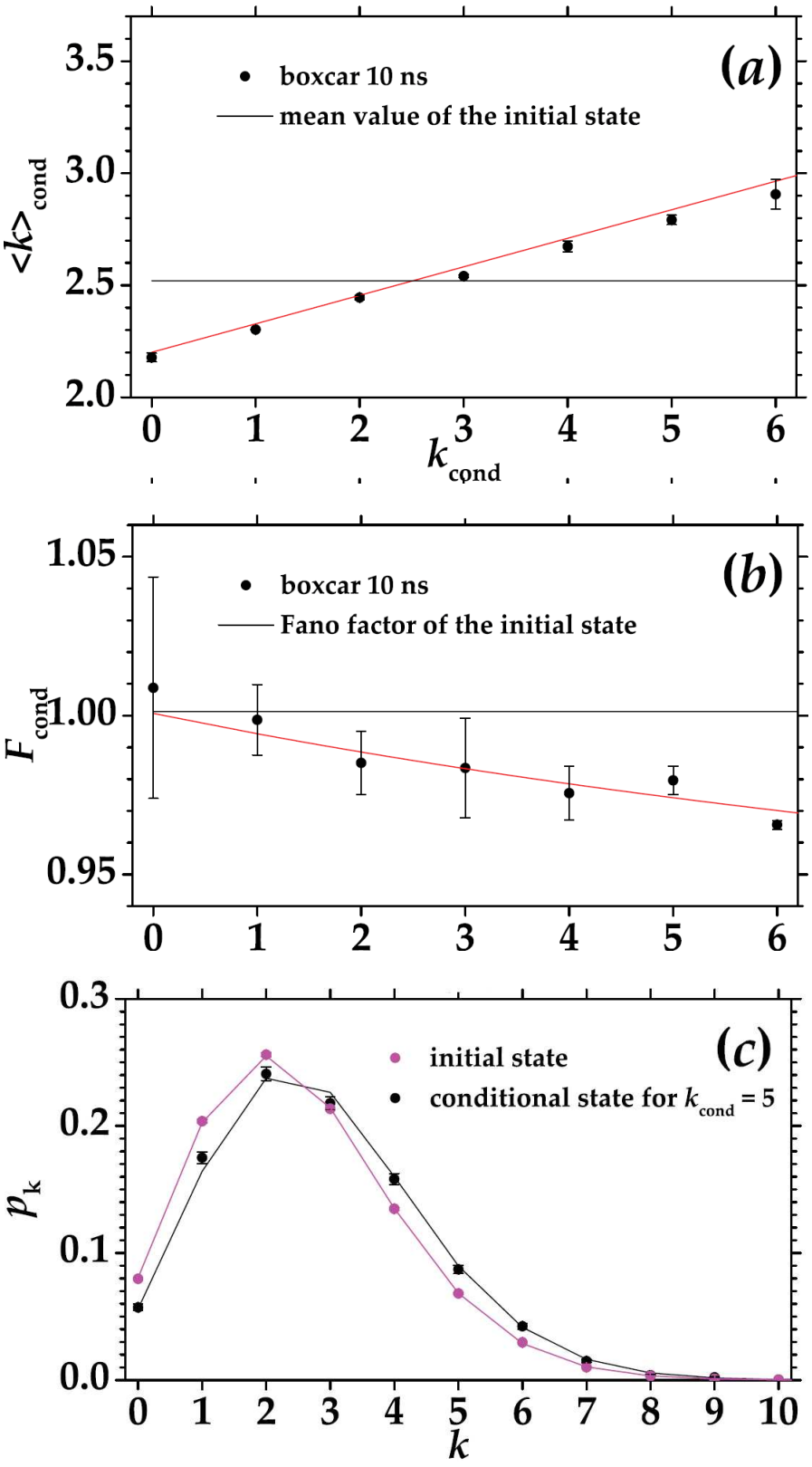

Fig. 3.4: (a) Mean value of the conditional states at different conditioning values; (b) Fano factor of the conditional states; (c) reconstructed photon-number statistics of unconditioned state (magenta) and conditional state (black) with $k_{cond} = 5$. The theoretical expectations are given by Eqs. (1.184) and (1.185). They are shown as lines and well superimposed to the data.

3.4 Glauber's correlation functions as complete estimators

So far, we have shown a whole procedure to test the capability of a new class of detectors of revealing sub-Poissonianity. In particular, we have proved that SiPMs can be successfully employed to this aim. The procedure basically consists in two parts: a proper characterization with classical states of light aimed at assessing the performance of the device and then the very measurement of nonclassical correlations. Till now, the estimator used to discriminate a classical state from a sub-Poissonian one has been the Fano factor, while the discrimination between quantum and classical correlations has been done by means of the NRF. However, the criterion at the roots of both the two estimators is based on Glauber's second-order correlation functions. Therefore, the whole procedure described above in principle can be repeated as well by uniquely exploiting Glauber's function. In the following, we are showing that they can be used for both the characterization of the detectors and the measurement of nonclassical states of light [49]. In this experimental sense, we can say that these estimators are *complete* since they allow to achieve an estimation for all the quantities of interest in the procedure: on the one hand, they can be used to find the main parameters of the detectors and, on the other hand, they are used to express the nonclassicality criterion based on sub-Poissonianity. In other words, they are ubiquitous from the beginning to the end of the detection chain.
The definition of Glauber's functions that we are often employing here is the one given in terms of measurable quantities in Eq. (1.169). For the sake of clarity, we will rename it $g^{(2)}_{meas}$. Note that, since the sub-Poissonianity criterion is defined for the normal-ordered Glauber's functions $g^{(2)}$, in the next Sections we will need to relate the operative definition $g^{(2)}_{meas}$ with the original one.

3.4.1 Experimental setup

For this analysis we used the experimental data providing the best results in the experiment described in the previous section [95]. They were obtained through the setup, shown in Fig. 3.5, where the boxcar-gated integrators were employed in the acquisition chain and a 10-ns gate was selected. Figs. 3.2 and 3.3 have proved that this is the optimal configuration we can obtain with our setup.

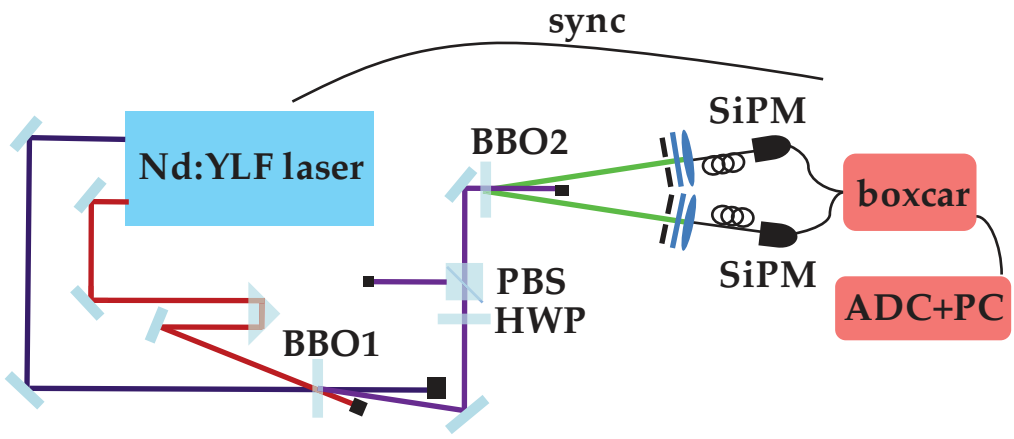

Fig. 3.5: Experimental setup for the measurement of multi-mode TWB states with SiPMs. It is the same as the one in Fig. (3.1) without the option of the digitizer in the acquisition chain.

3.4.2 Results

Estimation of dark counts and optical cross-talk

Our model for photodetection allows us to write the second-order autocorrelation function for measurable quantities as

$$g^{(2)}_{meas}(x_{out}) \equiv \frac{\langle x^2_{out}\rangle}{\langle x_{out}\rangle^2} = g^{(2)}_{meas}(k) = \frac{\langle \Delta k^2\rangle}{\langle k\rangle^2} + 1 \tag{3.10}$$

where $\langle k\rangle$ and $\langle \Delta k^2\rangle$ are given in Eq. (2.21). It can be shown with some simple algebra that the autocorrelation function thus defined depends on the proper Glauber's function for photons $g^{(2)}(n)$ in Eq. (1.143) as follows

$$g^{(2)}_{meas}(k) = 1 + \Big(g^{(2)}(n) - 1\Big)\left(1 - \frac{(1+\varepsilon)\langle m_{dc}\rangle}{\langle k\rangle}\right)^2 + \frac{1}{\langle k\rangle}\frac{1+3\varepsilon}{1+\varepsilon}. \tag{3.11}$$

This formulation of Glauber's functions provides both the information of the detector features and the information on the input light. Applying Eq. (3.11) to the case of a multi-mode thermal distribution, which consists in fixing $g^{(2)}(n)$ to $(1+1/\mu)$, one can fit the experimental data and provide an estimation of ε and $\langle m_{dc}\rangle$. Note that, while the maximum of the autocorrelation function for photons $g^{(2)}(n)$ is 2, here it can be larger, due to the dependence on $\langle k\rangle$. In the two panels of Fig. 3.6 we show $g^{(2)}(k)$ plotted as a function of the mean number of detected photons for the two beams. The experimental data are the black dots with the corresponding error bars, whereas the theoretical fit (Eq. (3.11)) is shown as magenta circles. We assumed the number of modes to be very large, i.e. $\mu = 1000$, and left ε and $\langle m_{dc}\rangle$ as free parameters. The assumption is based on our previous analysis for the detection of quantum states of light [95]. As to the cross-talk probability and the mean dark-count number, we found $\varepsilon_1 = 0.008$, $\langle m_{dc}\rangle_1 = 0.001$ (upper panel) and $\varepsilon_2 = 0.007$, $\langle m_{dc}\rangle_2 = 0.001$ (lower panel).

Note that these results for both dark counts and OCT probabilities are smaller than the same estimated by fitting the noise reduction factor in Figs. 3.2 and 3.3. However, in this case we expect that the fit is more reliable since we have less fitting parameters and we did not need the assumption of a perfect balancing between the two parties. In particular, by fitting the experimental data with the NRF in Eq. (3.9) we had to determine η, $\langle m_{dc}\rangle$ and ε, while the in fit of Eq. (3.11) we had just to fix $\langle m_{dc}\rangle$ and ε. Moreover, the values of $\langle m_{dc}\rangle$ and ε obtained in Figs. 3.2 and 3.3 are inferred from the quantum correlations between the two arms, which are more sensitive to noise than the classical autocorrelations referred to the single arms in Fig. 3.6. An experimental proof for this statement can be provided by computing for each plot the fit mean error, defined as

$$\Delta f = \sum_{i=1}^{N} \frac{|f_i^{(exp)} - f_i^{(th)}|}{N-p} \tag{3.12}$$

where N is the number of experimental data, f is a function of the experimental data (in this case either the NRF or the autocorrelation function) and p is the number of fitting parameters. We found that the fit mean error for the NRF in Figs. 3.2 and 3.3 is more than twice the fit mean error related to the autocorrelation functions in the two panels of Fig. 3.6. In particular, $\Delta R = 7\times 10^{-3}$ while $\Delta g^{(2)}_1 = 3\times 10^{-3}$ (upper panel) and $\Delta g^{(2)}_2 = 2\times 10^{-3}$ (lower panel).

Being the mean dark-count number and the cross-talk probability smaller than expected, we quantified their effective impact on the second-order autocorrelation function, whose relative variation, to a first approximation, can be defined as

$$\frac{\Delta g^{(2)}(k)}{g^{(2)}(k)} \sim \left.\frac{\partial_\alpha g^{(2)}(k)}{g^{(2)}(k)}\right|_{\alpha=0} \cdot \alpha \tag{3.13}$$

where α is either $\langle m_{dc}\rangle$ or ε and $\partial_\alpha \equiv \partial/\partial\alpha$. Since $\alpha \sim 10^{-3}$ and $\partial_\alpha g^{(2)}(k)/g^{(2)}(k)|_{\alpha=0} \sim 10^{-1}$, the impact of these nonidealities should be negligible up to the fourth decimal order. Thus, given that here we

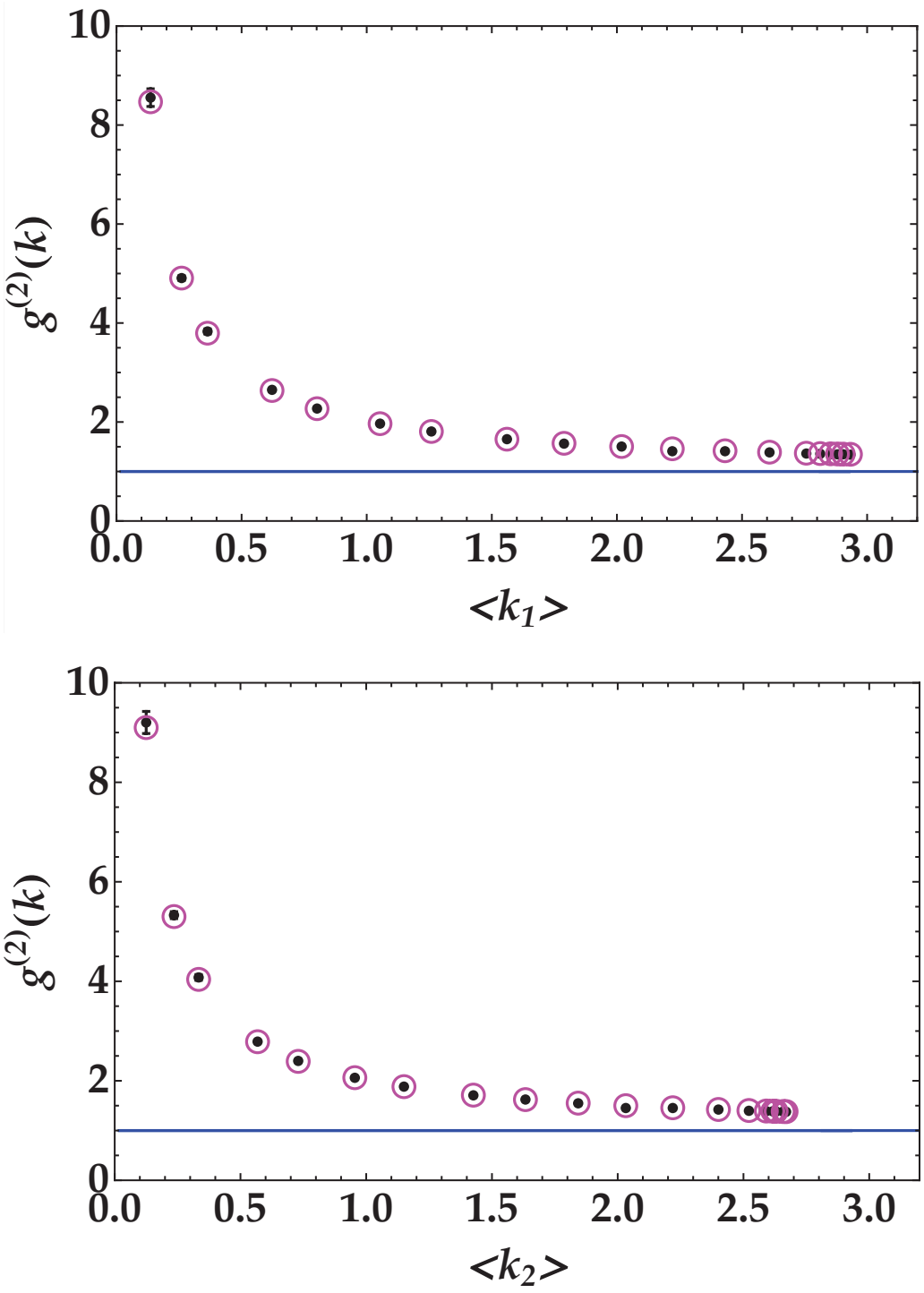

Fig. 3.6: Operative second-order autocorrelation function as a function of the mean detected-photon number $\langle k \rangle$ for each TWB arm. Black dots + error bars: experimental data; magenta circles: theoretical fitting curve, given by to Eq. (3.11); blue line: classical boundary. Here the y-axes is just labeled $g^{(2)}$, instead of $g^{(2)}_{meas}$, for the sake of simplicity.

hardly need three significant digits, in the following we will not consider the effects of dark counts and OCT.

Estimation of detected nonclassicality

The connection between the NRF R and Glauber's functions can be investigated by studying the operative second-order correlations of the photocurrent difference $\Delta m \equiv m_1 - m_2$, i.e.

$$g^{(2)}_{meas}(\Delta m) \equiv \frac{\langle (m_1 - m_2)^2 \rangle}{\langle m_1 - m_2 \rangle^2} = 1 + \frac{\langle m_1 + m_2 \rangle}{\langle m_1 - m_2 \rangle^2} R. \tag{3.14}$$

by definition of NRF. The normal-ordered Glauber's second-order correlation function for the photon-number difference $\Delta n \equiv n_1 - n_2$, after some simple algebra, is found to be given by

$$g^{(2)}(\Delta n) = g^{(2)}_{meas}(\Delta n) - \frac{\langle n_1 + n_2 \rangle}{\langle n_1 - n_2 \rangle^2}. \tag{3.15}$$

This function deserves a few considerations. Indeed it is not obvious that $g^{(2)}(\Delta n)$, expressed as a function of the single-arm number operators $\hat{n}_1$ and $\hat{n}_2$, inherits the same properties of $g^{(2)}(n)$, described in the first chapter. Indeed it is not true. For beams perfectly balanced in the photon numbers, i.e. $\langle \hat{n}_1 \rangle = \langle \hat{n}_2 \rangle$, as it happens for the entangled states but also for classical states equally divided at a beam splitter, $g^{(2)}(\Delta n)$ diverges, due to the normalization. However, in typical experimental conditions the quantum efficiencies of the detectors are not exactly the same, so that we can fairly use it for detected-photon numbers as long as the hypothesis of perfect balancing is smoothed out by requiring the more realistic condition $\eta_1 \sim \eta_2$. In the case of a coherent state, we still have $g^{(2)}(\Delta n) = 1$ and the sub-Poissonianity condition is again $g^{(2)}(\Delta n) < 1$.

In the mentioned case of almost-perfect balancing ($\eta_1 \sim \eta_2$), $g^{(2)}_{meas}(\Delta m)$ uniquely depends on the moments of the photon-number distribution. From its very definition and through Eq. (3.15), one gets

$$\begin{aligned} g^{(2)}_{meas}(\Delta m) &\sim \frac{\langle (m_1 + m_2)^2 \rangle + (1-\eta)\langle m_1 + m_2 \rangle}{\langle m_1 - m_2 \rangle^2} = \\ &= g^{(2)}_{op}(\Delta n) + (1-\eta)\frac{\langle m_1 + m_2 \rangle}{\langle m_1 - m_2 \rangle^2} = \\ &= g^{(2)}(\Delta n) + \frac{\langle n_1 + n_2 \rangle}{\langle n_1 - n_2 \rangle^2} + (1-\eta)\frac{\langle m_1 + m_2 \rangle}{\langle m_1 - m_2 \rangle^2} = \\ &= g^{(2)}(\Delta n) + \frac{\langle m_1 + m_2 \rangle}{\langle m_1 - m_2 \rangle^2} \end{aligned} \tag{3.16}$$

where in the first line we have exploited the second moment of the difference photocurrent in Eq. (1.166) under the hypothesis of quasi-perfect balancing. Hence, we see that $g^{(2)}_{meas}(\Delta m)$, through Eqs. (3.14) and (3.16), is a bridge between R and the correlations of photons, estimated by $g^{(2)}(\Delta n)$, as follows

$$g^{(2)}(\Delta n) - 1 = (R-1)\frac{\langle m_1 + m_2 \rangle}{\langle m_1 - m_2 \rangle^2}. \tag{3.17}$$

Two important observations are to be made now. First, note that the evaluation of purely experimental quantities gives us access to the proper correlation function of the photon-number difference. Then, we point out that the nonclassicality criterion applied on the NRF, i.e. $R < 1$, implies the negativity of $[g^{(2)}(\Delta n) - 1]$, which is nothing but the pristine sub-Poissonanity criterion $g^{(2)} < 1$ established at the very beginning of this voyage. As for the NRF in Figs. 3.2 and 3.3, we would like to plot the photon-number

correlations as a function of a mean measured quantity, such as $\langle m \rangle \equiv (\langle m_1 \rangle + \langle m_2 \rangle)/2$, so we have to conveniently rewrite Eq. (3.17). By exploiting the expression of the NRF in the absence of dark counts and OCT in Eq. (1.180), we get

$$\begin{aligned} g^{(2)}(\Delta n) - 1 &= \frac{1}{\mu} - \frac{\eta_1 \eta_2 (\eta_1 + \eta_2)}{(\eta_1 - \eta_2)^2} \frac{1}{\langle m \rangle} \\ &= \frac{1}{\mu} - \eta \tilde{n} \frac{1}{\langle m \rangle} \end{aligned} \tag{3.18}$$

where we have approximated $\eta_1 + \eta_2 \sim 2\eta$ and exploited the threshold $\tilde{n}(\eta_1, \eta_2)$ in Eq. (1.167). Note that $g^{(2)}(\Delta n) - 1 = 0$ is achieved for $\langle m \rangle = \mu \eta \tilde{n}$. However, in this case $\mu = 10^3$ and $\tilde{n} \gg 1$ due to the almost-perfect balancing condition, so that, for the explored ranges of mean detected-photon number (up to 3), we should never have $g^{(2)}(\Delta n) - 1 > 0$. Furthermore, note that, at variance with the NRF, even in the absence of dark counts and OCT, $[g^{(2)}(\Delta n) - 1]$ depends on $\langle m \rangle$ and, in particular, diverges for $\langle m \rangle \to 0$. We plotted $[g^{(2)}(\Delta n) - 1]$ in Fig. 3.7, where we named $g^{(2)}(\Delta n) \equiv g^{(2)}_{diff}(n)$, and found that the experimental data (the black dots with the error bars) are correctly fitted by this theoretical description (magenta circles), except for the first point, which does not match the model. However, note that the relative error bar is very large, so that the point is not reliable. The larger dimensions of the error bars for $\langle m \rangle \to 0$ are due to the signal to noise ratio collapsing as the signal decreases.

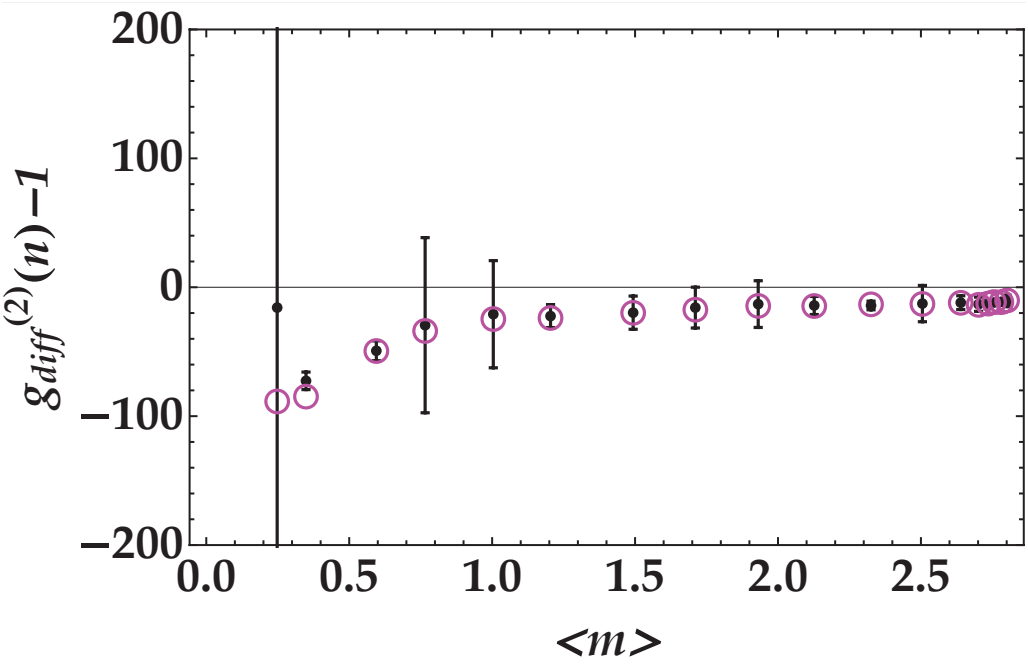

Fig. 3.7: Measured second-order correlation function for the photon-number difference $g^{(2)}_{diff}(n) - 1$ as a function of $\langle m \rangle \equiv (\langle m_1 \rangle + \langle m_2 \rangle)/2$. Black dots + error bars: experimental data; magenta circles: theoretical description in Eq. (1.169).

Finally, we would like to use Glauber's second-order autocorrelation function to estimate the nonclassicality of a conditional state. Again, we will refer to the measurements explained in the previous Section and replace the Fano factor F in Fig. (3.4b) with $g^{(2)}(n)$. The connection between the two quantities has already been given in Eq. (1.175), from which it is straightforward that the nonclassicality condition $F < 1$

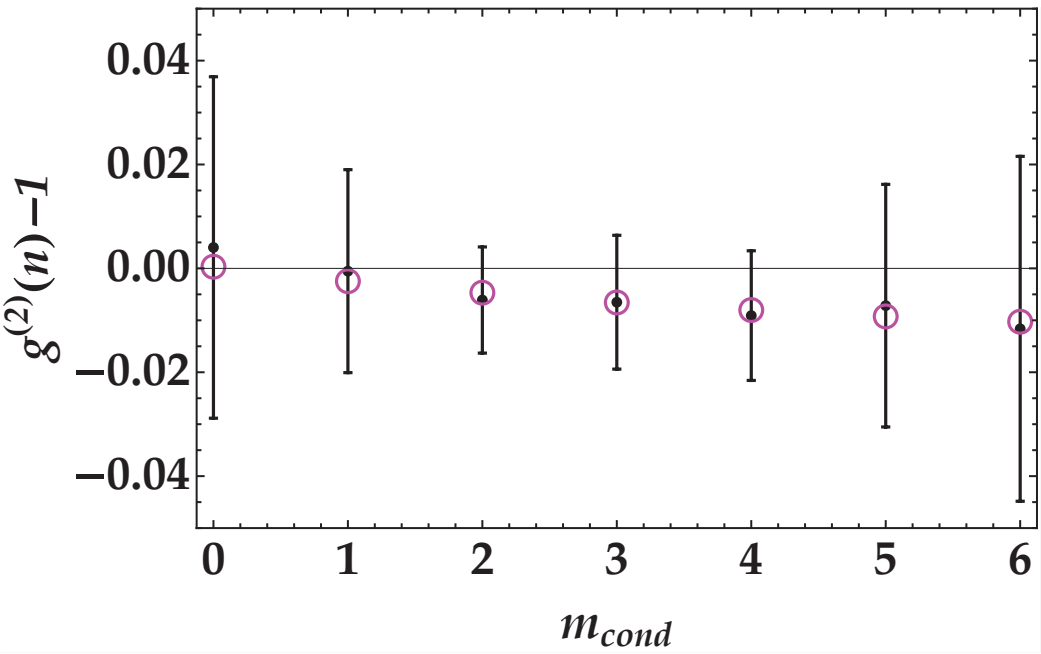

Fig. 3.8: Measured values of $g^{(2)}(n)-1$ as a function of the conditioning value, m_{cond}. Black dots + error bars: experimental data; magenta circles: theoretical model (see the text for details).

is equivalent to $g^{(2)}(n)-1<0$. The Fano factor for a conditional state is expressed in Eq. (1.185). We can see from Fig. 3.8 that the model for $[g^{(2)}(n)-1]$ (magenta circle) properly fits the experimental data (black dots with error bars). The negativity of the plotted function is not large, but it is enough to prove the sub-Poissonianity of the state. However, note that here the error bars challenge the reliability of the measurement. As a matter of fact, they are not larger than the error bars in Fig. 3.7, they are just larger than the negativity of $[g^{(2)}(n)-1]$.

4

Nonclassicality with second-harmonic generation

After that the paper [21] by Armstrong et al. had been published in 1962, the generation of second-harmonic light through a nonlinear crystal was extensively understood. Since the Jacobi elliptic functions in the long run are boring, in the following few years theoreticians started to work on a quantum description of the phenomenon. From the experimental point of view, at variance with frequency down-conversion, squeezed states of light required more time to be generated through up-conversion processes, such as SHG. As far as we know, the first who studied [97, 98, 99] and implemented [100, 101] a squeezing-generation and detection scheme via the SHG process was Kumar's group in the Nineties. Second-harmonic generated nonclassical states have attracted much attention, essentially because of the simplicity of the experimental setup, but not only. On the one hand it is not necessary to frequency double the laser first, as in typical parametric-amplification-based experiments; on the other hand, it can be demonstrated that, for a coherent input state, both the pump and the harmonic fields are nonclassical, which implies that bright squeezed light, analog to TWB states, can be generated.

The theoretical description of sub-Poissonian light from SHG is as challenging and hard as the design of a scheme for the observation of it. Basically, the main problem consists in the form of the interaction Hamiltonian, which is neither linear nor bilinear in the field modes, so that the evolution operator cannot be disentangled in a closed form [38] and the quantum dynamics of the process cannot be analytically retrieved. Many expedients have been suggested to overcome this problem. In 1967, Shen [102] retrieves the density matrix of the up-converted field by exploiting the *parametric approximation*, which consists in assuming that the pump field operators are c-numbers, due to the intensity of the field. In the absence of this assumption, Shen himself reports "*Ducuing and Armstrong [103] have discussed the statistical aspects of second-harmonic generation with high conversion using the classical approach. A corresponding quantum-statistical discussion would be extremely difficult, if the noncommutability of the operators* $\hat{a}$ *and* $\hat{a}^{\dagger}$ *is to be taken into account*". Note that the parametric approximation is typically used to describe the dynamics of the PDC through the evolution operators in Eqs. (1.116) and (1.121). In 1969, Bonifacio and Preparata [104] proved the equivalence between a system of N two-level atoms interacting with an electromagnetic field, described by the Dicke model, and a generic trilinear-boson-scattering process. Orszag et al. [105], in 1983, specified their results for the SHG and retrieved the n-photon-generation probability and the efficiency of the process. The equivalence is essentially based on the rotating-wave approximation, but, again, their analytic results can be achieved only by requiring a complete factorization of the bosonic operators, which is equivalent to treat the operators as c-numbers. The same factorization

hypothesis was employed by Crosignani et al. [106], even if they managed to retrieve a relevant property of the process independently from that assumption, i.e. the impossibility to end with a complete depletion of the fundamental mode, due to the fluctuations of the photon numbers in coherent light [107]. Note that such a conclusion is general in the sense that it requires no approximations but holds only for input Poissonian states.
A different approach was used by Kozierowski and Tanaś [108]. They studied the quantum process from the photon statistics point of view by expanding Glauber's correlation functions in series, thus retrieving approximated expressions for the photon-number moments. A similar work on the statistics was lately made by Ekert and Rzazewski [109] through a numeric approach. In particular, they found an approximation of the temporal evolution of the second-harmonic intensity for different pump input states, accounting also for damping effects. However, they just focused on the evolution of the intensities. The evolution of the correlations for a long interaction time was retrieved more recently by Bajer et al. [110, 111], thanks to the perturbative approach followed by a numeric analysis, but only in the case of coherent input states.
In a recent work of ours [112] we reviewed the Hamiltonian quantum description of the process starting from the perturbative approach and found some analytic and, as far as we know, new results on the generated second-harmonic intensity, the up-conversion probabilities and the output statistics for different input states. In particular, we analyzed the cases of coherent, chaotic and squeezed light, providing some comparisons with the classical results outlined in the introductory Theoretical Framework. Also, our results are supported by a deep investigation and interpretation of the underlying physical process.

4.1 Dynamics of the process

The trilinear boson interaction Hamiltonian describing SHG can be expressed as follows

$$\hat{H}_{int} = \hbar\gamma \hat{a}_{\mathrm{F}} \hat{a}_{\mathrm{F}} \hat{a}^{\dagger}_{\mathrm{SH}} + h.c. \tag{4.1}$$

where $\hat{a}_j$ and $\hat{a}^{\dagger}_j$ are the annihilation and creation boson operators for the input (j =F) and second-harmonic field (j =SH) with the usual commutation rules $\left[\hat{a}_j, \hat{a}^{\dagger}_k\right] = \delta_{j,k}$ and γ is the coupling constant, which depends on the second-order nonlinear susceptibility. The complete evolution should be given by $\hat{\mathrm{H}} = \hat{H}_0 + \hat{H}_{int}$, where $\hat{H}_0$ is the free-field single-mode Hamiltonian, i.e.

$$\hat{H}_0 = \hbar\omega \hat{a}^{\dagger}_{\mathrm{F}} \hat{a}_{\mathrm{F}} + 2\hbar\omega \hat{a}^{\dagger}_{\mathrm{SH}} \hat{a}_{\mathrm{SH}}. \tag{4.2}$$

In the following we will show that for this particular process H_0 does not play any particular role. However, note that [113] H_0 is a constant of motion. Therefore, also H_{int} does not depend on time, which is good to know because it means that the expression of the evolution operator is simple.
As mentioned above, no exact solution can be found for the output state since it is not possible to identify a finite-dimensional Lie algebra for this Hamiltonian [33]. Here we exploit a perturbative approach. A comparison with the classical regime will help to test the consistency of our results. The Heisenberg equation for the number operator $\hat{n}_{\mathrm{SH}} \equiv \hat{a}^{\dagger}_{\mathrm{SH}} \hat{a}_{\mathrm{SH}}$, with the Hamiltonian $\hat{\mathrm{H}}$ reads

$$\begin{aligned} i\hbar \frac{d\hat{n}_{\mathrm{SH}}}{dt} &= [\hat{n}_{\mathrm{SH}}, \hat{\mathrm{H}}] = \\ &= [\hat{n}_{\mathrm{SH}}, \hat{H}_0] + [\hat{n}_{\mathrm{SH}}, \hat{H}_{int}] = \\ &= [\hat{n}_{\mathrm{SH}}, \hat{H}_{int}] \end{aligned} \tag{4.3}$$

since $[\hat{n}_{\rm SH}, \hat{H}_0] = 0$. Equation (4.3) provides the coefficients of the Taylor expansion approximating $\hat{n}_{\rm SH}$ at a given time t, i.e.

$$\hat{n}_{\rm SH}(t) = \hat{n}_0 + \sum_k \frac{d^k \hat{n}_0}{dt^k} \frac{t^k}{k!}. \tag{4.4}$$

being $\hat{n}_0 \equiv \hat{n}_{\rm SH}(0)$.
As a consequence of the Stone-Von Neumann theorem, it is well known that one can equivalently study the evolution of the states. In particular, we are interested in the generated second-harmonic states, which will allow us to retrieve some simple transition amplitudes. The most general input for a SHG process can be expanded over the basis of the number states as

$$\hat{\rho}_0 = \sum_{n,m} c_n c_m^* |n\rangle\langle m| \otimes |0\rangle\langle 0| \tag{4.5}$$

where c_k are suitable coefficients such that $\sum_k |c_k|^2 = 1$. Given the evolution operator $\hat{U} = \exp\left(\frac{i}{\hbar}\hat{\mathrm{H}}t\right)$, we get the output state from

$$\hat{\rho}_0 \to \hat{\rho}(t) = \hat{U}^\dagger(t)\hat{\rho}_0\hat{U}(t), \tag{4.6}$$

by suitably expanding $\hat{U}$ via Baker-Hausdorff-Campbell relation. It is wise focusing on the evolution of the Fock states since we are representing any other state over this basis, which is also the eigenbasis of $\hat{H}_0$. Explicitly,

$$\hat{U}^\dagger(t)\hat{\rho}_0\hat{U}(t) = \sum_{n,m} c_n c_m^* \hat{U}^\dagger(t)|n\rangle\langle m| \otimes |0\rangle\langle 0|\hat{U}(t). \tag{4.7}$$

Note that the free Hamiltonian does not really contribute to the temporal evolution since $[H_0, H_{int}] = 0$. Thus, $\hat{U}^\dagger(t)\hat{\rho}_0\hat{U}(t) = e^{-i\hat{H}_{int}t/\hbar}\rho_0 e^{i\hat{H}_{int}t/\hbar}$. Under the hypothesis that no second-harmonic field is introduced in the crystal, the states transform according to

$$\begin{cases} |\psi(\tilde{\gamma})\rangle\rangle = \hat{U}^\dagger(\tilde{\gamma})|\psi(0)\rangle\rangle \\ |\psi(0)\rangle\rangle = |N,0\rangle \end{cases} \tag{4.8}$$

where $\tilde{\gamma} \equiv \gamma t$. For instance, up to the second order in γ, the output state reads

$$\begin{aligned} |\psi(\tilde{\gamma})\rangle\rangle \sim &\left[1 - \frac{1}{2}\tilde{\gamma}^2 N(N-1) + o(\tilde{\gamma}^3)\right]|N,0\rangle \\ &- \left[i\tilde{\gamma}\sqrt{N(N-1)} + o(\tilde{\gamma}^3)\right]|N-2,1\rangle, \end{aligned} \tag{4.9}$$

which is straightforward from the expansion of the evolution operator and its application to the input state, i.e.

$$\hat{U}^\dagger(\tilde{\gamma})|\psi(0)\rangle\rangle \sim \sum_k \frac{\left(-it\hat{H}_{int}/\hbar\right)^k}{k!}|N,0\rangle. \tag{4.10}$$

4.2 Photon-number distribution

In the following, we will exploit the expansion of the number operator in Eq. (4.4) to express the statistics of the second-harmonic field in terms of the statistics of the pump, whatever the initial state is. In particular, we will provide the expansion of the first and the second moment of the second-harmonic distribution and find and approximated expression for the conversion efficiency. Note that the moments of the output statistics are straightforward from

$$\langle \hat{n}_{\rm SH}^k \rangle = {\rm Tr}[\hat{\rho}_0 \mathbb{1}_{\rm F} \otimes \hat{n}_{\rm SH}^k(\tilde{\gamma})]$$

where $\hat{\rho}_0$ is the generic input state defined in Eq. (4.5).
As mentioned above, Kozierowski and Tanaś in [108] studied the statistical properties of the SHG field. They provided an expansion of the first moment of the output statistics $\langle \hat{a}^\dagger_{\rm SH}\hat{a}_{\rm SH}\rangle$ up to the fourth order as a function of Glauber's autocorrelation functions of the input field, described in Eq. (1.34) and Eq. (1.148) with $j=k$, i.e.

$$g^{(n)}_{\rm F} \equiv \frac{\langle (\hat{a}^\dagger_{\rm F})^n \hat{a}^n_{\rm F}\rangle}{\langle \hat{a}^\dagger_{\rm F}\hat{a}_{\rm F}\rangle^n}. \tag{4.11}$$

As shown in appendix A (Theorem 1), it is possible to demonstrate that every order of the perturbative expansion of the output mean photon-number can be expressed as a linear combination of Glauber's autocorrelation functions in Eq. (4.11). Therefore, we can express the second-harmonic moments as a convergent series over the order of the autocorrelation function for the fundamental field. In particular, we retrieved that, up to the sixth order in $\tilde{\gamma}$, the output mean value reads

$$\begin{aligned}\langle \hat{n}_{\rm SH}\rangle =& g^{(2)}_{\rm F}N^2\tilde{\gamma}^2 - \frac{2}{3}\left(g^{(2)}_{\rm F}N^2 + 2g^{(3)}_{\rm F}N^3\right)\tilde{\gamma}^4 + \\ &+ \frac{4}{45}\left(2g^{(2)}_{\rm F}N^2 + 16g^{(3)}_{\rm F}N^3 + 17g^{(4)}_{\rm F}N^4\right)\tilde{\gamma}^6 + o(\tilde{\gamma}^8)\end{aligned} \tag{4.12}$$

where $N = {\rm Tr}[\hat{\rho}_0\hat{n}_{\rm F}(0)\otimes \mathbb{1}_{\rm SH}]$ is the mean energy of the input state. Note that, for the sake of simplicity, we assumed $\gamma \in \mathbb{R}$. For what concerns the second moment, up to the fourth order in $\tilde{\gamma}$, we get

$$\langle \hat{n}^2_{\rm SH}\rangle = g^{(2)}_{\rm F}N^2\tilde{\gamma}^2 + \left[g^{(4)}_{\rm F}N^4 - \frac{2}{3}\left(g^{(2)}_{\rm F}N^2 + 2g^{(3)}_{\rm F}N^3\right)\right]\tilde{\gamma}^4 + o(\tilde{\gamma}^6). \tag{4.13}$$

In the case of Fock states, Theorem 1 allows to find a general expression for the asymptotic value of $\langle \hat{n}_{\rm SH}\rangle$ as a function of N (see Corollary 1 in Appendix B for details), which is

$$\langle \hat{n}_{\rm SH}\rangle \sim N\sum_j \tilde{\gamma}^{2j}N^j. \tag{4.14}$$

Note that, upon defining the *conversion efficiency* as

$$\eta \equiv \frac{\langle \hat{n}_{\rm SH}\rangle}{2N}, \tag{4.15}$$

we find that

$$\eta \sim \frac{1}{2}\sum_j \tilde{\gamma}^{2j}N^j, \tag{4.16}$$

which implies that the conversion efficiency related to every single interaction is proportional to the input intensity. This fact will be relevant in the analysis of the evolution of the input light statistics. It is interesting to see that, if $\tilde{\gamma}^2 N < 1$, Eq. (4.14) is a geometric series, yielding $\langle \hat{n}_{\rm SH}\rangle \sim N/(1-\tilde{\gamma}^2N)$ and $\eta \sim 1/[2(1-\tilde{\gamma}^2N)]$. The condition on the efficiency $\eta \leq 1$ implies a stricter bound, i.e. $\tilde{\gamma}^2N < \frac{1}{2}$, which is reasonable in a mesoscopic intensity regime since $\gamma \propto \chi^{(2)} \sim 10^{-12}$Hz and for the typical interaction time $t \sim 10$ ps. In this limit, the factor $\tilde{\gamma}^2N$ could be interpreted as the probability of generating a single second-harmonic photon in the interaction time t.
The physical meaning of the coefficients in the perturbative expansion of $\langle \hat{n}\rangle$ can be outlined by expressing the autocorrelations in Eq. (4.12) as a function of N, as shown in Appendix B for the Fock state. The inspection of the retrieved perturbative orders leads to some general considerations. In particular, we found that the first moment of the second-harmonic distribution can be rewritten as follows

$$\langle \hat{n}_{\rm SH}\rangle = \sum_{k=1}^{K}\tilde{\gamma}^{2k}\left[\frac{N!}{k!(N-2k)!}k + \alpha_k(N) + \beta_k(N)\right] + o(\tilde{\gamma}^{2(K+1)}) \tag{4.17}$$

for any given K. Up to the sixth order in $\tilde{\gamma}$, we have

$$\begin{aligned}
&\alpha_1 = 0 \qquad \beta_1 = 0 \\
&\alpha_2 = 0 \qquad \beta_2 = -\frac{1}{3}\left[\left(\frac{N!}{(N-2)!}\right)^2 + 2\frac{N!}{(N-4)!}\right] \\
&\alpha_3 = \frac{1}{36}\left[\left(\frac{N!}{(N-2)!}\right)^3 + 4\frac{N!(N-2)!}{[(N-4)!]^2}\right] \\
&\beta_3 = \frac{1}{60}\left(\frac{N!}{(N-2)!}\right)^3 + \frac{1}{90}\frac{(N!)^2}{(N-2)!(N-4)!} - \frac{4}{15}\frac{N!(N-2)!}{[(N-4)!]^2} + \frac{1}{10}\frac{N!}{(N-6)!}.
\end{aligned} \tag{4.18}$$

Note that the three terms in Eq. (4.17) can be viewed as three different processes concurring in SHG. The first one

$$\sum_k \tilde{\gamma}^{2k} N!/(N-2k)!$$

is related to the creation of k second-harmonic photons from N. This contribution comes from all and only the terms that in the expansion of $\hat{U}(\tilde{\gamma})$ in Eq. (4.6) are of the kind $(\hat{a}_{\rm SH}^\dagger)^k$. They correspond to pure up-conversion events, i.e. the annihilation of $2k$ pump photons from N at each order k.
The second process yields, for $k \geq 3$, the α_k terms, which corresponds to the alternating creation and annihilation of second-harmonic photons. For the sake of simplicity, we name these as *annihilation processes* since, at variance with the former, consist of back-conversion events. For instance, for $k = 3$ we have three different processes leading to a non-null value of $\langle \hat{n}_{\rm SH} \rangle$, which are the following: the creation process $(\hat{a}_{\rm SH}^\dagger)^3$ (creation of three second-harmonic photons, having annihilated six pump photons from N after three interactions) and the annihilation processes $\hat{a}_{\rm SH}^\dagger \hat{a}_{\rm SH} \hat{a}_{\rm SH}^\dagger$ and $\hat{a}_{\rm SH} \hat{a}_{\rm SH}^\dagger \hat{a}_{\rm SH}^\dagger$ (creation of one second-harmonic photon after three interactions). These last two provide respectively the first and the second term of α_3 in Eq. (4.18) and differ for the ordering of the operators only. In particular, both these processes lead to the same output state, i.e.$|N-2,1\rangle$, but, as to the first one, we have that a second-harmonic photon is created, annihilated and then created again, each of these events happening in $N!/(N-2)!$ possible ways, and, as to the second one, two second-harmonic photons are created (which is likely to happen in $N!/(N-4)!$ equivalent configurations) and then one of the two is down-converted in two photons of the fundamental field ($(N-2)!/(N-4)!$ possible configurations).
Finally, if $k \geq 2$, the annihilation processes can interfere either with one another or with creation events, giving rise to the third kind of contribution, expressed by the β_k terms in Eq. (4.17). We have superposition of processes whenever different processes lead to the same output state. It is something like Feynman's description of the Hong-Ou-Mandel effect. For instance, for $k = 2$ we find, together with the two-photon-creation process $(\hat{a}_{\rm SH}^\dagger)^2$ (creation of two second-harmonic photons, having annihilated four pump photons from N after two interactions), the superposition β_2 of the one-photon-creation process $\hat{a}_{\rm SH}^\dagger$ (creation of one second-harmonic photon from N after one interaction) with the annihilation processes $\hat{a}_{\rm SH}^\dagger \hat{a}_{\rm SH} \hat{a}_{\rm SH}^\dagger$ and $\hat{a}_{\rm SH} \hat{a}_{\rm SH}^\dagger \hat{a}_{\rm SH}^\dagger$ mentioned above. Note that all of these three provide the output state $|N-2,1\rangle$. More explicitly, the superposition of $\hat{a}_{\rm SH}^\dagger$ with $\hat{a}_{\rm SH}^\dagger \hat{a}_{\rm SH} \hat{a}_{\rm SH}^\dagger$ corresponds to a term $(\tilde{\gamma}\hat{a}_{\rm SH})(\tilde{\gamma}^3 \hat{a}_{\rm SH}^\dagger \hat{a}_{\rm SH} \hat{a}_{\rm SH}^\dagger)$ in the Taylor expansion of $\hat{U}(\tilde{\gamma})$. In particular, from that expansion it is straightforward that the factor $\tilde{\gamma}\hat{a}_{\rm SH}$ contributes with an amplitude $\sqrt{N!/(N-2)!}$, whereas $\tilde{\gamma}^3 \hat{a}_{\rm SH}^\dagger \hat{a}_{\rm SH} \hat{a}_{\rm SH}^\dagger$ contributes with $[N!/(N-2)!]^{3/2}$. Similarly, the superposition of $\hat{a}_{\rm SH}^\dagger$ with $\hat{a}_{\rm SH} \hat{a}_{\rm SH}^\dagger \hat{a}_{\rm SH}^\dagger$ is given by a term $(\tilde{\gamma}\hat{a}_{\rm SH})(\tilde{\gamma}^3 \hat{a}_{\rm SH} \hat{a}_{\rm SH}^\dagger \hat{a}_{\rm SH}^\dagger)$, where $\tilde{\gamma}^3 \hat{a}_{\rm SH} \hat{a}_{\rm SH}^\dagger \hat{a}_{\rm SH}^\dagger$ contributes with an amplitude $\sqrt{N!/(N-2)!}(N-2)!/(N-4)!$.
This hierarchy of processes concurring to the whole SHG phenomenon is just a logic consequence of the Hamiltonian evolution of the system, but it can help to better understand the underlying physics. A representation of the perturbative terms through double-sided Feynman diagrams can help to understand

the underlying physics. Moreover, such a representation may be used to retrieve higher-order terms in the expansion. In the following, the role of these different contributions will be further pointed out for what concerns the up-conversion probability and the evolution of the input light statistics.

4.2.1 Double-sided Feynman diagrams for quantum SHG

Double-sided Feynman diagrams are commonly used to display the different contributions to the cross-section of the SHG process, i.e. the components of the susceptibility tensor, within a semiclassical model [22, 114], where the atomic energy levels of the medium are described by the Schrödinger equation while the electromagnetic field is assumed to be a plane wave. Here we define these tools in a totally quantum frame. Feynman diagrams are commonly used to express the expansion of the transition amplitudes

$$\langle n,m|e^{-i\hat{H}_{int}t/\hbar}|N,0\rangle$$

with n, $m \in \mathbb{N}$. Double-sided Feynman diagrams are related to the mean values of the evolved state $\hat{\rho}(t)$ in Eq. (4.6), i.e.

$$\langle n,m|\hat{\rho}(t)|n,m\rangle = \langle n,m|e^{-i\hat{H}_{int}t/\hbar}|N,0\rangle\langle N,0|e^{i\hat{H}_{int}t/\hbar}|n,m\rangle = |\langle n,m|e^{-i\hat{H}_{int}t/\hbar}|N,0\rangle|^2,$$

which is the probability of getting n photons on the fundamental mode and m on the second-harmonic mode at time t. The diagrams describe the interaction between the quantized electromagnetic field and the energy levels of the materials. Both the fields are assumed to start with their ground states, respectively $|N,0\rangle\langle N,0|$ and $|0\rangle\langle 0|$. Furthermore, the atomic field is assumed to end with the ground state, i.e. we are not considering absorption processes. A unique representation can be given for the terms in the expansion of $\langle n,m|\hat{\rho}(t)|n,m\rangle$ via Feynman diagrams by applying the following rules:

1. A double-sided diagram is composed of two Feynman diagrams, one representing $\langle n,m|e^{-i\hat{H}_{int}t/\hbar}|N,0\rangle$ and the other $\langle n,m|e^{-i\hat{H}_{int}t/\hbar}|N,0\rangle^{\dagger}$. The arrows do not provide the time direction. The process starts at the bottom and ends at the top of the diagram.

2. The fields are represented by lines with arrows. If the arrow points towards the vertex, this is the ket-state of the field and the corresponding diagram is the one on the left. Vice versa for the bra-states of the field.

3. The electromagnetic field is represented by a wiggly line attached to a vertex  and generally is given in a state $|n,m\rangle$ on the left and $\langle n,m|$ on the right.

4. The atomic field is represented by a plain line attached to a vertex  and generally is given in a state $|k\rangle$ on the left and $\langle k|$ on the right.

5. The virtual levels of the electromagnetic field are represented by a wiggly line connecting two vertexes without the arrow .

6. The virtual levels of the atomic field are represented by a plain line connecting two vertexes without the arrow  .

7. The interaction is represented by a vertex •. Given that the input field states are $|n,m\rangle$ for the radiation and $|k\rangle$ for the material, every interaction consists of one of the following four events:

   - Annihilation of two photons on the pump mode. The energy of the material is increased to the next eigenstate $|k+1\rangle$. It is possible to retrieve the perturbative term related to the given diagram if one multiplies by a factor $\sqrt{(-i\tilde{\gamma})\frac{n!}{(n-2)!}}$ for each vertex on the left and a factor $\sqrt{i\tilde{\gamma}\frac{n!}{(n-2)!}}$ for each on the right.

- Creation of two photons on the pump mode. The energy of the material is decreased to the previous eigenstate $|k-1\rangle$. It is possible to retrieve the perturbative term related to the given diagram if one multiplies by a factor $\sqrt{(-i\tilde{\gamma})\frac{(n+2)!}{n!}}$ for each vertex on the left and a factor $i\tilde{\gamma}\sqrt{\frac{(n+2)!}{n!}}$ for each on the right.
- Annihilation of one photon on the second-harmonic mode. The energy of the material is increased to the next eigenstate $|k+1\rangle$. It is possible to retrieve the perturbative term related to the given diagram if one multiplies by a factor $\sqrt{(-i\tilde{\gamma})m}$ for each vertex on the left and a factor $\sqrt{i\tilde{\gamma}m}$ for each on the right.
- Creation of one photon on the second-harmonic mode. The energy of the material is decreased to the previous eigenstate $|k-1\rangle$. It is possible to retrieve the perturbative term related to the given diagram if one multiplies by a factor $\sqrt{(-i\tilde{\gamma})(m+1)}$ for each vertex on the left and a factor $\sqrt{i\tilde{\gamma}(m+1)}$ for each on the right.

8. Only the diagrams ending with the state $|n',m',0\rangle\langle n',m',0|$ can survive. Therefore, the output states on the left and on the right must share the same number of pump and second-harmonic photons.

9. Divide by the symmetry factor, i.e. the number of equivalent diagrams representing the same term.

By construction, the double-sided Feynman diagrams can help to distinguish among creation, annihilation and superposition processes.
A creation term in $\langle n,m|\hat{\rho}(t)|n,m\rangle$ was defined as a process where only second-harmonic-photon creation events occur, which at the order $\tilde{\gamma}^{2k}$ is described by the transition

$$|\langle n,m|\hat{a}_{\mathrm{F}}^{2k}(\hat{a}_{\mathrm{SH}}^{\dagger})^{k}|N,0\rangle|^{2}. \tag{4.19}$$

Then, the related diagram is the following

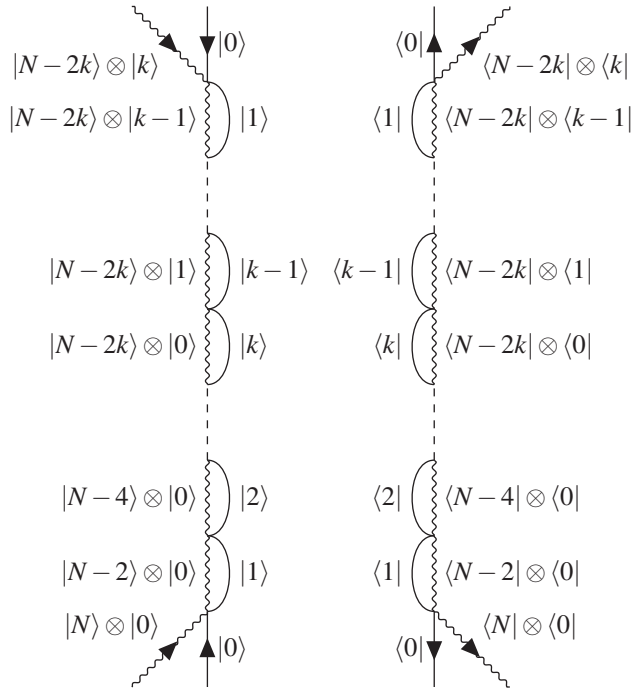

Note that the direction of the diagram on the right is reversed because it describes the adjoint of the diagram on the right. Diagrams representing creation processes can be reduced to the simpler one-loop diagram

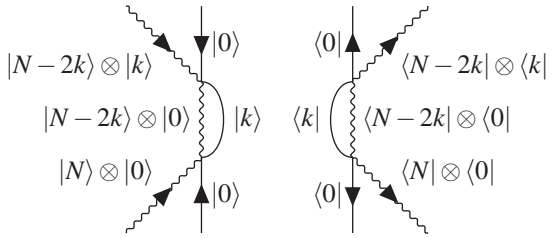

Here the single loop stands for all the intermediate virtual processes, where either two pump photons are annihilated or two second-harmonic photons are created. Such a simplification is possible just because these diagrams describe only two of the four events listed at rule 7., so that every field operator here commutes with each other, implying that the order of the events does not affect the result.
On the contrary, the so-called annihilation processes involve non-commuting field operators, such as $\hat{a}_{\mathrm{SH}}$ and $\hat{a}^{\dagger}_{\mathrm{SH}}$, since all of the four events listed at rule 7. occur. Therefore, they cannot be resumed as a one-loop diagram because different sequences of annihilation and creation processes determines different terms in the perturbative expansion. The lowest-order example for these processes is found at the $\tilde{\gamma}^4$ order. Such term explicitly reads

$$|\langle n,m|\hat{a}^{\dagger}_{\mathrm{F}}\hat{a}^{\dagger}_{\mathrm{F}}\hat{a}_{\mathrm{F}}\hat{a}_{\mathrm{F}}\hat{a}_{\mathrm{SH}}\hat{a}^{\dagger}_{\mathrm{SH}}|N,0\rangle|^2, \tag{4.20}$$

i.e. a second-harmonic photon is created and then annihilated. Note that this event cannot be found in the expansion of the mean value in Eq. (4.17) since the number of second-harmonic photons related to the output state is $m=0$. The diagram related to the transition (4.20) is given by

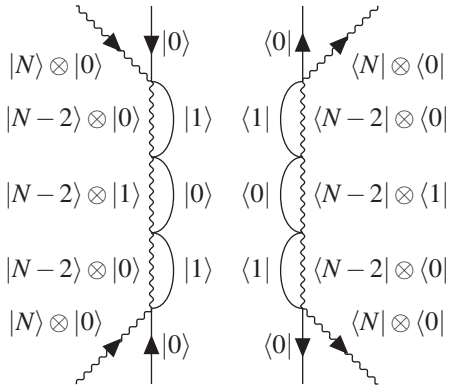

Finally, the superposition processes are represented by diagrams where one side is not the adjoint of the other. As mentioned above, we read these contributions as an interference between different events. For instance, at the order $\tilde{\gamma}^4$ we can also find two distinct terms related to the superposition of the events at the order $\tilde{\gamma}^3$ and $\tilde{\gamma}$. They are

$$\langle n,m|\hat{a}^{\dagger}_{\mathrm{F}}\hat{a}^{\dagger}_{\mathrm{F}}\hat{a}_{\mathrm{F}}\hat{a}_{\mathrm{F}}\hat{a}_{\mathrm{F}}\hat{a}_{\mathrm{F}}\hat{a}_{\mathrm{SH}}\hat{a}^{\dagger}_{\mathrm{SH}}\hat{a}^{\dagger}_{\mathrm{SH}}|N,0\rangle\langle N,0|\hat{a}^{\dagger}_{\mathrm{F}}\hat{a}^{\dagger}_{\mathrm{F}}\hat{a}_{\mathrm{SH}}|n,m\rangle \tag{4.21}$$

$$\langle n,m|\hat{a}_{\mathrm{F}}\hat{a}_{\mathrm{F}}\hat{a}^{\dagger}_{\mathrm{F}}\hat{a}^{\dagger}_{\mathrm{F}}\hat{a}_{\mathrm{F}}\hat{a}_{\mathrm{F}}\hat{a}^{\dagger}_{\mathrm{SH}}\hat{a}_{\mathrm{SH}}\hat{a}^{\dagger}_{\mathrm{SH}}|N,0\rangle\langle N,0|\hat{a}^{\dagger}_{\mathrm{F}}\hat{a}^{\dagger}_{\mathrm{F}}\hat{a}_{\mathrm{SH}}|n,m\rangle \tag{4.22}$$

and fix $n=N-2$ and $m=1$. The diagrams related to these terms are the following

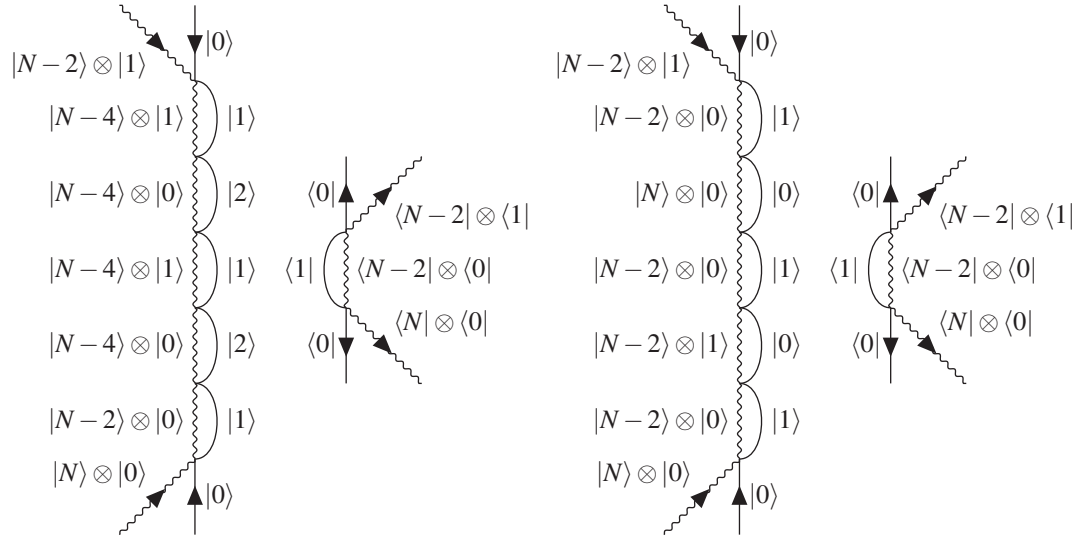

where the double-sided diagram on the right stands for the transition (4.21) while the second for (4.22). Note that in this case the output state, as mentioned above, is $|N-2,1\rangle\langle N-2,1|$. Therefore, these contributions play a role for the mean value of the second-harmonic photon number $\langle\hat{n}_2\rangle$ in Eq. (4.17). Indeed the transitions (4.21) and (4.22) correspond to the two terms in β_2 (Eq. (4.18)).
Here we use this raw quantum version of the double-sided quantum diagrams to better show the distinction among the three processes that we highlighted above, but note that they could be also employed to find all the processes occurring at a given perturbation order or even to retrieve the cross-section for a specific process. However, a generalization of this procedure to nonlinear phenomena more complicated than SHG would probably imply giving up with the virtual levels and considering proper propagators.
Finally, we remark that actually the creation processes are a particular case of the annihilation processes. We isolated them because they can be easily described through a general analytic formula and a simple diagram. This distinction will help in the following analysis.

4.3 Up-conversion probability

Now we focus on the *up-conversion probabilities*, i.e. the probability of converting $2k$ photons of the fundamental field into k second-harmonic photons. In this case, we exploited the Schrödinger picture because, for a small number of input photons, from a computational point of view it is easy to retrieve a large number of perturbative orders for the evolved state. On the contrary, in the case of a large input mean energy, achieving an analytic expression for the up-conversion probability is a hard task because the number of perturbative terms in the expansion of the second-harmonic state (see Eq. (4.6)) is generally insufficient to recognize the convergence to a known analytic function, as for the moments of the distribution. Moreover, there is no guarantee at all that such a function exists. However, there are some simple cases where a large number of perturbative orders (up to 30) can be computed and found to be the perturbative expansion of some analytical functions. As mentioned few lines above, this is the case if the number of up-converted photons k is assumed to be small. In particular, we found out that the probability $p_1(N,\tilde{\gamma})$ of generating a single second-harmonic photon from $2 \leq N < 6$ input photons converges, up to

the order 30, to a periodic function, i.e.

$$\begin{aligned} p_1(N,\tilde{\gamma}) &= |\langle N-2,1|\psi(\tilde{\gamma})\rangle\rangle|^2 \\ &= \frac{N!}{(N-2)!}\frac{1}{\zeta}\sin^2(\sqrt{\zeta}\tilde{\gamma}) \end{aligned} \tag{4.23}$$

where

$$\zeta = \sum_{k=1}^{N/2} k\frac{[N-2(k-1)]!}{(N-2k)!}.$$

The interplay among multiple creation and annihilation processes and their superposition is periodic up to 6 input photons, as shown in Fig. 4.1. For $N \geq 6$ this is no more true, but still $p_1(N,\tilde{\gamma})$ converges to an analytic function. The reason for the aperiodic behavior of $p_1(N,\tilde{\gamma})$ for $N \geq 6$ is due to the contribution of a larger number of processes at every order, resulting in a squared sum of different periodic functions. The ratio between the periods of these functions comes out to be incommensurable, so that their sum is not a periodic function.
The red solid lines in Fig. 4.1 stand for the numeric prediction retrieved by expanding the evolution operator as in Eq. (4.10). The black solid lines are the analytic functions in Eq. (4.10). Up to the thirtieth order, the expansion seems to converge to a closed form.

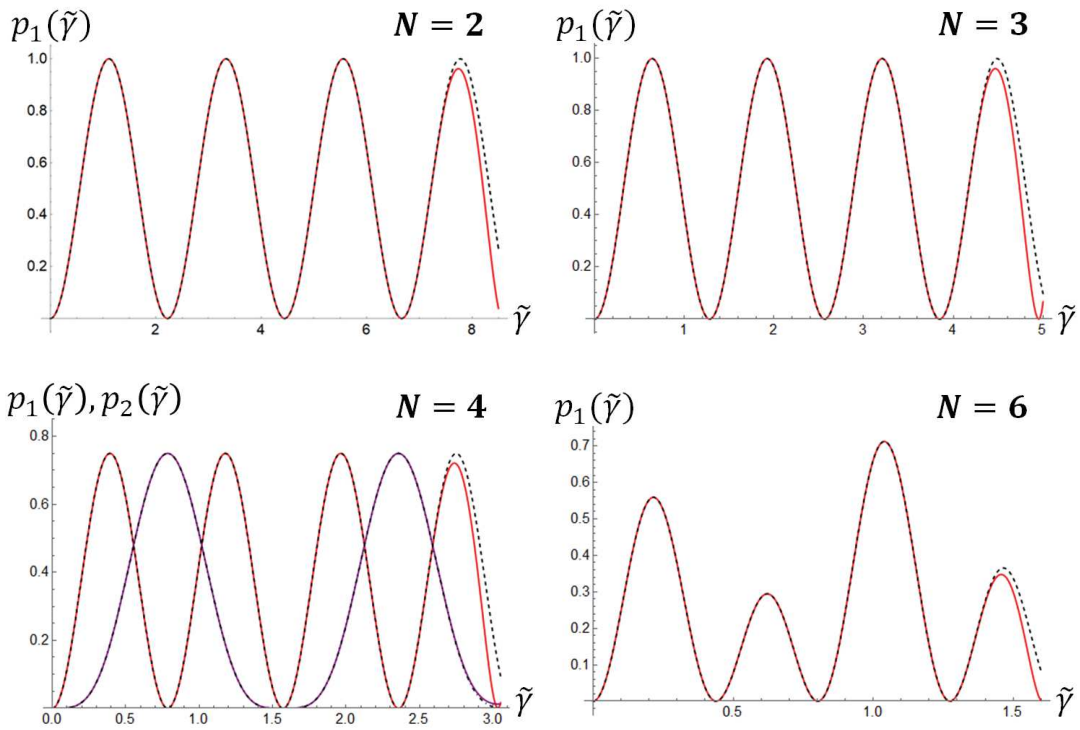

Fig. 4.1: Evolution of the probability of generating one SH photon from N pump photons. Solid red line: $\mathrm{Tr}[\hat{\rho}(\tilde{\gamma})\mathbb{1}_F \otimes \hat{n}^k]$ where $\hat{\rho}(\tilde{\gamma})$ is obtained by expanding $\hat{U}(\tilde{\gamma})$ in Eq. (4.6) up to $k = 30$. Dashed line: theoretical prediction from Eq. (4.23). The purple solid line in the bottom left panel is the probability of generating two photons from four. It is of the form $A\sin^4(\omega\tilde{\gamma})$.

4.4 Statistics of the output second-harmonic field

Here we focus on the transformation of the statistics for specific input states. We will choose a particular input statistics by suitably setting the coefficients c_n of the input density matrix in Eq. (4.5). In particular, we will investigate and compare the evolution of Fock, coherent, chaotic and squeezed states. Moreover, we will point out the role of the creation and annihilation processes together with their superpositions, outlined in Eq. (4.18). If our previous results are correct, one should expect that the SHG increases with the mean input photon-number (Eq. (4.16)), but is hampered by the annihilation and superposition processes (Eqs. (4.17, 4.18)).
In analogy with Eq. (4.12), the variance can be expressed as an expansion over the autocorrelation functions of the input field in Eq. (4.11), i.e.

$$\begin{aligned}\langle \Delta \hat{n}^2_{\mathrm{SH}} \rangle &= g^{(2)}_{\mathrm{F}} N^2 \tilde{\gamma}^2 - \frac{8}{3}\left(g^{(2)}_{\mathrm{F}} N^2 + 2 g^{(3)}_{\mathrm{F}} N^3 \right) \tilde{\gamma}^4 + o(\tilde{\gamma}^6) \\ &= \langle \hat{n} \rangle - \frac{4}{3}\left(g^{(2)}_{\mathrm{F}} N^2 + 2 g^{(3)}_{\mathrm{F}} N^3 \right) \tilde{\gamma}^4 + o(\tilde{\gamma}^6). \end{aligned} \tag{4.24}$$

As shown in Eq. (1.144), in general the second-order autocorrelation function can be expressed as a function of the first moments of the number operator as follows

$$g^{(2)} = 1 + \frac{\langle \Delta \hat{n}^2 \rangle - \langle \hat{n} \rangle}{\langle \hat{n} \rangle^2}. \tag{4.25}$$

Hence, the second-order autocorrelation function of the second-harmonic field can be easily found from Eqs. (4.17) and (4.24).
A couple of special remarks should be made about the zero-order of Glauber's function for the second-harmonic field. First, a trivial one: note that it is not given just by the zero order of the expansion of the moments, which is explicit if we rewrite Eq. (4.25) as

$$g^{(2)}_{\mathrm{SH}} = \frac{\langle \hat{n}^2_{\mathrm{SH}} \rangle - \langle \hat{n}_{\mathrm{SH}} \rangle}{\langle \hat{n}_{\mathrm{SH}} \rangle^2}. \tag{4.26}$$

where the first and the second moments are given by Eqs. (4.12) and (4.13). Indeed, some simple algebra shows that the zero-order of this function depends on the $\tilde{\gamma}^2$ and on the $\tilde{\gamma}^4$ order of the moments and, in particular, it reads

$$g^{(2)}_{\mathrm{SH}} = \frac{g^{(4)}_{\mathrm{F}}}{\left(g^{(2)}_{\mathrm{F}} \right)^2}, \tag{4.27}$$

which is a particular case of Eq. (1.61). We have proved it for our case in Appendix C. Also, note that in the difference $\langle \hat{n}^2_{\mathrm{SH}} \rangle - \langle \hat{n}_{\mathrm{SH}} \rangle$ not only the $\tilde{\gamma}^2$ orders cancel each other, but also all the superposition terms β_2 of Eq. (4.17). Therefore, no interference process contributes to this order. In the following, we will plot the second-order autocorrelation function for different input states together with the same computed in the absence of any interference and annihilation process. The goal is highlighting the role of the different processes. We will see that, as expected, for $\tilde{\gamma} = 0$ the two functions are coincident.
As a last remark, we would like to outline that the zero order of the second-harmonic autocorrelation function inherits the most relevant properties of the autocorrelation function for the fundamental field, which is reasonable, since it is the less negligible term in the expansion. We will better specify this fact case by case.

4.4.1 Fock state

From Eq. (4.25) we immediately get

$$g_{\mathrm{SH}}^{(2)} = \frac{(N-2)(N-3)}{N(N-1)}(1+4\tilde{\gamma}^2) + o(\tilde{\gamma}^4). \tag{4.28}$$

which is consistent with the theoretical expectations. Indeed, by exploiting the expression of Glauber's functions for Fock states retrieved in Appendix B, we see that the second- and fourth-order autocorrelation functions respectively read

$$\begin{aligned} g_{\mathrm{F}}^{(2)} &= 1 - \frac{1}{N} \\ g_{\mathrm{F}}^{(4)} &= \frac{1}{N^3}\frac{(N-1)!}{(N-4)!} \end{aligned}$$

so that, applying Eq. (4.27), the zero order of the expansion for the expected second-harmonic autocorrelation function must be

$$g_{\mathrm{SH}}^{(2)} = \frac{(N-2)(N-3)}{N(N-1)} \tag{4.29}$$

which is consistent with Eq. (4.28). Note that $g_{\mathrm{F}}^{(2)}$ is not definite for $N=0$ and is null for $N=1$, while it tends to 1 if $N \to \infty$. Similarly, $g_{\mathrm{SH}}^{(2)}$ is not definite for $N=0$ or 1, but is null for $N=2$ and 3 and converges to 1 as $N \to \infty$.

4.4.2 Coherent state

As to the case of a coherent input state, one just needs to require the coefficients in Eq. (4.5) to be given by

$$c_n = e^{-|\alpha|^2/2}\frac{\alpha^n}{\sqrt{n!}} \tag{4.30}$$

where $|\alpha|$ is the amplitude of the generic coherent state $|\alpha\rangle = e^{-|\alpha|^2/2}\sum_{k=0}^{\infty}\left(\alpha^k/\sqrt{k!}\right)|k\rangle$.
Up to $k=2$, the output second-order autocorrelation function reads

$$g_{\mathrm{SH}}^{(2)} = 1 - \frac{4}{3}\tilde{\gamma}^2 + o(\tilde{\gamma}^4) \tag{4.31}$$

thus showing that the second-harmonic output state displays a sub-Poissonian statistics at the first perturbative order. Therefore, the second-harmonic field from a coherent pump field is expected to be endowed with quantum correlations. This effect is due to the very nature of coherent light, whose statistics, as mentioned in the first chapter, is the boundary case between super- and sub-Poissonian light, by definition. Then, heuristically speaking, the effect of converting $2k$ input photons into k second-harmonic photons results in an anti-bunching effect, so that the output statistics is sub-Poissonian. It is a well-known result [110, 111], which was also experimentally tested [100, 101].
Moreover, note that the perturbative orders in the expansion of the moments (see for instance Eq. (4.17)) contribute only if the input number of photons is large enough, i.e. you need at least 2j input photons to see the j-th order. However, also the conversion efficiency depends on N. In particular, we found from Eq. (4.16) that η tends to a growing function of N, i.e. $\eta \sim 1/[2(1-\tilde{\gamma}^2 N)]$. But then we find that at higher perturbative orders we can convert only large numbers of photons and, thus, they are more likely to be converted. This is the reason why we see in Fig. 4.2 that, in the case where only creation processes are considered (red dot-dashed line), quantum correlations increase as a function of $\tilde{\gamma}$.

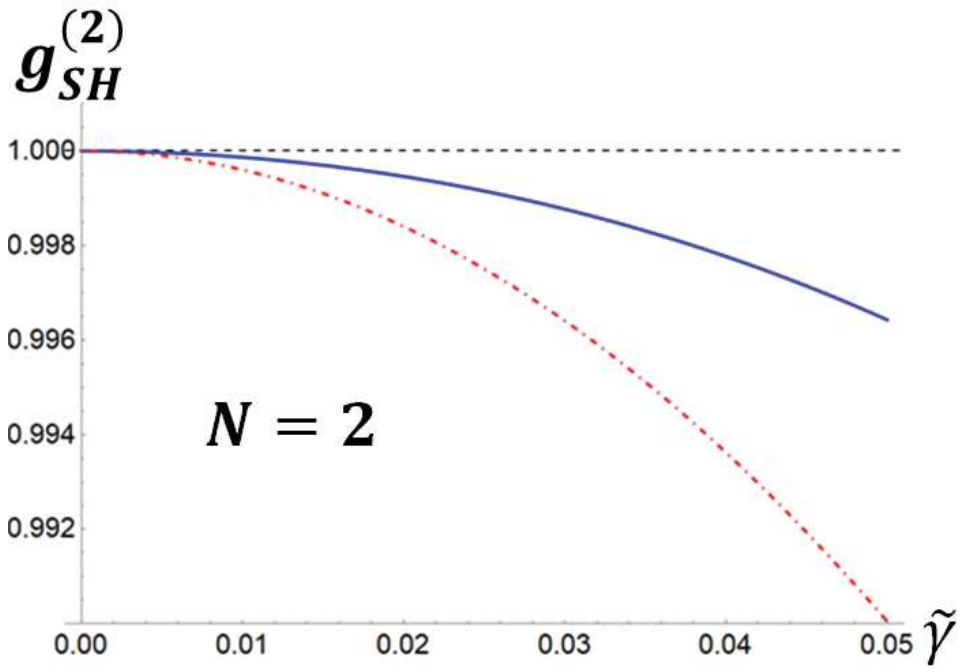

Fig. 4.2: Coherent input state. Solid blue line: second-harmonic autocorrelation function, from Eq. (4.31). Dot-dashed line: second-harmonic autocorrelation function in the absence of annihilation processes and superpositions. The function are plotted for an input mean value $N = 2$.

The second-order autocorrelation function of the SHG process in Eq. (4.17) is plotted as the blue line. The annihilation processes and the interference between different processes, as expected, contribute to reduce quantum correlations and, consequently, the nonclassicality of the output state.
However, as expected, we do not have this contribution for $\tilde{\gamma} = 0$. We do not insist on the analogy between $g^{(2)}_{\rm SH}(\tilde{\gamma} = 0)$ and $g^{(2)}_{\rm F}$ because in this case is self-evident: $g^{(2)}_{\rm SH}(\tilde{\gamma} = 0) = g^{(2)}_{\rm F} = 1$.

4.4.3 Chaotic state

Let us write again the photon-number distribution for multi-mode thermal light, already expressed in Eq. (1.114), as

$$p(n) = \binom{n+\mu-1}{n} \frac{N_{th}^n}{(N_{th}+1)^{n+\mu}}. \tag{4.32}$$

where the mean number N_{th} is the average boson-number from the Bose-Einstein statistics

$$p(n) = \frac{N_{th}^n}{(N_{th}+1)^{n+1}}. \tag{4.33}$$

so that the mean value and the variance are here expressed as

$$N = \mu N_{th} \tag{4.34}$$
$$\Delta N^2 = \mu N_{th}(N_{th}+1). \tag{4.35}$$

We also recall that a generic input state of the SHG process with multi-mode thermal statistics is the mixed state

$$\hat{\rho}_0 = \sum_n p_\mu(n)|n,0\rangle\langle n,0|.$$

Here, we explicitly write the mean value and the variance of the output statistics since this case is amenable to a comparison with the classical one:

$$\langle \hat{n}_{\rm SH}\rangle = \frac{(\mu+1)}{\mu}N^2\tilde{\gamma}^2 - \frac{2}{3}\frac{(\mu+1)}{\mu}N^2\left[1+2\frac{\mu+2}{\mu}N\right]\tilde{\gamma}^4 + o(\tilde{\gamma}^6) \tag{4.36}$$

$$\langle \Delta\hat{n}^2_{\rm SH}\rangle = \langle \hat{n}_{\rm SH}\rangle + 2\frac{(2\mu+3)(\mu+1)}{\mu^3}N^4\tilde{\gamma}^4 + o(\tilde{\gamma}^6). \tag{4.37}$$

We remark that $\langle \hat{n}_{\rm SH}\rangle$ and $\langle \Delta\hat{n}^2_{\rm SH}\rangle$ in Eqs. (4.36) and (4.37) exhibit the same dependence on the number of modes μ and on the input mean value N retrieved in Eqs. (1.52) and (1.54) for the classical case.
Thus, at the first order we find again the moments of a superthermal distribution. Note that, at higher orders we still have that annihilation and superposition processes result in a reduction of correlations, as shown in Fig. 4.3. From Eqs. (4.36) and (4.37), the second-harmonic autocorrelation function reads

$$g^{(2)}_{\rm SH} = \frac{(\mu+2)(\mu+3)}{\mu(\mu+1)}\left[1-\frac{4}{3}\left(1+4\frac{N}{\mu}\right)\tilde{\gamma}^2\right] + o(\tilde{\gamma}^4). \tag{4.38}$$

If we compare the second panel of Fig. (4.3) with Fig. (4.2), we find again that if the number of modes is large we are left with a Poissonian statistics. Again, the contribution of the only creation processes (dashed red line) highlights the effect of the back-conversion, which increases as $\tilde{\gamma}$ grows while it is absent for $\tilde{\gamma}=0$. Note that the second-harmonic autocorrelation function inherits the dependence on the number of modes from the fundamental one.

4.4.4 Squeezed state

The autocorrelation function for a single-mode squeezed state, defined in Eq. (1.119), is given by

$$g^{(2)}_{\rm F} = 3 + \frac{1}{N} \tag{4.39}$$

where here $N = |\nu|^2$. In this case, we found that the second-harmonic autocorrelation function reads

$$g^{(2)}_{\rm SH} = \frac{3[3+5N(5+7N)]}{(1+3N)^2} - \frac{12}{(1+3N)^3}\left[1+5N(9+43N^2+87N^2+56N^3)\right]\tilde{\gamma}^2 + o(\tilde{\gamma}^4). \tag{4.40}$$

Firstly, we remark that the order zero in Eq. (4.40) is the usual first approximation of the second-harmonic autocorrelation function, which can be obtained through Eq. (4.27). As expected, by inspecting the autocorrelation functions in the presence (blue line) and in the absence (red line) of superposition processes for $\tilde{\gamma}=0$ in Fig. (4.4), we find that no superposition process occurs at this order. We retrieve here the dependence on N shared by $g^2_{\rm F}$. In particular, for large N, both approach a plateau. But while the squeezed-state autocorrelation function tends to 3, the asymptotic value in the second-harmonic case is larger, i.e. 35/3.
For what concerns the evolution of the correlations, as usual, the multiple back-conversion events occurring for $\tilde{\gamma}>0$ contribute to reduce them.
The large fluctuations retrieved for this SH field are a signature of the quantum properties of both the input state and the SHG process: since the squeezed state is a superposition of pairs of photons (Eq. (1.119)) and the process always annihilates even numbers of pump photons, then SHG enhances the correlations of the input statistics.

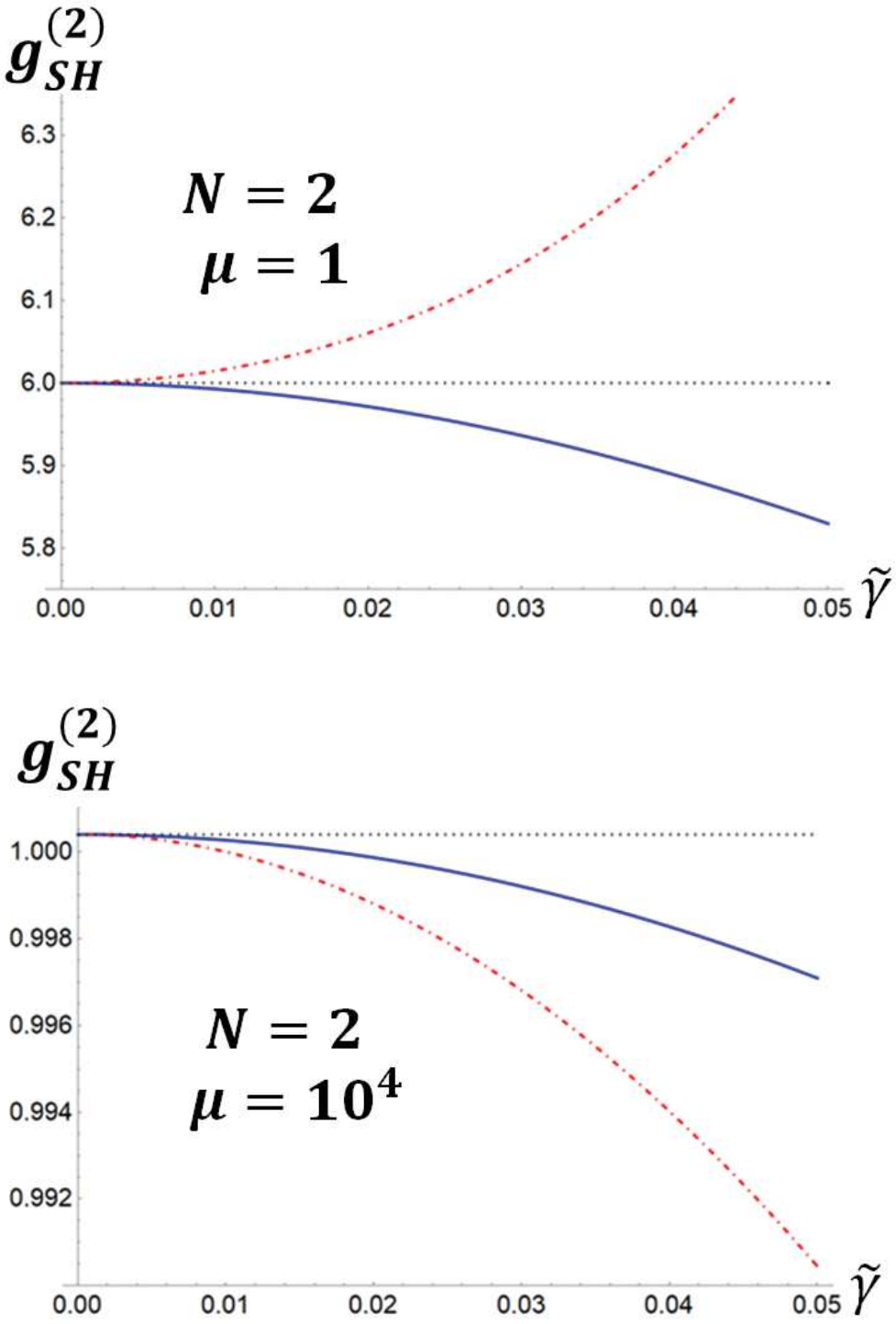

Fig. 4.3: Chaotic input state. Solid blue line: second-harmonic autocorrelation function, given by Eq. (4.38). Dashed line: second-harmonic autocorrelation function in the absence of annihilation processes and superpositions.

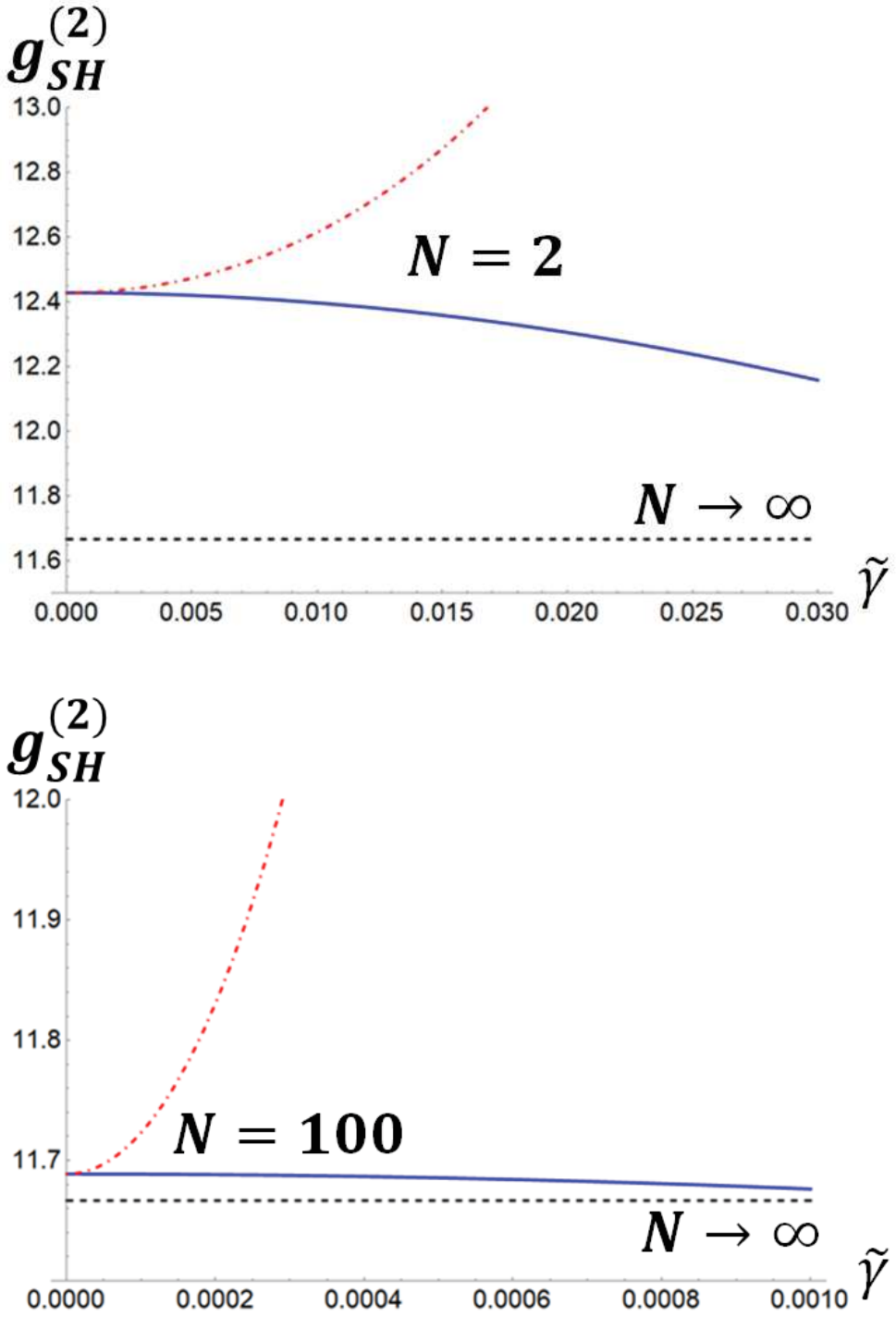

Fig. 4.4: Squeezed input state. Solid blue line: second-harmonic autocorrelation function, given by Eq. (4.40). Dashed line: second-harmonic autocorrelation function in the absence of annihilation processes and superpositions.

4.5 Concluding remarks

Here we investigated the statistics of the second-harmonic field from a quantum point of view. We had introduced the classical results in the first chapter, where the transformation of the light statistics via SHG was retrieved for Poissonian and chaotic fields by exploiting an approximation of the output intensity which is consistent with the more general results obtained by Armstrong et al. These results, also, are based on an assumption, i.e. the slowly varying amplitude approximation in Eq. (1.9). Our quantum description in the cases of coherent and multi-mode thermal input states reproduces the classical predictions. This fact is not trivial, since it implies that the perturbative approach to the quantum dynamics of SHG somehow is equivalent to the classical approximations. In this sense, our results open the way to a quantum formalization of those approximations.
The most controversial result presented here is the decomposition of the SHG in three sub-processes, which could be deemed as a mere interpretation. However, we showed that the evolution of the second-harmonics distributions, investigated through the second-order autocorrelation functions, is consistent with this description for every input state we analyzed.
Our findings on the up-conversion probabilities are promising. The existence of a closed form for the simple cases we investigated stimulates further investigation in this direction. In particular, numeric methods could help to find a large number of perturbative orders also for less trivial input states so that an analytic expression for more complicated up- and down-conversion probabilities may be found. On the other hand, it is not trivial that inferences from perturbative expansion are reliable. Therefore, an alternative to the Hamiltonian approach should be searched too, so that an analytic form for the second-harmonic moments could be found.
Last but not the least, here we put forward the perturbative approach by providing a further perturbative order to the expansion of the moments and by retrieving the expression of the second-harmonic autocorrelation functions for some significant input states. However, in this case it was not possible to find a closed form for these quantities.

4.6 Appendix A

Here we state the theorem which guarantees that the perturbative expansion of the output mean photon-number is an expansion over Glauber's autocorrelation functions of the input state $g_{\mathrm{F}}^{(n)}$.

Theorem 1. *Given a Hamiltonian $\hat{H}(\hat{a}_{\mathrm{F}}, \hat{a}_{\mathrm{F}}^{\dagger}, \hat{a}_{\mathrm{SH}}, \hat{a}_{\mathrm{SH}}^{\dagger})$ of the form 4.1 with $N = \langle \hat{a}_{\mathrm{F}}^{\dagger}\hat{a}_{\mathrm{F}} \rangle$ and $\langle \hat{n} \rangle = \hat{a}_{\mathrm{SH}}^{\dagger}\hat{a}_{\mathrm{SH}}$ and assuming the initial condition $\hat{a}_{\mathrm{SH}}^{\dagger}(0) = \hat{a}_{\mathrm{SH}}(0) = 0$, then every perturbative order of $\langle \hat{n} \rangle$ can be expressed as a linear combination of the fundamental mode Glauber's autocorrelation functions $g_{\mathrm{F}}^{(n)}$.*

Proof. All the terms which are a combination of $(\hat{a}_{\mathrm{SH}}^{\dagger})^k$ or $\hat{a}_{\mathrm{SH}}^k$, with $k \in \mathbb{N}$, do not contribute to $\langle \hat{n} \rangle$ because the state is empty on the SH mode and

$$\langle 0|(\hat{a}_{\mathrm{SH}}^{\dagger})^k|0\rangle = \langle 0|\hat{a}_{\mathrm{SH}}^k|0\rangle = 0.$$

Thus, a term survives at the k-th order in the expansion Eq. (4.3) just if $\hat{a}_{\mathrm{SH}}^{\dagger}$ and $\hat{a}_{\mathrm{SH}}$ commute, so that they are transformed via commutation relations into the identity multiplied for the unchanged operators of the fundamental mode. *These terms are the only ones surviving in the mean value.*
Among the survived terms, the commutation relations select just the combinations having the same number of $\hat{a}_{\mathrm{F}}$ and $\hat{a}_{\mathrm{F}}^{\dagger}$ operators because of the form Eq. 4.1 of the Hamiltonian and of the operator $\hat{n}$.
Moreover, note that the odd derivatives of $\hat{n}$ all depend on the SH operators, which means that they do not contribute to $\langle \hat{n} \rangle$.
Therefore, the only surviving terms at a given order j are $(\hat{a}_{\mathrm{F}}^{\dagger})^k \hat{a}_{\mathrm{F}}^k$, where the exponents k are increased

by two for every even derivative, but lowered by one for every odd derivative, so that $k \leq \frac{j}{2}+1$. More explicitly, k is increased by two for every even derivative because the Hamiltonian contributes with $(\hat{a}_{\rm SH}^{\dagger})^2$ and $\hat{a}_{\rm SH}^2$ and these terms do not commute; on the other hand, it is decreased by one for every odd derivative because in this case no new surviving terms are generated.
Hence, we can conclude that $\langle \hat{n} \rangle$ is a linear combination of $\langle (\hat{a}_{\rm F}^{\dagger})^k \hat{a}_{\rm F}^k \rangle = \tilde{\gamma}^k g_{\rm F}^{(k)} N^k$. □

4.7 Appendix B

The first and second moments of the second-harmonic distribution in Eqs. (4.12) and (4.13) can be expressed for a given input state by specifying the corresponding kth-order autocorrelation functions $g_{\rm F}^{(k)}$. In the case of a Fock state $|N\rangle$, we get

$$\begin{aligned} g_{\rm F}^{(k)}(N) &= \frac{\langle N| : \hat{n}_{\rm F}^k : |N\rangle}{\langle N|\hat{n}_{\rm F}|N\rangle^k} = \\ &= \frac{\langle N|(\hat{a}_{\rm F}^{\dagger})^k \hat{a}_{\rm F}^k |N\rangle}{\langle N|\hat{n}_{\rm F}|N\rangle^k} = \\ &= \frac{N!}{N^k (N-k)!} \end{aligned} \tag{4.41}$$

where in the last line we have used $\hat{a}^k|N\rangle = \sqrt{N!/(N-k)!}|N-k\rangle$, which is straightforward from Eqs. (1.102).
Here, the transformation of the number-state basis is the starting point for the evolution of other light distributions. Hence, the search for the implications of the Theorem 1 given an input number state. One of these is expressed in the following corollary of Theorem 1.

Corollary 1. *If the fundamental input mode is a Fock state* $|\psi(0)\rangle = |N,0\rangle$*, then*

$$\langle \hat{n}_{\rm SH} \rangle \sim N \sum_j (\tilde{\gamma}^2 N)^j. \tag{4.42}$$

Proof. $\langle (\hat{a}^{\dagger})^k \hat{a}^k \rangle = N!/(N-k)! \sim N^k$. The highest k at the order j is $\frac{j}{2}+1$, but, since the odd j terms do not contribute, we only sum over the even j orders and replace j with $2j$. □

4.8 Appendix C

Up to the first order, the autocorrelation function can be approximated to Eq. (4.27). The result is obtained through a first-order assumption on the modes, i.e. $a_{\rm SH} = \gamma a_{\rm F} a_{\rm F}$. Then, from Eq. (4.25), we find

$$\begin{aligned} g_{\rm SH}^{(2)} &= \frac{\langle : \hat{n}_{\rm SH} \hat{n}_{\rm SH} : \rangle}{\langle : \hat{n}_{\rm SH} : \rangle^2} = \frac{\langle \hat{a}_{\rm SH}^{\dagger} \hat{a}_{\rm SH}^{\dagger} \hat{a}_{\rm SH} \hat{a}_{\rm SH} \rangle}{\langle \hat{a}_{\rm SH}^{\dagger} \hat{a}_{\rm SH} \rangle^2} = \\ &= \frac{\langle \hat{a}_{\rm F}^{\dagger} \hat{a}_{\rm F}^{\dagger} \hat{a}_{\rm F}^{\dagger} \hat{a}_{\rm F}^{\dagger} \hat{a}_{\rm F} \hat{a}_{\rm F} \hat{a}_{\rm F} \hat{a}_{\rm F} \rangle}{\langle \hat{a}_{\rm F}^{\dagger} \hat{a}_{\rm F}^{\dagger} \hat{a}_{\rm F} \hat{a}_{\rm F} \rangle^2} = \\ &= \frac{\langle \hat{a}_{\rm F}^{\dagger} \hat{a}_{\rm F}^{\dagger} \hat{a}_{\rm F}^{\dagger} \hat{a}_{\rm F}^{\dagger} \hat{a}_{\rm F} \hat{a}_{\rm F} \hat{a}_{\rm F} \hat{a}_{\rm F} \rangle}{\langle \hat{a}_{\rm F}^{\dagger} \hat{a}_{\rm F} \rangle^4} \left(\frac{\langle \hat{a}_{\rm F}^{\dagger} \hat{a}_{\rm F} \rangle^2}{\langle \hat{a}_{\rm F}^{\dagger} \hat{a}_{\rm F}^{\dagger} \hat{a}_{\rm F} \hat{a}_{\rm F} \rangle} \right)^2 = \frac{g_{\rm F}^{(4)}}{\left(g_{\rm F}^{(2)} \right)^2}. \end{aligned} \tag{4.43}$$

5

Conclusions and outlooks

This thesis is focused on our last-three-year research, covering topics which are different for what concerns the field and the investigation methods.

On the one hand, we tested the new generation of SiPMs for Quantum Optics and Quantum Information. In the second chapter, we presented a specific characterization of these devices aiming at a fair reconstruction of the statistics of the detected field and optimized their response by engineering the duration of the integration gate. Eventually, in the third chapter, we employed them to reveal the entanglement of nonclassical states of light, i.e. TWBs generated via PDC.

On the other hand, we investigated the problem of a quantum description of the SHG process. In the fourth chapter, we explored the output statistics given different input states of light by exploiting perturbative methods and provided some new analytical results for the up-conversion amplitudes.

The results we obtained in both the research lines are promising.

The new class of photodetectors we analyzed has shown to satisfy the necessary conditions for being employed in Quantum Optics applications. We have proved that SiPMs can reveal the quantum correlations of entangled states of light as well as the sub-Poissonian statistics of conditional states. Moreover, we have found that the impact of the nonidealities of these detector can be controlled and limited, leading to better results for these applications. Our optimization strategy can be further improved by employing a proper peak-and-hold circuit replacing the digitizer. Such a scheme should give access to an online shot-by-shot determination of the detected-photon number. In particular, the new acquisition system should also allow for an online reconstruction of the light statistics.
These results open the possibility of using SiPMs for quantum sensing and quantum estimation. For instance, they could be tested in the latest multi-parameter estimation experiments, e.g. for the application to the rotation of light polarization in sugary solutions limited by reduced visibility [118] or in the presence of a dynamic process [119].
Furthermore, the future perspectives for the applications of SiPMs in Quantum Optics are not limited to direct-detection schemes. Olivares et al. [115] recently proved that PNR detectors can be successfully employed in a homodyne-like scheme for the tomography of quantum light states. Furthermore, homodyning have been shown to be more efficient than direct schemes as to the detection of quantum states in the presence of losses and phase noise [116]. The extension of this analysis to the case of homodyne-like detection and an experimental test with SiPMs could be fruitful for Quantum Communication implementations [117].

For what concerns our results on quantum SHG, we tried to outline the intrinsic structure of the process. It may be possible that the glimpse of this structure will help to find more general analytic predictions about the up-conversion probabilities, since our results, till now, are restricted to simple cases. However, a general expression for the perturbative second-harmonic Glauber's autocorrelation function still misses. Finally, we note that the convergence of the up-conversion probabilities to well-known analytic functions feeds the hope that the same may be possible for the output statistics.
The perturbative approach could be extended to the analysis of PDC in the absence of the parametric approximation, since the Hamiltonian of the process (Eq. (1.126)) shares the same structure as the interaction Hamiltonian describing SHG (Eq. (4.1)). Basically, this is the reason why the squeezing can be observed also via SHG.
As a last remark on possible future perspectives, we address the classical description of SHG described by Armstrong et al. [21] (see the first chapter for details). Note that the slowly-varying-amplitude approximation in Eq. (1.9), which is used to linearize the nonlinear equations, may correspond to a WKB approximation in the quantum case [120]. Further investigations are needed.

This is the end of our journey. Aware of being a poor player that struts and frets his hour upon the stage and then is heard no more, I hope that this work may have interested the reader anyway. To me, it's been deep and free as the sea.

Bibliography

[1] Einstein, A. Über einen die Erzeugung und Verwandlung des Lichtes betreffenden heuristischen Gesichtspunkt. *Ann. d. Phys.* **1905**, *32*, 132-148.

[2] Lamb, W. E Jr., Scully, M. O. The photoelectric effect without photons. *Polarisation matière et rayonnement* **1969**, 363-369.

[3] Einstein, A. The Quantum Theory of Radiation. *Physikalische Zeitschrift* **1917**, *18*, 1-15.

[4] Graffi, D. *Rendiconti del Seminario Matematico della Università di Padova* **1936**, *7*, 36.

[5] Bloembergen, N. *Nonlinear Optics*; World Scientific Publishing Co. Pte. Ltd., 1965.

[6] Franken, P. A., Hill, A. E., Peters, C. W., and Weinreich, G. *Phys. Rev. Lett.* **1961**, *7*, 118–120.

[7] Kaiser, W. and Garrett C. G. B. Two-photon excitation in $CaF_2 : Eu^{2+}$. *Phys. Rev. Lett.* **1961**, *7*, 229-231.

[8] Kimble, H. J., Dagenais, M. and Mandel, L. Photon Antibunching in Resonance Fluorescence. *Phys. Rev. Lett.* **1977**, *39*, 691-695.

[9] Haderka, O., Peřina, J. Jr., Hamar, M. and J. Peřina, Direct measurement and reconstruction of nonclassical features of twin beams generated in spontaneous parametric down-conversion. *Phys. Rev. A* **2005**, *71*, 1-5.

[10] Jedrkiewicz, O., Jiang, Y.-K., Brambilla, E., Gatti, A., Bache, M., Lugiato, L. A. and Di Trapani, P. Detection of Sub-Shot-Noise Spatial Correlation in High-Gain Parametric Down Conversion. *Phys. Rev. Lett.* **2004**, *93* 1-4.

[11] Mičuda, M., Haderka, O. and Ježek, M. High-efficiency photon-number-resolving multichannel detector. *Phys. Rev. A* **2008**, *78*, 1-4.

[12] Avenhaus, M., Laiho, K., Chekhova, M. V. and Silberhorn, C. Accessing Higher Order Correlations in Quantum Optical States by Time Multiplexing. *Phys. Rev. Lett.* **2010**, *104*, 1-4.

[13] Kim, J., Takeuchi, S., Yamamoto, Y. and Hogue, H. H. Multiphoton detection using visible light photon counter. *Appl. Phys. Lett.* **1999**, *74*, 902-904.

[14] Stevens, M. J., Baek, B., Dauler, E. A., Kerman, A. J., Molnar, R. J., Hamilton, S. A., Berggren, K. K., Mirin, R. P. and Nam, S. W. High-order temporal coherences of chaotic and laser light. *Opt. Express* **2010**, *18*, 1430-1437.

[15] Bondani, M., Allevi, A., Agliati, A. and Andreoni, A. Self-consistent characterization of light statistics. *J. Mod. Opt.* **2009**, *56*, 226-231.

[16] Lita, A. E., Miller, A. J. and Nam, S. W. Counting near-infrared single photons with 95% efficiency. *Opt. Expr.* **2008**, *16*, 3032-3040.

[17] Caccia, M., Nardo, L., Santoro, R. and Schaffhauser, D. Silicon Photomultipliers and SPAD imagers in biophotonics: Advances and perspectives. *Nuclear Instruments and Methods in Physics Research Section A: Accelerators, Spectrometers, Detectors and Associated Equipment* **2019**, *926*, 101-117.

[18] Grodzicka-Kobylka, M., Moszyński, M. and Szczęśniak, T. Silicon photomultipliers in gamma spectroscopy with scintillators. *Nuclear Instruments and Methods in Physics Research Section A: Accelerators, Spectrometers, Detectors and Associated Equipment* **2019**, *926*, 129-147.

[19] Simon, F. Silicon photomultipliers in particle and nuclear physics. *Nuclear Instruments and Methods in Physics Research Section A: Accelerators, Spectrometers, Detectors and Associated Equipment* **2019**, *926*, 85-100.

[20] Bisogni, M. G., Del Guerra, A. and Belcari N. Medical applications of silicon photomultipliers. *Nuclear Instruments and Methods in Physics Research Section A: Accelerators, Spectrometers, Detectors and Associated Equipment* **2019**, *926*, 118-128.

[21] Armstrong, J. A., Bloembergen, N., Ducuing J. and Pershan, P. S. Interactions between Light Waves in a Nonlinear Dielectric. *Phys. Rev.* **1962**, *127*, 1918–1939.

[22] Boyd, R. W. *Nonlinear Optics*, Third Edition; Academic Press, Elsevier, 2008.

[23] Yariv, A. *Quantum Electronics*, Second Edition; California Institute of Technology, 1975.

[24] Yariv, A. *Optical Electronics*, Fourth Edition.

[25] Qu, Y. and Singh, S. Measurements of photon statistics in second-harmonic generation. *Phys. Rev. A* **1995**, *51*, 2530-2536.

[26] Allevi, A., Cassina, S., and Bondani, M. Super-thermal light for imaging applications. *Quantum Meas. Quantum Metrol.* **2017**, *4*, 26-34.

[27] Allevi, A. and Bondani, M. Direct detection of super-thermal photon-number statistics in second-harmonic generation. *Opt. Lett.* **2015**, *40*, 3089-3092.

[28] Hanbury Brown, R. and Twiss, R. Q. Interferometry of the intensity fluctuations in light - I. Basic theory: the correlation between photons in coherent beams of radiation. *Proc. R. Soc. Lond. A* **1957**, *242*, 300-324.

[29] Mandel, L. and Wolf, E. *Optical Coherence and Quantum Optics*; Cambridge University Press, 1995.

[30] Spasibko, K. Yu., Kopylov, D. A., Krutyanskiy, V. L., Murzina, T. V., Leuchs, G. and Cekhova, M. V. Multiphoton effects enhanced due to ultrafast photon-number fluctuations. *Phys. Rev. Lett.***2017**, *119*, 1-5.

[31] Srednicki, M. *Quantum Field Theory*; Cambridge University Press, 2012.

[32] Hanamura, E., Kawabe, Y. and Yamanaka, A. *Quantum Nonlinear Optics*; Springer-Verlag Berlin Heidelberg, 2007.

[33] Puri, R. R. *Mathematical methods of quantum optics*; Springer-Verlag, 2001.

[34] Brambilla, E., Gatti, A. , Bache, M. and Lugiato, L. A. Simultaneous near-field and far-field spatial quantum correlations in the high-gain regime of parametric down-conversion. *Phys.Rev.A* **2004**, *69*, 1-19.

[35] Hamar, M., Peřina, J., Haderka, O. and Michálek, V. Transverse coherence of photon pairs generated in spontaneous parametric down-conversion. *Phys.Rev.A* **2010**, *81*, 1-10.

[36] Glauber, R. J., Coherent and Incoherent States of the Radiation Field. *Phys. Rev.* **1963**, *131*, 2766-2788.

[37] Glauber, R. J., The Quantum Theory of Optical Coherence. *Phys. Rev.* **1963**, *130*, 2529-2539.

[38] Ferraro, A., Olivares, S., and Paris, M. G. A. *Gaussian states in continuous variable quantum information*; Biliopolis, Napoli, 2005.

[39] Allevi, A., and Bondani, M. Nonlinear and quantum optical properties and applications of intense twin-beams, *Adv. in At., Mol. and Opt. Phys.* **2017** *66*, 49-110.

[40] Klyshko, D., Chekhova, N., and Kulik, S., *Physical foundation of quantum electronics*; World Scientific Publishing Company, Singapore, 2011.

[41] Agliati, A., Bondani, M., Andreoni, A., De Cillis, G. and Paris, M. G. A. Quantum and classical correlations of intense beams of light investigated via joint photodetection. *Journ. of Opt. B* **2005**, *7*, S652–S663.

[42] Allevi, A., Bondani, M., and Andreoni, A. Photon-number correlations by photon-number resolving detectors. *Opt. Lett.* **2010**, *35*, 1707–1709.

[43] Helstrom, C. W. *Quantum Detection and Estimation Theory*; Academic Press, New York, 1976.

[44] Bachor, H. A., and Ralph, T. C. *A Guide to Experiments in Quantum Optics*; WILEY-VCH Verlag, 2004.

[45] Kelley, P. L., and Kleiner, W. H. Theory of Electromagnetic Field Measurement and Photoelectron Counting. *Phys. Rev.* **1964**, *136*, 316-334.

[46] Leonhardt, U. *Measuring the Quantum State of Light*; Cambridge University Press, Cambridge, 1997.

[47] Vogel, W. and Welsch, D.-G. *Quantum Optics*; Vch Verlagsgesellschaft Mbh, 2006.

[48] Horodecki, R., Horodecki, P., Horodecki, M. and Horodecki, K. Quantum entanglement. *Rev. Mod. Phys.* **2009**, *81*, 865-942.

[49] Chesi, G., Allevi, A. and Bondani, M. Autocorrelation functions: a useful tool for both state and detector characterisation. *Quantum Meas. Quantum Metrol.* **2019**, *6*, pp. 1-6.

[50] Allevi, A., Olivares, S. and Bondani, M. Measuring high-order photon-number correlations in experiments with multimode pulsed quantum states. *Phys. Rev. A* **2012**, *85*, 1-5.

[51] Allevi, A. and Bondani, M. Antibunching-like behavior of mesoscopic light. *Sci. Rep.* **2017**, *7*, 1-10.

[52] Paris, M. G. A., Cola, M. and Bonifacio, R. Quantum-state engineering assisted by entanglement. *Phys. Rev. A* **2003**, *67*, 1-10.

[53] Paris, M. G. A. The modern tools of quantum mechanics. *Eur. Phys. J. Spec. Top.* **2012**, *203*, 61-86.

[54] Allevi, A., Andreoni, A., Beduini, F. A., Bondani, M., Genoni, M. G., Olivares, S. and Paris, M. G. A. Conditional measurements on multimode pairwise entangled states from spontaneous parametric downconversion. *EPL* **2010**, *92*, 1-6.

[55] Lamperti, M., Allevi, A., Bondani, M., Machulka, R., Michálek, V., Haderka, O. and Peřina, J. Jr. Optimal sub-Poissonian light generation from twin beams by photon-number resolving detectors. *J. Opt. Soc. Am. B* **2014**, *31*, 20-25.

[56] Klyshko, D. The nonclassical light. *Phys.-Usp.* **1996**, *39*, 573-596.

[57] Akindinov, A. V., Martemianov, A. N., Polozov, P. A., Golovin, V. M. and Grigoriev, E. A. New results on MRS APDs. *Nucl. Instr. and Meth.* in *Phys. Res. A* **1997**, *387*, 231–234 and references therein.

[58] Bondarenko, G., Dolgoshein, B, Golovin, V., Ilyin, A., Klanner, R., Popova, E. Limited Geiger-mode silicon photodiode with very high gain. *Nucl. Phys. B* **1998**, *61 B*, 347-352 and references therein.

[59] Buzhan, P., Dolgoshein, B., Ilyin, A., Kantserov, V., Kaplin, V., Karakash, A., Pleshko, A., Popova, E., Smirnov, S., Volkov, Yu. An advanced study of silicon photomultiplier. *ICFA Instrum. Bull.* **2001**, *23*, 28-42.

[60] Piemonte, C. A new silicon photomultiplier structure for blue light detection. *Nucl. Instrum. Methods A* **2006**, *568*, 224-232.

[61] Cova, S., Lacaita, A., Ghioni, M., Ripamonti, G., and Louis, C. A. 20 ps timing resolution with single-photon avalanche diodes. *Rev. Sci. Instrum.* **1989**, *60*, 1104–1110.

[62] Cova, S., Ghioni, M., Lacaita, A. L., Samori, C., and Zappa, F. Avalanche photodiodes and quenching circuits for single-photon detection, *Appl. Opt.* **1996**, *35*, 1956—1976.

[63] https://www.hamamatsu.com/eu/en/index.html

[64] https://www.picoquant.com/products/category/picosecond-pulsed-driver/pdl-800-d-picosecond-pulsed-diode-laser-driver-with-cw-capability

[65] Nagy, F., Mazzillo, M., Renna, L., Valvo, G., Sanfilippo, D., Carbone, B., Piana, A., Fallica, G., Molnar, J. Afterpulse and delayed crosstalk analysis on a STMicroelectronics silicon photomultiplier. *Nucl. Instrum. Methods Phys. Res. A* **2014**, *759*, 44–49.

[66] Eckert, P., Schultz-Coulon, H. C., Shen, W., Stamen, R., Tadday, A. Characterisation studies of silicon photomultipliers. *Nucl. Instrum. Methods Phys. Res. A* **2010**, *620*, 217–226.

[67] https://www.electronicsdatasheets.com/manufacturers/hamamatsu/parts/s1036211025c

[68] Caccia, M., Chmill, V., Ebolese, A., Locatelli, M., Martemiyanov, A., Pieracci, M., Risigo, F., Santoro, R. and Tintori, C. An Educational Kit Based on a Modular Silicon Photomultiplier System. *ANIMMA. IEEE Trans. on Nucl. Sci.* **2013**, *978*, 1-7.

[69] https://www.sensl.com/downloads/ds/TN%20-%20Intro%20to%20SPM%20Tech.pdf

[70] Newman, R. Visible Light from a Silicon p-n Junction. *Phys. Rev.* **1955**, *100*, 700 - 703.

[71] Renker, D. Geiger-mode avalanche photodiodes, history, properties and problems. *Nucl. Instrum. Methods Phys. Res. A* **2006**, *A567*, 48–56.

[72] Dietzinger, Ch., Iskra, P., Ganka, T., Eggert, T., Höllt, L., Pahlke, A., Miyakawa, N., Fraczek, M., Knobloch, J., Wiest, F., Hansch, W. and Fojt, R. Reduction of optical crosstalk in silicon photomultipliers. *Proc. SPIE 8460, Biosensing and Nanomedicine V* **2012**, 84601L.

[73] Stoykov, A., Musienko, Y., Kuznetsov, A., Reucroft, S. and Swain, J. On the limited amplitude resolution of multipixel Geiger-mode APDs. *JINST* **2007**, *2*, 1-4.

[74] Johnson, N. L. and Kotz, S., *Urn models and their application*; John Wiley & Sons, Inc. (1977).

[75] https://www.caen.it/products/sp5600e/

[76] https://www.thinksrs.com/products/sr250.html

[77] Chesi, G., Malinverno, L., Allevi, A., Santoro, R., Martemiyanov, A., Caccia, M., and Bondani, M. Optimizing Silicon Photomultipliers for Quantum Optics. *Sci. Rep.* **2019**, *9*, 1-12.

[78] Piemonte, C. and Gola, A. Overview on the main parameters and technology of modern Silicon Photomultipliers. *Nucl. Instrum. Methods A* **2019**, *226*, 2-15.

[79] Afek, I., Natan, A., Ambar, O. and Silberberg, Y. Quantum state measurements using multipixel photon detectors. *Phys. Rev. A* **2009**, *79*, 1-6.

[80] Humer, G., Peev, M., Schaeff, C., Ramelow, S., Stipčević, M. and Ursin, R. A Simple and Robust Method for Estimating Afterpulsing in Single Photon Detectors. *Journal of Lightwave Technology* **2015**, *33*, 3098-3107.

[81] Ramilli, M., Allevi, A., Chmill, V., Bondani, M., Caccia, M. and Andreoni, A. Photon-number statistics with silicon photomultipliers. *J. Opt. Soc. Am. B* **2010**, *27*, 852-862.

[82] Achilles, D., Silberhorn, C., Sliwa, C., Banaszek, K., Walmsley, I. A., Fitch, M. J., Jacobs, B. C., Pittman, T. B., Franson, J. D. Photon-number-resolving detection using time-multiplexing. *J. of Mod. Opt.* **2004**, *51*, 1499-1515.

[83] Fitch, M. J., Jacobs, B. C., Pittman, T. B. and Franson J. D. Photon-number resolution using time-multiplexed single-photon detectors. Phys. Rev. A **2003**, *68*, 1-6.

[84] Arecchi, F. T. Measurement of the statistical distribution of Gaussian and laser sources. *Phys. Rev Lett.* **1965**, *15*, 912–916.

[85] Mandel, L. Sub-Poissonian photon statistics in resonance fluorescence. *Opt. Lett.* **1979**, *4*, 205-207.

[86] Curty, M., Moroder, T., Ma, X. and Lütkenhaus, N. Non-Poissonian statistics from Poissonian light sources with application to passive decoy state quantum key distribution. *Opt. Lett.* **2009**, *34*, 3238-3240.

[87] Zambra, G., Andreoni, A., Bondani, M., Gramegna, M., Genovese, M., Brida, G., Rossi, A. and Paris, M. G. A. Experimental Reconstruction of Photon Statistics without Photon Counting. *Phys. Rev. Lett.* **2005**, *95*, 1-4.

[88] Ferri, F., Magatti, D., Gatti, A., Bache, M., Brambilla, E. and Lugiato, L. A. High-Resolution Ghost Image and Ghost Diffraction Experiments with Thermal Light. *Phys. Rev. Lett* **2005**, *94*, 1-4.

[89] Genovese, M. Real applications of quantum imaging. *J. Opt.* **2016**, *18*, 1-10.

[90] Allevi, A., Andreoni, A., Bondani, M., Genoni, M. G. and Olivares, S. Reliable source of conditional states from single-mode pulsed thermal fields by multiple-photon subtraction. *Phys. Rev. A* **2010**, *82*, 1-8.

[91] Lamperti, M., Allevi, A., Bondani, M., Machulka, R., Michálek, V., Haderka, O. and Peřina, J. Optimal sub-Poissonian light generation from twin beams by photon-number resolving detectors. *J. Opt. Soc. Am. B* **2014**, *31*, 20-25.

[92] Peřina, J., Haderka, O. and Michálek, V. Sub-Poissonian-light generation by postselection from twin beams. *Opt. Express* **2013**, *21*, 19387-19394.

[93] Peřina, J., Michálek, V. and Haderka, O. Higher-order sub-Poissonian-like nonclassical fields: Theoretical and experimental comparison. *Phys. Rev. A* **2017**, *96*, 1-7.

[94] Peřina, J., Haderka, O. and Michálek, V. Simultaneous observation of higher-order non-classicalities based on experimental photocount moments and probabilities. *Sci. Rep.* **2019**, *9*, 1-8.

[95] Chesi, G., Malinverno, L., Allevi, A., Santoro, R., Caccia, M. and Bondani, M. Measuring nonclassicality with silicon photomultipliers. *Opt. Lett.* **2019**, *44*, 1371-1374.

[96] Kalashnikov, D. A., Tan S. H., Iskhakov, T. S., Chekhova, M. V. and Krivitsky, L. A. Measurement of two-mode squeezing with photon number resolving multipixel detectors. *Opt. Lett.* **2012**, *37*, 2829-2831.

[97] Kumar, P. Quantum frequency conversion. *Opt. Lett.* **1990**, *15*, 1476-1478.

[98] Li, R.-D. and Kumar, P. Squeezing in traveling-wave second-harmonic generation. *Opt. Lett.* **1993**, *18*, 1961-1963.

[99] Li, R.-D. and Kumar, P. Quantum-noise reduction in traveling-wave second-harmonic generation. *Phys. Rev. A* **1994**, *49*, 2157-2166.

[100] Huang, J. and Kumar, P. Observation of Quantum Frequency Conversion. *Phys. Rev. Lett.* **1991**, *68*, 2153-2156.

[101] Youn, S., Choi, S.-K., Kumar, P. and Li, R.-D. Observation of sub-Poissonian light in traveling-wave second-harmonic generation. *Opt. Lett.* **1996**, *21*, 1597-1599.

[102] Shen, Y. R. Quantum Statistics of Nonlinear Optics. *Phys. Rev.* **1967**, *155*, 921-928.

[103] Ducuing, J. and Armstrong, J. A. *Proceedings of the Third Quantum Electronics Conference Paris, 1963*; Columbia University Press, New York (1964).

[104] Bonifacio, R. and Preparata, G. Coherent Spontaneous Emission. *Phys. Rev. A* **1969**, *2*, 336-347.

[105] Orszag, M., Carrazana, P. and Chuaqui, H. Quantum Theory of Second-harmonic Generation. *Int. J. Opt.* **1983**, *30*, 259-266.

[106] Crosignani, B., Di Porto, P. and Solimeno, S. Quantum effects in second harmonic generation. *J. Phys. A: Gen. Phys.* **1972**, *5*, 119-121.

[107] Chmela, P. Generation of light of second harmonic frequency in a Gaussian light. *Czech. J. Phys. B* **1973**, *23*, 884-887.

[108] Kozierowski, M. and Tanaś, R. Quantum fluctuations in second-harmonic light generation. *Opt. Commun.* **1977**, *21*, 229-230.

[109] Ekert, A. and Rzazewski, K. Second harmonic generation and statistical properties of light. *Opt. Commun.* **1988**, *65*, 225-227.

[110] Bajer, J. and Peřina, J. Symbolic computation of photon statistics for higher harmonics generation. *Opt. Commun.* **1992**, *92*, 99-104.

[111] Bajer, J., Haderka, O. and Peřina, J. Sub-Poissonian behaviour in the second harmonic generation. *J. Opt. B: Quantum Semiclass. Opt.* **1999**, *1*, 529-533.

[112] Chesi, G., Wauters, M. M., Fasola, N., Allevi, A. and Bondani, M. Second Harmonic Revisited: An Analytic Quantum Approach. *Appl. Sci.* **2019**, *9*, 1-14.

[113] Mostowski, J. and Rzązewski, K. Photon bunching and antibunching in second harmonics generation. *Phys. Lett. A* **1978**, *66*, 275-278.

[114] Shen, Y. R. *The Principles of Nonlinear Optics*, First Edition; John Wiley & Sons, 2002. Yariv, A. *Quantum Electronics*, Second Edition; California Institute of Technology, 1975.

[115] Olivares, S., Allevi, A., Caiazzo, G., Paris, M. G. A. and Bondani, M. Quantum tomography of light states by photon-number-resolving detectors. *New J. Phys.* **2019**, *21*, 1-10.

[116] Chesi, G., Olivares, S. and Paris, M. G. A. Squeezing-enhanced phase-shift-keyed binary communication in noisy channels. *Phys. Rev. A* **2018**, *97*, 1-6.

[117] Wittmann, C., Andersen, U. L., Takeoka, M., Sych, D. and Leuchs, G. Demonstration of Coherent-State Discrimination Using a Displacement-Controlled Photon-Number-Resolving Detector. *Phys. Rev. Lett.* **2010**, *104*, 1-4.

[118] Roccia, E., Cimini, V., Sbroscia, M., Gianani, I., Ruggiero, L., Mancino, L., Genoni, M. G., Ricci, M. A. and Barbieri, M. Multiparameter approach to quantum phase estimation with limited visibility. *Optica* **2018**, *5*, 1171-1176.

[119] Cimini, V., Gianani, I., Ruggiero, L., Gasperi, T., Sbroscia, M., Roccia, E., Tofani, D., Bruni, F., Ricci, M. A. and Barbieri, M. Quantum sensing for dynamical tracking of chemical processes. *Phys. Rev. A* **2019**, *99*, 1-5.

[120] Ehlers, J. and Prasanna, A. R. A WKB formalism for multicomponent fields and its application to gravitational and sound waves in perfect fluids. *Class. Quantum Grav.* **1996**, *13*, 2231-2240.